Regulating peptide self-assembly toward precision & compartmentalization

DEEPIKA GUPTA

A thesis submitted for the partial fulfillment of the
degree of Doctor of Philosophy

Institute of Nano Science and Technology,
Knowledge City, Sector-81, SAS Nagar, Manauli PO, Mohali, 140306, Punjab, India.

Indian Institute of Science Education and Research
Knowledge city, Sector-81, SAS Nagar, Manauli PO, Mohali, 140306, Punjab, India.

December 2021

Dedicated to my parents

Declaration

The work presented in this thesis has been carried out by me under the guidance of Prof. Asish Pal at the Institute of Nano Science and Technology, Mohali. This work has not been submitted in part or in full for a degree, a diploma, or a fellowship to any other university or institute. Whenever contributions of others are involved, every effort is made to indicate this clearly, with due acknowledgement of collaborative research and discussions. This thesis is a bonafide record of original work done by me and all sources listed within have been detailed in the bibliography.

Deepika Gupta

In my capacity as the supervisor of the candidate's thesis work, I certify that the above statements by the candidate are true to the best of my knowledge.

Prof. Asish Pal

Acknowledgments

The journey of Ph.D. is more than just performing research. Learning, brainstorming, collaborating are important parts of my life during the last five years. Looking back, I see individuals who have been supportive, kind and inspirational and I'm full of gratitude to them.

First and foremost, I would like to give my sincerest thanks to my Ph.D. supervisor, Prof. Asish Pal, for giving me this fantastic opportunity to be a part of his research group. His consistent guidance, scientific vision, words of encouragement, enthusiasm and knowledge positively impact my research work. I am grateful for all the support, trust and creative freedom you gave me. Thank you for encouraging me to join all the conferences, workshops, courses, lectures and meetings where I learned a lot. I really appreciate all the time you spent on correcting manuscripts and quickly reviewing the thesis in spite of your busy schedule. Thank you for all the dinners, for taking us on wonderful trips to Dalhousie, Nepli trek and for encouraging to participate in marathons. At last, thanks a lot for suggestions and help with my post-doc applications also.

I would also like to thank my doctoral committee members, Dr. Sharmistha Sinha and Dr. Debabrata Patra for annually reviewing and giving valuable suggestions for uplifting the quality of my research work. I would like to thank my external SRF committee member, Prof Sanjay Jachak from NIPER Mohali for his amiable support and advice in work.

I would like to appreciate my lab members with whom I have spent most of my time during the last five years. It is my pleasure to pay sincere thanks to Dr. Ashmeet Singh, for teaching me various instruments, techniques, installing useful software and assisting me to initially kick off my research journey in the field of peptide self-assembly. Thanks for being there as a supportive senior and I hope to never disappoint you for the trust you have in me. Dr. Jojo P. Joseph, thank you for arranging chemicals in urgency and doing some experiments for me during the lockdown. I really enjoyed working with you in PU and CIAB labs. I would like to acknowledge a special person, Chirag for being there in my highs and lows. I am blessed to have such a kind and supportive person working closely with me. Thank you for all characterization at PU, analyzing the SAXS data and also teaching me patiently. I really appreciate your hard work and time invested to set up and manage our lab for smooth functioning. Nimisha, Antarlina, Debasish, Jahanvi, Pratibha and Vysakh: many thanks for the cheerful and healthy time together in the group, chats and small parties with you people that lightened my days. You people are amazing lab-mates and thanks for all proof-readings. I acknowledge Dr. Nidhi Gupta, Nitha George and Dharmendra Sablaniya for being kind and supportive to my work.

A big thank is due to my collaborator Dr. Sarit Agasti, Simanta Kalita and Ranjan Sasmal from JNCASR, Bengaluru for all SIM-super-resolution experiments and for providing valuable insights into the work. I really appreciate you for making my stay in JNCASR a comfortable and fruitful one. Thanks to Dr. Aasheesh Srivastava and Manas from IISER Bhopal for all the discussions regarding transient and anion responsive self-assembly.

I am indebted to our internal collaborators Dr. Md. Ehesan Ali and Aashish Bhatt for performing computational studies that enriched our understanding regarding host-guest complexation for our system. I am grateful to Dr. Dipankar Mandal and Varun for introducing me to piezoelectric materials and performing as well as teaching PFM for our collaborative work. I really respect the efforts of all the collaborators from bottom of my heart.

I would like to thank the founder-director of INST, Prof. Ashok Kumar Ganguli for giving me an opportunity in INST as a Ph.D. student, former director, Prof. H. N Ghosh and present director Prof. Amitava Patra for support, encouragement and research facilities.

I would like to record my gratitude to wonderful girls, my roomies for four years- Babita, Arti, Navneet, Taniya and Antara. They have enriched my life in one way or another and made those days so unforgettable. Big thanks to Neha, Shaifali and Neethu for being fantastic people, helping friends and neighbors in my hostel room. I will remember those endless chats with loads of fun.

Initial four years, I have spent maximum time in the INST lab at IISER, Panjab University and CIAB campus and worked in a common lab space with fantastic and cooperative people with diverse scientific backgrounds. I would like to express my gratitude to all of them for sharing their experience and knowledge especially Dr. Naimat and Dr. Praveen for helping me with their expertise. I cannot forget my batch mates and lab mates in shared labs- Selim, Aashish, Venu, Khalid, Soumadri, Sushil, Prabhleen, Aditi, Aashima, Ruby, Ajay, Mujeeb, Rohit, Zubair, Ankush ma'am, Arpana, Pooja, Mishra ji and others for making every moment of my tenure worth remembering. There are so many fellow scholars whose name is not mentioned but they made my days happy with their bright smile.

I want to acknowledge HPLC engineers - Shyam, Arvind, Jitesh Thakur Mayank and Hiteshwar- for all the timely installation, troubleshooting and demonstrations. I am also grateful to the peptide synthesizer engineers (Balbir and Jayati) for providing quick technical assistance. I really appreciate that you people try to solve problems over phone calls and plan the visit as soon as possible. Thanks to Malvern GPC engineers (Vikrant and Sombir) for teaching me GPC instrumentation.

I am also thankful to Ravinder Singh Ji for shuttling us between various labs in the transient campus, Vikram Ji and hostel mess members for serving delicious, hygienic food and security guards for ensuring a safe environment.

I would like to acknowledge INST for providing the research facilities, instruments, research funding, space and state-of-art infrastructure for conducting my research and hostel room for staying during last year.

Last but not least, big hugs to the most special people in my life. Dad, Mom, Pooja and Vishal, thanks for trusting me, inspiring me and giving me full support over the years.

Table of contents

Acronyms

pH	The negative logarithm of hydronium-ion concentration ($-\log_{10} [H_3O^+]$)
UV-vis	UV-Visible Spectroscopy
FTIR	Fourier Transform Infrared
TEM	Transmission Electron Microscopy
CD	Circular Dichroism
SAXS	Small-Angle X-ray Scattering
NMR	Nuclear Magnetic Resonance
AFM	Atomic Force Microscopy
PFM	Piezoresponse Force Microscopy
CLSM	Confocal Laser Scanning Microscopy
ITC	Isothermal Calorimetry
HPLC	High-Performance Liquid Chromatorgraphy
FRET	Förster Resonance Energy Transfer
HFIP	Hexafluoroisopropanol
α-CD	α-Cyclodextrin
β-CD	β-Cyclodextrin
Fmoc	Fluorenylmethyloxycarbonyl
ITO	Indium Tin Oxide
ATP	Adenosine Tri-Phosphate
ADP	Adenosine Di-Phosphate
DNA	Deoxyribonucleic Acid
CDSA	Crystallization-Driven Self-Assembly
SSP	Seeded Supramolecular Polymerization

Abbreviations

λ	Wavelength
α	Alpha
β	Beta
Σ	Sigma
Δ	Delta
π	Pi
°C	Degree Centigrade
Å	Angstrom
pm	Picometer
nm	Nanometer
µm	Micrometer
cm	Centimeter
mL	Millilitre
µL	Microlitre
µM	Micromolar
mM	Millimolar
mV	Millivolt
nA	Nanoampere
mdeg	Millidegrees

Synopsis

Chapter 1: Introduction

The chapter discusses molecular self-assembly, a powerful approach to fabricate well-ordered multicomponent multifunctional materials in a bottom-up manner. Such self-assembly processes are rather ubiquitous in nature and employ out-of-equilibrium pathways. A number of strategies to realize out-of-equilibrium self-assembly in synthetic systems are discussed. With regards to the kinetically controlled nanostructures, parameters such as solvent composition, temperature, intramolecular H bonding, folded and unfolded states of monomer play a vital role to alter the self-assembly pathways that are elaborated for different design strategies. Moreover, seeded supramolecular polymerization exploiting the living nature of seeds to exhibit a precise control over the size and shape of self-assembled structures are discussed in detail for a number of diverse systems.

Next, biocompatible short peptides as the building blocks for supramolecular polymerization under non-equilibrium conditions are elaborated owing to their multiple non-covalent interactions. We discussed various reports about orthogonal self-assembly encoded by the molecular recognition in the building blocks such as the site of non-covalent interaction, pK_a, chirality *etc*. With this regard, a special focus is laid on the chirality effects on regulating peptide self-assembly towards chiral self-sorting and coassembly of racemic peptides. The objective of the work described here is to enhance our understanding of rationally designing artificial smart materials with precise spatiotemporal control over the nanoarchitectures and compartmentalization mediated by orthogonal self-assembly.

Chapter 2: Photochemically sequestered off-pathway dormant states of peptide amphiphiles for predictive on-demand piezoresponsive nanostructures

Supramolecular assemblies are essential for specific biological functions and mandate precise control over the mesoscopic scale for higher functional efficiency. Such well-defined biomimetic self-organization can be accessed through kinetically controlled non-equilibrium transformations rather than the typical downhill thermodynamically driven processes. Recently, spatiotemporal control for the living supramolecular polymerization has rendered a paradigm shift towards designing complex multicomponent supramolecular active materials; however, directing the active monomer towards predictive kinetically trapped materials still remains a considerable challenge as that necessitates circumventing spontaneous nucleation of the monomers during the self-assembly process. Herein, we demonstrate dual strategies (chemical and photo) to sequester the active peptide self-assembling motifs in dormant states that upon judicious activation, engage in controlled seeded supramolecular polymerization in aqueous milieu for the first time (Scheme 2.1). Amyloid inspired peptide with pendant azobenzene moiety demonstrates the formation of on-pathway metastable nanoparticles by the interplay of solvent and temperature that could be transformed into kinetically controlled nanofibers and thermodynamically controlled twisted bundles.

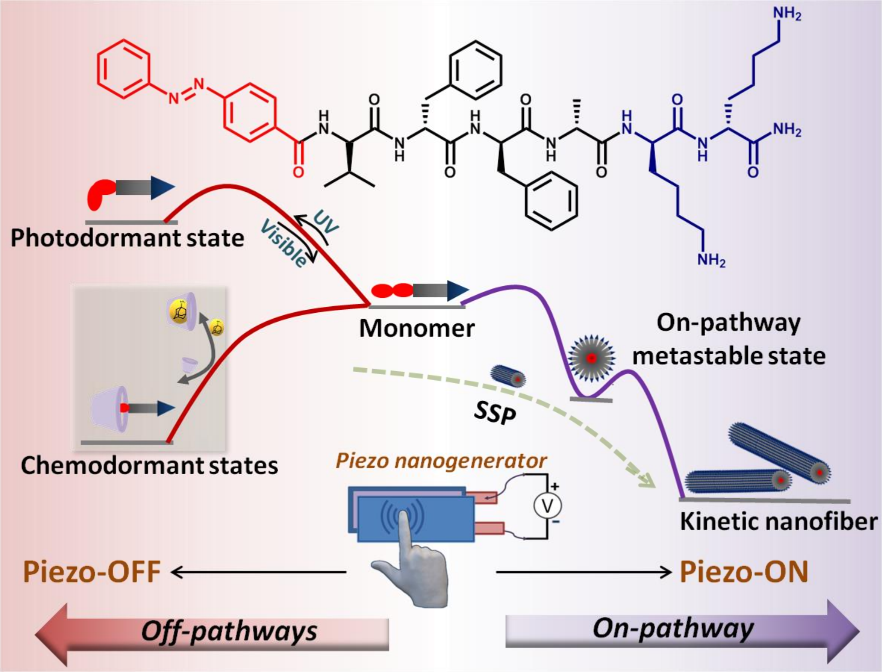

Scheme 2.1: Chemo- and photo regulated coupled equilibria to sequester the active monomers of azobenzene tethered peptide amphiphile into off-pathway dormant states and on-demand activation to employ in seeded supramolecular polymerization for programmable on-off piezoresponsive peptide nanostructures.

Further, using coupled equilibrium such as host-guest inclusion complex with cyclodextrin or photoisomerization with UV light leads to the formation of two distinct off-pathway metastable states that retard the spontaneous supramolecular polymerization. A judicious manipulation of the free energy landscapes in tandem with suitable chemical and photo stimuli renders activation of the dormant states for peptide self-assembly through a seeded growth strategy. Finally, such photochemical sequestrations of self-assembly pathways result in on-off piezoresponsive peptide nanostructures. In summary, we demonstrated for the first time the non-equilibrium peptide self-assembly coupled with dormant metastable states to allow access to an interesting repertoire of structural diversities and attenuated piezoresponse control in supramolecular peptide nanostructures.

Chapter 3: Stimuli-responsive self-assembly-disassembly in peptide amphiphiles to endow block-co-fibers and tunable piezoelectric response

Peptide nanofibrous networks having a unique and spatially controlled response to the assembled and disassembled states have emerged as suitable class of futuristic materials. This necessitates tethering stimuli-responsive components to the peptide amphiphiles to induce on-demand response for materials' applications. In this context, ferrocene (Fc) can be exploited as a redox-responsive building unit owing to its reversible oxidation and reduction between non-polar ferrocenyl and polar ferrocenium cation. Conjugation of ferrocene with self-assembling peptides endows supramolecular polymers with modular properties to design precisely regulated supramolecular systems.

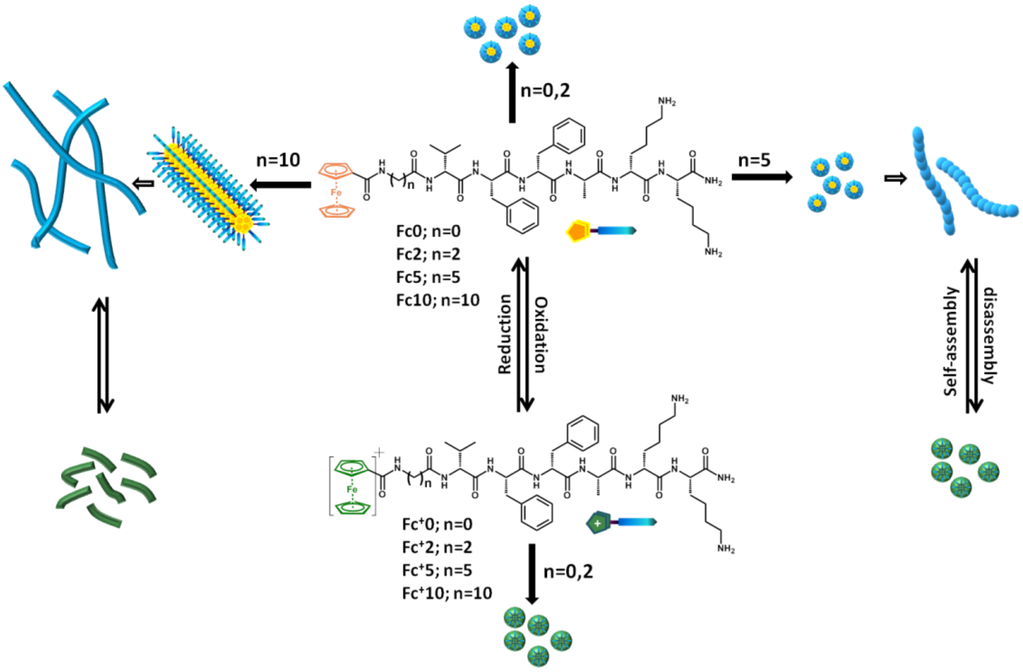

Scheme 3.1: Chemical structure of ferrocene conjugated peptide amphiphiles. Schematics showing the variation of the alkyl spacer results into different nanostructures and redox-responsive assembly/disassembly.

We anchored ferrocene moieties to short amyloid inspired peptide fragment using hydrophobic alkyl spacers of variable chain lengths (Scheme 3.1) to furnish Fc-VFFAKK (**Fc0**), Fc-C_2-VFFAKK (**Fc2**), Fc-C_5-VFFAKK (**Fc5**), Fc-C_{10}-VFFAKK (**Fc10**). The self-assembly in water exhibited that a long methylene spacer (C_{10}) in **Fc10** increased the propensity to form nanofibers, while a critical methylene spacer length of C_5 is essential for robust self-assembly. Moreover, judicious oxidation and reduction of the ferrocene moiety provided an additional tool to obtain structural control over the assembly-disassembly of the peptide amphiphiles. Lastly, we demonstrated the formation of mixed block co-fibers comprised of redox-responsive periphery and redox-insensitive cores as mediated by the seeded supramolecular polymerization.

Chapter 4: Enzyme responsive chiral self-sorting in amyloid-inspired minimalistic peptide amphiphiles

Self-sorting is a spontaneous phenomenon that ensures the formation of complex yet ordered multicomponent systems and conceptualizes the design of artificial and orthogonally functional compartments. In the present study, we envisage the chirality mediated self-sorting in β-amyloid inspired minimalistic peptide amphiphiles (C_{10}-*L/D*-VFFAKK) based nanofibers (Scheme 4.1). The fidelity and stereo-selectivity of the chiral self-sorting was ascertained by Förster Resonance Energy Transfer (FRET) by judicious choice of pyrene-hydroxy coumarin donor-acceptor pair tethered to the peptide sequences.

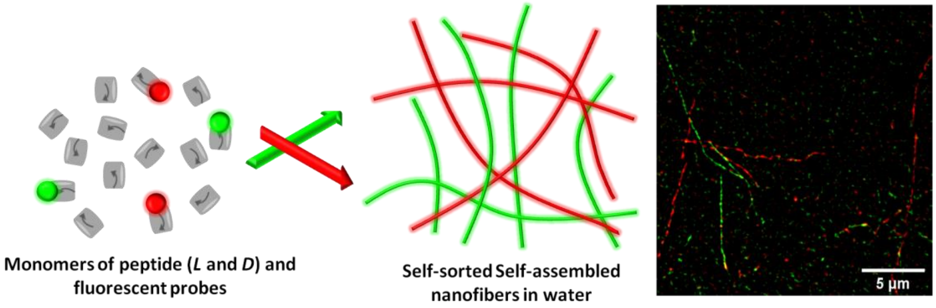

Scheme 4.1: Chirality-driven self-sorting in peptide nanofibers that further exhibits enantioselective enzymatic degradation for *L*-peptide fibers over their *D*-counterpart as visualized by super-resolution microscopy

Seed promoted elongation of the homochiral peptide amphiphiles through AFM image analyses and Thioflavin-T (ThT) binding study further validated the chiral recognition of the *L/D* peptide nanofibers. Moreover, direct visualization of the chirality-driven self-sorted nanofibers are reported through super-resolution microscopy that exhibits enantioselective enzymatic degradation for *L*-peptide fibers. Such enantioselective weakening of the hydrogels may be used in designing stimuli-responsive orthogonal compartments for delivery applications.

Chapter 5: Fidelity of self-sorting and mixed co-block supramolecular polymerization in peptide amphiphiles as dictated by the methylene spacer between bis-urea motifs

Nature has its elegant and ubiquitous manner of retaining multiple self-assembled compartments as dictated by the orthogonal and precisely controlled molecular recognition that is rather challenging to mimic in the lab. Despite recent advances in supramolecular polymerization, such control over the spatial distribution and order in complex self-assembled systems is still in its nascent stage. In this regard, multicomponent systems with minimum structural variation are of significant importance to design highly complex functional materials. Thus, we investigated the structural fidelity of multiple peptide amphiphiles to furnish possible self-assembled scenarios such as randomly co-assembled, self-sorted or co-block nanofibers. We design the two peptide amphiphiles that differ in the methylene chain length between bis-urea motifs (Scheme 5.1). Here, the chain length of methylene spacer (*i.e.* four and six) between the bis-urea motifs controls the fidelity of self-assembly towards either self-sorting or co-assembly.

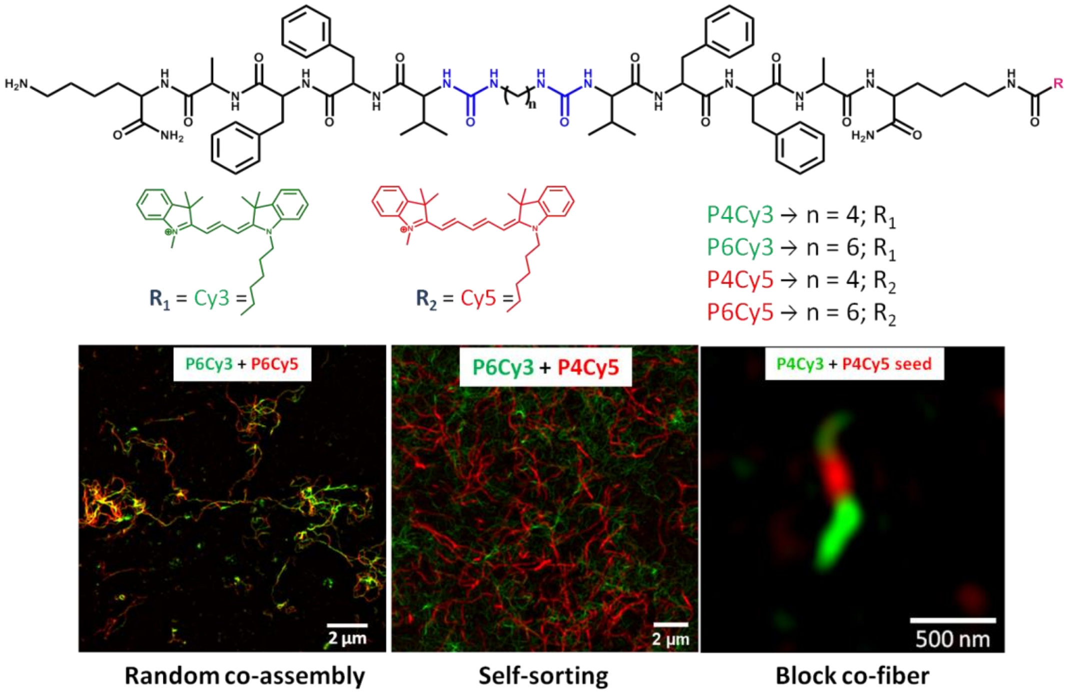

Scheme 5.1: Molecular structures of fluorescent dye conjugated bis-urea peptides amphiphiles. Molecular recognition among the amphiphiles furnish co-assembled nanofibers with matching spacer, self-sorted nanofibers with non-matching spacer and block co-fiber through seeded supramolecular polymerization.

Further, green colored Cy3 and red colored Cy5 fluorophore are anchored on the peptide bolaamphiphiles to gain more insight into self-assembly pattern using super-resolution microscopy. The two-component peptide system differing in spacer size is realized to create randomly co-assembled and orthogonal networks. Co-assembly of monomers (either **P4Cy3** & **P4Cy5** or **P6Cy3** & **P6Cy5**) results in the random sequence of monomers in a fiber owing to efficient intermolecular H bonding between urea units with the same methylene spacer. On the other hand, self-sorted homomeric nanofibers are achieved with amphiphiles with non-matching spacer size (either **P4Cy3** & **P6Cy5** or **P6Cy3** & **P4Cy5**). Finally, supramolecular block co-fibers with seeds and monomers of matching spacer length are achieved with seed-mediated supramolecular polymerization and are validated through FRET and SIM-super-resolution microscopy.

1

Introduction

Molecular self-assembly is a powerful "bottom-up" approach to fabricate well-ordered multicomponent functional materials and has been studied extensively over the last few decades. The ubiquitous self-assembly present in nature is governed by the non-equilibrium pathway that furnishes controlled organization and functioning of complex components. However, in the laboratory, such precise control over the fate of self-assembly has not yet been achieved properly with detailed mechanistic control.

The objective of the work described in this thesis is to enhance our understanding of rationally designed artificial systems with precisely controlled activity and compartmentalization. In order to do so, we studied different aspects of molecular design to dictate the fate of the self-assembly processes. These studies are foreseen to have important implications for developing structurally and functionally complex yet controlled materials taking inspiration from natural self-assembled systems.

1.1. Supramolecular polymerization

Supramolecular polymerization is a ubiquitous process where the molecular building blocks are connected spontaneously and autonomously into the ordered structure through reversible, specific, directional and tunable non-covalent interactions such as hydrogen bonds, ionic forces, aromatic π-π stacking, hydrophobic interactions, van der Waals interactions and host-guest complexation.[1-7] Dynamic nature of these reversible non-covalent interactions within the components leads to a plethora of exciting nanoarchitectures with tunable properties which can have next-generation applications ranging from biomedical fields to energy harvesting devices.[8-13] Living active matter has complex composition and precise structures with such supramolecular interactions playing a remarkable role in the functioning of biological systems. Mimicking anatural living system demands a thorough understanding of the concept of self-assembly, molecular recognition, confinement or compartmentalization, and cascade enzymatic reactions to achieve tremendous complexity and precise spatiotemporal control in heterogeneous environments. The emergent properties of natural material rely on its toolbox *i.e.* structural and chemical properties of building motifs.[14] For instance, in the cell cytoskeleton the protein monomers self-assemble to furnish ordered long filaments and disassemble to render monomers, the cell membrane is formed through the hydrophobic interactions among phospholipids.[15] Similarly, hydrogen bonding among nucleobases of DNA leads to the formation of double-helical structure, protein folding through various non-covalent interactions into the tertiary and quaternary structures, and triple helical structure of collagen[16] are a few sources of inspiration from nature to understand mechanistic details of self-assembly processes.

Thus understanding the principle of natural self-assembly, we aim to design and develop smart functional biomimetic materials. Moreover, it also provides us more insight about the understanding of evolution and the origin of life by self-replication of simple building blocks with selectivity at nanometer scale. Over the past few decades, researchers have successfully engineered artificial materials with encoded chemical information as the functionalities in the building blocks. These molecules result into self-assembled architectures whose fate can be dictated by environmental conditions like pH, temperature, solvent, composition and method of preparation. Further, the fascinating stimuli-responsive molecules are unique, interesting and versatile for a variety of applications ranging from biomedical devices in regenerative medicine to nanoelectronics.

To develop materials with such futuristic applications, we should have a fundamental understanding of supramolecular systems to rationally create new innovative functional materials. Supramolecular polymerization can be divided into three categories according to growth mechanisms (Scheme 1.1).[17-19]

<u>Isodesmic</u>: Binding constants among the building blocks are same throughout the self-assembly process with the nucleation constant (K_N) equal to the elongation constant (K_E); $K_N = K_E$. Here, usually, only one kind of non-covalent interaction is dominating. This is similar to the "step-growth" polymerization of conventional covalent polymers.[20]

<u>Anti-cooperative</u>: The nucleation rate is faster than the elongation rate with $K_N > K_E$. Here, usually repulsive interactions become dominating after initial aggregation.

<u>Cooperative</u>: The nucleation rate is much slower than the elongation rate with $K_N < K_E$. This can also be termed as nucleation-elongation mechanism and can be understood in two steps. The first nucleation step is slow aggregation process which happens at some critical concentration and temperature (Scheme 1.1). Once a nucleus is formed, further aggregation of the monomers is comparatively faster. This is similar to the "chain-growth" polymerization with an "active" growing chain that can further control dispersity through living supramolecular polymerization.[21]

Generally, the isodesmic model drives the supramolecular polymerization towards single thermodynamically stable aggregates but in the case of cooperative (nucleation-elongation) mechanism, multiple structures are possible which are achieved through contributions of the kinetic pathway.[22] Such different processes are elaborated in detail in the next section.

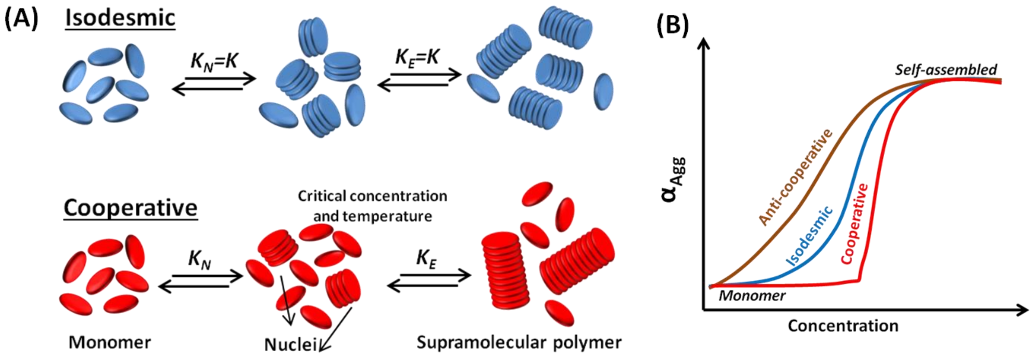

Scheme 1.1: (A) Supramolecular polymerization in isodesmic and cooperative mechanisms. (B) The plot of the fraction of aggregated molecules with concentration depicts the curve for different growth mechanisms.

1.2. Energy landscapes for self-assembly processes

The chemical reactions normally carried out in the laboratory fundamentally differ from what happens in natural systems. Traditionally, chemists have been focusing on the design and synthesis of molecules which are thermodynamically stable (*i.e.* the systems at equilibrium). However, the kinetic products have only been viewed as transition states or high energy intermediates and have not been explored much. The self-assembled structures that sustain life do not have an on and off switch akin to the thermodynamic self-assembly but it is a dynamic process where a stop of energy flow results in the end of life. Hence the natural processes exist in far-from-equilibrium conditions. However, in recent times scientists are developing chemical systems that can emulate such non-equilibrium processes. Broadly, three different systems can be identified as follows:

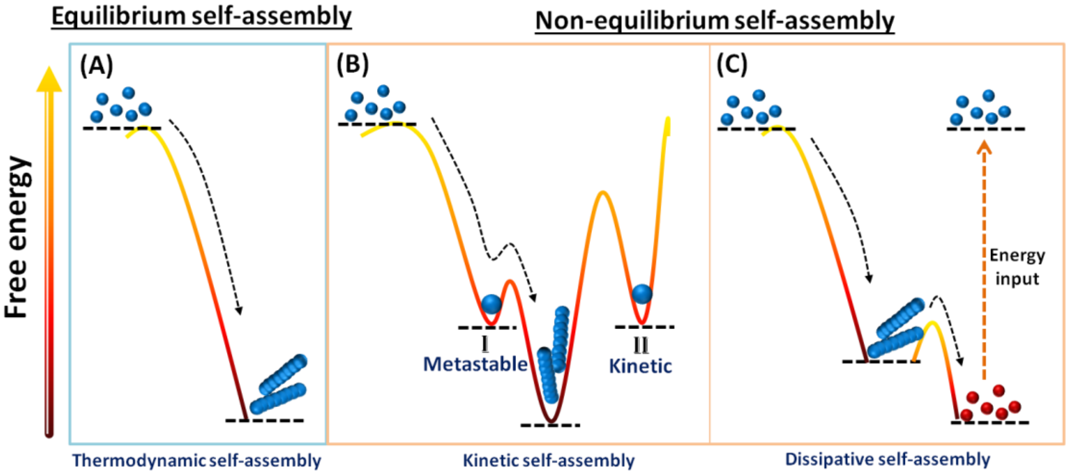

Scheme 1.2: Energy Landscape diagram for different self-assembly processes. (A) Thermodynamically driven self-assembly. (B) Non-dissipative non-equilibrium self-assembly with pathway complexities to (I) metastable state and (II) kinetically trapped state. (C) Dissipative non-equilibrium self-assembly.

1.2.1. Thermodynamic in-equilibrium self-assembly

Equilibrium self-assembled product resides in the global minima of the energy landscape diagram (Scheme 1.2A). Here, the obtained self-assembled structure as dictated by the non-covalent interactions is the most stable assembled state that does not depend on the timescale, path or rate to reach equilibrium. Such equilibrium structures are reversible leading to the dynamic nature of assemblies with continuous exchange of monomers between solution and self-assembled states and always keeps on self-correcting themselves to remain in global minima. The energy is neither introduced nor released from the system. However, it is noteworthy that the morphology of thermodynamically stable assembly may still depend on multiple factors *e.g.* solvent, temperature, order of addition *etc*. and still may be manipulated by varying any of these external parameters. A number of mathematical models have been studied to understand the mechanism of self-assembly for such one-dimensional aggregate.[23] Such supramolecular polymers held by various non-covalent interactions have also been explored for various applications including muscle-like active matter.[24]

The thermodynamic self-assembly started with the evolution of the field of supramolecular self-assembly. However, to harness the maximum benefit out of self-assembly, this field is gradually making a shift towards far-from-equilibrium systems. As already discussed, equilibrium structures reside in the minimum energy state and thus, by tweaking this free energy, new states can be created to achieve non-equilibrium systems.

1.2.2. Non-equilibrium self-assembly

1.2.2.1. Non-dissipative non-equilibrium self-assembly: Non-equilibrium systems are confined in the local minimum and not in the global minimum of the energy landscape (Scheme 1.2B). Interestingly, the height of the energy trap in the energy landscape gives rise to two interesting scenarios - kinetically trapped states and metastable states. If the system is trapped and the energy barrier to cross for attaining thermodynamic minimum is small then it can eventually reach the global minimum with time. This non-equilibrium condition is termed as metastable state (I) and multiple metastable states are possible along the way to reach equilibrium. These metastable states are like intermediate steps of supramolecular reaction with the limited time period. On the other hand, if the energy barrier is high enough and cannot be crossed over for a reasonable time scale, this is the characteristic of a kinetically trapped state (II). They remain trapped in the local minima and can be eventually released to the equilibrium state with meticulously designed experimental modifications. Thus, such non-equilibrium systems are really fascinating, as starting with the same building block a variety of desired assembly states can be accessed by rationally developing the preparation methodology to dictate the pathway. In one such example, bilayer of vesicles was formed by phospholipids under kinetic conditions with transient products while the size and shape of self-assembly was controlled by trapping the molecules into different kinetic states as dictated by the concentration.[25] Such pathway-dependent self-assembly opens up a plethora of opportunities to develop materials with features like adaptive and self-replication properties.

1.2.2.2. Dissipative non-equilibrium self-assembly: These systems continuously consume energy or matter to stay in dissipative non-equilibrium states and as soon as the influx of energy stops, the system self-relaxed to either a thermodynamic state or kinetic state (Scheme 1.2C). These processes involve the use of chemical or photo fuel with continuous generation and removal of waste products. A typical dissipative self-assembled system can be understood in the following characteristics: The precursor molecules are very stable with minimum energy profile and the driving forces for these processes are usually irreversible chemical reactions. These inactive precursors can be converted to an activated molecule in the presence of fuel; these active molecules with relatively more energy (higher local minimum) are building blocks for further self-assembly (lower local minimum). After some time, another *in-situ* chemical reaction converts the active building blocks to the original inactive precursor molecules with the lowest energy. Here, the system continuously dissipates and absorbs energy but a constant supply of energy can maintain a steady state. Dynamic self-assembly of actin filament by the hydrolysis of ATP (chemical reaction; ATP to ADP conversion) is an excellent example of dissipative out-of-equilibrium self-assembly. The whole process is regulated by the kinetics of the reaction cycle and molecular assemblies. This opens up interesting opportunities for chemists to develop smart functional materials with emerging structures possessing unique properties that can perform complex functions.

1.3. Kinetically controlled supramolecular systems

Over the last few decades, scientists have extensively designed thermodynamically controlled materials that undergo chemical and physical changes in response to external stimuli such as reaction conditions, mechanical agitation, light or magnetic field. Thermodynamically controlled static and at equilibrium structures involving specific molecular recognition can only make crystals but nothing close to the living cells. Very recently, the incredible active and adaptive synthetic non-equilibrium materials have been developed that are inherently metastable akin to the biological systems.[26] Such non-equilibrium systems can be accessed by varying experimental conditions, for instance, designing molecules with competitive intra- and inter-molecular hydrogen bonding, using “good solvent” and “bad solvent” for monomers, retarding aggregation at low temperatures. Basically, these specific parameters are defined to keep the individual monomers in such states that are not prone to spontaneous nucleation. Thus, inactive/dormant monomers are trapped in kinetic state and induce aggregation only in the presence of some activators.[27] Moreover, the emerging field of system chemistry[28] in the quest of understanding the origin of life encourages the chemists to explore the self-replicating, dynamic chemical networks, dissipative non-equilibrium peptide materials.[29-33]

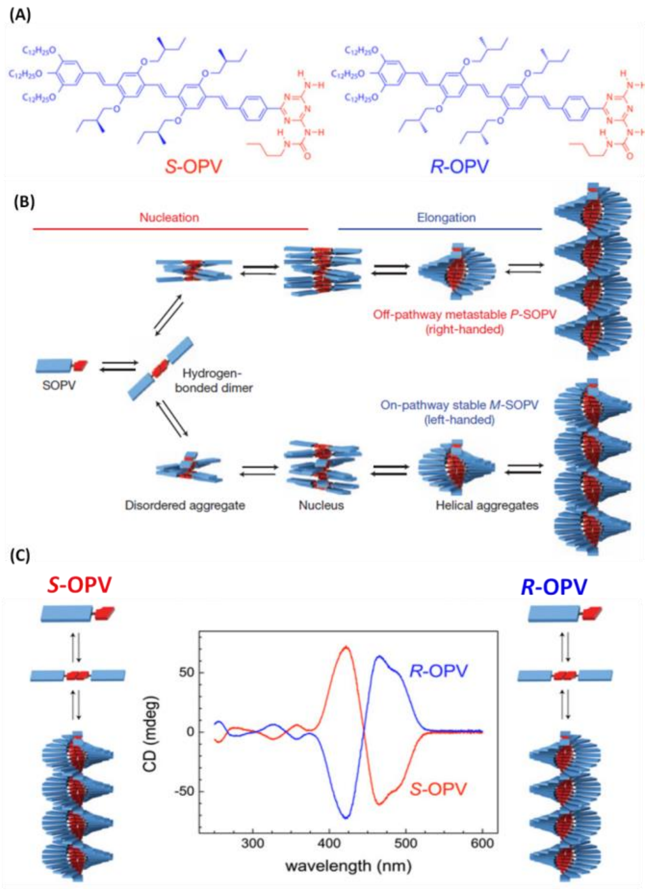

Scheme 1.3: (A) Molecular structures of *S*- and *R*-chiral OPV. (B) Schematic representation of the two competing aggregation pathways of *S*-OPV. Initially formed hydrogen-bonded dimer self-assembles into helical stacks via a nucleation–elongation growth mechanism where right-handed *P*-helices form quickly but are less stable than the slowly formed left-handed *M*-helices. Reprinted with permission from reference 34. Copyright © 2012 Springer Nature. (C) CD spectra depict both enantiomers assemble into helical stacks with left-handed (*S*-OPV) and right-handed (*R*-OPV) helicity. Reprinted with permission from reference 35. Copyright © 2013 National Academy of Sciences.

The pathway complexity in supramolecular systems with metastable aggregates which eventually converted to thermodynamic stable assemblies is elegantly described by Korevaar *et al*. They monitored the supramolecular polymerization kinetics of *S*-chiral oligo(*p*-phenylenevinylene) (*S*OPV) using stopped-flow CD spectroscopy (Scheme 1.3A). The initial formation of less stable right-handed helical off-pathway metastable aggregate (*P*-*S*OPV) eventually converted to left-handed helical on-pathway thermodynamically stable aggregate (*M*-*S*OPV) through a nucleation-elongation mechanism (Scheme 1.3B). Detailed kinetic model calculations revealed that two parallel and competing pathways lead to different helical aggregates.[34] Later in 2013, they further investigated the co-assembly kinetics of two monomers, the *R*- and *S*-chiral enantiomers of a π-conjugated oligo(*p*-phenylene vinylene) derivative. Here, the overall chirality is dictated by the "majority rule" where all the aggregates take over the helicity directed by the major enantiomer (Scheme 1.3C).[35]

Further, achieving precise structural control over the dispersity of the self-assembled states in artificial materials is a rather challenging task and has been of great interest for chemists in the recent past. Materials with narrow polydispersity values are attractive as various properties can be reproduced and tailor-made as per requirement. In the case of covalent polymers, the technique called living polymerization can control the molecular weight distribution of polymer and revolutionize the synthesis protocol of block copolymers. Atom transfer radical polymerization (ATRP), reversible addition fragmentation chain-transfer polymerization (RAFT), ring-opening polymerization (ROP) andnitroxide-mediated radical polymerization (NMP) are different types of living radical polymerization techniques. Similar to this concept, structural precision can be attained in supramolecular systems by "living supramolecular polymerization". The supramolecular structures with narrow polydispersity create structurally precise artificial functional materials to take the scientific community one step closer to mimicking nature. In a pioneer work by Winnik, Manners and co-workers, the cylindrical block copolymer micelles having semicrystalline core-forming polyferrocenylsilane block self-assemble by solvophobic-solvophilic balance utilizing crystallization-driven self-assembly (CDSA). Sonicated seed micelles (initiator) with narrow polydispersity propagate in the presence of fresh monomers through bidirectional epitaxial growth resulting in monodisperse nanocylinders of controlled length (Scheme 1.4).[36, 37]

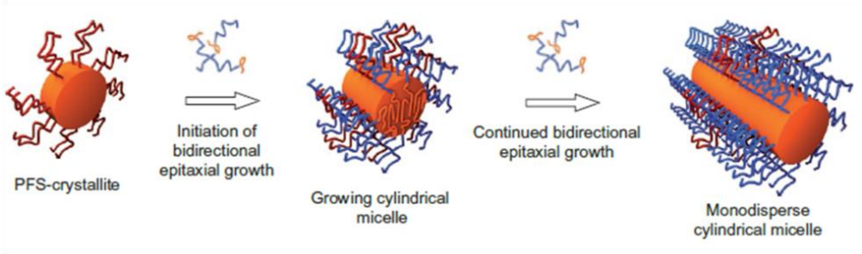

Scheme 1.4: Schematic representation of growth from small, uniform, stub-like crystallites into monodisperse cylindrical micelles through bidirectional epitaxial by CDSA. Reprinted with permission from reference 36. Copyright © 2010, Nature Publishing Group.

In another report, Aida *et al.* presented an elegant strategy by transforming the intramolecular H bonding of the initiator into intermolecular H bonding to tune the length and size of the polymer with monomer to initiator ratio. The corannulene-based chiral monomer was trapped into a metastable state by intramolecular H bonding in methylcyclohexane disabling the spontaneous supramolecular polymerization (Scheme 1.5). However, the addition of n-methylated derivative of monomer initiates unidirectional chain growth with initiator unit at one end and other growing end having free amide C=O groups forming an initiator-monomer complex that further propagates.[38]

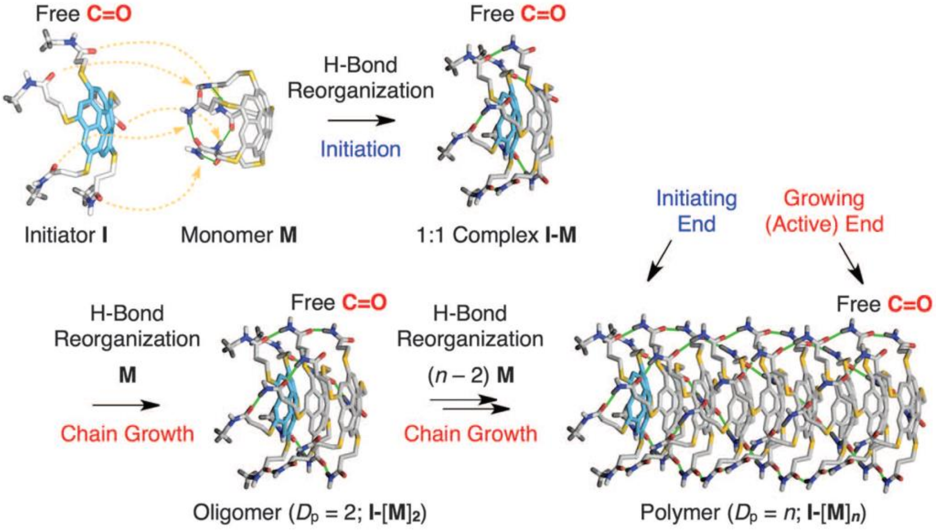

Scheme 1.5: Schematic representation of chain-growth supramolecular polymerization by the H bond reorganization of monomer (M). The growing chain carries an initiating end and a growing (active) end which has free amide C=O groups. Here, bimolecular coupling of the propagating ends is not possible. Reprinted with permission from reference 38. Copyright © 2015 American Association for the Advancement of Science.

The pioneer group of Takeuchi, Sugiyasu and co-workers demonstrated the bi-directional growth with length and shape control by living supramolecular polymerization. The Zn-complexed porphyrin derivatives assemble to form J-aggregated ($\mathbf{1}_{\mathbf{J\text{-}agg}}$) nanoparticles upon cooling and eventually rearrange to form H-aggregated ($\mathbf{1}_{\mathbf{H\text{-}agg}}$) nanofibers (Scheme 1.6A). However, both J- and H-aggregates disassemble to the monomer on heating. The formation of kinetic off-pathway J-aggregates follows the isodesmic model while thermodynamically stable H-aggregates are formed using a cooperative model. The monodisperse seeds from H-aggregates were prepared and added to the J-aggregates which resulted in spontaneous polymerization without any lag time.[39] The phenomenon of living supramolecular polymerization was further realized to control the shape of assemblies ranging from nanoparticles to one-dimensional nanofibers and two-dimensional nanosheets respectively

(Scheme 1.6B-C).[40] Recently, CDSA approach was applied to study B−A−B type tri-block supramolecular copolymer from such metal complexed porphyrins.[41]

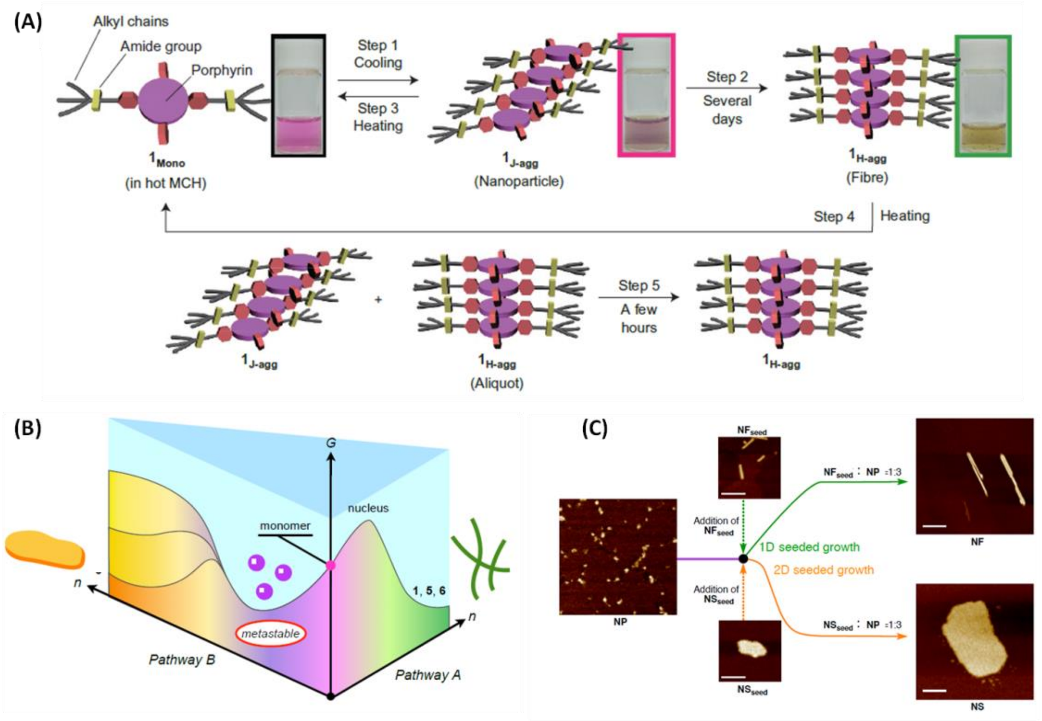

Scheme 1.6: (A) Schematic representation of the self-assembling behavior of Zn-porphyrin derivative (**1**) in methylcyclohexane (MCH). **1$_{\mathbf{Mono}}$** self-assembles on cooling to form nanoparticles (**1$_{\mathbf{J\text{-}agg}}$**) and after several days converted in fibers (**1$_{\mathbf{H\text{-}agg}}$**). These steps are reversible and heating the self-assembled fibers renders to **1$_{\mathbf{Mono}}$.** Growth of **1**$_{J\text{-}agg}$ to **1$_{\mathbf{H\text{-}agg}}$** speed up in the presence of an aliquot of **1$_{\mathbf{H\text{-}agg}}$.** Reprinted with permission from reference 39. Copyright © 2014 Springer Nature. (B) Pathway A transforms monomer of porphyrin derivatives into nanofibers by nucleation-elongation mechanism and pathway B follows the isodesmic model to render kinetically controlled nanofibers that with lag time covert to nanosheets. (C) Seed-mediated growth of 1-D nanofibers (NF) or 2-D nanosheets (NS). Reprinted with permission from reference 40. Copyright © 2016 Springer Nature.

Würthner *et al.* generalize the seeded supramolecular polymerizations by coupling the nucleation step with thermal hysteresis that is applicable to a large number of molecules and not limited to the cases where off-pathway aggregates sequester the active monomers. They investigated the cooperative nucleation−growth process in perylene bisimide based molecules to furnish nanofibrous assemblies (Scheme 1.7A). The monomer was trapped in inactive conformation under particular conditions of temperature, concentration and solvent, thereby restricting spontaneous nucleation and leading to lag time up to more than an hour (Scheme 1.7B). The introduction of preassembled nanofiber seeds to the monomer under appropriate conditions within the hysteresis loop leads to seeded polymerization with low dispersity.[42] Recently, they demonstrated the formation of supramolecular block copolymers A-BA and B-A-B block patterns by two-component seeded living polymerization of properly designed core-substituted perylene bisimides (PBIs) under precise kinetic control (Scheme 1.7C). Kinetically trapped states are prepared by rapid cooling of monomeric solution and addition of seeds constitute of other monomer that will lead to the formation of block copolymer with control over the length of each individual polymer block and low polydispersity.[43]

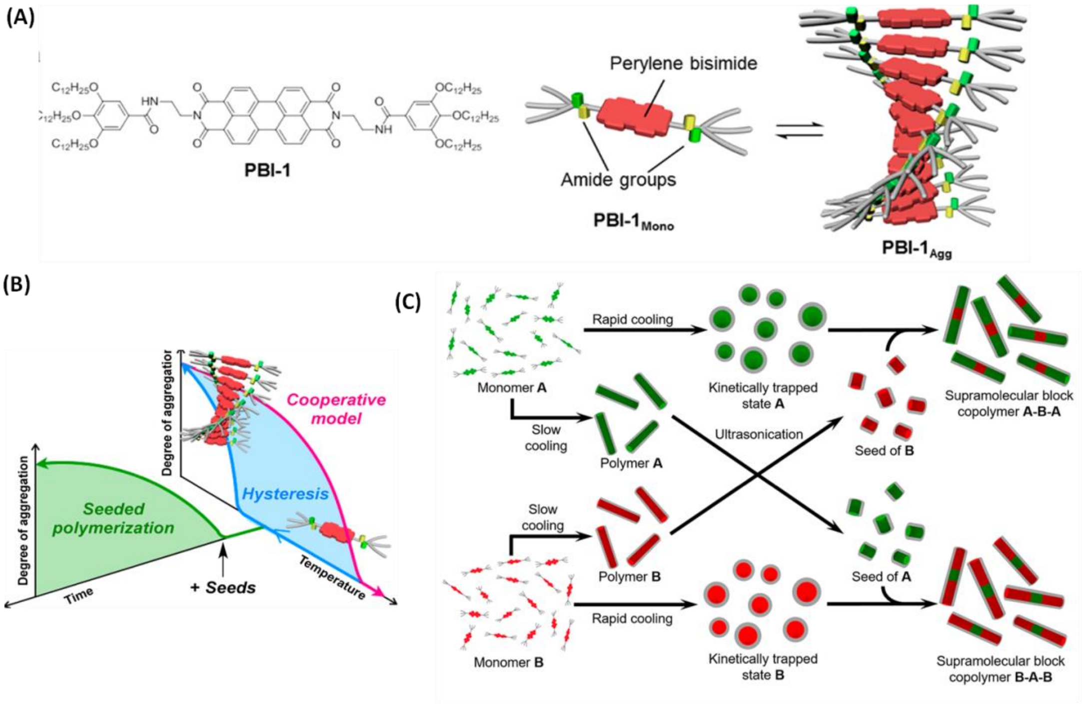

Scheme 1.7: (A) Molecular structure of perylene bisimide derivative (PBI-**1**) that facilitate the self-assembly by hydrogen-bond. (B) Schematic illustration of cooperative polymerization accompanied by thermal hysteresis that can be controlled in a living manner by seeded polymerization. Reprinted with permission from reference 42. Copyright © 2015 American Chemical Society. (C) Schematic representation of the formation of A-B-A or B-A-B tri-blocks by two-component seeded living polymerization. Reprinted with permission from reference 43. Copyright © 2019 American Chemical Society.

The above reports show that chemists have achieved mechanistic control over the dimensions and length regime of self-assembled structures using specialized conditions and molecule designs. However, still there are many challenges to overcome in order to understand the concept in detail for extending to biologically relevant applications. It is beyond doubt that such diverse approaches enriched our knowledge and scientists are actively working with a variety of molecules and strategies. As the definition of self-assembly itself suggests that it is “spontaneous” self-organization and owing to spontaneous behavior, we lack control and precision over the whole process of self-assembly. Despite of the intelligent design, the complex molecules with specific properties for targeted applications have not been harnessed owing to a lack of control over the self-assembly process.

In this context, Takeuchi and Sugiyasu *et al.* reported an elegant approach to build an energy landscape by combining concepts of supramolecular polymerization and photoisomerization process of azobenzene (Scheme 1.8A). The light-responsive monomer can be trapped as an inactive "dormant" monomer and on activation by light in the presence of seed. The free monomer was grown at the ends of the seed thereby resulting in supramolecular polymers with a controlled length and a low polydispersity value.[44] In 2019, the group showed an interesting strategy to inhibit spontaneous nucleation by using a "dummy" monomer that is structurally similar to the reactive monomer but lacks the ability to undergo spontaneous supramolecular polymerization (Scheme 1.8B-C). The presence of porphyrin-based dummy monomer will keep the active monomer in a kinetically trapped dormant state but addition of seeds would initiate the supramolecular polymerization without a lag time.[45]

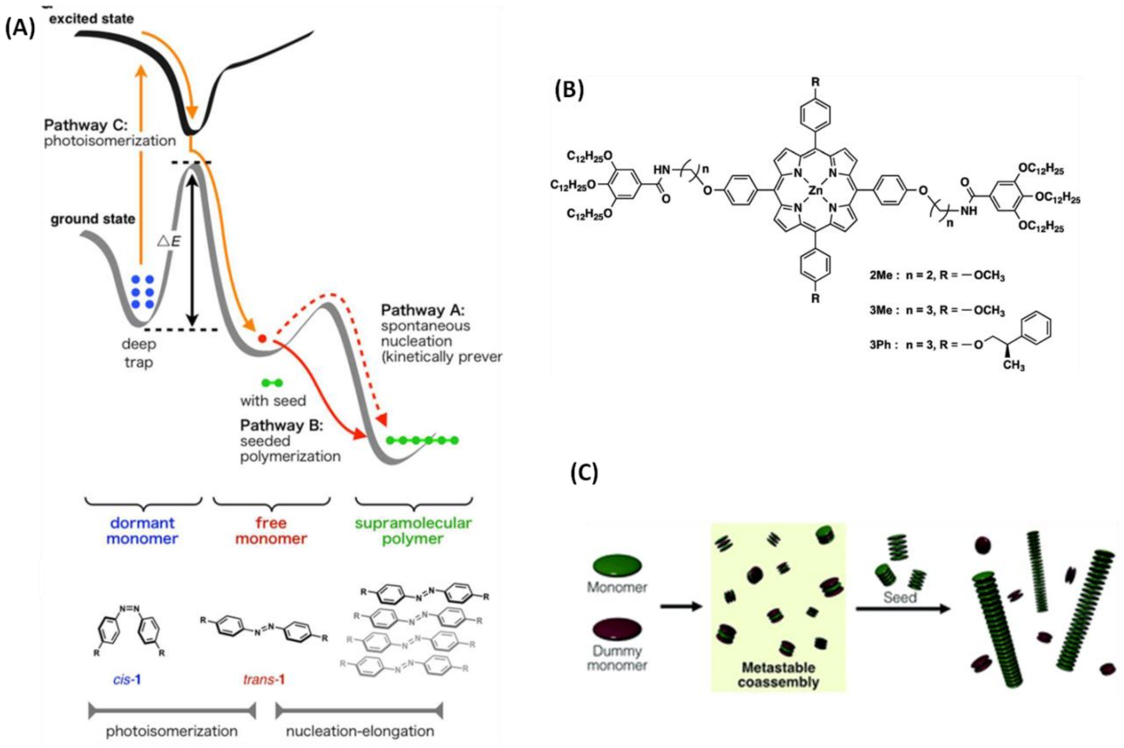

Scheme 1.8: (A) Energy landscape diagram of the nucleation−elongation process coupled with photoisomerization of azobenzene to create a deep kinetic trap. This trap can be circumvented through photo-isomerization of monomer in seeded supramolecular polymerization. Reprinted with permission from reference 44. Copyright © 2016 American Chemical Society. (B) Chemical structures of active (2Me and 3Me) and dummy monomers (3Ph), the structure of both is similar but the dummy monomer is unable to undergo supramolecular polymerization. (C) This can be realized to achieve nanostructures of the controlled length by seeded supramolecular polymerization. Reprinted with permission from reference 45. Copyright © 2019 Royal Society of Chemistry.

Later, Ogi, Yamaguchi and co-workers exploited the interplay of folding and aggregation of pyrene-substituted amino acid based diamide towards seed-mediated supramolecular polymerization (Scheme 1.9). The folding of the diamide moiety as a result of intramolecular hydrogen bonds retarded spontaneous nucleation required for supramolecular polymerization (inactive state). The addition of seeds solution effectively initiated the supramolecular polymerization mediated by intermolecular H bonding in such out-of-equilibrium conditions.[46]

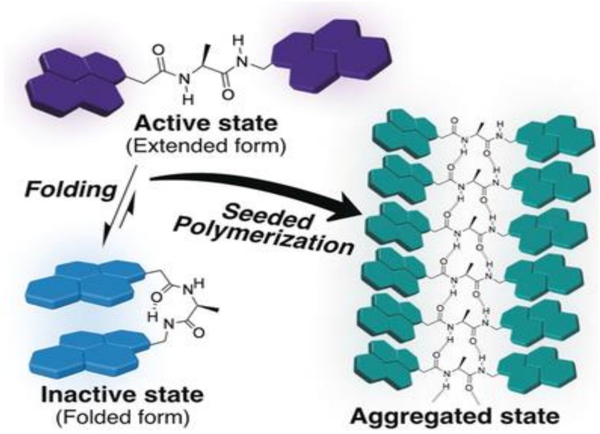

Scheme 1.9: Schematic representation of seeded polymerizations by coupling the equilibria between inactive folded states generated by intramolecular and active extended form as dictated by the intermolecular hydrogen bonds. Reprinted with permission from reference 46. Copyright © 2018 Wiley-VCH Verlag GmbH & Co. KGaA, Weinheim.

These reports make us understand that it is essential to have knowledge about the importance of pathway complexity and generation of an out-of-equilibrium state where monomers can be trapped in an inactive form. The inhibition of spontaneous nucleation by trapping monomer in metastable states can be mediated by temperature and solvent composition, competition of inter- and intramolecular H bonding, photoisomerization and by creating dummy monomer. However, such metastable trapped states either transform quickly into kinetic or thermodynamic states or remain stable only for a few hours thereby leaving us with poor control over supramolecular polymers. Thus, it is important to molecularly design such inactive states with a long enough lifetimes and should initate nucleation upon activation by external trigger. The studies in chapters 2 and 3 provide a better understanding of such trapped monomeric states with photochemical and redox triggers respectively. These inactive monomers are thereby studied for a single component or two-component controlled seeded supramolecular polymerization. While seeded self-assembly has evolved so much in the last decade, it still remains a challenging task to establish predictive on-demand self-assembling strategies. The work in this thesis addresses this research gap by preparing dormant monomers to achieve precise control over the onset of self-assembly.

1.4. Peptide based kinetic nanostructures

Among the self-assembled materials, peptide mediated self-assembly is one of the most promising research areas where monomers with primary sequence of amino acids self-organize themselves spontaneously into well-ordered aggregates. Various types of peptide building blocks are reported in literature[47] including dipeptides,[48, 49] peptide amphiphiles,[50] bolaamphiphilic peptides, ion-complementary peptides and cyclic peptides[51] to be the most explored classes of the peptides. Short peptides are of great interest as they are easy to be synthesized thus avoiding the complication to make larger proteins. Interestingly, such minimalistic functional peptides can also be studied as model systems to understand the structural and functional aspects of complex proteins. During the last two decades, various research groups demonstrated minimalistic peptides to self-assemble into physically crosslinked hydrogels[52, 53] with interesting morphologies ranging from nanofibrous filaments, tubes, spheres, helices to 2D sheets.[54-56] Interestingly, the fate of peptide self-assembly is efficiently manipulated by varying the sequence, chirality, number and type of constituent natural and unnatural amino acids.[57-59] Moreover, specific and selective functional modifications can be introduced at either terminal or at the side chain of peptide and are pivotal for designing better synthetic systems. Further, other than tweaking primary structures, peptide aggregates can form secondary structures such as β-sheet and α-helix due to the H bonding between amide bonds and interactions among side group functionalities of amino acids.[60] β-sheet secondary structure can emanate from parallel or anti-parallel conformation based on the intra-peptide stacking. Various biological structures like bacterial compartments, virus capsids, and collagen fibers possess α-helix conformation[16] whereas the structures in fibers of silk and amyloid protein exhibit β-sheet secondary structure. Recently, there has been a great development in the preparation of complex life-like peptide materials[61] by tethering peptide with other biomolecules, *i.e.*, nucleic acids, oligo-, or polysaccharides.[26] Peptides are widely exploited for biological applications owing to their excellent biocompatibility as they are naturally present in the body. Further, the ability to create a large library of molecules with structural diversity makes peptide self-assembly a fast expanding field of research. Self-assembled peptide structures have received significant attention and have been studied for applications in tissue engineering, bone regeneration, cancer therapy, enzymatic catalysis, bio-mimetic scaffold, therapeutics, conducting soft materials and bioelectronics.[62-65]

Peptide self-assembly has been investigated for pathway complexity and controlled growth in aqueous milieu in the last few years. Samuel Stupp and coworkers extensively studied the peptide amphiphiles that assemble into the broad range of nanostructures such as fibers, cylinders, ribbons, twisted structures having mostly β-sheet domain and induce structural changes with varying pH, concentration or ionic strength.[66] In 2014, they investigated self-assembling pathways for C_{16} alkyl chain conjugated $V_3A_3K_3$ peptide sequence to dictate the assembly rate and resulting structures with varying ratios of HFIP-water solvent mixture. Increasing HFIP concentration in solution resulted in slower kinetics and smaller aggregates.[67, 68] Moreover, the fate of peptide fibers can be efficiently controlled by critical ionic strength (I_c): below the I_c, annealing the peptide solution form fairly short yet monodisperse thermodynamic fibers, However, above the I_c long fibers are formed (Scheme 1.10). These thermodynamic fibers can be perturbed by the addition of salt or dilution to change the β-sheet characteristics. However, after few days short fibers also converted into thermodynamically favoured long fibers, suggesting a metastable state with a low energy barrier. The long fibers transformed to the short fibers upon heating, suggesting a kinetically trapped state with an intermediate energy barrier. Further, they also explored the dynamics of these systems at the molecular level through stochastic optical reconstruction microscopy (STORM) and electron paramagnetic resonance (EPR).[66, 69] Recently, they have shown a strategy to have perfect control over the length of supramolecular assemblies mediated by non-covalent to covalent bond conversion upon photo-irradiation and demonstrated increased cell viability on increasing fiber length.[70]

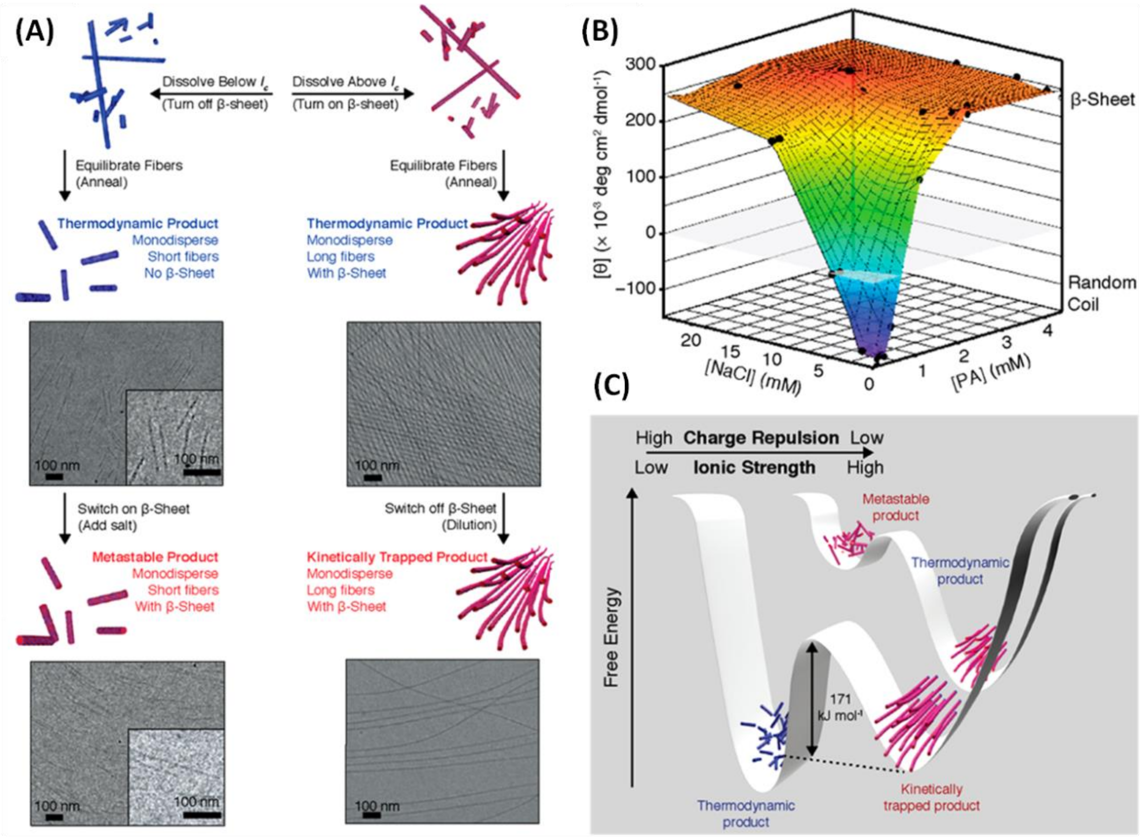

Scheme 1.10: Schematic illustration and cryo-TEM images of the thermodynamically favoured product by annealing and kinetic products by adding salt or dilution. (B) CD spectra at λ = 202 nm as a function of the concentration of peptide and NaCl. (C) Energy landscapes of peptide aggregates below and above the I_c (front and back, respectively). Reprinted with permission from reference 66. Copyright © 2017 American Chemical Society.

Sijbren Otto and co-workers have been working on self-replicating peptide-derived macrocycles coupled with dynamic covalent bond.[71] The molecule of study contains two components: a peptide sequence with alternating hydrophobic (leucine) and hydrophilic (lysine) domains that can assemble through the nucleation-elongation process into a β-sheet structure and benzenedithiol motif that can undergo oxidative disulfide bond formation with each other resulting in multiple macrocycles (Scheme 1.11A). The hexamer or heptamer formation takes place through mechanically responsive sigmoidal growth. Further, the seeding experiments furnish self-replicating fibers with controlled length and narrow PDI (Scheme 1.11B-C).[72,73] Recently, they demonstrated low symmetry foldamers of unprecedented complexity emerging from similar molecules with the peptide tethered 1,3-benzenedithiol aromatic core.[74]

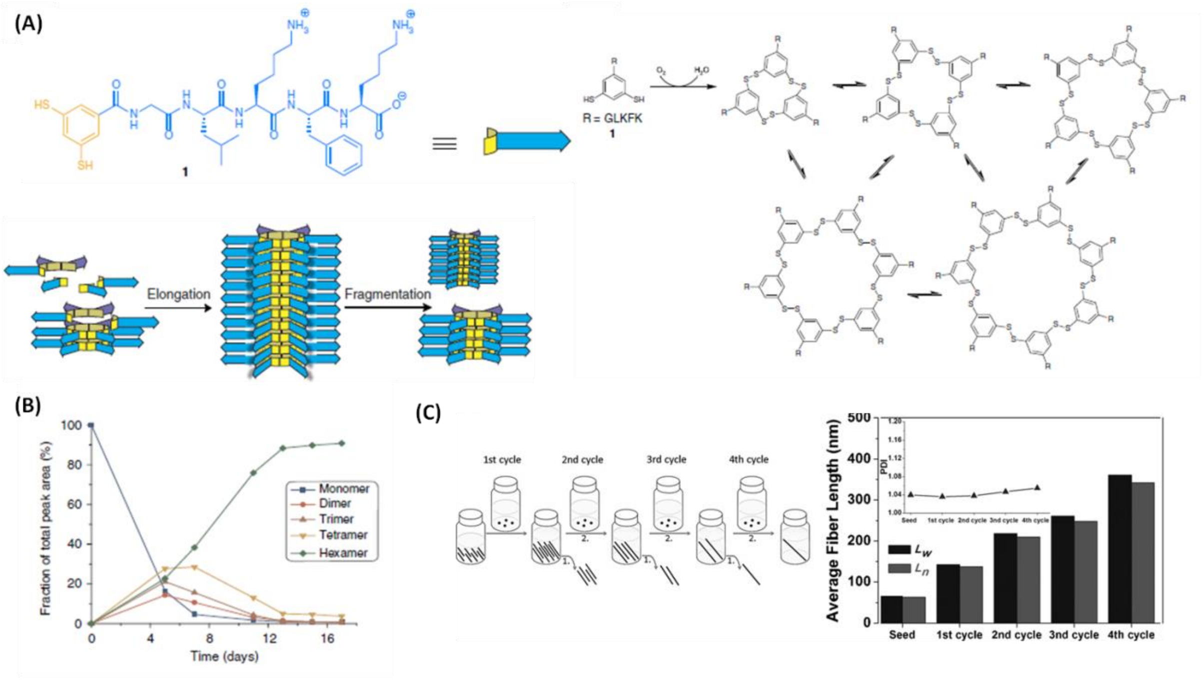

Scheme 1.11: (A) Chemical structure of two precursors, peptide and benzenedithiol. Disulfide bond formation between two thiol functionalities resulted in a mixture of interconverting macrocycles. Schematic representation depicts the self-assembly of the self-replicators to form fibers. (B) Distribution of different macrocycles as a function of time. Reprinted with permission from reference 72. Copyright © 2015, S. Otto *et al.* (C) Seeded growth of hexamer fibers upon sequential addition of trimers or tetramers up to four cycles. Reprinted with permission from reference 73. Copyright © 2015 WILEY-VCH Verlag GmbH & Co. KGaA, Weinheim.

Our group has explored the pathway complexity in Aβ-amyloid inspired peptide amphiphiles to achieve structural control in one and two dimensions through living supramolecular polymerization. The peptide amphiphiles showed step-wise self-assembly in water and a judicious choice of temperature or solvent composition arrests the self-assembly to result in metastable nanoparticles. With the gradual increase in temperature, the metastable state produces kinetically controlled nanofibers at 25 ºC and eventually thermodynamically stable twisted helical bundles (Scheme 1.12A). Moreover, seeded growth depicts the living nature of such peptide nanofibers.[75] In another report, peptide coupled with photo responsive 4-methylcoumarin moiety self-assembles into 1D nanofibers (Scheme 1.12B). The addition of γ-cyclodextrin to the peptide with subsequent irradiation with UV light resulted in 2D nanosheets. Seeded supramolecular polymerization provides structural and temporal control that were exploited to tune the mechanical strength of hierarchical hydrogel materials.[76]

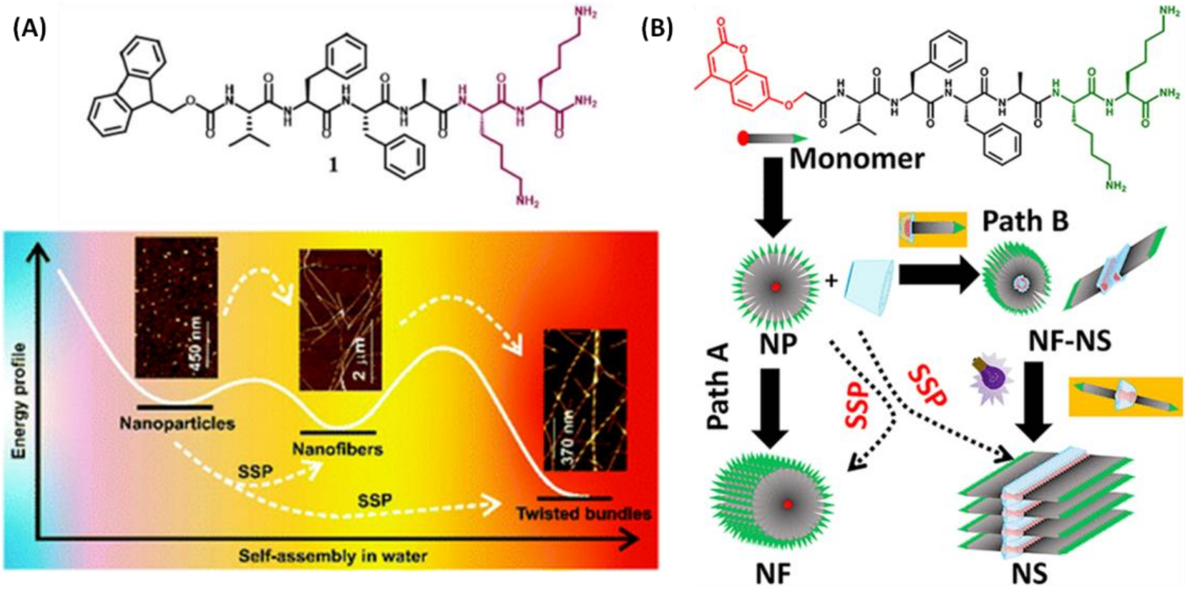

Scheme 1.12: (A) Chemical structure of the peptide amphiphile and pathway complexity in self-assembly to produce different nanostructures. Reprinted with permission from reference 75. Copyright © 2018 Royal Society of Chemistry. (B) The tandem interplay of host-guest interactions and photo-dimerization to form 1d and 2d nanostructures. Reprinted with permission from reference 76. Copyright © 2019 American Chemical Society.

In the quest of mimicking the biological polymers like actin filaments and microtubules, the transient formation of assemblies is the current research interest in artificial biomimetic materials.[77, 78] In this regard, dissipative self-assembly in presence of biochemical energy source (fuel) and disassembly on complete consumption of fuel is a characteristic signature of such transient materials.[79, 80] The first report of chemical fuel-driven transient self-assembly in synthetic systems was presented by van Esch *et al.* with the pH-responsive dibenzoyl-*L*-cystine gelator. The diacid state of molecule does not self-assemble, but upon introduction of methyl iodide (chemical fuel), diesters are formed resulting in fibrous assemblies. However, diesters are rather prone to hydrolysis and exhibit disassembly after some time (energy dissipation).[81] Later, the group changed the alkylating agent, chemical fuel (dimethyl sulfate) and optimized the pH level to modify the timescale of transient self-assembly in hours.[82] In the last decade, a number of model artificial systems have been described with fuel triggered activation of building blocks and a concurrent and chemically distinct pathway to cause deactivation.[83-85] In this context, the self-assembly derived from peptides is of great interest as the enzymatic conversion can be coupled with kinetic peptide assemblies to achieve transient functional nanostructures.[86]

Boekhoven and colleagues presented an elegant strategy for transiently regulating peptide self-assembly in an aqueous buffer. The interplay of attractive and repulsive interaction among peptide precursors dictates the behavior from no assembly, fuel-driven assemblies to permanent assemblies. A chemical reaction cycle system with the peptide sequence containing aspartic acid at C-terminal and chemical fuel, 1-ethyl-3-(3-dimethylaminopropyl)carbodiimide (EDC) results in a transient anhydride state with nanofibrous morphology (Scheme 1.13).[87-89] The system employs an activation reaction that involves suppression of the repulsive interactions to self-aggregate. While the simultaneous hydrolysis of the *in-situ* formed anhydride to aspartic acid derivative constitutes the deactivation reaction. In aspartic acid form, the repulsive interaction between the peptide molecules increases resulting in disassembly.

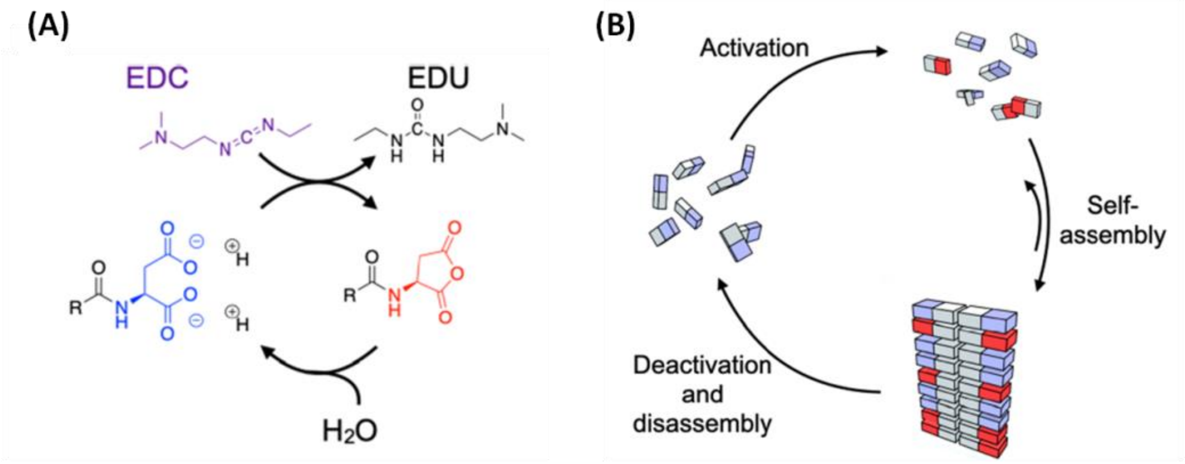

Scheme 1.13: (A) A chemical reaction cycle employed for dissipated self-assembly comprises an activation and deactivation reaction. (B) Chemically fuel-driven assembly with a balance of attractive and repulsive interactions among the precursor peptides. Reprinted with permission from reference 88. Copyright © 2020 American Chemical Society.

1.5. Orthogonal self-assembly

Selection and self-organization processes are of great importance and have its relevance since the prebiotic earth era for sustaining life on this planet. Mimicking such recognition mediated phenomenon akin to the biological systems demands rational design of the structural and functional complexity with great selectivity in synthetic supramolecular systems. DNA replication is the most important part of biological inheritance that produces two identical replicas of DNA starting from one original DNA molecule. During this process, an extraordinary level of molecular recognition is maintained with such a large number of nucleobases duplicating without any mistake. Another exciting biological system is microtubules, these are cylindrical protein structures made up of co-assembly of α-tubulin and β-tubulin (dimers) to form protofilament. Interestingly, this co-assembly process happens only after the self-discrimination of α-tubulin and β-tubulin. Similarly, the molecular recognition in the proteins to form multi-protein complexes and enzymes utilize various non-covalent interactions to bind with specific substrates. In supramolecular polymerization, identical copies of the same building blocks are recognized to form self-assembled nanostructures. Moreover, nature generates precisely selective and functional orthogonal assemblies from multiple building blocks to realize various functions in biological systems like transportation, energy conversion and mechanical motion. Apart from self-assembly, nature's machinery relies on the self-sorting phenomenon to correctly and precisely position the interacting sites with orthogonal recognition. Such systems possessing compartmentalization and confinement of reactions during biological manufacturing processes also have been explored with synthetic building motifs.[90] Here non-equilibrium supramolecular polymerization is of vital importance as molecular recognition alone can only assemble static, equilibrium structures that can just make crystals but not cells.

1.5.1. Self-sorted nanostructures

The term "self-sorting" can be described as the ability to spontaneously recognize their self and distinguish from non-self in a complex mixture. This phenomenon involves a rather high selectivity and competing recognition due to the delicate balance among all the competing interactions between the monomer molecules resulting in specific outcomes rather than all possible complexes out of the mixture (Scheme 1.14). This selection enables the self-sorted systems to contain higher information that helps to distinguish themselves from other self-assembled structures where identical building blocks are just repetitively assembled without much fidelity. Self-sorting in the systems designed from distinct building motifs has been investigated extensively over the last few decades. However, it remains challenging to master and tune the nanostructures obtained from the structurally similar binding blocks.[91]

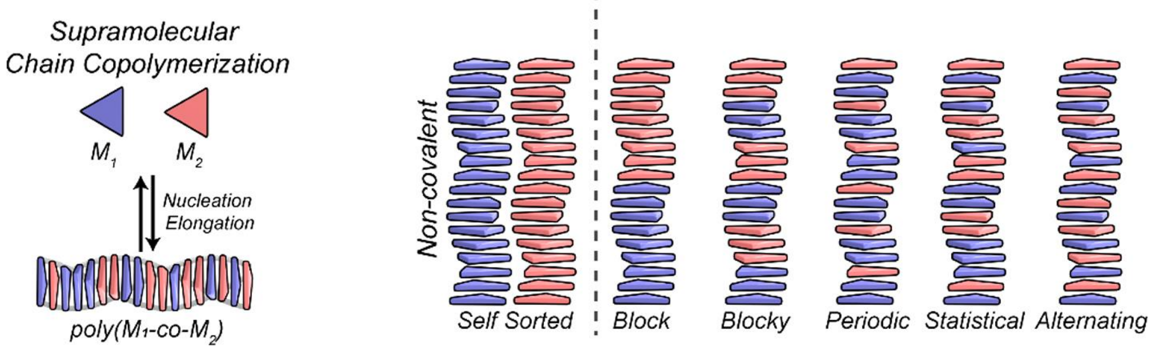

Scheme 1.14: Possible structures in two-component supramolecular polymerization. Reprinted with permission from reference 91. Copyright © 2019 American Chemical Society.

Previous reports documented a number of molecular recognition mediated self-sorting using specially designed molecules or controlling factors such as H bonding, pH, chirality, stereoselectivity *etc*. In 2010, Sijbesma *et al.* demonstrated self-sorting in rod-like micelles of bisurea bola-amphiphiles by tweaking the spacer length and chirality. FRET experiments and pyrene exciplex formation were used to decipher the self-sorting phenomenon.[92, 93] Ulijn, Pires, Pashkuleva *et al.* investigated bi-component systems, the aromatic carbohydrate (Fmoc-glucosamine-6-sulfate or –phosphate) and peptide-based monomer (Fmoc-FF) to generate synergistic modular system mimicking proteoglycans. These molecules co-assemble where the peptide provides the structural component and Fmoc-carbohydrate is exposed in the solvent to provide a functional element. Such a co-assembled system can be organized into supramolecular hydrogels that preserve the cell viability and prolong the stability of growth factors.[94] Adams and co-workers reported the pH-controlled self-sorted gels where the order of assembly can be predefined by programming difference in pK_a of both gelators. The apparent pK_a for one molecule is 5.9 and should self-assemble at higher pH than other molecule with a pK_a of 5.1.[95]

Further, Adams, Tovar *et al.* reported three distinct peptide-based multi-chromophoric hydrogelator systems containing either of these π-electron units oligo(*p*-phenylenevinylene), quaterthiophene, and naphthalenediimide with different inherent spectral energies (Scheme 1.15). These peptides self-assemble in water and can create localized energy gradients by rapidly mixed co-assembled nanostructures in acidic conditions. The self-sorted nanostructures can be obtained by slow pH change as a result of the hydrolysis of glucono-δ-lactone (GdL). They determined the conditions of self-sorting or co-assembly by ^1H NMR spectroscopy and fiber X-ray diffraction.[96]

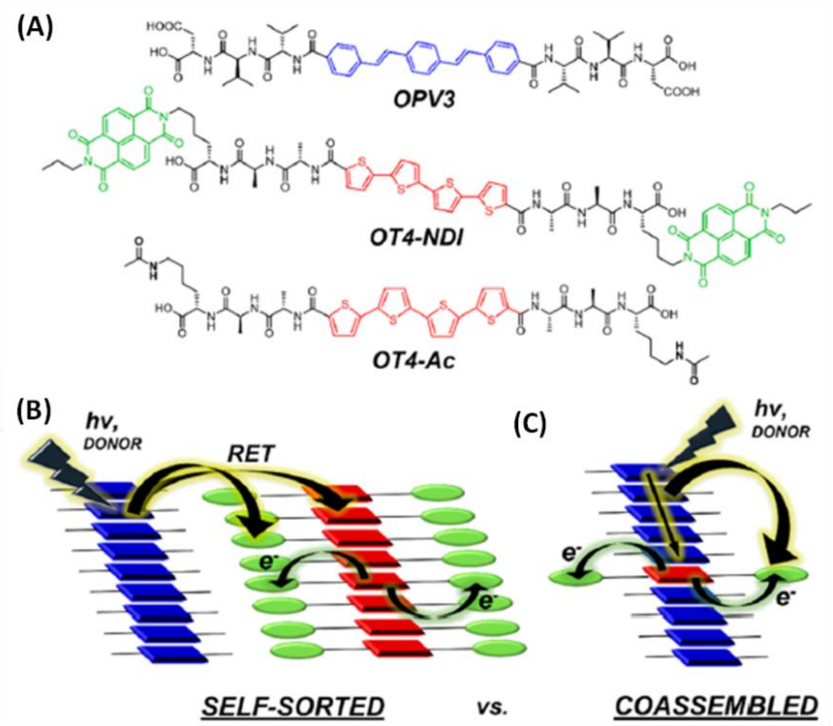

Scheme 1.15: (A) Molecular structures of oligo(*p*-phenylenevinylene), quaterthiophene, and naphthalenediimide and only quaterthiophene conjugated with the peptides. (B) Schematic diagrams of resonance-energy transfer (RET)) and electron-transfer events in self-sorted and (C) randomly co-assembled systems. Reprinted with permission from reference 96. Copyright © 2017 American Chemical Society.

Hamachi and co-workers demonstrated the first example of *in-situ* real-time visualization of self-sorted fibers entangled in two and three dimensions (Scheme 1.16A). Self-sorted hydrogels consist of two distinct building blocks: peptide-based gelator and lipid-like hydrogelator tagged with different fluorescent probes to facilitate their imaging under confocal laser scanning microscopy and super-resolution microscope (STED). The fiber formation takes place through a cooperative mechanism and fibers with different building blocks have different rates of formation with an orthogonal and distinct fluidity and chemical responsiveness.[97, 98] Further, the group demonstrated self-sorted double network gel with orthogonal stimuli-responsiveness towards bacterial alkaline phosphatase and $Na_2S_2O_4$. These multicomponent hydrogels show the bidirectional change in the mechanical properties with the individual property retained even after mixing (Scheme 1.16B).[99] In 2019, the group showed post assembly fabrication of hydrogel formed from a self-sorting double network. The dual-biomolecule response to two adenosine triphosphate (ATP) and sarcosine was used to render gel–sol transition programmed in an AND logic gate. [100]

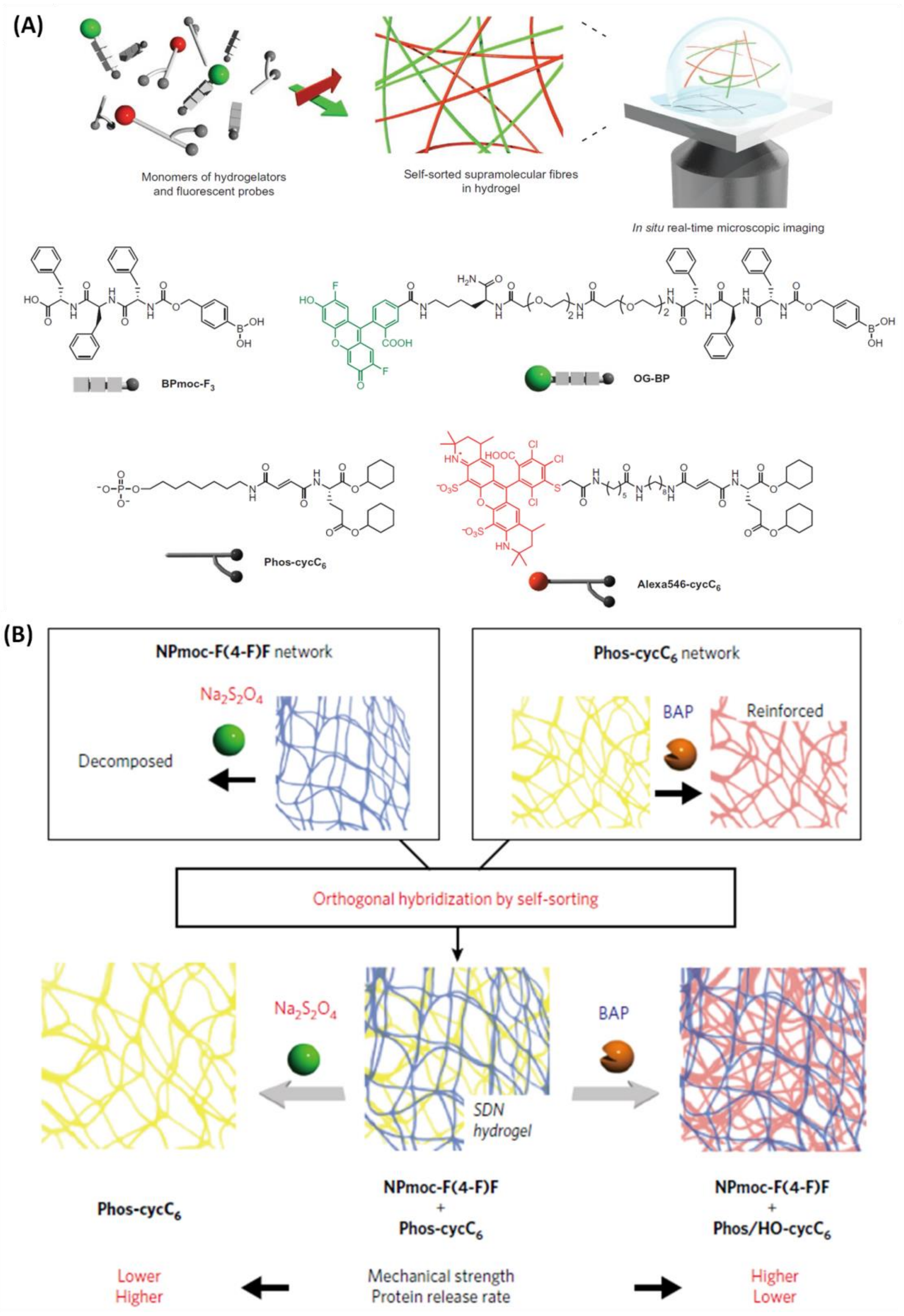

Scheme 1.16: (A) Schematic illustration of the self-sorted self-assembled fibers and molecular structures of the hydrogelators and fluorescent probes. Reprinted with permission from reference 97. Copyright © 2016 Springer Nature. (B) Orthogonal stimuli-responsiveness of the self-sorting double network (SDN) hydrogel to tune mechanical strength and protein release rate. Reprinted with permission from reference 99. Copyright © 2018. I. Hamachi *et al.*

Recently, they have reported an interpenetrated and parallel self-sorting network by exploiting the kinetics of seed formation with dynamic covalent oxime chemistry. The addition of O-benzylhydroxylamine to a benzaldehyde-tethered peptide-type hydrogelator along with lipid-type nanofibers resulted in interpenetrated self-sorting while the self-sorted network are formed through the deceleration of seed formation using a slow oxime exchange reaction.[101]

In 2020, George *et al.* explored two distinct core-substituted naphthalene diimides (cNDI) fluorescent monomers through extensive molecular dynamic simulations and structured illumination microscopy (SIM) to attain various possible outcomes (Scheme 1.17). The resultant supramolecular nanostructures such as self-sorted homopolymers, random (statistical) copolymer, alternate copolymer or complex block copolymer, were achieved by manipulating the thermodynamic and kinetic routes in the pathway driven self-assembly. [102] Later, the group further explored the tri-component system for the formation of multi-block supramolecular copolymers mediated by sequential seeded growth.[103]

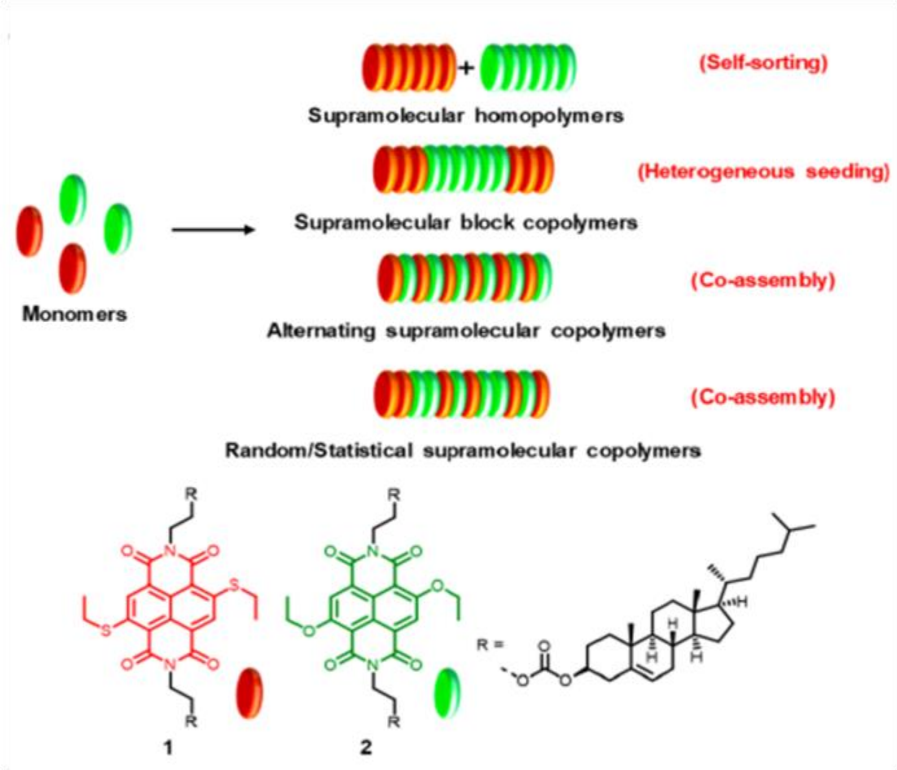

Scheme 1.17: (A) Schematics of supramolecular polymerization into narcissistically self-sorted homopolymers, seed-mediated block co-polymers and co-assembled random or alternate supramolecular co-polymers. (B) Molecular structures of fluorescent monomers for two-component studies. Reprinted with permission from reference 102. Copyright © 2020 American Chemical Society.

The self-sorting events occur based on the information encoded in the building blocks. Although, it is fascinating to directly visualize the self-sorting process through CLSM and super-resolution microscopy, employing two entirely different building blocks (lipid-based and peptide-based) makes the self-sorting phenomenon obvious. However, it is challenging and exciting to visualize the fate of assemblies with minimum structural perturbation. Chapter 5 of this thesis discusses two peptide amphiphiles differing by only two methylene units to investigate the self-sorting events. Literature reports demonstrate the visualization of self-assembly and co-block formation in organic solvents, usually along with some co-solvent. However, employing such molecules that self-assemble in an organic solvent for soft biomimetic materials is not appealing. In this regard, triblock formation in water is beautifully demonstrated in chapter 5.

1.5.2. Chiral self-sorting

Most of the complex bio-macromolecules available in nature contain chiral building blocks such as the *L* isomer of amino acids (in proteins) and the *D* isomer of sugars (nucleic acids). This leads to particular macromolecular chirality in the self-assembled biomolecules that is vital for normal functions of natural materials. The concept of chirality based discrimination has fascinated the chemists since Louis Pasteur's discovery of molecular chirality in *L* and *D* enantiomers of tartaric acid in 1848. Also, the thalidomide incident in the 1950s underlines the power of molecular chirality and recognizes the importance of chirality in the peptide and amino acids for biomaterials applications.[104]

During the self-sorting process, if the chirality of molecules is the differentiating factor towards specific selective interactions, the phenomenon is called chiral self-sorting. The enantiomeric species in the mixture result in self-assembled products with one isomer talking with their like ones and ignoring the unlike individual isomers to render homochiral self-sorted product. An enantiomeric mixture of monomers are structurally the same and possess the same non-covalent interaction sites. Therefore, specific and selective recognition is obviously a difficult and challenging task. In chiral self-sorting, monomers may act as competitors thus reducing the effectiveness of self-sorting. Detection and quantification of chiral self-sorting is also restricted by current experimental tools with specific detection limits and resolution. In the realm of chiral self-assembly, the discussion is not complete without the mention of the following two models: Sergeants and soldiers principle, where a few chiral units can control the chirality of the whole achiral system;

Majority rules principle, where the overall chirality of the system is dictated by the isomer which is present in slight excess in a mixture of enantiomers.

In literature, there are few examples that perfectly fit in the category of chiral self-sorting. George and co-workers describe chiral self-sorting through enantioselective 1,2-bis(amido)cyclohexane coupled with naphthalene diimide (NDI) and 1,5-dialkoxy naphthalene (DAN) derivatives as acceptor and donor chromophores. The molecular design offered mixed and segregated donor-acceptor stacks in supramolecular co-assembly and form p-n nanostructures.[105] Later, they developed chiral donor and acceptor molecules having minimum structural mismatch with fluorescent core-substituted naphthalene-diimide. The appropriate substitutions, two –OEt groups (-diOEt), for green-emissive donor and –OEt and –iPa groups (-OEtiPa) for red-emissive acceptor (Scheme 1.18). The stereoselective supramolecular polymerization render control over energy transfer through FRET and further these molecules were studied for visualization of chirality driven self-sorting.[106]

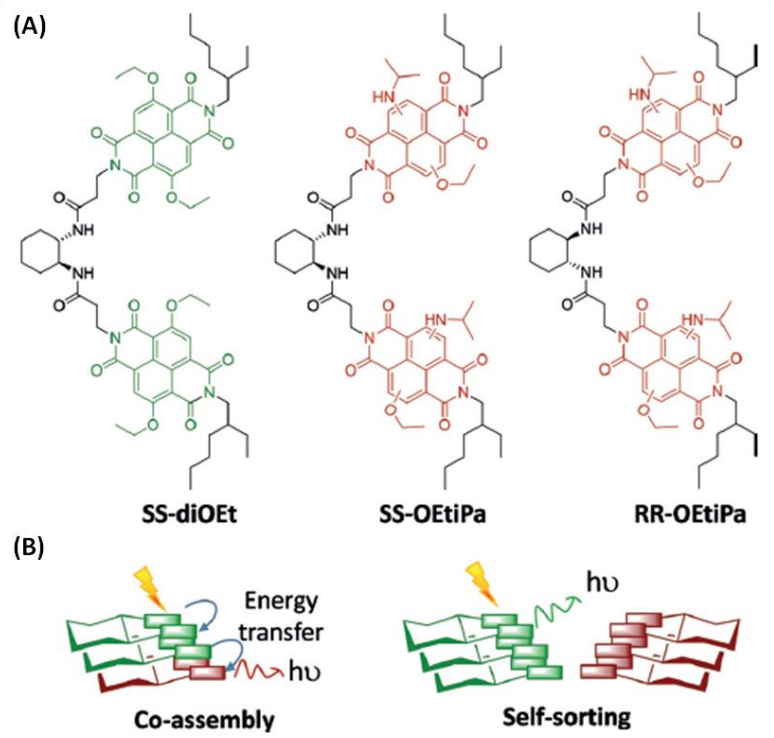

Scheme 1.18: (A) Chemical structures of the donor, (*SS*-diOEt) and acceptor (*SS*-OEtiPa or *RR*-OEtiPa). (B) Schematic illustration of chirality-driven co-assembly and self-sorting, and resultant energy transfer process. Reprinted with permission from reference 106. Copyright © 2017 Wiley-VCH Verlag GmbH & Co. KGaA, Weinheim.

As we discussed in the last section peptide self-assembly is highly dependent on encoded information, we focus on the chirality effects for regulating peptide self-assembly towards the chiral self-sorting and co-assembly of the racemic peptides. Tweaking *L*-peptides with *D*-amino acids can distort their structure and inhibits the formation of secondary structures. For instance, *D*-amino acid could induce a kink to break and destabilize α-helix structure.[107,108]

Peptide sequence EAK16 with *L*-amino acids self-organizes to form nanofibers, while *D*-amino acid incorporated peptides E^{D}AK16 and ^{D}EA^{D}K16 disrupt the β-sheet secondary structures resulting in no assemblies.[109] However, tweaking the chirality can change the handedness and morphology of the self-assembled nanostructures in some cases.[110-112] Rudra and co-workers explored the block heterochiral peptides (Ac-FKFEFKFE-NH2), where two FKFE repeat units are of opposite chirality. These heterochiral peptides assemble into helical tapes with large dimensions as compared to the fibrillar homochiral counterparts. MD simulations suggested the kink and internal strain generation between two repeating motifs that flatten the natural twist of the β-sheet secondary structure to make it flat ribbon.[113] Gazit *et al.* explored the aromatic amino acids (phenylalanine and tryptophan) where the chirality of the amino acids plays a significant role in the self-assembling process. Co-assembled systems have different kinetics and morphology to result in different nanostructures with superior mechanical properties as compared to pure enantiomers.[114] The self-assembly of fatty acid chain-conjugated dialanine with homochirality and heterochirality showed the handedness of the fibers to be determined by the chirality of the terminal alanine.[115] Similarly, Xu and co-workers developed short amphiphilic peptides I$_3$K with varying chiral manipulations, ^{L}I$_3$^{L}K and ^{D}I$_3$^{D}K, ^{L}I$_3$^{D}K and ^{D}I$_3$^{L}K, and ^{L}αI$_3$^{L}K and ^{D}αI$_3$^{D}αK. These peptides showed twisted handedness of nanofibers guided by the chirality of lysine at the hydrophilic terminal.[116] In some cases, the chirality of terminal amino acid in peptide sequence is of paramount importance to dictate supramolecular chirality while in some peptide sequences supramolecular chirality is determined by some specific amino acids usually phenylalanine.[117, 118]

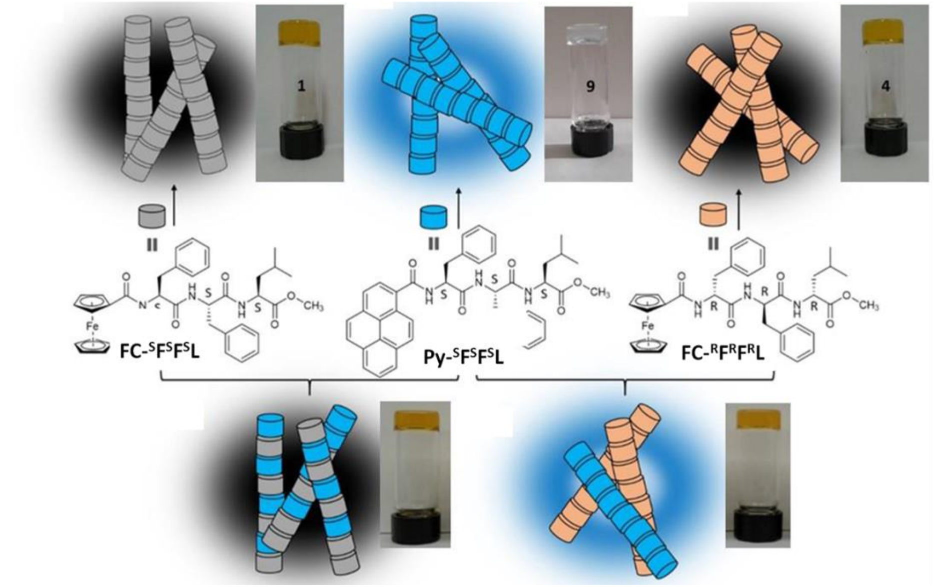

Scheme 1.19: Chemical structures of few stereoisomers of ferrocene- and pyrene-appended tri-peptides. Homochiral Fc-based gelator renders non-fluorescent fibers, whereas Py-based gelator forms fluorescent fibers. Mixing of Py-^{S}F^{S}F^{S}L with Fc-^{S}F^{S}F^{S}L in the same pot (matching chiral centers) produced non-fluorescent fibers, indicating mixed assemblies. However, mixing of gelator Fc-^{R}F^{R}F^{R}L and Py-^{S}F^{S}F^{S}L in the same pot (opposite chiral centers) results in fluorescent fibers, indicating self-sorted fiber formation. Reprinted with permission from reference 121. Copyright © 2017 WILEY-VCH Verlag GmbH & Co. KGaA, Weinheim.

Biological systems prefer homochiral stacks through chiral selectivity with amyloid fibril formed by *L*- and *D*-stereoisomers of β2-microglobulin (*L*-K3 and *D*-K3 peptides) are stereospecific resulting in homologous fibers.[119] Schneider *et al.* reported a co-assembly from a racemic mixture of β-hairpin peptides (MAX1 and DMAX1) to result in four times more mechanically rigid gels than formed by either peptide alone.[120]

Kraatz *et al.* investigated the effect of peptide stereochemistry on the self-assembly of a series of stereoisomers of the tripeptide FFL (Scheme 1.19). Self-assemblies guided by the homochiral peptides have uniform, thermally and mechanically robust nanofibers whereas heterochiral systems result in self-sorted systems with heterogeneous morphology.[121]

In 2019, Stupp *et al.* demonstrated elegant interactions of the peptide assemblies with lipid bilayer membranes in a stereospecific manner. The *L*-peptide showed a stronger affinity for the liposome compared to the *D*-peptide to render increased cell viability with *D*-peptide (Scheme 1.20).[122] Recently, the group has reported self-sorting in a supramolecular system comprised of a negatively charged peptide amphiphiles doped with a small fraction of fluorescent dye anchored peptide (FITC-PA and TAMRA-PA) doping. FITC-peptide is dispersed throughout the sample while the TAMRA conjugated peptide is present in micron-scale domains.[123]

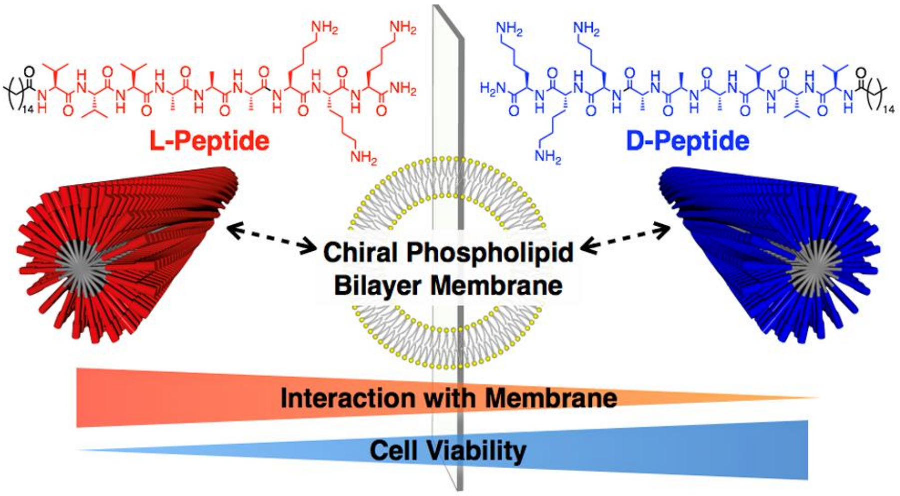

Scheme 1.20: (A) Schematics of chiral recognition of lipid bilayer membranes by enantiomeric peptide amphiphiles. Reprinted with permission from reference 122. Copyright © 2019 American Chemical Society.

The chiral self-sorting is rather intersting to addresses the evolution of homochirality in prebiotic earth with the preference for one enantiomer in natural molecules by employing autocatalytic self-replication process. However, controlling the self-assembly with stereo-specificity in a multicomponent system involving an enantiomeric pair in one pot is rather daunting task for chemists owing to the labile conformation and adaptability towards similar recognition sites of the enantiomers.

1.6. Applications of self-assembled peptides

Self-assembled peptide amphiphiles with emergent and adaptive properties have proven to be a versatile tool in various applications including scaffolds for tissue engineering, drug delivery, mimicking hierarchical self-assembly in protein-misfolding disorders, antimicrobial agents, catalysis, energy storage devices, fabrication of piezoelectric-based sensors, super hydrophobic surfaces for self-cleaning applications *etc*.[124] Peptide-based hydrogels can mimic structural morphology and composition of the extracellular matrix with controlled porosity and rigidity and hence shows great potential as biomimetic 3D scaffolds for cell growth.[125] Peptide matrix provides mechanical support for cell-adhesion to enable cell proliferation, migration, differentiation and organization for tissue regeneration.[126-128] Integrin-binding Arg-Gly-Asp (RGD) peptide and amyloid-like peptide nanofibers have been demonstrated for stem cell adhesion and differentiation to generate biomaterials for therapeutic applications.[129-132] Short peptide amphiphiles are interesting synthetic motifs to study sustained drug-delivery mediated by assembly and disassembly of nanostructures.[133-136] Moreover, the peptide amphiphiles have been used for the development of new antimicrobial agents. The cationic antimicrobial peptides interact with the anionic bacterial lipid bilayer membranes and enable membrane permeation, depolarization and destabilization.[137-139] Similarly, cyclic peptides can also cause bacterial cell death and exhibit more antibacterial and antiviral activity as compared to their linear counterpart.[51,140] Since cationic peptide amphiphiles binds to cancerous cells through electrostatic interactions and hence can disrupt cellular and organelle membranes, making them a perfect candidate for cancer therapeutics.[141-144] Furthermore, peptide amphiphiles comprised of inorganic components have gained attention in order to mimic nature's hard and stiff materials like bone, enamel and seashell nacre.[145-149] Interestingly, peptide–inorganic nanocomposites can incorporate noble metal nanoparticles or photoactive materials which found applications in energy harvesting or energy storage applications.[150,151]

1.6.1. Piezoelectricity in peptide amphiphiles

Piezoelectricity is the generation of electric response on applied mechanical stress or vice-versa in non-centrosymmetric crystals. In the 1950s, Fukada discovered shear piezoelectricity in various biopolymers like cellulose and collagen.[152] In synthetic materials, ceramics like barium titanate, lead-zirconate-titanate, zinc oxide, and molybdenum disulfide exhibit good piezoelectricity, but possess poor biocompatibility. In this context, peptide nanostructures being compatible with biological systems emerge as a promising candidate for applications like piezoresponsive nanogenerator, sensors, harvesters, actuators, piezotronics and optical wave guiding devices. In literature, particularly diphenylalanine peptide had been extensively explored as a piezoelectric biomaterial due to its exceptional piezoelectricity and remarkable mechanical properties.[153-157] In 2010, Ghazit, Rosenman *et al.* reported self-assembled diphenylalanine peptide nanotubes having electric polarization directed along the axis of nanotube possess strong shear piezoelectricity with effective piezoelectric coefficient values of at least 60 pmV^{-1} (Scheme 1.21A).[154] Rusen Yang and co-workers demonstrated strong piezoelectricity in vertical FF peptide with fully controlled polarization with an electric field applied during the peptide self-assembly process that further improved piezoelectricity of the fabricated power generator (Voltage = 1.4 V; Power density = 3.3 nWcm^{-2}; $\mathbf{d_{33}}$ = 17.9 pmV^{-1}) (Scheme 1.21B).[158] In another report by Seuk-Wuk Lee, in 2018, aligned diphenylalanine (FF) nanotubes exhibit piezoelectric properties and unidirectional polarization. Further, they fabricated peptide-based piezoelectric energy harvesters to generate voltage up to 2.8 V (Scheme 1.21C).[159] Piezoelectric devices manufactured from self-assembled peptides can find future applications in multi-functional electronics compatible with human tissue.[160]

The above reports describe the influence of peptide self-assembly on the piezoelectric response, largely focused only on FF peptides. Therefore, more peptides with unique properties and stimuli responsiveness towards the piezo-response are needed to be explored. The second and third chapters of this thesis demonstrate the stimuli-responsive ON and OFF piezo-response owing to self-assembly and disassembly. Moreover, exploring such peptides with specific optical or redox properties working in tandem with piezoelectric properties is promising for fabricating biocompatible multifunctional devices.

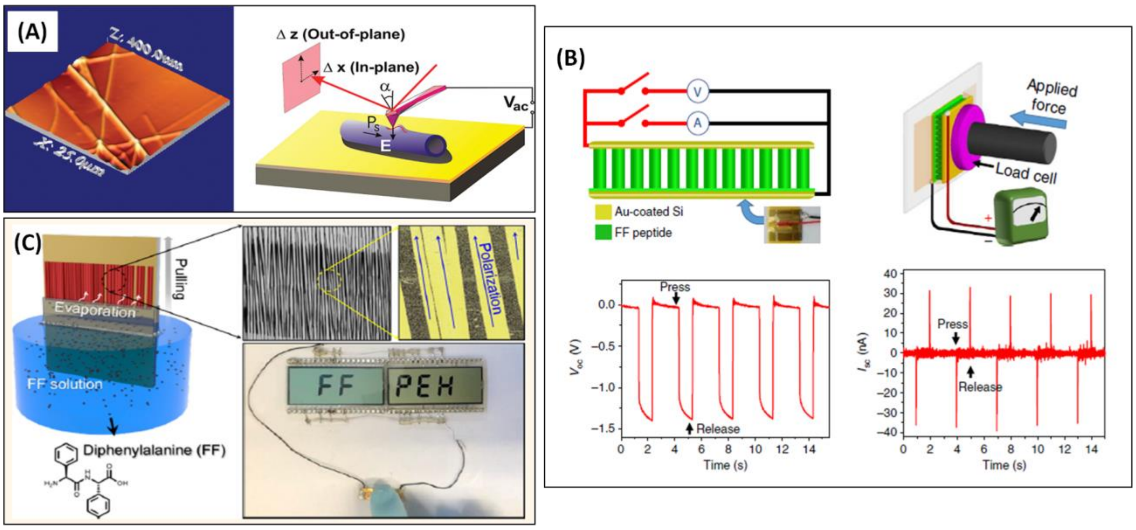

Scheme 1.21: (A) AFM image of as-deposited FF peptide nanotube on Au-coated substrate and schematic of the nanoscale in-plane measurements by piezoresponse force microscopy (PFM). Reprinted with permission from reference 154. Copyright © 2010 American Chemical Society. (B) Top panel: Schematic representation of FF peptide-based generator (inset: photograph of a real device) and measurement set-up. Bottom panel: Open circuit voltage and short-circuit current from a generator. Reprinted with permission from reference 158. Copyright © 2016, R. Yang *et al*. (C) Schematic diagram depicting meniscus-driven dip-coating process to synthesize aligned FF nanotubes with unidirectional polarization as observed in PFM image. Further, Piezoelectric energy harvester showed LED by finger pressing. Reprinted with permission from reference 159. Copyright © 2018 American Chemical Society.

1.7. Scope of research

The peptide-mediated self-assembly is an attractive approach to induce and control precision and compartmentalization. In order to realize these features in an aqueous environment amyloid inspired minimalistic peptide amphiphiles can be employed. The pathway complexity in peptide self-assembly can be exploited to create complex nanostructures with functional applications.

In this regard, Chapter 2 demonstrates the sequestration of peptide by chemical and photo cues in dormant states that upon judicious activation, engage in controlled seeded mediated supramolecular polymerization in aqueous milieu for the first time. Such self-assembly pathways result in excellent on-off piezoresponsive peptide nanostructures.

In chapter 3, short redox-responsive peptide amphiphiles were studied where varying spacer chain length between the stimuli-responsive unit and self-assembling unit furnishes different nanostructures. Moreover, an elegant demonstration of seeded supramolecular polymerization led to mixed block co-fiber of redox-responsive and non-responsive peptide heterostructures.

Chapter 4 deals with the chirality mediated fidelity and stereo-selectivity in enantiomeric peptide amphiphiles based nanofibers to furnish chirally self-sorted peptide nanofibers. This self-sorted system exhibits enantioselective enzymatic degradation for *L*-peptide fibers and selective weakening of the specific hydrogel materials.

Chapter 5 demonstrates the self-assembly phenomenon in fluorescent peptide bola-amphiphiles with two-components having minimum structural variation. The matching spacer between peptide motifs can render co-assembled nanofibers, non-matching spacer forms self-sorted and homomeric spacer seeding experiments furnish block co-fibers.

1.8. References

1. J. M. Lehn, *Polym. Int.*, 2002, **51**, 825-839.
2. J. M. Lehn, *Science*, 2002, **295**, 2400-2403.
3. L. S. Shimizu, *Polym. Int.*, 2007, **56**, 444-452.
4. G. Armstrong and M. Buggy, *J. Mater. Sci.*, 2005, **40**, 547-559.
5. A. Harada, Y. Takashima and H. Yamaguchi, *Chem. Soc. Rev.*, 2009, **38**, 875-882.
6. E. Obert, M. Bellot, L. Bouteiller, F. Andrioletti, C. Lehen-Ferrenbach and F. Boué, *J. Am. Chem. Soc.*, 2007, **129**, 15601-15605.
7. L. Yang, X. Tan, Z. Wang and X. Zhang, *Chem. Rev.*, 2015, **115**, 7196-7239.
8. S. I. Stupp and L. C. Palmer, *Chem. Mater.*, 2014, **26**, 507-518.
9. D. B. Amabilino, D. K. Smith and J. W. Steed, *Chem. Soc. Rev.*, 2017, **46**, 2404-2420.
10. T. F. A. De Greef, M. M. J. Smulders, M. Wolffs, A. P. H. J. Schenning, R. P. Sijbesma and E. W. Meijer, *Chem. Rev.*, 2009, **109**, 5687-5754.
11. T. Aida, E. W. Meijer and S. I. Stupp, *Science*, 2012, **335**, 813-817.
12. R. Dong, Y. Zhou, X. Huang, X. Zhu, Y. Lu and J. Shen, *Adv. Mater.*, 2015, **27**, 498-526.
13. M. J. Webber, E. A. Appel, E. W. Meijer and R. Langer, *Nat. Mater.*, 2016, **15**, 13-26.
14. U. G. K. Wegst, H. Bai, E. Saiz, A. P. Tomsia and R. O. Ritchie, *Nat. Mater.*, 2015, **14**, 23-36.
15. D. A. Fletcher and R. D. Mullins, *Nature*, 2010, **463**, 485-492.
16. L. E. R. O'Leary, J. A. Fallas, E. L. Bakota, M. K. Kang and J. D. Hartgerink, *Nat. Chem.*, 2011, **3**, 821-828.
17. L. Brunsveld, B. J. B. Folmer, E. W. Meijer and R. P. Sijbesma, *Chem. Rev.*, 2001, **101**, 4071-4098.
18. Z. Chen, A. Lohr, C. R. Saha-Möller and F. Würthner, *Chem. Soc. Rev.*, 2009, **38**, 564-584.
19. D. Zhao and J. S. Moore, *Org. Biomol. Chem.*, 2003, **1**, 3471-3491.
20. R. B. Martin, *Chem. Rev.*, 1996, **96**, 3043-3064.
21. M. M. J. Smulders, M. M. L. Nieuwenhuizen, T. F. A. de Greef, P. van der Schoot, A. P. H. J. Schenning and E. W. Meijer, *Chem. Eur. J.*, 2010, **16**, 362-367.
22. A. Lohr, M. Lysetska and F. Würthner, *Angew. Chem. Int. Ed.*, 2005, **44**, 5071-5074.
23. M. Hartlieb, E. D. H. Mansfield and S. Perrier, *Polym. Chem.*, 2020, **11**, 1083-1110.
24. G. Du, E. Moulin, N. Jouault, E. Buhler and N. Giuseppone, *Angew. Chem. Int. Ed.*, 2012, **51**, 12504-12508.
25. V. Guida, *Advances in Colloid and Interface Science*, 2010, **161**, 77-88.
26. D. M. Raymond and B. L. Nilsson, *Chem. Soc. Rev.*, 2018, **47**, 3659-3720.
27. J. Y. Rho and S. Perrier, *ACS Macro Lett.*, 2021, **10**, 258-271.
28. J. Stankiewicz and L. H. Eckardt, *Angew. Chem. Int. Ed.*, 2006, **45**, 342-344.
29. E. Mattia and S. Otto, *Nat. Nanotechnol.*, 2015, **10**, 111-119.
30. Y. Bai, A. Chotera, O. Taran, C. Liang, G. Ashkenasy and D. G. Lynn, *Chem. Soc. Rev.*, 2018, **47**, 5444-5456.
31. B. Rieß, R. K. Grötsch and J. Boekhoven, *Chem*, 2020, **6**, 552-578.
32. A. Sorrenti, J. Leira-Iglesias, A. Sato and T. M. Hermans, *Nat. Commun.*, 2017, **8**, 15899.
33. M. Altay, Y. Altay and S. Otto, *Angew. Chem. Int. Ed.*, 2018, **57**, 10564-10568.
34. P. A. Korevaar, S. J. George, A. J. Markvoort, M. M. J. Smulders, P. A. J. Hilbers, A. P. H. J. Schenning, T. F. A. De Greef and E. W. Meijer, *Nature*, 2012, **481**, 492-496.
35. P. A. Korevaar, C. Grenier, A. J. Markvoort, A. P. H. J. Schenning, T. F. A. de Greef and E. W. Meijer, *Proc. Natl. Acad. Sci.*, 2013, **110**, 17205.
36. J. B. Gilroy, T. Gädt, G. R. Whittell, L. Chabanne, J. M. Mitchels, R. M. Richardson, M. A. Winnik and I. Manners, *Nat. Chem.*, 2010, **2**, 566-570.
37. S. K. Patra, R. Ahmed, G. R. Whittell, D. J. Lunn, E. L. Dunphy, M. A. Winnik and I. Manners, *J. Am. Chem. Soc.*, 2011, **133**, 8842-8845.
38. J. Kang, D. Miyajima, T. Mori, Y. Inoue, Y. Itoh and T. Aida, *Science*, 2015, **347**, 646-651.
39. S. Ogi, K. Sugiyasu, S. Manna, S. Samitsu and M. Takeuchi, *Nat. Chem.*, 2014, **6**, 188-195.

40. T. Fukui, S. Kawai, S. Fujinuma, Y. Matsushita, T. Yasuda, T. Sakurai, S. Seki, M. Takeuchi and K. Sugiyasu, *Nat. Chem.*, 2017, **9**, 493-499.
41. S. H. Jung, D. Bochicchio, G. M. Pavan, M. Takeuchi and K. Sugiyasu, *J. Am. Chem. Soc.*, 2018, **140**, 10570-10577.
42. S. Ogi, V. Stepanenko, K. Sugiyasu, M. Takeuchi and F. Würthner, *J. Am. Chem. Soc.*, 2015, **137**, 3300-3307.
43. W. Wagner, M. Wehner, V. Stepanenko and F. Würthner, *J. Am. Chem. Soc.*, 2019, **141**, 12044-12054.
44. M. Endo, T. Fukui, S. H. Jung, S. Yagai, M. Takeuchi and K. Sugiyasu, *J. Am. Chem. Soc.*, 2016, **138**, 14347-14353.
45. T. Fukui, N. Sasaki, M. Takeuchi and K. Sugiyasu, *Chem. Sci.*, 2019, **10**, 6770-6776.
46. S. Ogi, K. Matsumoto and S. Yamaguchi, *Angew. Chem. Int. Ed.*, 2018, **57**, 2339-2343.
47. R. Otter and P. Besenius, *Org. Biomol. Chem.*, 2019, **17**, 6719-6734.
48. J. Raeburn, T. O. McDonald and D. J. Adams, *Chem. Commun.*, 2012, **48**, 9355-9357.
49. D. J. Adams, *Macromol. Biosci.*, 2011, **11**, 160-173.
50. D. Hartgerink Jeffrey, E. Beniash and I. Stupp Samuel, *Science*, 2001, **294**, 1684-1688.
51. S. Fernandez-Lopez, H.-S. Kim, E. C. Choi, M. Delgado, J. R. Granja, A. Khasanov, K. Kraehenbuehl, G. Long, D. A. Weinberger, K. M. Wilcoxen and M. R. Ghadiri, *Nature*, 2001, **412**, 452-455.
52. X. Du, J. Zhou, J. Shi and B. Xu, *Chem. Rev.*, 2015, **115**, 13165-13307.
53. J. Li, X. Du, S. Hashim, A. Shy and B. Xu, *J. Am. Chem. Soc.*, 2017, **139**, 71-74.
54. A. Lampel, R. V. Ulijn and T. Tuttle, *Chem. Soc. Rev.*, 2018, **47**, 3737-3758.
55. K. Tao, A. Levin, L. Adler-Abramovich and E. Gazit, *Chem. Soc. Rev.*, 2016, **45**, 3935-3953.
56. S. Fleming and R. V. Ulijn, *Chem. Soc. Rev.*, 2014, **43**, 8150-8177.
57. K. Sato, M. P. Hendricks, L. C. Palmer and S. I. Stupp, *Chem. Soc. Rev.*, 2018, **47**, 7539-7551.
58. L. Adler-Abramovich and E. Gazit, *Chem. Soc. Rev.*, 2014, **43**, 6881-6893.
59. P. W. J. M. Frederix, G. G. Scott, Y. M. Abul-Haija, D. Kalafatovic, C. G. Pappas, N. Javid, N. T. Hunt, R. V. Ulijn and T. Tuttle, *Nat. Chem.*, 2015, **7**, 30-37.
60. I. W. Hamley, *Angew. Chem. Int. Ed.*, 2014, **53**, 6866-6881.
61. A. Lampel, *Chem*, 2020, **6**, 1222-1236.
62. H. Cui, M. J. Webber and S. I. Stupp, *Peptide Sci.*, 2010, **94**, 1-18.
63. S. C. Larnaudie, J. Sanchis, T.-H. Nguyen, R. Peltier, S. Catrouillet, J. C. Brendel, C. J. H. Porter, K. A. Jolliffe and S. Perrier, *Biomaterials*, 2018, **178**, 570-582.
64. D. M. Ryan and B. L. Nilsson, *Polym. Chem.*, 2012, **3**, 18-33.
65. E. D. Spoerke, S. G. Anthony and S. I. Stupp, *Adv. Mater.*, 2009, **21**, 425-430.
66. M. P. Hendricks, K. Sato, L. C. Palmer and S. I. Stupp, *Acc. Chem. Res.*, 2017, **50**, 2440-2448.
67. P. A. Korevaar, C. J. Newcomb, E. W. Meijer and S. I. Stupp, *J. Am. Chem. Soc.*, 2014, **136**, 8540-8543.
68. F. Tantakitti, J. Boekhoven, X. Wang, R. V. Kazantsev, T. Yu, J. Li, E. Zhuang, R. Zandi, J. H. Ortony, C. J. Newcomb, L. C. Palmer, G. S. Shekhawat, M. O. de la Cruz, G. C. Schatz and S. I. Stupp, *Nat. Mater.*, 2016, **15**, 469-476.
69. R. M. P. da Silva, D. van der Zwaag, L. Albertazzi, S. S. Lee, E. W. Meijer and S. I. Stupp, *Nat. Commun.*, 2016, **7**, 11561.
70. K. Sato, W. Ji, L. C. Palmer, B. Weber, M. Barz and S. I. Stupp, *J. Am. Chem. Soc.*, 2017, **139**, 8995-9000.
71. M. A. Carnall Jacqui, A. Waudby Christopher, M. Belenguer Ana, C. A. Stuart Marc, J. P. Peyralans Jérôme and S. Otto, *Science*, 2010, **327**, 1502-1506.
72. M. Colomb-Delsuc, E. Mattia, J. W. Sadownik and S. Otto, *Nat. Commun.*, 2015, **6**, 7427.
73. A. Pal, M. Malakoutikhah, G. Leonetti, M. Tezcan, M. Colomb-Delsuc, V. D. Nguyen, J. van der Gucht and S. Otto, *Angew. Chem. Int. Ed.*, 2015, **54**, 7852-7856.
74. C. G. Pappas, P. K. Mandal, B. Liu, B. Kauffmann, X. Miao, D. Komáromy, W. Hoffmann, C. Manz, R. Chang, K. Liu, K. Pagel, I. Huc and S. Otto, *Nat. Chem.*, 2020, **12**, 1180-1186.

75. A. Singh, J. P. Joseph, D. Gupta, I. Sarkar and A. Pal, *Chem. Commun.*, 2018, **54**, 10730-10733.
76. J. P. Joseph, A. Singh, D. Gupta, C. Miglani and A. Pal, *ACS Appl. Mater. Interfaces*, 2019, **11**, 28213-28220.
77. N. Singh, G. J. M. Formon, S. De Piccoli and T. M. Hermans, *Adv. Mater.*, 2020, **32**, 1906834.
78. K. Das, L. Gabrielli and L. J. Prins, *Angew. Chem. Int. Ed.*, 2021, **60**, 20120-20143.
79. S. A. P. van Rossum, M. Tena-Solsona, J. H. van Esch, R. Eelkema and J. Boekhoven, *Chem. Soc. Rev.*, 2017, **46**, 5519-5535.
80. A. Sorrenti, J. Leira-Iglesias, A. J. Markvoort, T. F. A. de Greef and T. M. Hermans, *Chem. Soc. Rev.*, 2017, **46**, 5476-5490.
81. J. Boekhoven, A. M. Brizard, K. N. K. Kowlgi, G. J. M. Koper, R. Eelkema and J. H. van Esch, *Angew. Chem. Int. Ed.*, 2010, **49**, 4825-4828.
82. J. Boekhoven, E. Hendriksen Wouter, J. M. Koper Ger, R. Eelkema and H. van Esch Jan, *Science*, 2015, **349**, 1075-1079.
83. B. G. P. van Ravensteijn, W. E. Hendriksen, R. Eelkema, J. H. van Esch and W. K. Kegel, *J. Am. Chem. Soc.*, 2017, **139**, 9763-9766.
84. A. Jain, S. Dhiman, A. Dhayani, P. K. Vemula and S. J. George, *Nat. Commun.*, 2019, **10**, 450.
85. S. Bal, K. Das, S. Ahmed and D. Das, *Angew. Chem. Int. Ed.*, 2019, **58**, 244-247.
86. C. G. Pappas, I. R. Sasselli and R. V. Ulijn, *Angew. Chem. Int. Ed.*, 2015, **54**, 8119-8123.
87. B. Rieß, C. Wanzke, M. Tena-Solsona, R. K. Grötsch, C. Maity and J. Boekhoven, *Soft Matter*, 2018, **14**, 4852-4859.
88. K. Dai, J. R. Fores, C. Wanzke, B. Winkeljann, A. M. Bergmann, O. Lieleg and J. Boekhoven, *J. Am. Chem. Soc.*, 2020, **142**, 14142-14149.
89. M. Tena-Solsona, B. Rieß, R. K. Grötsch, F. C. Löhrer, C. Wanzke, B. Käsdorf, A. R. Bausch, P. Müller-Buschbaum, O. Lieleg and J. Boekhoven, *Nat. Commun.*, 2017, **8**, 15895.
90. B. A. Grzybowski and W. T. S. Huck, *Nat. Nanotechnol.*, 2016, **11**, 585-592.
91. B. Adelizzi, N. J. Van Zee, L. N. J. de Windt, A. R. A. Palmans and E. W. Meijer, *J. Am. Chem. Soc.*, 2019, **141**, 6110-6121.
92. A. Pal, S. Karthikeyan and R. P. Sijbesma, *J. Am. Chem. Soc.*, 2010, **132**, 7842-7843.
93. A. Pal, P. Besenius and R. P. Sijbesma, *J. Am. Chem. Soc.*, 2011, **133**, 12987-12989.
94. A. Brito, Y. M. Abul-Haija, D. S. da Costa, R. Novoa-Carballal, R. L. Reis, R. V. Ulijn, R. A. Pires and I. Pashkuleva, *Chem. Sci.*, 2019, **10**, 2385-2390.
95. K. L. Morris, L. Chen, J. Raeburn, O. R. Sellick, P. Cotanda, A. Paul, P. C. Griffiths, S. M. King, R. K. O'Reilly, L. C. Serpell and D. J. Adams, *Nat. Commun.*, 2013, **4**, 1480.
96. H. A. M. Ardoña, E. R. Draper, F. Citossi, M. Wallace, L. C. Serpell, D. J. Adams and J. D. Tovar, *J. Am. Chem. Soc.*, 2017, **139**, 8685-8692.
97. S. Onogi, H. Shigemitsu, T. Yoshii, T. Tanida, M. Ikeda, R. Kubota and I. Hamachi, *Nat. Chem.*, 2016, **8**, 743-752.
98. R. Kubota, S. Liu, H. Shigemitsu, K. Nakamura, W. Tanaka, M. Ikeda and I. Hamachi, *Bioconjug. Chem.*, 2018, **29**, 2058-2067.
99. H. Shigemitsu, T. Fujisaku, W. Tanaka, R. Kubota, S. Minami, K. Urayama and I. Hamachi, *Nat. Nanotechnol.*, 2018, **13**, 165-172.
100. W. Tanaka, H. Shigemitsu, T. Fujisaku, R. Kubota, S. Minami, K. Urayama and I. Hamachi, *J. Am. Chem. Soc.*, 2019, **141**, 4997-5004.
101. R. Kubota, K. Nagao, W. Tanaka, R. Matsumura, T. Aoyama, K. Urayama and I. Hamachi, *Nat. Commun.*, 2020, **11**, 4100.
102. A. Sarkar, R. Sasmal, C. Empereur-mot, D. Bochicchio, S. V. K. Kompella, K. Sharma, S. Dhiman, B. Sundaram, S. S. Agasti, G. M. Pavan and S. J. George, *J. Am. Chem. Soc.*, 2020, **142**, 7606-7617.
103. A. Sarkar, R. Sasmal, A. Das, A. Venugopal, S. S. Agasti and S. J. George, *Angew. Chem. Int. Ed.*, 2021, **60**, 18209-18216.
104. Y. Zheng, K. Mao, S. Chen and H. Zhu, *Front. Bioeng. Biotechnol.*, 2021, **9**, 517.
105. B. Narayan, K. K. Bejagam, S. Balasubramanian and S. J. George, *Angew. Chem. Int. Ed.*, 2015, **54**, 13053-13057.

106. A. Sarkar, S. Dhiman, A. Chalishazar and S. J. George, *Angew. Chem. Int. Ed.*, 2017, **56**, 13767-13771.
107. E. Krause, M. Bienert, P. Schmieder and H. Wenschuh, *J. Am. Chem. Soc.*, 2000, **122**, 4865-4870.
108. V. Punitha, S. S. Raman, R. Parthasarathi, V. Subramanian, J. R. Rao, B. U. Nair and T. Ramasami, *J. Phys. Chem. B*, 2009, **113**, 8983-8992.
109. Z. Luo, S. Wang and S. Zhang, *Biomaterials*, 2011, **32**, 2013-2020.
110. S. Kralj, O. Bellotto, E. Parisi, A. M. Garcia, D. Iglesias, S. Semeraro, C. Deganutti, P. D'Andrea, A. V. Vargiu, S. Geremia, R. De Zorzi and S. Marchesan, *ACS Nano*, 2020, **14**, 16951-16961.
111. K. McAulay, B. Dietrich, H. Su, M. T. Scott, S. Rogers, Y. K. Al-Hilaly, H. Cui, L. C. Serpell, Annela M. Seddon, E. R. Draper and D. J. Adams, *Chem. Sci.*, 2019, **10**, 7801-7806.
112. A. M. Gil, J. Casanovas, E. Mayans, A. I. Jiménez, J. Puiggalí and C. Alemán, *J. Phys. Chem. B*, 2020, **124**, 5913-5918.
113. T. M. Clover, C. L. O'Neill, R. Appavu, G. Lokhande, A. K. Gaharwar, A. E. Posey, M. A. White and J. S. Rudra, *J. Am. Chem. Soc.*, 2020, **142**, 19809-19813.
114. S. Bera, B. Xue, P. Rehak, G. Jacoby, W. Ji, L. J. W. Shimon, R. Beck, P. Král, Y. Cao and E. Gazit, *ACS Nano*, 2020, **14**, 1694-1706.
115. Y. Fu, B. Li, Z. Huang, Y. Li and Y. Yang, *Langmuir*, 2013, **29**, 6013-6017.
116. M. Wang, P. Zhou, J. Wang, Y. Zhao, H. Ma, J. R. Lu and H. Xu, *J. Am. Chem. Soc.*, 2017, **139**, 4185-4194.
117. M. Qin, Y. Zhang, C. Xing, L. Yang, C. Zhao, X. Dou and C. Feng, *Chem. Eur. J.*, 2021, **27**, 3119-3129.
118. C. Zheng, S. Lin, C. Hu, Y. Li, B. Li and Y. Yang, *New J. Chem*, 2020, **44**, 20726-20733.
119. H. Wadai, K.-i. Yamaguchi, S. Takahashi, T. Kanno, T. Kawai, H. Naiki and Y. Goto, *Biochemistry*, 2005, **44**, 157-164.
120. K. Nagy-Smith, P. J. Beltramo, E. Moore, R. Tycko, E. M. Furst and J. P. Schneider, *ACS Cent. Sci.*, 2017, **3**, 586-597.
121. S. Basak, I. Singh, A. Ferranco, J. Syed and H. B. Kraatz, *Angew. Chem. Int. Ed.*, 2017, **56**, 13288-13292.
122. K. Sato, W. Ji, Z. Álvarez, L. C. Palmer and S. I. Stupp, *ACS Biomater. Sci. Eng.*, 2019, **5**, 2786-2792.
123. C. H. Chen, L. C. Palmer and S. I. Stupp, *Soft Matter*, 2021, **17**, 3902-3912.
124. A. Levin, T. A. Hakala, L. Schnaider, G. J. L. Bernardes, E. Gazit and T. P. J. Knowles, *Nat. Rev. Chem.*, 2020, **4**, 615-634.
125. S. Kocabey, H. Ceylan, A. B. Tekinay and M. O. Guler, *Acta Biomater.*, 2013, **9**, 9075-9085.
126. N. Huettner, T. R. Dargaville and A. Forget, *Trends Biotechnol.*, 2018, **36**, 372-383.
127. J. H. Collier, J. S. Rudra, J. Z. Gasiorowski and J. P. Jung, *Chem. Soc. Rev.*, 2010, **39**, 3413-3424.
128. J. Liu, Z. Sun, Y. Yuan, X. Tian, X. Liu, G. Duan, Y. Yang, L. Yuan, H.-C. Lin and X. Li, *ACS Appl. Mater. Interfaces*, 2016, **8**, 6917-6924.
129. M. N. Bongiovanni, D. B. Scanlon and S. L. Gras, *Biomaterials*, 2011, **32**, 6099-6110.
130. N. P. Reynolds, M. Charnley, R. Mezzenga and P. G. Hartley, *Biomacromolecules*, 2014, **15**, 599-608.
131. R. S. Jacob, D. Ghosh, P. K. Singh, S. K. Basu, N. N. Jha, S. Das, P. K. Sukul, S. Patil, S. Sathaye, A. Kumar, A. Chowdhury, S. Malik, S. Sen and S. K. Maji, *Biomaterials*, 2015, **54**, 97-105.
132. S. Das, K. Zhou, D. Ghosh, N. N. Jha, P. K. Singh, R. S. Jacob, C. C. Bernard, D. I. Finkelstein, J. S. Forsythe and S. K. Maji, *NPG Asia Mater.*, 2016, **8**, e304-e304.
133. S. M. Standley, D. J. Toft, H. Cheng, S. Soukasene, J. Chen, S. M. Raja, V. Band, H. Band, V. L. Cryns and S. I. Stupp, *Cancer Res.*, 2010, **70**, 3020.
134. J. J. Panda, A. Mishra, A. Basu and V. S. Chauhan, *Biomacromolecules*, 2008, **9**, 2244-2250.
135. R. Ischakov, L. Adler-Abramovich, L. Buzhansky, T. Shekhter and E. Gazit, *Bioorg. Med. Chem.*, 2013, **21**, 3517-3522.
136. R. Huang, W. Qi, L. Feng, R. Su and Z. He, *Soft Matter*, 2011, **7**, 6222-6230.
137. L. Timofeeva and N. Kleshcheva, *Appl. Microbiol. Biotechnol.*, 2011, **89**, 475-492.

138. A. A. Bahar and D. Ren, *Pharmaceuticals*, 2013, **6**.
139. A. Giuliani and A. C. Rinaldi, *Cell. Mol. Life Sci.*, 2011, **68**, 2255-2266.
140. A. Montero, P. Gastaminza, M. Law, G. Cheng, Francis V. Chisari and M. R. Ghadiri, *Chem. Biol.*, 2011, **18**, 1453-1462.
141. D. Gaspar, A. S. Veiga and M. A. R. B. Castanho, *Front. microbiol.*, 2013, **4**, 294.
142. J. Chen, B. Zhang, F. Xia, Y. Xie, S. Jiang, R. Su, Y. Lu and W. Wu, *Nanoscale*, 2016, **8**, 7127-7136.
143. M. Li, P. Liu, G. Gao, J. Deng, Z. Pan, X. Wu, G. Xie, C. Yue, C. H. Cho, Y. Ma and L. Cai, *ACS Appl. Mater. Interfaces*, 2015, **7**, 8005-8012.
144. S. Soukasene, D. J. Toft, T. J. Moyer, H. Lu, H.-K. Lee, S. M. Standley, V. L. Cryns and S. I. Stupp, *ACS Nano*, 2011, **5**, 9113-9121.
145. N. Reznikov, J. A. M. Steele, P. Fratzl and M. M. Stevens, *Nat. Rev. Mater.*, 2016, **1**, 16041.
146. C. Li, A.-K. Born, T. Schweizer, M. Zenobi-Wong, M. Cerruti and R. Mezzenga, *Adv. Mater.*, 2014, **26**, 3207-3212.
147. Y. Cao, S. Bolisetty, G. Wolfisberg, J. Adamcik and R. Mezzenga, *Proc. Natl. Acad. Sci.*, 2019, **116**, 4012.
148. C. J. Newcomb, R. Bitton, Y. S. Velichko, M. L. Snead and S. I. Stupp, *Small*, 2012, **8**, 2195-2202.
149. N. Gupta, A. Singh, N. Dey, S. Chattopadhyay, J. P. Joseph, D. Gupta, M. Ganguli and A. Pal, *Chem. Mater.*, 2021, **33**, 589-599.
150. D. Oh, J. Qi, B. Han, G. Zhang, T. J. Carney, J. Ohmura, Y. Zhang, Y. Shao-Horn and A. M. Belcher, *Nano Lett.*, 2014, **14**, 4837-4845.
151. N.-M. Dorval Courchesne, M. T. Klug, K. J. Huang, M. C. Weidman, V. J. Cantú, P.-Y. Chen, S. E. Kooi, D. S. Yun, W. A. Tisdale, N. X. Fang, A. M. Belcher and P. T. Hammond, *J. Phys. Chem. C*, 2015, **119**, 13987-14000.
152. E. Fukada, *IEEE Trans. Ultrason. Ferroelectr. Freq. Control*, 2000, **47**, 1277-1290.
153. K. Ryan, J. Beirne, G. Redmond, J. I. Kilpatrick, J. Guyonnet, N.-V. Buchete, A. L. Kholkin and B. J. Rodriguez, *ACS Appl. Mater. Interfaces*, 2015, **7**, 12702-12707.
154. A. Kholkin, N. Amdursky, I. Bdikin, E. Gazit and G. Rosenman, *ACS Nano*, 2010, **4**, 610-614.
155. V. Nguyen, K. Jenkins and R. Yang, *Nano Energy*, 2015, **17**, 323-329.
156. S. Vasilev, P. Zelenovskiy, D. Vasileva, A. Nuraeva, V. Y. Shur and A. L. Kholkin, *J. Phys. Chem. Solids*, 2016, **93**, 68-72.
157. H. Yuan, P. Han, K. Tao, S. Liu, E. Gazit and R. Yang, *Research*, 2019, **2019**, 9025939.
158. V. Nguyen, R. Zhu, K. Jenkins and R. Yang, *Nat. Commun.*, 2016, **7**, 13566.
159. J.-H. Lee, K. Heo, K. Schulz-Schönhagen, J. H. Lee, M. S. Desai, H.-E. Jin and S.-W. Lee, *ACS Nano*, 2018, **12**, 8138-8144.
160. Y.-M. Wang, Q. Zeng, L. He, P. Yin, Y. Sun, W. Hu and R. Yang, *iScience*, 2021, **24**, 102274.

2

Photochemically Sequestered Off-Pathway Dormant States of Peptide Amphiphiles for Predictive On-demand Piezoresponsive Nanostructures

Supramolecular assemblies are essential for specific biological functions and mandate precise control over the mesoscopic scale for higher functional efficiency. Recently, spatiotemporal control for the living supramolecular polymerization has rendered a paradigm shift toward designing complex multicomponent supramolecular active materials; however, directing the active monomer toward predictive kinetically trapped materials still remains a considerable challenge as this necessitates circumventing spontaneous nucleation of the monomers during the self-assembly process. Herein, we demonstrate dual strategies (chemical and photo) to sequester the active peptide self-assembling motifs in dormant states that, upon judicious activation, engage in controlled seeded supramolecular polymerization in aqueous milieu for the first time. Amyloid-inspired peptide 1 with a pendant azobenzene moiety demonstrates the formation of on-pathway metastable nanoparticles by the interplay of solvent and temperature that could be transformed into kinetically controlled nanofibers and thermodynamically controlled twisted bundles. Further, using coupled equilibrium such as the host −guest inclusion complex with cyclodextrin or photoisomerization with UV light leads to the formation of two distinct off-pathway metastable states that retard the spontaneous supramolecular polymerization. A judicious manipulation of the free-energy landscapes in tandem with suitable chemical and photostimuli renders the activation of the dormant states for the peptide selfassembly through a seeded growth strategy. Finally, such photochemical sequestration of self-assembly pathways results in on −off piezoresponsive peptide nanostructures.

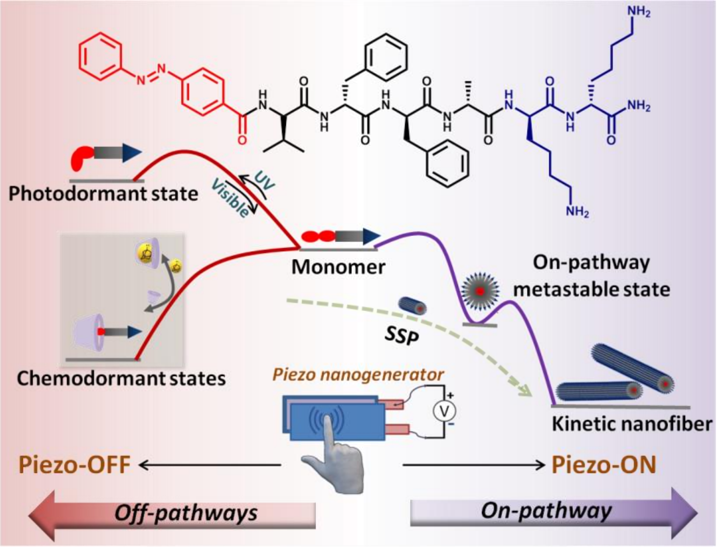

2.1. Introduction

Supramolecular polymerization,[1-2] a bottom-up self-assembly strategy ubiquitous in various natural biological processes, has witnessed immense interest in the design of biomimetic materials in recent years. These polymers are held together by various reversible, dynamic and non-covalent interactions among the monomer units, thereby furnishing structurally programmed and functionally enhanced adaptive architectures[3-4] that are sensitive to a plethora of stimuli, for example temperature, pH, chirality and the microenvironment imparted by the solvent molecules.[5-10] In contrast to the non-equilibrium self-assembly processes abundant in nature, such polymerizations performed in the laboratories are usually dictated by the free energy of self-assembled supramolecular polymers under thermodynamic control. However, since the last decade, our understanding of the off-pathway assembly from the monomer building blocks under kinetic control[11-13] leading to living supramolecular polymerization has undergone a paradigm shift[14-17] with a concomitant upsurge in the efforts to develop synthetic life-like systems.[18-21] Such non-equilibrium or dissipative control over the supramolecular polymer endows us with the flexibility to tweak around with the monomer design to produce the desired assembled state.[22-25] For most of the monomer building blocks the polymerization process initiates instantly after they are dissolved in the solvent, thereby resulting in an uncontrolled morphology, chain length and composition. In seed-mediated supramolecular self-assembly, the assembly process may be triggered by a macro-initiator (preformed seeds) to render a precise control over length and shape of the final products. This, *in turn*, circumvents the spontaneous nucleation process of the monomers that otherwise acts as an antagonist to such dimensional control.[26-29] Thus, the control over the monomer reactivity through tweaking the activation energy barriers for the nucleation process significantly retards the spontaneous self-assembly process and leads to an interesting strategy to design polymerswith dimensional precision utilizing living supramolecular polymerization.[30-32] If the monomers are trapped in metastable states and do not have sufficient activation energy to cross the energy barrier, the spontaneous nucleation process is suppressed. Such inactive states are “dormant” in nature, but can be activated on demand using external stimuli such as solvent, temperature, snap cooling and competitive hydrogen bonding to promote spontaneous supramolecular polymerization.[33-34] Aida *et al.* and Würthner *et al.* demonstrated the inhibition of the spontaneous polymerization of a bowl-shaped corannulene monomer and planar perylene bisimide monomer, respectively, owing to the trapping of the monomeric state in an intramolecular hydrogen bonded conformation.[27,35] In another approach, Sugiyasu and Takeuchi *et al*. reported kinetic off-pathway metastable states that can be envisaged as the appropriate inactive states for the living supramolecular polymerization in porphyrin based systems in methylcyclohexane.[28,30] Recently, George *et al*. reported the redox-responsive dormant states of amphiphilic charge-transfer monomer with a donor-acceptor sequence for the controlled activation and deactivation of the monomers.[36] However, the energy parameters and dynamics of monomer exchange and their mechanisms are system-specific and vary with the type of supramolecular building blocks.[37-40] Moreover, the extension of the strategy to design precise peptide nanostructures in aqueous milieu would have an immense application in designing ECM mimetic scaffolds for tissue engineering, biocatalysis, energy harvesting and so forth which is *hitherto* not reported.[41-44] Recently, our group has explored amyloid-inspired peptide amphiphiles for orthogonal and pathway-driven self-assembly,[45-47] that involves shape and size evolution of transient metastable nanoparticles to one-dimensional nanofibers and two-dimensional nanosheets for application in ECM mimetic bioglass composites.[48] However, controlling the self-assembly with such on-pathway states at low temperature or optimal good/bad solvent composition may not be sufficient enough to design an intelligent biomimetic complex network, that rather demands an intervention of stable off-pathway intermediates to prevent spontaneous self-assembly. Such a strategy employing the concept of pathway complexity in the peptide self-assembly has so far been unexplored, even though such biomolecular systems may draw inspirations from functionally regulated proteins such as bacteriorhodopsin that actuate ion pumps using the *cis-trans* photoisomerization of intrinsic fluorophores. Moreover, the peptides owing to the directional amide hydrogen bonding possess correlation between the electric pulse and mechanical behaviour to generate active piezo electricity;[49,50] however, a control over such functional behaviour has so far been lacking in the literature. Thus, we resort to using light or chemical cues as efficient stimuli that can exhibit spatiotemporal control toward self-assembly/disassembly in supramolecular peptide nanostructures to finally realize the on-demand piezoelectric response. In this regard, multi-stimuli-responsive moieties such as azobenzene are notably fascinating, as they can undergo photo responsive isomerization and host-guest inclusion complexation.[51-55] However, such multiresponse behaviour of azobenzene has so far not been exploited toward designing on-demand programmable and precise supramolecular peptide nanostructures mediated by the judicious sequestration of the self-assembly to off-pathway dormant states with an on-demand piezoresponse.

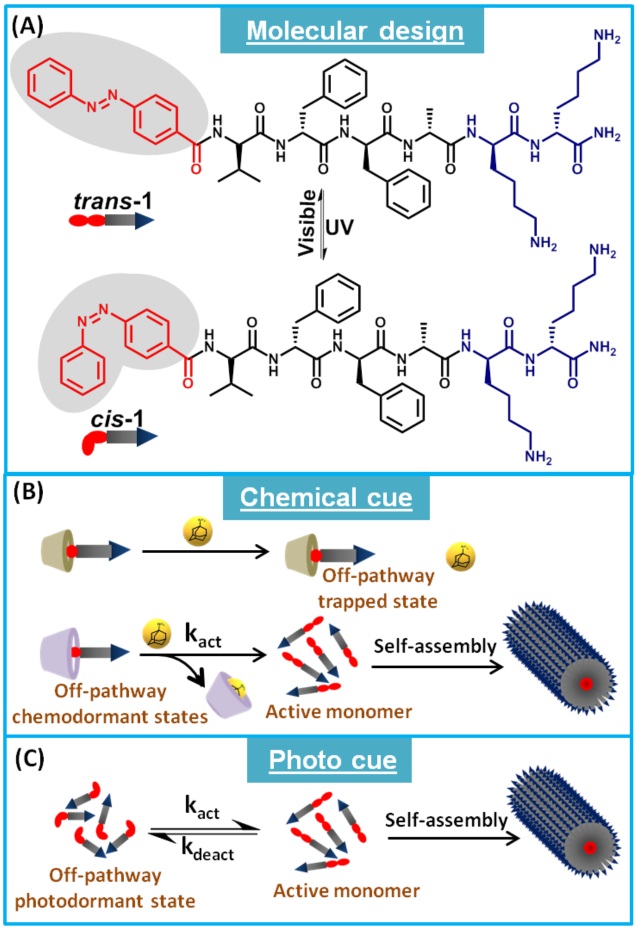

Scheme 2.1: Design strategies for controlled self-assembly/disassembly in peptide amphiphile using external stimuli such as light and chemical cues. (A) Schematic of reversible photoisomerization to furnish *trans* and *cis* isomers for peptide **1**. (B) Inhibition of spontaneous self-assembly by forming a chemodormant state mediated by host-guest inclusion complex involving *trans*-**1** with α-cyclodextrin or β-cyclodextrin, which can be retrieved upon addition of adamantyl amine as the competitive guest for the *trans*-**1** ⊂ β-CD complex. (C) Reversible photocontrolled deactivation of *trans*-**1** in the photodormant state of *cis*-**1** (λ = 365 nm), which upon activation with visible light (λ = 405 nm) reforms active *trans*-**1** state to render supramolecular nanofibers.

Herein, we report the controlled self-assembly/disassembly of an Aβ(1-42) inspired minimalistic peptide **1** (azo-VFFAKK) anchored with a photochemically responsive azobenzene moiety (Scheme 2.1). A judicious choice of temperature and solvent composition favored the formation of on-pathway metastable nanoparticles of *trans*-**1** that eventually evolved to form 1D self-assembled nanofibers in water. Further, two distinct strategies based on photochemical stimuli were employed to render off-pathway dormant states, which inactivated the spontaneous supramolecular polymerization. First, the complexation of the azobenzene moiety of peptide **1** with the guest molecule of cyclodextrin (α-CD and β-CD) exhibited the formation of off-pathway chemodormant nanoparticles. Second, the photo regulated geometrical change of azobenzene (*trans* to *cis*) inhibited the spontaneous nucleation of peptide **1** to render off-pathway photodormant nanoparticles. Such photochemically trapped off-pathway dormant metastable states act as a reservoir for the active monomer and can be activated on demand by the introduction of competitive guests or by photomediated reconversion to *trans*-**1** to trigger the peptide self-assembly. The competitive interactions were validated in the energy landscape to rationalize the evolution of different metastable species and concomitant supramolecular polymerization. Such on-demand activation to monomers can be efficiently exploited toward seeded supramolecular polymerization to render programmable supramolecular peptide nanostructures with precision. Finally, we demonstrated for the first time an elegant photochemical sequestration strategy to design an on-demand piezoelectric nanogenerator from the peptide nanostructures. Taken together, the work stresses on the importance of controlling the pathway complexity in peptide building blocks and unravels a new strategy to access complex and functional supramolecular peptide nanostructures in a rational manner toward energy harvesting devices.

2.2. Results and discussion

2.2.1. Molecular design and self-assembly of *trans*-1

Peptide **1** was designed by tethering a hydrophobic azobenzene group at the *N*-terminal and two hydrophilic lysine units at the *C*-terminal of an amyloid Aβ(1−42) inspired peptide sequence, $^{N}VFFA^{C}$ (Scheme 2.1). Owing to the efficient hydrogen bonding among the amide moieties and strong *π*−*π* interactions among the phenyl side chains and azobenzene moieties, *trans*-**1** was found to self-assemble in water (Figure 2.1A). To alleviate any possible pre-assembled aggregates, *trans*-**1** was taken in hexafluoroisopropanol (HFIP) to disrupt the hydrogen bonding among the amide moieties.[56,57] Spectroscopic and microscopic investigations showed the presence of metastable nanoparticles in HFIP guided by π−π stacking interactions among the phenylalanine side chains and azobenzene motifs (Figure 2.1B). However, upon increasing the volume fraction of water in a mixture of solvents (HFIP-water) or upon increasing the temperature, the initial nanoparticles at specific solvent composition were found to convert into 1D nanofibers, This suggested the kinetic nature of the self-assembly, with the on-pathway nanoparticles exhibiting spontaneous nucleation and subsequent conversion to the nanofibers upon increasing the temperature or changing the solvent composition. The transmission electronic microscopy (TEM) and atomic force microscopy (AFM) images of *trans*-**1** in water exhibited nanofibers (diameter ~ 8 nm) with a high aspect ratio (Figure 2.1F, H). However, a repeated annealing of the nanofibers rendered the formation of thermodynamically stable twisted bundle morphology (Figure 2.1I-J).

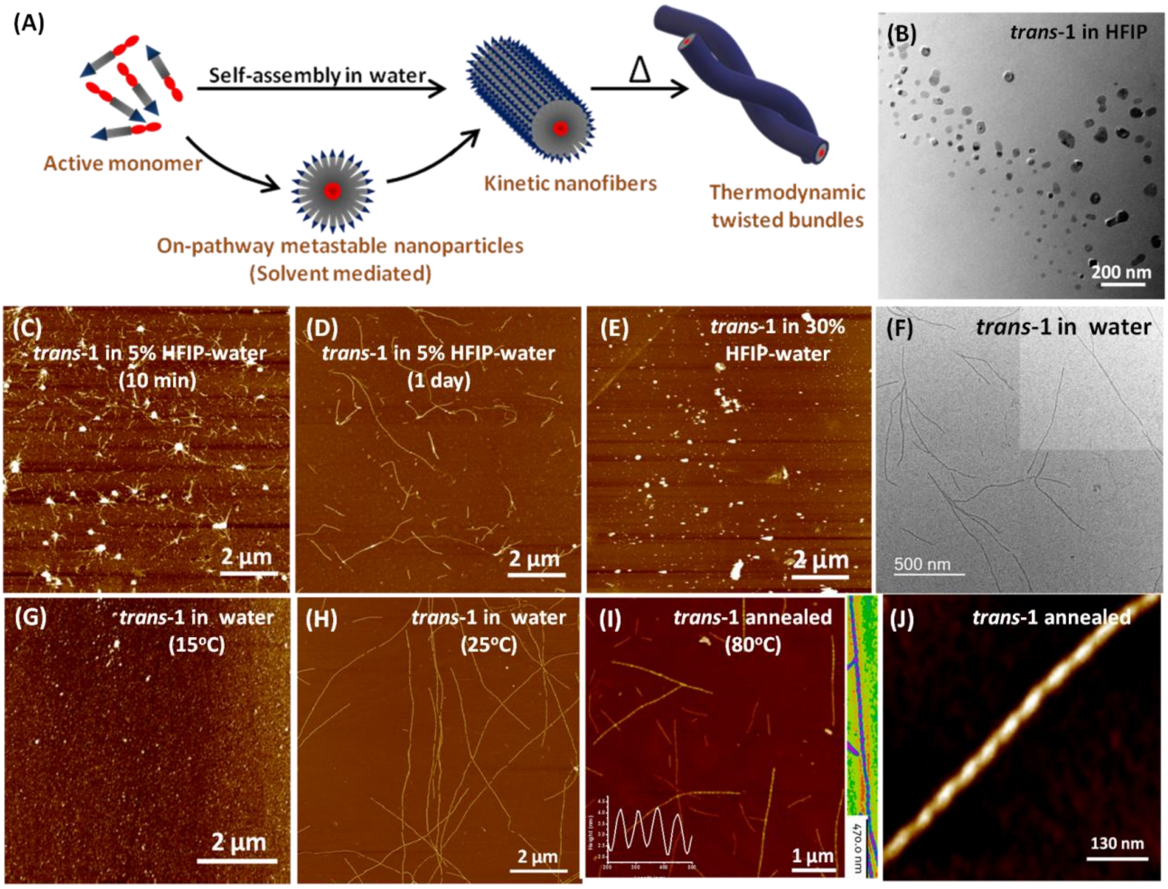

Figure 2.1: Self-assembly of *trans*-**1** peptide amphiphiles in aqueous milieu. (A) Schematic for pathway-dependent self-assembly of *trans*-**1** showing the conversion of monomers to on-pathway metastable nanoparticles, exhibiting conversion to kinetically controlled nanofiber and thermodynamically stable twisted bundles. Solvent controlled self-assembly of *trans*-**1.** (B) TEM images of *trans*-**1** on-pathway nanoparticles in HFIP. AFM image of (C) *trans*-**1** in 5**%** HFIP-water showing metastable nanoparticles converting to kinetically controlled nanofibers within 10 minutes of water addition. (D) Self-assembled nanofibers of *trans*-**1** after one day of incubation in 5**%** HFIP-water. (E) Nanofibers formation of *trans*-**1** was retarded in 30**%** HFIP-water solvent mixture and exhibited presence of nanoparticles even after 3 h. (F) *trans*-**1** in only water exhibited robust nanofibers after one day incubation. Temperature driven self-assembly of *trans*-**1** in water monitored using AFM. (G) *trans*-**1** at low temperature (15 ºC) furnishes on-pathway metastable nanoparticles, (AFM image recorded after 3 h) (H) that converts to self-assembled nanofibers of *trans*-**1** after 1 day. (I) Upon repeated annealing to 80 ºC, *trans*-**1** showed formation of twisted bundles. (J) Zoomed AFM image recorded after 3 h of thermal annealing showing thermodynamically controlled twisted bundle of *trans*-**1** in water (concentration = 40 μM).

We monitored such pathway-driven self-assembly process of *trans*-**1** in water using UV-vis and CD spectroscopy analyses. A freshly dissolved solution of *trans*-**1** in water showed UV-vis absorbance bands at 323 nm and 430 nm due to characteristic $\pi-\pi^*$ and weak $n-\pi^*$ bands respectively (Figure 2.2A). However, with time, the absorption maxima exhibited a hypsochromic shift that suggested the formation of supramolecular H-aggregates due to the presence of azobenzene moieties[58] (Figure 2.2B). Next, we conducted kinetic experiments at 25 °C with different concentrations of *trans*-**1** and monitored the absorbance ratios at 300 and 323 nm with time. We observed an initial lag phase at lower concentrations owing to the formation of on-pathway aggregates; however, at higher concentrations the diminishing lag phase indicated faster conversation to nanofibers (Figure 2.2C). Thus, the time at which 50% of the aggregation was completed was found to be decreasing in a nonlinear manner with an increasing concentration of *trans*-**1** (Figure 2.2D). Further, the CD spectra exhibited a gradual increase in intensity for the negative cotton band indicating the formation of β-sheet secondary structures in a self-assembled state (Figure 2.2E).

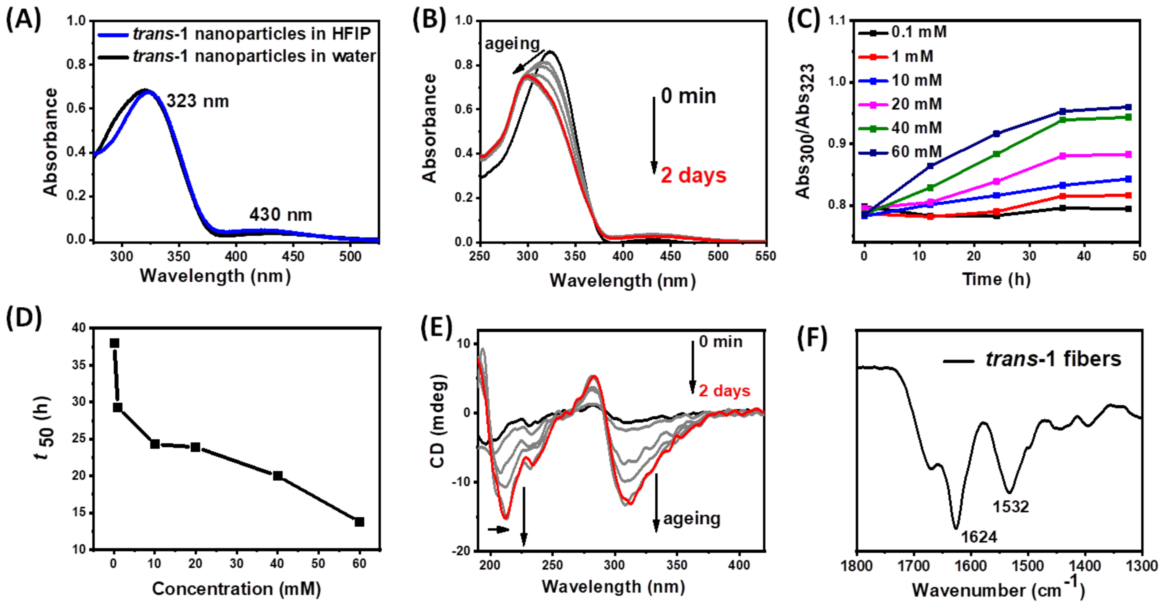

Figure 2.2 (A) UV spectra of peptide **1** in HFIP and water at 15ºC (concentration = 70 µM), spectra was recorded after 3 h. (B) UV-vis spectra exhibiting gradual hypsochromic shift with time corresponding to the aging of the fibers (concentration = 70 µM, pH = 6.5). (C) Concentration dependent evolution of *trans*-**1** self-assembly as monitored by the ratio of absorbances at 300 and 323 nm. (D) Concentration dependent self-assembly in water as monitored by UV-vis spectra depicting t_{50} values (time taken for 50% completion of the supramolecular polymerization) decreases with concentration. (E) Time-dependent CD spectra showing the appearance of peaks at 193 nm, 213 nm and at 309 nm owing to the β-sheet secondary structures and π-π stacking of the azobenzene moiety (concentration = 70 µM, pH = 6.5). (F) FTIR spectra indicating parallel β-sheet stacking in the nanofibers of *trans*-**1**.

A gradual build-up of an induced CD band at 309 nm with time was ascribed to the stacking of the azobenzene moiety as a consequence of the peptide self-assembly, which transfers the chiral information of the peptide sequence to the azobenzene moiety. FT-IR signals at 1624 and 1532 cm^{-1} confirm the presence of the parallel arrangement of β-sheets in the secondary structure (Figure 2.2F). All these findings corroborated the involvement of ordered H aggregates in the kinetically controlled nanofibers, with concomitant parallel β-sheet arrangement at ambient conditions.

2.2.2. Off-pathway chemodormant state by host-guest interactions

Azobenzene has a strong affinity to α-cyclodextrin (α-CD) and β-cyclodextrin (β-CD) cavities to form a host-guest inclusion complex (Figure 2.3A). We exploited such host-guest complexation as a strategy to render off-pathway dormant states that retard the spontaneous nucleation of the *trans*-**1** amphiphile. The complexation behaviors of *trans*-**1** (guest) with α-CD and β-CD (host) were investigated using ^{1}H NMR spectroscopy in D_2O. The azobenzene protons *a*, *b*, *c*, *d* and *e* showed remarkable downfield shifts upon the introduction of equimolar host molecules (α-CD or β-CD) (Figure 2.3B, 2.4 & 2.5). The protons of α-CD or β-CD also exhibited a remarkable upfield shift upon host-guest complexation. For a better understanding of the complexation between α-CD or β-CD and *trans*-**1**, we performed Job's plot analysis that indicated a 1**:**1 complexation stoichiometry (Figure 2.6 & 2.7). We further conducted isothermal titration calorimetry (ITC) experiments at 25 °C to gain more insights into the thermodynamics of the complexation process. The titration of an aqueous solution of α-CD (10 mM) against *trans*-**1** (0.25 mM) provided a satisfactory sigmoidal curve, allowing the determination of various thermodynamic parameters (Figure 2.3C). The association constant (K_a) of *trans*-**1** with α-CD was calculated to be 9900 M^{-1}, with the number of sites of interactions = 1. The enthalpy (ΔH), free energy (ΔG) and $T\Delta S$ of complexation were estimated to be -3.14 kcal/mol, -5.45 kcal/mol and 2.31 kcal/mol respectively. However, *trans*-**1** and β-CD formed an inclusion complex with a relatively lower binding affinity (K_a = 6134 M^{-1}, ΔH = -0.619 kcal/mol, ΔG = -5.17 kcal/mol and $T\Delta S$ = 4.55 kcal/mol) (Figure 2.3D).–The computed free energy (ΔG) as obtained from the MD simulations also confirmed a more favorable association of *trans*-**1** with α-CD compared to that with β-CD by 8.11 kcal/mol (Figure 2.8 & Table 2.1).

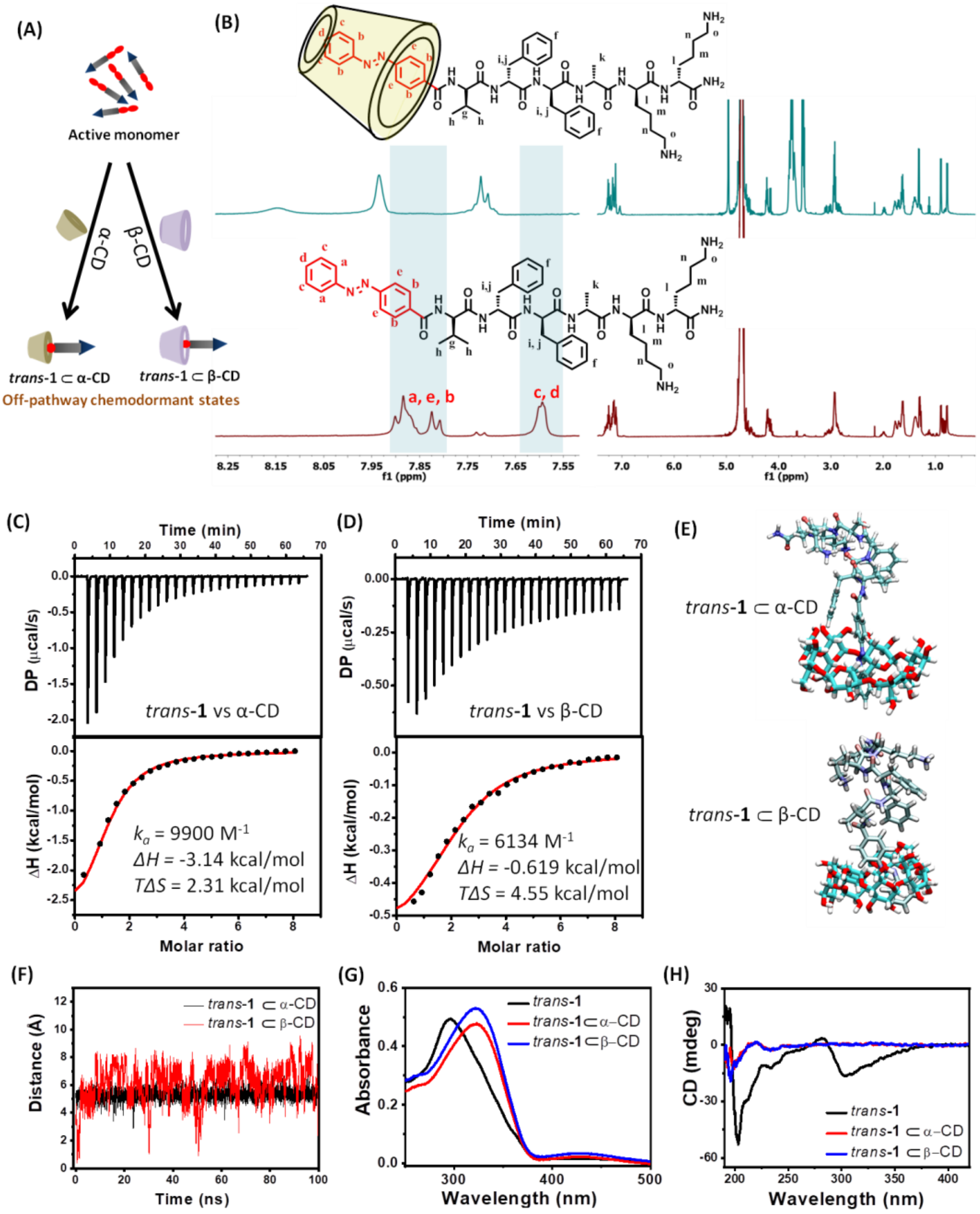

Figure 2.3: Schematic representation of the host-guest complexation for trapping *trans*-**1** in off-pathway chemodormant states. (B) Comparative ^{1}H NMR spectra of *trans*-**1** before and after the formation of the inclusion complex with equimolar α-CD in D_2O (4 mM). (C-D) ITC data showing exothermic heat release and integrated heat profile for the binding interaction of *trans*-**1** (0.25 mM) with α-CD and β-CD (10 mM) in water at 25 °C after. (E) MD simulations depicting the inclusion complexes, *trans*-**1** ⊂ α-CD and *trans*-**1** ⊂ β-CD. (F) Probability distribution distance plots (center of mass distance between the azobenzene moiety of *trans*-**1** and glycosidic oxygen of α-CD/β-CD) indicating lower fluctuations in *trans*-**1** ⊂ α-CD and higher fluctuations in *trans*-**1** ⊂ β-CD. (G) UV-vis spectra of the off-pathway inclusion complexes, *trans*-**1** ⊂ α-CD and *trans*-**1** ⊂ β-CD showing a significant red shift as compared to the *trans*-**1** peptide fibers. (H) CD spectra of the inclusion complexes show the absence of the β-sheet secondary structure in the presence of host α-CD or β-CD molecules (concentration = 40 μM).

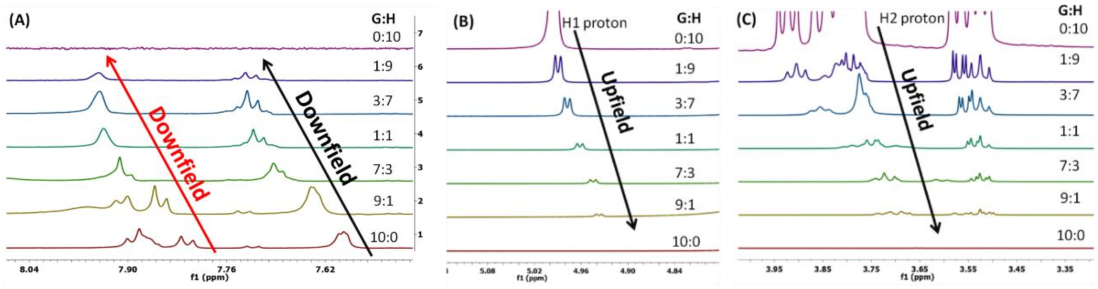

Figure 2.4: Partial ^{1}H-NMR spectra of α-CD (Host, H) titrated with *trans*-**1** (Guest, G) solution in D_2O at different ratios at room temperature. The total concentration of the solution was kept at 4 mM. The downfield shifts of (A) *a*, *e*, *b* protons (shown by red arrow) and *c*, *d* protons (shown by black arrow) of *trans*-**1**. (B) *H1* and (C) *H2* protons of α-CD moiety showed upfield shift with increasing amount of guest moiety, *trans*-**1**.

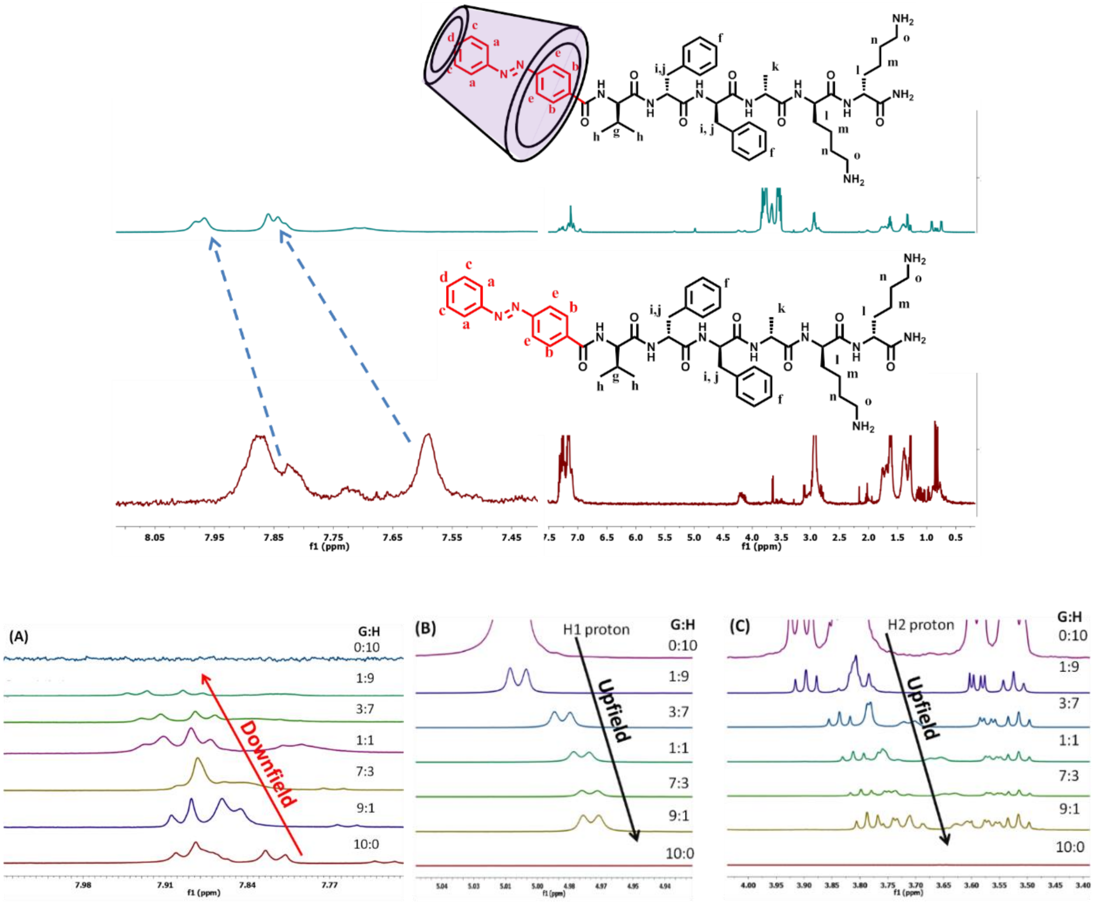

Figure 2.5: Comparative ^{1}H-NMR spectra of *trans*-**1** peptide (8 mM) and host-guest complex of *trans*-**1** ⊂ β-CD (1:1) in D_2O showing downfield shift of protons of azobenzene moiety. Partial ^{1}H-NMR spectra of β-CD (Host, H) titrated with *trans*-**1** (Guest, G) solution in D_2O at different ratios at room temperature. The total concentration of the solution was kept at 4 mM. The downfield shifts of (A) azobenzene protons of *trans*-**1**. (B) *H1* and (C) *H2* protons of the β-CD moiety showed upfield shift with increasing amount of *trans*-**1**.

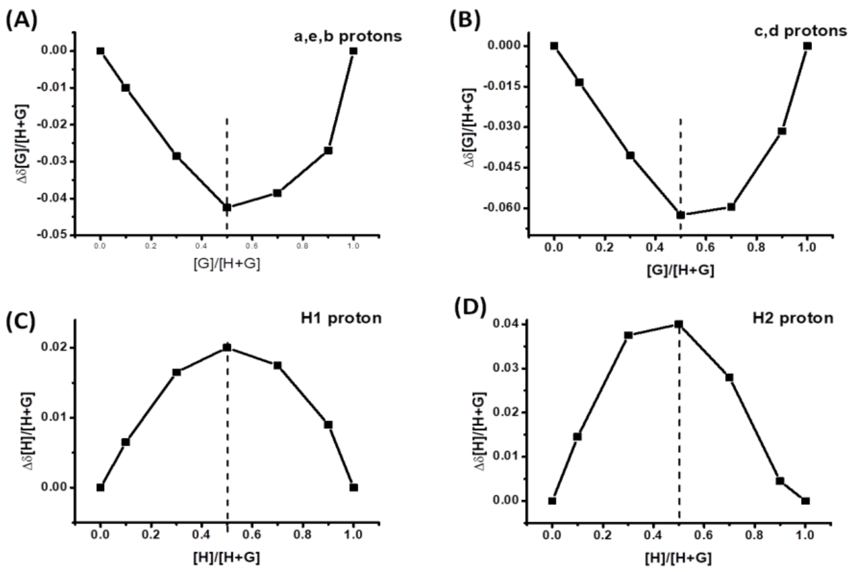

Figure 2.6: Job's plot obtained by titrating *trans*-**1** (G) with α-CD (H) at different ratios in D_2O at 25 ºC. Changes in the chemical shift values of (A) *a*, *e*, *b* protons (B) *c*,*d* protons of azobenzene moiety of *trans*-**1** plotted with mole fraction of *trans*-**1**. (C) Change in chemical shift values of *H1* and (D) *H2* protons of α-CD are plotted with the mole fractions of α-CD.

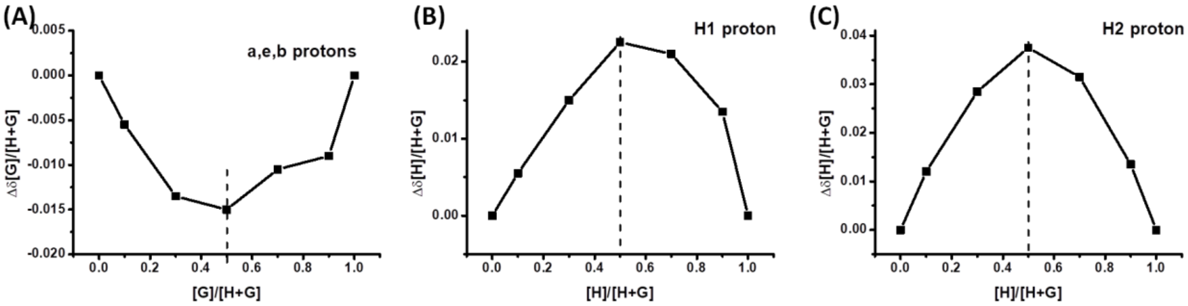

Figure 2.7: Job's plot obtained by titrating *trans*-**1** with β-CD at different ratios in D_2O at 25 ºC. Changes in the chemical shift values of (A) *a*, *b*, *e* protons of azobenzene moiety of *trans*-**1** plotted with mole fraction of *trans*-**1**. (B) Change in the chemical shift values of *H1* and (C) *H2* protons of α-CD plotted with the mole fraction of α-CD.

Thus, both experimental and computation data corroborated a stronger interaction in *trans*-**1** ⊂ α-CD as compared to the *trans*-**1** ⊂ β-CD complex, although the interaction in the latter inclusion complex was also significant to inhibit the inherent self- assembly of *trans*-**1**. Moreover, the variation of thermodynamic parameters such as enthalpy (*ΔH*) and entropy factors (*TΔS*) for the complexes indicated a tight binding for the inclusion complex, *trans*-**1** ⊂ α-CD. It is noteworthy that *trans*-**1** with β-CD shows a more favorable entropy factor, with a higher change in the absolute value of entropy upon complexation. This indicated a relatively high conformational and transitional flexibility between the azobenzene moiety of *trans*-**1** and β-CD cavity, resulting in loose binding. For deeper insights of the mechanism simulations of *trans*-**1** with α-CD and β-CD using the classical host-guest complexation, we performed molecular dynamics MD simulations.

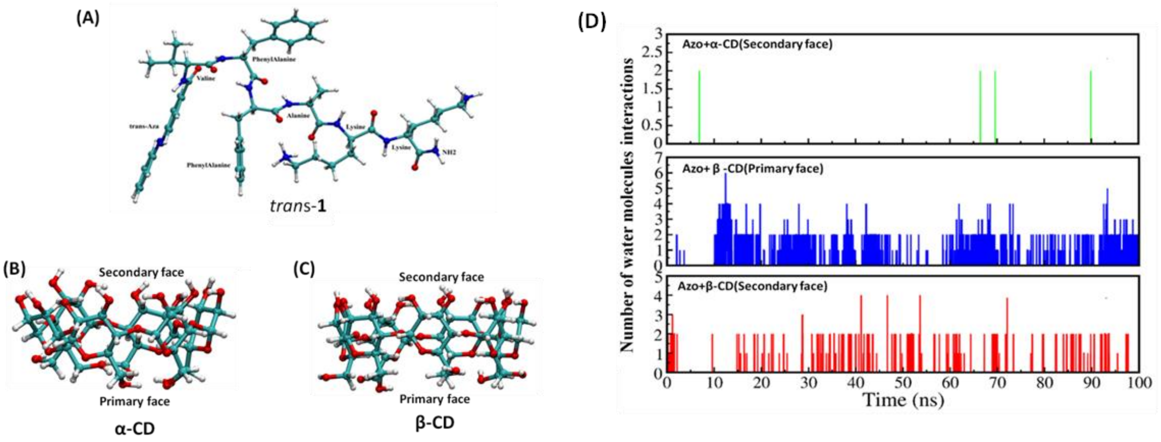

Figure 2.8: (A-C) Molecular geometry optimization of *trans*-**1** peptide and cyclodextrins using B3LYP/6-31G* methodology. (D) The number of water molecules interacting with the pendant azobenzene over a simulated trajectory for 100 ns with α-CD and β-CD from different faces.

The analysis of the MD trajectories clearly indicated the formation of stable inclusion complexes with *trans*-**1** approaching from both the faces that is primary and secondary faces of cyclodextrin (Figure 2.3E). The absence of water molecules inside α-CD clearly suggested the strong binding in *trans*-**1** ⊂ α-CD even prohibiting any further water molecules to enter; however *trans*-**1** ⊂ β-CD inclusion complex engaged a substantial amount of water molecules in its cavity (Figure 2.8D). We analyzed the distance between the center of mass for all the glycosidic oxygen atoms of cyclodextrin and the azobenzene moiety for both the inclusion complexes. The probability distribution of the center of mass distances exhibited larger fluctuations in the *trans*-**1** ⊂ β-CD complex and corroborated a tighter inclusion complex in *trans*-**1** ⊂ α-CD as compared to *trans*-**1** ⊂ β-CD (Figure 2.3F). Next, we investigated the effect of host-guest interactions on the self-assembly behavior by UV and CD spectroscopy analyses. A solution of *trans*-**1** upon 1**:**1 complexation with both α-CD and β-CD exhibited a significant bathochromic shift, as compared to the native *trans*-**1** that clearly indicated the disruption of the π-π interaction among the pendant azobenzene moieties (Figure 2.3G). Further, the CD spectra clearly demonstrated the absence of the β-sheet secondary structure and induced a CD signature of azobenzene upon complexation with either of α-CD or β-CD (Figure 2.3H).

Table 2.1: Simulation time and atomistic details for the host-guest interaction

System	No. of atoms/Molecules	Periodic cell boundary	Length of Trajectory
trans-**1** + α-CD (Primary Face)	Total atoms = 12494 *trans*-**1** = 138 α-CD = 126 Cl- = 2 (ions) Water = 12228	56.210 x 55.386 x 53.455	100 ns
trans-**1** + α-CD (Secondary Face)	Total atoms = 12734 *trans*-**1** = 138 α-CD = 126 Cl- = 2 (ions) Water = 12468	56.210 x 55.386 x 53.455	100 ns
trans-**1** + β-CD (Primary Face)	Total atoms = 12986 *trans*-**1** = 138 β-CD = 147 Cl- = 2 (ions) Water = 12699	56.742 x 54.554 x 54.498	100 ns
trans-**1** + β-CD (Secondary Face)	Total atoms = 12363 *trans*-**1** = 138 β-CD = 147 Cl^- = 2 (ions) Water = 12650	55.908 x 52.317 x 55.969	100 ns
Ada	Total atoms = 8911 Ada = 28 α-CD = 126 Water = 8757	45.347 x 47.301 x 45.547	100 ns
Ada	Total atoms = 9481 Ada = 28 β-CD = 147 Water = 9306	47.389 x 46.834 x 46.627	100 ns

Such observations clearly indicated that the azobenzene moiety of *trans*-**1** formed an inclusion complex with α-CD/β-CD molecules, thereby inhibiting *trans*-**1** to undergo spontaneous supramolecular polymerization. The AFM images from the uncomplexed and complexed samples of *trans*-**1** corroborated the role of the cyclodextrin molecules to arrest the self-assembly process. Thus, while *trans*-**1,** in the absence of any guest moiety, can self-assemble to nanofibers, the amphiphile upon complexation with α-CD or β-CD traps the process to yield metastable nanoparticles, as indicated by AFM and DLS data (Figure 2.9A-D). It is noteworthy that already self-assembled *trans*-**1** was not affected by the presence of host moieties and showed unchanged nanofibrous morphology (Figure 2.9E-F) indicating the dominant role of robust hydrogen bonding over the host-guest inclusion complexation.

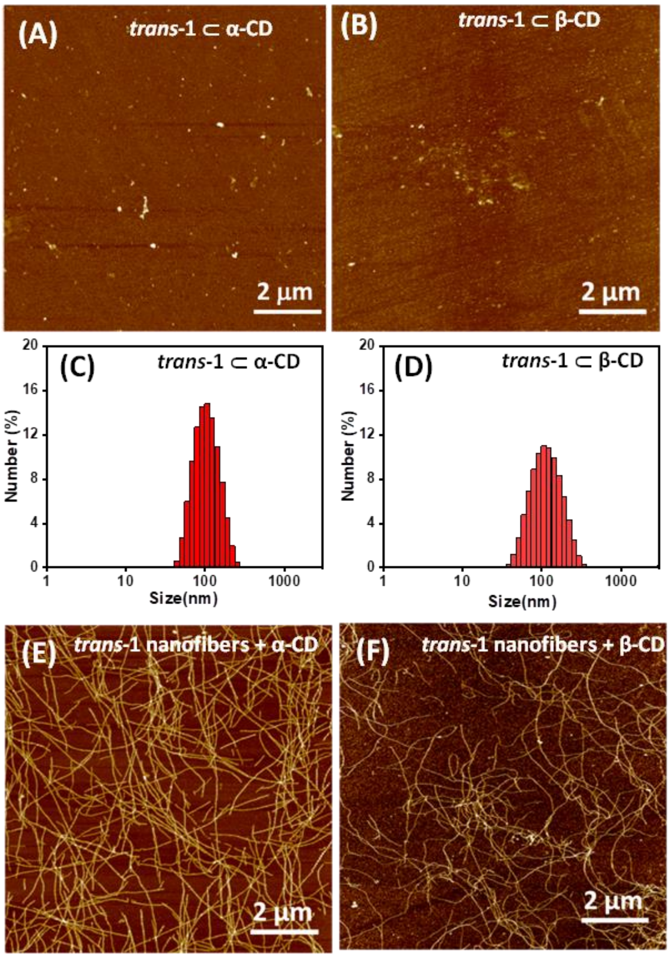

Figure 2.9: A AFM images showing the off-pathway dormant metastable nanoparticles of (A) *trans*-**1** ⊂ α-CD, (B) *trans*-**1** ⊂ β-CD upon dissolution of *trans*-**1** with α-CD or β-CD. Dynamic light scattering (DLS) data for the metastable nanoparticles of (C) *trans*-**1** ⊂ α-CD (~90 nm), (D) *trans*-**1** ⊂ β-CD (~100 nm), (E-F) Addition of α-CD or β-CD to the self-assembled nanofibers of *trans*-**1** did not change the fiber morphologies. AFM images were recorded after 3 days.

2.2.3. Off-pathway photodormant state

Next, we explored the photoswitchable behavior of the pendant azobenzene moiety in peptide **1** in a bid to regulate the photoresponsive structural control between the *trans* and *cis* isomers around the –N=N– group upon UV or visible irradiation. Interestingly, the *trans* conformation of the azobenzene moiety is planar *sans* dipole moment, while the *cis* conformation has a dipole moment of ~3 Debye owing to the bent out-of-plane conformation with phenyl rings.[53] As discussed earlier, *trans*-**1** in HFIP at 25 °C or freshly dissolved in water at low temperature (15 °C) resulted in an on-pathway metastable nanoparticle exhibiting a prominent UV peak at 323 nm (π–π*) and a broad peak at 440 nm (n–π*).

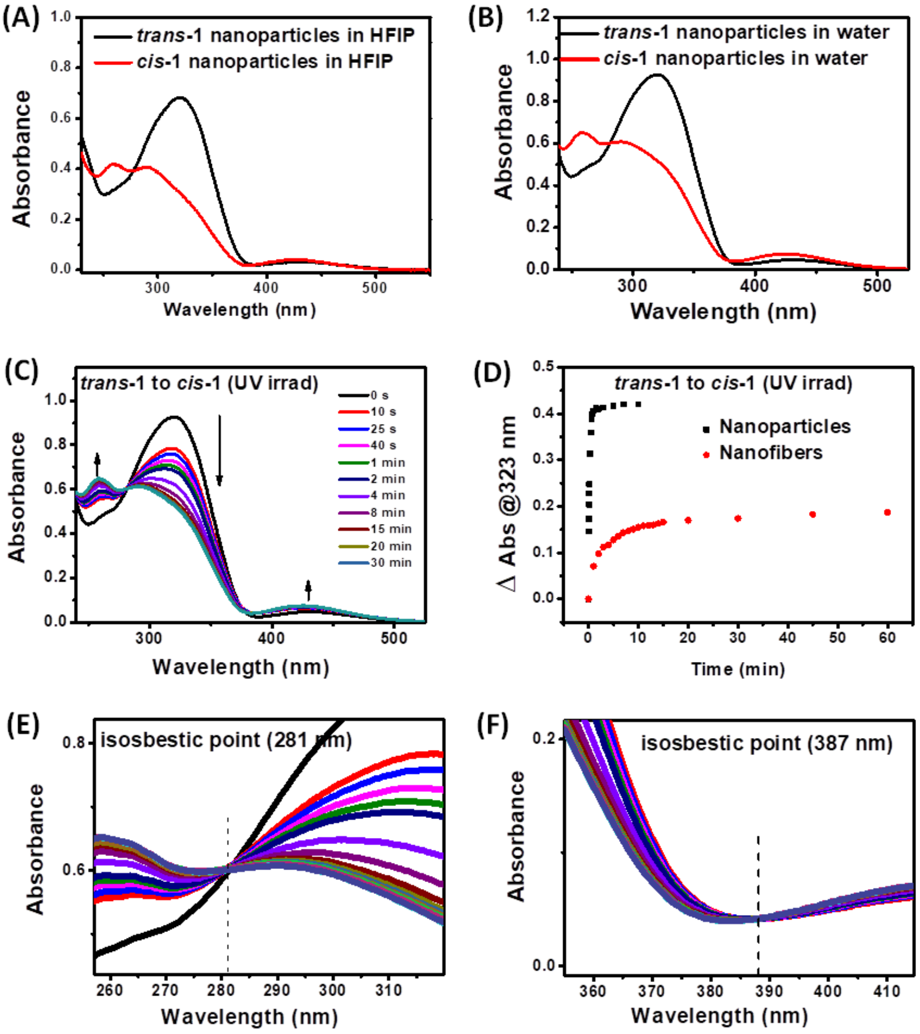

Figure 2.10: UV-vis spectra showing fast photoswitching of on-pathway state of *trans*-**1** to off-pathway photodormant nanoparticles of *cis*-**1** (A) in HFIP and (B) in water immediately after dissolution. (C) Faster photoisomerization of *trans*-**1** nanoparticles to *cis*-**1** upon UV irradiation. (D) Comparative photoisomerization kinetics for *trans*-**1** nanoparticles and self-assembled nanofibers. (E-F) Two isosbestic points at 281 nm and 387 nm characteristc of *trans-cis* conversion in azobenzene for *trans*-**1** nanoparticles. (Concentration = 70 μM).

However, upon UV irradiation ($\lambda = 365$ nm), the *trans*-to-*cis* isomerization rendered an off-pathway metastable nanoparticle with a gradual decrease in the intensity of the π–π* band with the appearance of a new peak at 255 nm, whereas the n–π* band intensity became prominent as well (Figure 2.10A-B). Further, for the on-pathway metastable nanoparticles of *trans*-**1** in HFIP or in water, the equilibrium between *trans*-**1** and *cis*-**1** was established quite fast (3 min, 2.10C). However, for the self-assembled nanofibers of *trans*-**1**, the photoregulated disassembly took a rather longer time (30 min) to reach the photostationary state (PSS) (Figure 2.10D & 2.11A). The presence of strong attractive forces such as H bonding and π-π interactions in assembled nanofibers made it rather constrained for azobenzene to alter its stereo-chemical geometry. The isosbestic points were observed at 281 and 387 nm, corresponding to the *trans*-to-*cis* isomerization (Figure 2.10E-F).

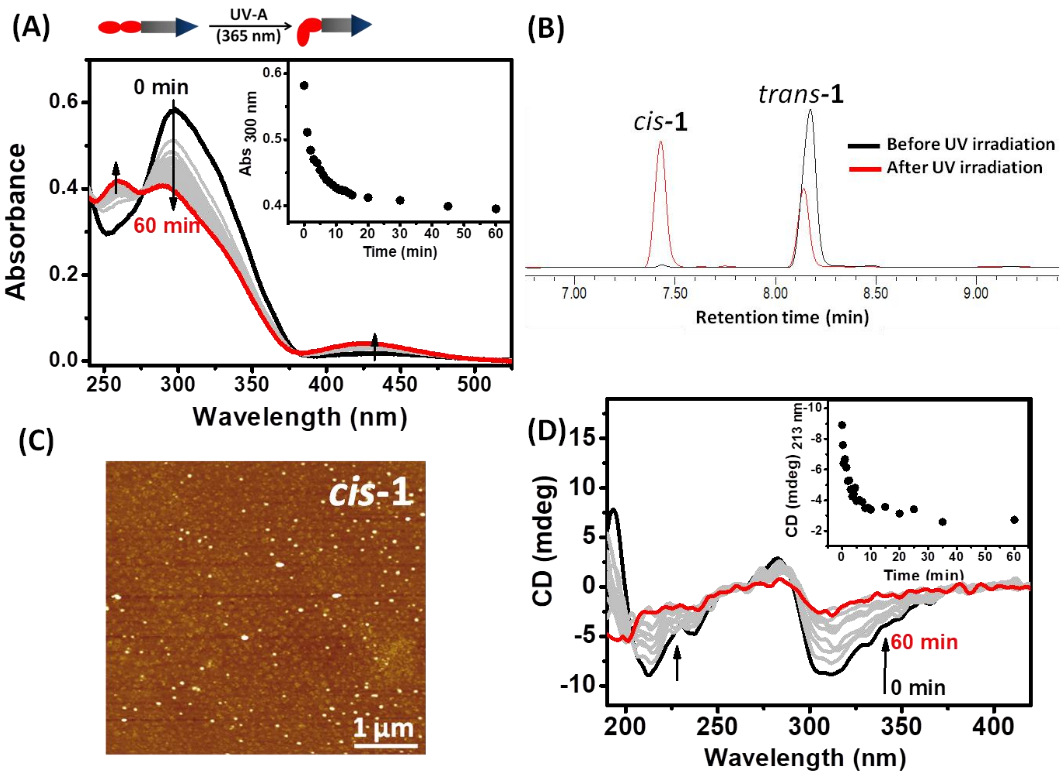

Figure 2.11: Schematic strategy to disassemble *trans*-**1** nanofibers to be trapped in off-pathway photodormant states *cis*-**1** in water. (A) Photoregulated gradual change in UV-vis spectra for the nanofibers of *trans*-**1** in water to result in *cis*-**1**. Inset depicts the time-dependent change in absorbance at 300 nm. (B) HPLC chromatogram at an isosbestic point of 281 nm shows 65% conversion of *trans*-**1** (1 mM) to *cis*-**1** upon UV irradiation for 1 h (λ = 365 nm). (C) AFM imaging depicts the off-pathway dormant metastable nanoparticles of *cis*-**1** at the photostationary state. (D) CD spectra show β-sheet with peaks at 193, 213, and 308 nm that gradually diminish upon UV irradiation (λ = 365 nm). Inset depicts the time-dependent change in ellipticity at 213 nm (Concentration = 70 µM).

However, a substantial overlap in the UV-vis spectra for the *trans* and *cis* isomers of peptide **1** made the calculation of the amount of isomers at the PSS difficult. However, an HPLC analysis at the isosbestic point (λ = 281 nm) allowed us to determine the relative distribution of *cis*-**1** (7.4 min) and *trans*-**1** (8.2 min) at PSS. Thus, UV irradiation significantly decreased the ratio of *trans*-**1** to *cis*-**1** from 99:1 to 33:67 (Figure 2.11B). The AFM image of the UV irradiated sample, exhibited a complete disassembly of the nanofibers for the dominant *cis*-**1** isomer at the photostationary state to render off-pathway metastable nanoparticles of *cis*-**1** (Figure 2.11C). Upon irradiation at 365 nm, the characteristic β-sheet CD signature of *trans*-**1** gradually disappeared with time, indicating disassembly of supramolecular nanofibers (Figure 2.11D). The higher dipole moment of *cis*-**1** relative to *trans*-**1** and the altered molecular geometry that restricts the π-π stacking of the peptide molecules account for the photoregulated disassembly. It is noteworthy that even at a maximal PSS of 67% for *cis*-**1** the self-assembled nanofibers are disassembled. Such PSS state with predominantly *cis*-**1**, was conceived as the off-pathway photodormant metastable state that can be activated with visible light.

2.2.4. Activation of the dormant metastable states

After understanding the self-assembly and disassembly behavior of *trans*-**1** so as to trap the active monomer in two distinct off-pathway metastable states, we further investigated the activation of the dormant states using chemical and photo cues to control the concomitant supramolecular self-assembly process. Such trapping of the dormant states and strategies for activation are thoroughly elucidated through the energy landscape diagrams. Thus, the off-pathway metastable states could be envisaged as a deterrent for the spontaneous nucleation process, until external stimuli were introduced. The deep energy trap for the metastable states ensured the complete inhibition of spontaneous nucleation caused by the active monomer of *trans*-**1**. To the inclusion complexes of *trans*-**1** ⊂ α-CD and *trans*-**1** ⊂ β-CD, a competitive guest, 1-adamatylamine (Ada), was introduced that resulted in a shift in the thermodynamic equilibrium favoring the host-guest complex with a superior binding affinity of Ada toward the β-CD cavity, thereby setting the *trans*-**1** monomer free for supramolecular polymerization (Figure 2.12A). Pertinently, ITC data exhibited a higher binding for β-CD with Ada than the azobenzene moiety (K_a of Ada ⊂ β-CD ~ 2.7 x10^4 M^{-1}, Figure 2.13). MD simulation corroborated a stronger binding of Ada with β-CD with no fluctuation in the centre of mass distances over an observable timescale and a shorter distance (1.1 Å) between the centre of mass of β-CD and Ada (Figure 2.12B). Such preference for Ada to form a stronger inclusion complex with β-CD came at the expense of the preformed *trans*-**1** ⊂ β-CD inclusion complex paving for the release of the *trans*-**1** monomer. The free peptide molecule could act as an “active monomer” to self-assemble in water-HFIP (9:1) with time. The CD spectra showed a recurrence of the β-sheet secondary structure of the peptide upon incubating Ada with the *trans*-**1** ⊂ β-CD complex (Figure 2.12C). The AFM images exhibited appearance of the nanofibers upon activation of dormant states by chemical cues (Figure 2.124D). Remarkably, the *trans*-**1** ⊂ α-CD complex solution was quite stable and did not get affected by the presence of Ada as the competitive guest. The ITC studies suggested no significant interaction of Ada with α-CD, which was further corroborated by MD simulations suggesting an unstable inclusion complex (Figure 2.12F). Further, the addition of Ada molecule in the *trans*-**1** ⊂ α-CD solution did not result in any observable change in the CD signal at 213 nm with the AFM images showing thermodynamically stable trapped nanoparticles (Figure 2.12G-H). This clearly indicated *trans*-**1** ⊂ α-CD as an off-pathway trapped state, which remained unaffected by chemical cues during the observable time period.

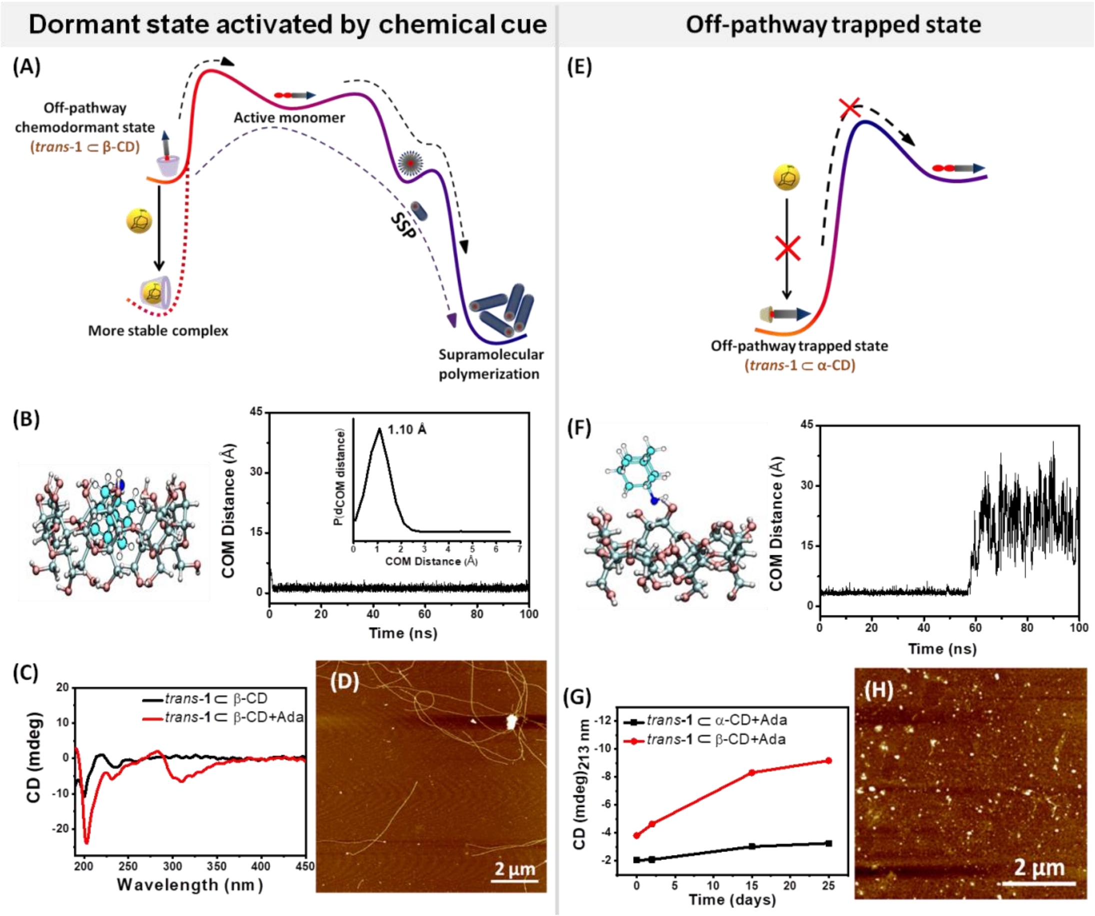

Figure 2.12: Chemical cue-mediated strategy to activate the dormant state for supramolecular polymerization. (A) Energy profile diagrams to summarize the trapping of the dormant state, *trans*-**1** ⊂ β-CD, to be reactivated by 1-adamantyl amine (Ada) for supramolecular polymerization. (B) Center of mass (COM) distance between Ada and β-CD (glycosidic oxygen) in MD simulation showing the formation of a stable inclusion complex *trans*-**1** ⊂ β-CD. (C) CD spectra of the dormant state, *trans*-**1** ⊂ β-CD (black) and chemically activated *trans*-**1** after 2 days of incubation with the competitive guest, Ada. (D) AFM image showing the formation of nanofibers from the dormant metastables particle of *trans*-**1** ⊂ β-CD in 2 days. (E) Energy profile diagrams showing a deeper energy well for chemically dormant *trans*-**1** ⊂ α-CD complex dictated by thermodynamics. (F) Transition to higher value in the plot of the center of mass (COM) distance between Ada and α-CD (glycosidic oxygen), indicating no inclusion complex formation. (G) Time evolved CD spectra of dormant states (*trans*-**1** ⊂ α-CD and *trans*-**1** ⊂ β-CD) incubated with the competitive guest, Ada. (H) AFM images showing the presence of trapped nanoparticles of *trans*-**1** ⊂ α-CD.

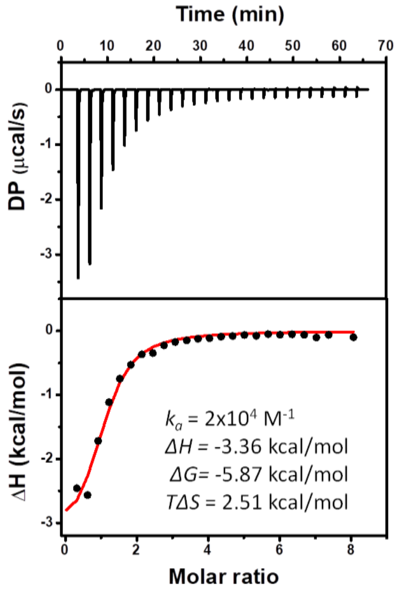

Figure 2.13: Isothermal titration calorimetry data obtained for the binding interaction of β-CD (0.25 mM) to 1-adamantylamine, Ada (10 mM) in water at 25 ºC.

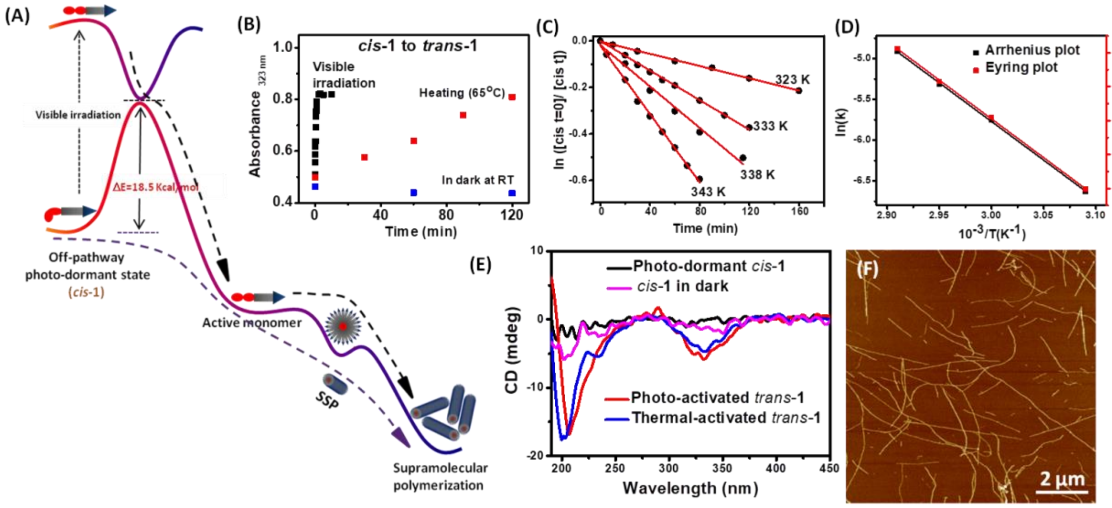

Figure 2.14: (A) Strategy and representation of energy pathways for the photoattenuated activation of dormant states toward supramolecular polymerization. (B) UV-vis spectra depicting *cis*-**1** to *trans*-**1** isomerization on visible irradiation (C) Photoregulated conversion of *cis*-**1** to *trans*-**1** under conditions of visible irradiation, heating at 65 ˚C and incubation in dark at 25 ˚C. (D) Thermal response of the *cis*-**1** to *trans*-**1** conversion at different temperatures to calculate (E) various thermodynamic parameters using Arrhenius and Eyring plots. (F) Photoswitching of Peptide **1** multiple times upon consecutive UV and visible irradiation. (G) CD spectra of the dormant state, *cis*-**1** (black), and photo activated *trans*-**1** after visible light irradiation. (H) AFM images showing the formation of nanofibers upon activation of the dormant metastable particles of *cis*-**1** by visible light.

Next, we envisaged the photo regulated activation of dormant metastable states to *trans*-**1** "active monomer" by irradiation with visible light (λ = 405 nm). The photodormant state of *cis*-**1** was trapped in a deep energy well and exhibited metastable nanoparticles even after 30 days in the dark; however upon activation with visible light, it was converted to the excited state of *trans*-**1** (Figure 2.14A), which could easily cross the activation barrier to render the active monomers of *trans*-**1** and promote nucleation-mediated self-assembled fiber formation. Next, we explored the reverse isomerization of *cis*-**1** to *trans*-**1** in different conditions and monitored with UV-vis spectra, which exhibited a gradual increase in intensity at 323 nm and a decrease in intensity at 255 nm (Figure 2.14B). While the visible light-mediated reconversion to *trans*-**1** took 10 min, heating at 65 °C exhibited a slower thermal isomerization (>2 h). It is noteworthy that *cis*-**1** was found to be stable in dark conditions even after 24 h at 25 °C (Figure 2.14C). Further, *cis*-**1** to *trans*-**1** conversion was performed at different temperatures to calculate the energy parameters using Arrhenius and Eyring plots (Figure 2.14D-E). Fitting in Arrhenius equation, the activation energy (E_a) was calculated to be 18.55 kcal/mol (50 °C), with the half-life time ~ 525 min (50 °C),, while the Eyring equation endowed the following parameters: $\Delta G^{\ddagger}$ = 17.8 kcal/mol, $\Delta H^{\neq}$ = 17.9 kcal/mol and $T\Delta S^{\neq}$ = 0.0181 kcal/mol/K. E_a and $\Delta H^{\neq}$ correspond to the energy barrier required for the conversion of *cis*-**1** to the transition state. The activation entropy $\Delta S^{\neq}$ dictated the redistribution of the energy of the molecule through the rotational modes of the transition states. Further, upon consecutive UV and visible irradiation, the peptide exhibited more than five *cis-trans* isomerization cycles, ensuring complete reversibility and absence of any photo damage (Figure 2.14F). The CD spectra exhibited the recovery of characteristic β-sheet secondary structures upon activation of the dormant state with visible light, which was further confirmed by AFM images showing the self-assembled nanofibers of *trans*-**1** (Figure 2.14G-H).

2.2.5. Seeded supramolecular polymerization

Next, we envisaged seeded supramolecular polymerization (SSP) toward controlling the peptide nanostructures, where a pre-formed peptide fiber seeds upon addition of the active monomers initiated a rapid growth of the fiber in a nucleation-elongation pathway. Even though the seed-mediated growth circumvents the activation energy required for the nuclei formation, the otherwise reactive monomer unit might always be promoting secondary nucleation. This in turn, renders supramolecular polymers with uncontrolled morphology and dimension. However, in our present system, the in situ activation of off-pathway dormant states by photochemical cues might alleviate the chances of high concentration of the reactive monomers; thereby promoting seamless seed-mediated growth. We demonstrated two distinct SSP strategies mediated by photochemical cues for nanofiber growth to yield supramolecular polymers with a low degree of polydispersity

(Figure 2.15A). In this context, we prepared seeds by probe sonication of an aliquot of pre-assembled nanofiber solution of *trans*-**1**. Such uniform seeds (L_{n} = 75 nm, PDI = 1.06 in Figure 2.15G) served as a reactive centers to trigger spontaneous and rapid growth of the supramolecular fibers upon addition and subsequent activation of the chemo-/photo dormant off-pathway metastable particles. We performed time-dependent CD spectroscopy and monitored the increase in the characteristic β-sheet CD signal at 213 nm to follow the progress of the SSP process. The CD signal of the *trans*-**1** seeds at 213 nm did not change with time, while the unseeded supramolecular polymerization of *trans*-**1** exhibited a gradual enhancement of CD signal with a certain lag time to indicate spontaneous nucleation, followed by the elongation process. We incubated a mixture of *trans*-**1** seeds and chemodormant nanoparticles of *trans*-**1** ⊂ β-CD (seed**:**dormant nanoparticles = 1**:**4) at 25 ºC to observe no change in the CD signal as the seeds remain unaffected in the presence of dormant species. However, the addition of Ada in this mixture resulted in a rapid enhancement in the CD signal at 213 nm followed by the saturation plateau (Figure 2.15B). This indicated the seeded growth of peptide nanofiber in the first cycle of monomer addition to furnish peptide nanofibers with L_{n} = 440 nm, PDI = 1.09 (Figure 2.15H). The nanofibers obtained after completion of first cycle will acts as seed for seeds for next cycle. Upon second addition of chemodormant nanoparticles and chemo-activation of the off-pathway nanoparticles, the CD signal increased again signifying the living nature of the peptide fibers (Figure 2.15I). For second cycle, the ratios of new seeds and chemodormant nanoparticles is 1**:**4, therefore the CD singnal at 213 nm decrease in the beginning of first cycle that subsequently increases with time due to seed-mediated growth. Remarkably, the off-pathway-trapped *trans*-**1** ⊂ α-CD incubated with *trans*-**1** seeds, upon addition of chemical cue, did not lead to any observable change in the CD signal indicating an unsuccessful seeding experiment (Fig. 2.15D). This signified the important role of the coupled equilibrium involving a stronger association of the *trans*-**1** ⊂ α-CD complex. Next, we investigated the seeding experiment upon incubating a mixture of *trans*-**1** seeds and photodormant *cis*-**1** nanoparticles (seed**:**dormant nanoparticles = 1:4). Interestingly, there was no visible change in the CD signal at 213 nm. However, upon visible light irradiation, the photoisomerization of *cis*-**1** to active *trans*-**1** paved the way for nucleation-mediated peptide fibre elongation to render an increase of the CD signal (Figure 2.15C). A concomitant saturation of the signal indicated the consumption of the active monomer by the *trans*-**1** seeds. The AFM height image analyses of the resulting nanofiber demonstrated an excellent control over the length regime with L_n = 387 nm and PDI = 1.10 (Figure 2.15F).

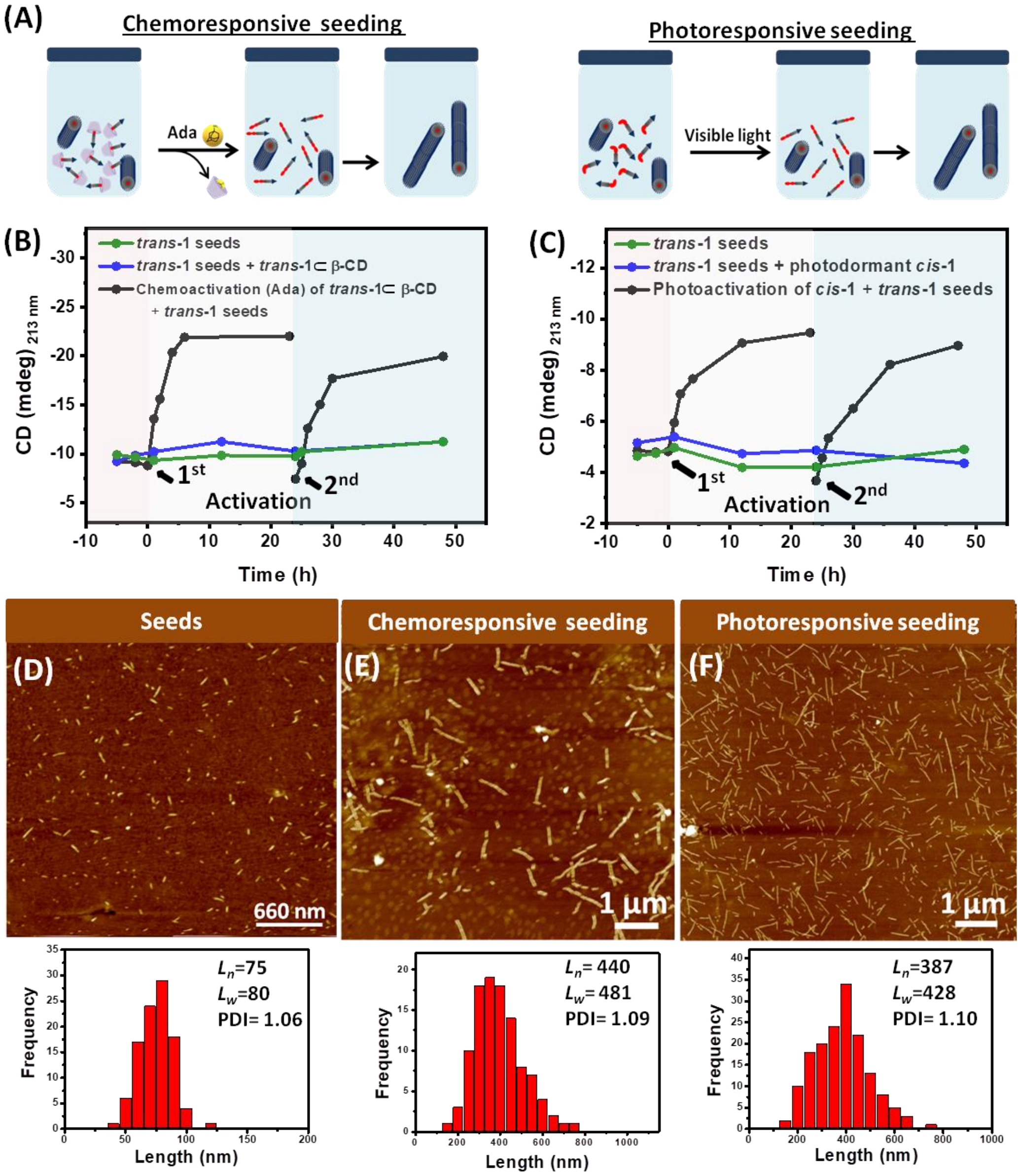

Figure 2.15: (A) Schematic representation of the seeded supramolecular polymerization to control the length of the nanofibers using off-pathway metastable states by the intervention of photo and chemical cues. Time-evolved CD spectra (λ = 213 nm) for monitoring the seeded supramolecular polymerization upon addition and activation of (B) chemodormant metastable nanoparticles of *trans*-**1** $\subset$ β-CD and (C) photodormant metastable nanoparticles of *cis*-**1** to *trans*-**1** seeds (seed:dormant nanoparticles = 1:4). Sequential addition of dormant nanoparticle followed by chemo or photo activation over two cycles showing living nature of the seeding process. Concentration of the seeds = 1 mM. (C) Time dependent CD spectra for *trans*-**1** seeds and off-pathway chemo-trapped state of *trans*-**1** $\subset$ α-CD incubated with Ada and monitored at λ = 213 nm. It showed that the off-pathway chemo-trapped state (*trans*-**1** $\subset$ α-CD) did not get activated upon adding competitive guest, Ada. AFM image with (F) Histogram recorded for seeding experiments. (G) AFM image of probe-sonicated seeds with histogram analysis (L_n = 75 nm, PDI = 1.03). AFM height images and the corresponding histogram analyses of the seeded nanofibers after incubating with (H) chemodormant *trans*-**1** $\subset$ β-CD and (F) photodormant *cis*-**1** and judicious activation of the solution. (I, E) Chemo and photo-seeding was performed up to two cycles. Images were recorded after 1 days of un-agitated incubation after activation.

These nanofibers with controlled length regime obtained at the end of cycle 1 will now become new seeds to perfrom second cycle. A sequential addition of photodormant nanoparticles and activation marked an onset of living supramolecular polymerization for the second cycle and led to peptide fibres with a predictable length regime (Figure 2.15E). However, it is noteworthy that the chemo-activated SSP generated byproducts out of the cyclodextrin-Ada complexation that gradually accumulated over sequential SSP and might influence the competitive host-guest equilibrium further on. This opens up a future possibility to excrete the byproducts akin to the metabolic waste or reuse them in designing a cyclic feedback network. On the contrary, the photoregulated equilibrium of the peptide amphiphile could be envisaged as a better strategy owing to the photostability over multiple reversible cycles. The final outcome with regard to the dimensional control and polydispersity of the supramolecular nanostructures as a result of the sequestration strategy was comparable to the system with cosolvent mediated on-pathway nanoparticles were employed. However, it is noteworthy that such photo-chemo sequestration of the active *trans*-**1** monomer is much elegant strategy as it efficiently retards the spontaneous elongation, secondary nucleation and promotes the seeded growth immediately, after employing photo/chemical trigger.

2.2.6. Photochemically tunable piezoelectric response

Further, we were intrigued by the correlation of such structural transformation between the metastable nanoparticles and self-assembled nanofibers with possible piezoelectric behavior. In a typical piezoelectric material, an external mechanical stimulus renders an electrical response due to the direct piezoelectric effect, or a mechanical strain is caused under an electrical stimulus due to the converse piezoelectric effect. The amplitude versus applied bias curve has a characteristic “butterfly” loop. Typically, when the electric field changes from the negative polarity to the positive it changes gradually and then increases abruptly. Similarly, when the field is reversed the polarization decreases gradually and then abruptly. This response is influences by the factor like structural defects and stress. Recent literatures suggest a simple dipeptide FF moiety to exhibit piezoelectricity owing to the noncentrosymmetric nature of the β-sheet.[44,59–61] However, a perfect structure−functional control of the peptides, as desired for electro-mechanical actuation, is rather lacking, and it prompted us to investigate the photochemically controlled β-sheet of *trans*-**1** toward the modulation of the piezoresponse. The individual dipole moments of the amide bonds in the peptide nanofibers add up to a large resulting dipole owing to the directional hydrogen-bonding and aromatic interactions, while in the nanoparticles, the dipoles get randomly distributed over all directions (Figure 2.16A-B). Such specific alignment of the dipoles mediated by the self-assembly could produce spontaneous polarization along the fibers.

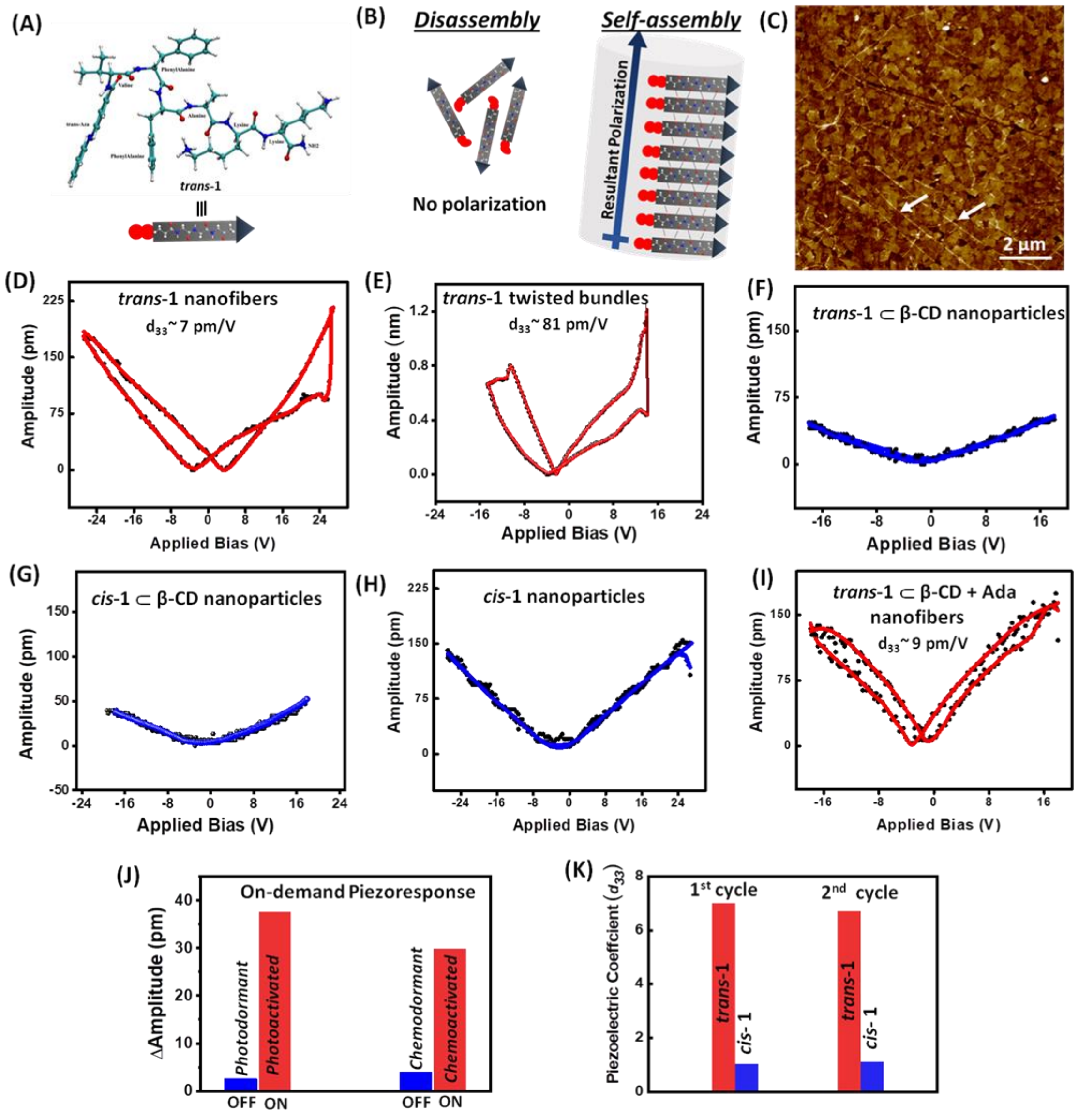

Figure 2.16: Schematics depicting (A) energy-minimized structures of *trans*-**1** with (B) random orientation of the amide dipoles in the disassembled state to result in no polarization and the strong H bonding between the amide bonds leading to the resultant polarization in the self-assembled nanofibers. (C) AFM image of *trans*-**1** nanofibers (marked with arrow) on an ITO-coated glass substrate. PFM amplitude loops acquired for (D) self-assembled *trans*-**1**, (E) twisted bundles of *trans*-**1**, (F) chemodormant *trans*-**1** ⊂ β-CD, (G) irradiated chemodormant cis-1 ⊂ β-CD, (H) and photodormant cis-1. (I) Chemoactivation of *trans*-**1** ⊂ β-CD upon addition of Ada furnished *trans*-**1** with subsequent self-assembly to retrieve the amplitude loop. (J) On-demand piezoresponse, as mediated by photochemically dormant and self-assembled states. (K) Variation of the piezoelectric coefficients (**d_{33}**) upon repeated photoactivation and deactivation of *trans*-**1** over two cycles.

Thus, we investigated our peptide amphiphiles towards on-demand piezoresponse as mediated by the off-pathway dormant states and their photochemical activation through piezoresponse force microscopy (PFM).[62] The samples were prepared on conducting ITO-coated glass substrates (Figure 2.16C) and subsequent PFM measurements were acquired by monitoring the response of sample to an applied external bias (Figures 2.16D-I). We measured the vertical PFM in the peptide nanostructures lying flat on the substrate using the piezo- coefficient ($\mathbf{d}_{33}$). The self-assembled *trans*-**1** exhibited enhanced piezoresponse with a characteristic butterfly (amplitude) loop opening ($\mathbf{d}_{33} = 7$ pm/V). Interestingly, the twisted bundle nanostructures of *trans*-**1** exhibited a much profound piezo response ($\mathbf{d}_{33} = 81$ pm/V) owing to the robust intertwining bundles contributing to a higher component of polarization in the vertical $\mathbf{d}_{33}$ direction. However, photodormant *cis*-**1** and chemodormant *trans*-**1** ⊂ β-CD before and after irradiation did not exhibit such amplitude or phase change response (Figure 2.16F-H), presumably due to the lack of robust self-assembled states. Thus, the off-pathway dormant states drastically suppressed the piezoelectric nature of the peptide amphiphiles. Remarkably, the activation of the dormant metastable states upon addition of Ada, followed by the self-assembly of *trans*-**1** resulted in the retrieval of piezoresponse (Figure 2.16I). Thus, in comparison to the non-piezoresponsive dormant metastable states, piezoresponsive *trans*-**1** showed 30-40 times higher change in amplitude at -3.5V (Figure 2.16J). The retrieval of the piezoelectric coefficients ($\mathbf{d}_{33}$) of the *trans*-**1** nanofibers upon repeated photoactivation and deactivation over two cycles confirmed the excellent photoreversibility of the system (Figure 2.16K).

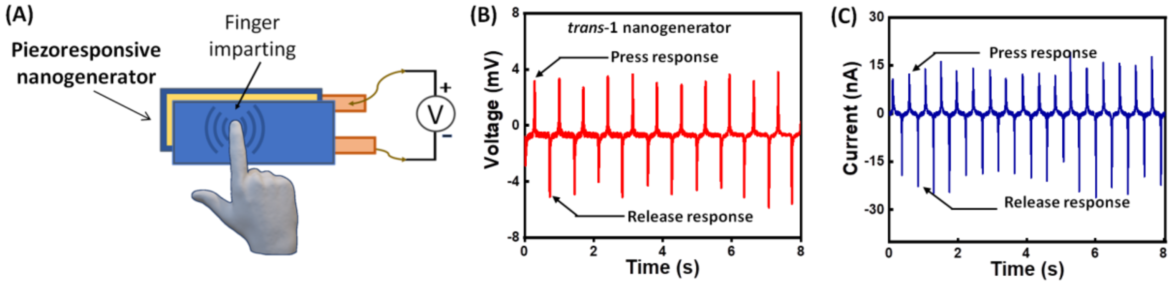

Figure 2.17: (A) Schematic diagram of the fabricated nanogenerator of self-assembled *trans*-**1** and (B − C) piezoelectric open-circuit voltage and shortcircuit current response for the fabricated nanogenerator under finger imparting motion of self-assembled *trans*-**1**.

Further, we utilized the PFM response for designing the energy-harvesting device (Figure 2.17). The direct piezoelectric response of the fabricated piezoelectric nanogenerator from the self-assembled fibers of *trans*-**1** was recorded by repetitive finger imparting press-release motion. The voltage response of ~8 mV (peak-to-peak) and the current response of ~30 nA (peak to peak) from the fabricated nanogenerator confirmed the direct piezoresponse of peptide nanofibers at the macroscopic scale.[62-63]

2.3. Conclusions

In conclusion, we established for the first time an elegant pathway-driven supramolecular polymerization in amyloid-inspired peptide amphiphile tethered with dual responsive azobenzene moieties to be exploited toward designing precise peptide nanostructures with predictive piezoresponse. A judicious choice of temperature and solvent composition led to on-pathway metastable nanoparticles that eventually converted into kinetically controlled nanofibers. The conundrum of the spontaneous nucleation of monomers was addressed using interesting strategies to trap the active peptide monomers in off-pathway dormant nanoparticles using light and chemical cue-regulated coupled equilibrium. The off-pathway chemodormant metastable nanoparticles were conceived by the host-guest inclusion complex *trans*-**1** $\subset$ β-CD that was further activated by a competitive complexation with Ada, thereby setting *trans*-**1** monomer free to self-assemble. Alternatively, the off-pathway photodormant metastable nanoparticles and their activation were accessed through light-regulated *cis-trans* isomerization of peptide **1.** The understanding of the photochemical strategy to arrest and activate the supramolecular peptide assembly by means of energy landscape provided us tools to tweak the monomer release kinetics to be utilized in seeded growth strategy and rendered controllable peptide nanostructures. Finally, we showed the on-off piezoresponse for the different peptide nanostructures, as mediated by the photochemical activation-deactivation strategy to design an elegant nanogenerator device. The present study unravels an interesting approach towards complex and functional peptide nanostructures that may find future applications in developing smart ECM matrices with precise network elasticity, self-powered device and peptide engineering for programmable bioelectronics. Work toward that direction is already underway in our laboratory.

2.4. Experimental section

2.4.1. Materials and methods

All the Fmoc protected amino acids, piperazine, oxyma pure, diisopropyl carbodiimide (DIC), 4-(Phenylazo)benzoic acid, α-cyclodextrin, β-cyclodextrin, 1-adamantylamine were purchased from Sigma. Fmoc-Rink Amide MBHA resin (0.52 mmol/g loading) from NovaBiochem (EMD Millipore) was used as solid support to synthesize *C*-terminal amide peptides on 0.1 mmol scale. All solvents were analytical grade and used without any further purification. Milli-Q water was used throughout the studies.

Peptide was synthesized using a *Liberty Blue CEM*, Matthews, NC, USA microwave-assisted peptide synthesizer. Reverse phase HPLC was performed with *Waters* binary HPLC system, using Nucleodur analytical column (C_{18} stationary phase, 5 µm, 4.6 × 250 mm). The sample was injected with autosampler and detected by photodiode array (PDA) detector. Electrospray Ionization Mass Spectrometry (ESI/MS) was performed with *Waters Acquity QDa* detector. NMR spectra were acquired on a 500 MHz FT-NMR spectrometer model Avance Neo (*Bruke*r). The chemical shifts (δ) are reported in ppm downfield of tetramethylsilane using the resonance of the deuterated solvent as internal standard.

FTIR spectra were recorded in the range of 4000 to 400 cm^{-1} as an attenuated total reflectance (ATR) mode using *Bruker Vertex 70* FTIR spectrophotometer and analysed through opus software. UV-A light (365 nm) was supplied with 16 W and irradiated for 1 h. Setup was made with two UV-A rods from OSRAM L company (each 8 W) placed inside cardboard box and sample to be irradiated was placed at a distance of one cm. Visible light was irradiated with xenon lamp (350 W) with cut-on filter of 390 nm. Sample was sonicated using *QSonica* (model number Q700, power 700 watts and frequency 20 kHz) at an amplitude of 20% for ~10 min (5 sec on and 5 sec off to avoid heating) with probe microtip.

2.4.2. Synthesis and characterization of peptides

Peptide was synthesized on rink amide MBHA resin at 0.1 mmol scale following standard microwave Fmoc-solid phase peptide Synthesis (SPPS) protocols. Fmoc protected amino acids (0.2 M) were coupled using diisopropyl carbodiimide (DIC) and oxyma pure in *N, N*-dimethylformamide (DMF). Fmoc deprotection was carried out with 20% piperazine in DMF (containing 10% ethanol) in microwave at 75 °C. Resin bound peptide was filtered, washed with DMF and dichloromethane. The peptide was cleaved from the resin using 10 mL of the cleavage cocktail mixture (trifluoroacetic acid (TFA)/water (95:5, v/v)). The mixture was shaken for 3 h at room temperature followed by removal of the resin through filtration and the filtrate was concentrated by nitrogen purging. The resultant residue was precipitated by dropwise addition to ice cold diethyl ether. The precipitates were washed 3

times with cold diethyl ether and dried to obtain white powder. The peptide was purified by RP-HPLC using a *Waters* Semi-Preparative binary HPLC system using a C18-reverse phase column with an acetonitrile-water mobile phase containing 0.1% formic acid. It was dissolved in minimum amount of HFIP and dried once again. This erased any assembly history of the peptides during lyophilisation/freeze drying process. The purified peptide was confirmed by positive ion electrospray mass spectrometry recorded with *Waters* HPLC Q-TOF mass instrument. The standard gradient used for analytical HPLC was 5 → 95% CH_3CN in H_2O (0.1% HCOOH additive) with flow rate of 1 mL/min over 30 min. *trans*-**1** was well characterized by HPLC-MS and ^{1}H-NMR.
Yield = 60 mg (63%); Purity = 97 %

^{1}H NMR (D_2O): δ= 7.88-7.74 (m, 6 H, a-H, e-H, b-H), 7.59 (m, 3 H, c-H, d-H), 7.33-7.10 (m, 12 H, f-H, f'-H), 4.21 (m, 4 H, i-H, j-H), 2.93 (m, 11 H, l-H, n-H, k-H), 1.28 (m, 4 H, m-H), 0.87-0.89 (d, 6 H, h-H) ppm.

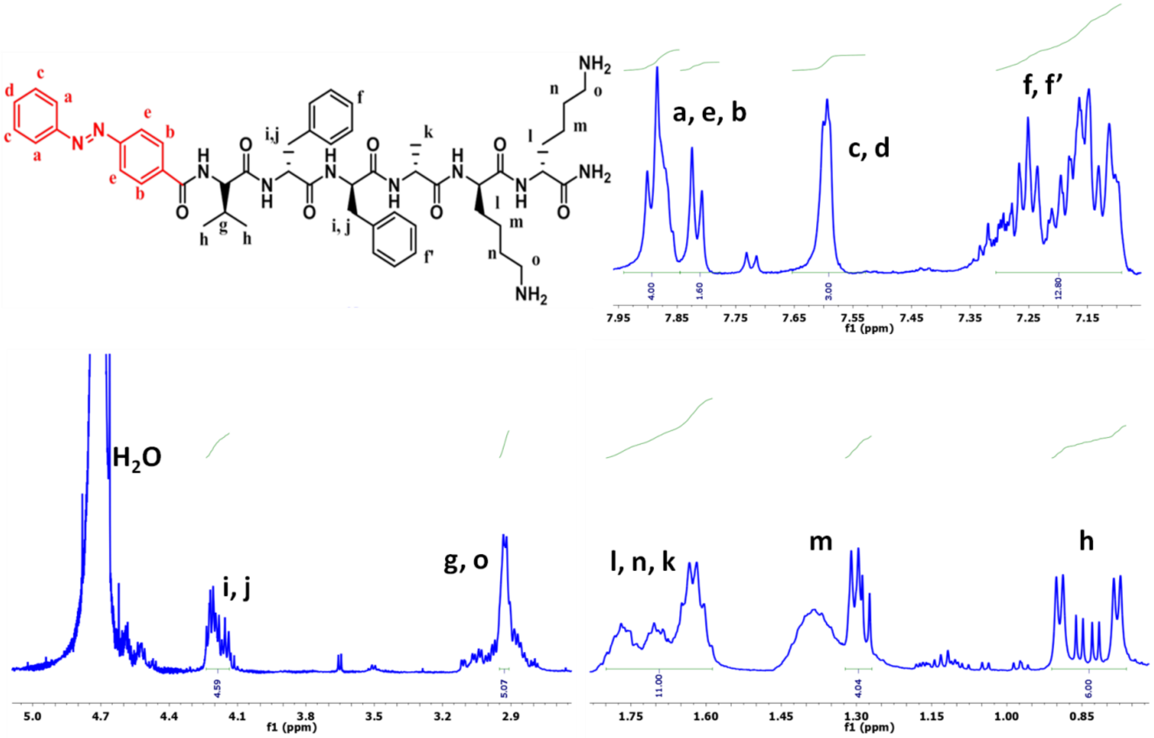

Figure 2.19 (A): ^{1}H-NMR of *trans*-**1** (4 mM) in D_2O at 298 K (500 MHz).

The calculated exact mass for $C_{48}H_{77}N_9O_7$ = 945.59 Da, In positive mode: found $[MH^+]$ = 946.82 Da, $[MH_2]^{2+}$ = 474.21 Da.

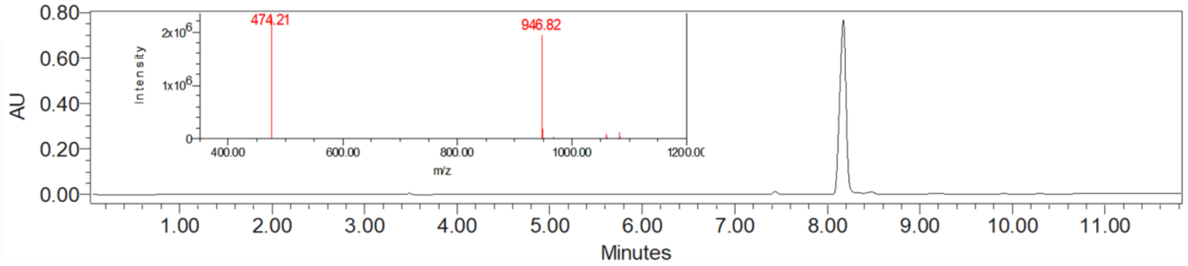

Figure 2.19 (B): HPLC chromatogram associated with ESI-MS spectra for *trans*-**1**.

2.4.3. Self-assembly of the peptide

On-pathway metastable nanoparticle, kinetic nanofiber and thermodynamically controlled twisted bundle*:* *trans*-**1** was taken in HFIP over a diverse concentration regime (0.1 to 40 mM) and microscopic investigation indicated the formation of on-pathway metastable nanoparticles.

An aliquote of 50 μL *trans*-**1** stock solution in HFIP (40 mM) was added to water to obtain 0.5 mL of peptide solution with a final concentration = 4 mM at 10 ºC (HFIP content ≈ 10 v/v %). However, the nanoparticles were found to be stable for 6 h at low temperature before they started to convert into self-assembled nanofibers. This indicated a solvent-dictated control over the self-assembly pattern upon convertion of the on-pathway metastable nanoparticles.

Upon increasing the temperature to 25 ºC and subsequent incubation for an hour, the metastable nanoparticles of *trans*-**1** in 10% HFIP-water exhibited conversion into self-assembled nanofibers. This indicated a temperature-mediated self-assembly pathway.

The nanofibrous solution, upon repeated thermal annealing (controlled rise in temperature from 25 to 80 °C for 10 min followed by a cooling to 25 ºC for 10 min, three cycles) furnished thermodynamically controlled twisted bundles of *trans*-**1**.

Off-pathway chemodormant state and its activation: For the host-guest inclusion complex, 20 μL of *trans*-**1** in HFIP (40 mM) was injected in an aqueous solution of α-CD or β-CD (concentration = 4.5 mM) to render 4 mM final concentration of the complexes, *trans*-**1** $\subset$ α-CD or *trans*-**1** $\subset$ β-CD. Microscopic analysis suggested formation of off-pathway chemodormant metastable nanoparticles. Upon addition of a competitive guest (2 μL of 80 mM 1-adamatylamine) to the chemodormant inclusion complexes, *trans*-**1** ⊂ β-CD got converted to ada ⊂ β-CD and activated the self-assembly of *trans*-**1.** However, *trans*-**1** ⊂ α-CD did not exhibit any observable change in the self-assembly pattern, indicating *trans*-**1** ⊂ α-CD as an off-pathway trapped state.

Off-pathway photodormant state and its activation: *trans*-**1** (4 mM) in water was photoirradiated with UV-A light (365 nm, 16 W) for 1 h to result in an off-pathway photodormant metastable nanoparticle of *cis*-**1**. However, upon irradiation with visible light using a xenon lamp (350 W, cut-on filter of 390 nm) the photodormant state *cis*-**1** isomerized to *trans*-**1** to furnish self-assembled nanofibers.

2.4.4. Microscopic investigation

TEM was performed using a *JEOL JEM 2100* microscope with a tungsten filament at an accelerating voltage of 200 kV. A sample of 6 µL was deposited on a carbon coated copper grid (Agar scientific), and stained with an aqueous solution of uranyl acetate (1%; w/v) for 2 min and the excess solution was wicked off with filter paper. The samples were then kept overnight under vacuum.

AFM imaging was performed on a *Bruker multimode 8* scanning probe microscope. A drop of the peptide solution (concentration = 40 µM) was deposited on a silicon wafer and kept for 7 minutes so that assemblies stick to the silicon wafer surface. After that silicon wafer was washed with water to remove the buffer or excess sample. After drying the samples with nitrogen, AFM images were recorded in tapping mode with a silicon cantilever (scan rate of 0.9 Hz). The images were analyzed using *NanoScope Analysis* 1.5.

2.4.5. Spectroscopic investigation

The temporal evolution of peptide nanostructures was investigated using UV-vis and CD spectroscopy (peptide concentration = 70 µM). UV-vis measurements were carried out on a *Shimadzu UV-2600* spectrophotometer in the wavelength range of 800 to 200 nm. Circular dichroism spectra were recorded using a *JASCO J-1500* spectrometer, Easton, MD, USA. The 400 µL of the peptide solution was added to a cuvette (2 mm path length, Hellma) and scanned in wavelength range from 190 to 450 nm (scan speed of 100 nm min^{-1}) at 25 ºC.

Host-guest complexation to furnish off-pathway chemodormant metastable states was studied using NMR spectroscopy on a 500 MHz FT-NMR spectrometer model Avance Neo (*Bruker*). The chemical shifts (δ) are reported in parts per million (ppm) downfield of tetramethylsilane using the resonance of the deuterated solvent as an internal standard.

trans-**1** (guest) was titrated with α-CD or β-CD (host) in the ratio 10:0 to 0:10, while maintaining the total concentration at 4 mM. Job's plot was obtained by plotting the variation of chemical shifts against the function of molar ratio of either guest or host molecules.

2.4.6. Isothermal titration calorimetry studies

The thermodynamic parameters of host-guest complexation were studied using ITC on a MicroCal PEAQ-ITC *(Malvern pan Analytical*) instrument. 300 µL of *trans*-**1** (0.25 mM) was taken in a sample cell and titrated with α-CD or β-CD (10 mM) over 26 injections using a syringe. All the titrations were carried out in milli-Q water at 25 ºC. In a total of 26 injections, 37.65 µL of α-CD or β-CD solution was injected with the first injection of 0.15 µL followed by 25 injections of 1.5 µL at intervals of 150 s. As a control experiment, water was titrated against α-CD or β-CD solution (10 mM). Subsequently, the results of control experiments were subtracted from that of the test samples and were fitted using MicroCal PEAQ-ITC analysis software to furnish K_a, ΔH, ΔG and $T\Delta S$.

2.4.7. Computational methodology

The molecular geometries of *trans*-**1** and *cis*-**1** were optimized at the B3LYP/6-31G* level. ESP charges for *trans* and *cis* azobenzene were calculated using the HF/6-31G* level theory. Using PyMOLmol 1.8, we designed the inclusion complexes by inserting *trans*-**1** into the cavity of α-CD or β-CD from both the faces. The corresponding force-fields in Amber-18 led us to the initial system parameters. The TIP3P model potential for was used for the solvent water. Orthorhombic simulation cells containing *trans*-**1**, α-CD or β-CD, and solvent molecules were considered with the dimensions specified in Table S1. Periodic boundary conditions were applied in all the systems. At first, 50,000 steps of energy minimization using the conjugated gradient algorithm were performed for all the considered systems. Particle Mess Ewald (PME) method was used for long-range bonding calculations. Details of MD simulations optimization and setup are explained below:

Geometry optimization: Initial geometry of the *trans*-**1** peptide was built using Avogadro software[54] and was further optimized employing density functional theory based B3LYP/6-31G* methodology. The electrostatic potential (MK) charges for azobenzene were calculated with the HF/6-31G* level theory in Gaussian software.[64, 65]

Force-field preparation: Azobenzene unit with valine was modelled using XLEAP. Residual electrostatic potential charge fitting were done through the RESPGEN utility present in the AMBERTOOL.[66, 67] The bonded and non-bonded parameters of the *trans* isomer of azobenzene moiety were obtained from the generalized amber force field (GAFF2).[59] The α-CD and β-CD force field parameters are taken from the GLYCAM06, while ff14SB force field was used for the peptide fragment.[68-69]

System set up for molecular dynamics simulations: We manually prepared an inclusion complex with the help of PyMOL 1.8 by inserting the *trans*-**1** amphiphile into the cavity of the α-CD and β-CD molecule from both the faces.[70] Insertion of *trans*-**1** in the cyclodextrin cavity led us with the system parameters with the corresponding force-fields in amber-18 (Table 2.1).[71] The TIP3P water model were used as a solvent.[72] Periodic boundary conditions were applied in all the systems. Using the conjugated gradient algorithm, 50,000 steps of energy minimization were performed for all the considered systems. Particle Mess Ewald (PME) method was used for long range non-bonding interactions with cut-off distance of 12 Å.[73] After initial 5 ns (only) solvent equilibration at 300 K, the system were subjected to harmonic restraints dynamics for 1.9 ns with the force constants of 99, 25, 1.0, 0.1, and 0.001 kcal $mol^{-1}Å^{-2}$. Then 10 ns of the system equilibration were performed followed by generation of 100 ns MD trajectory for the production dynamics adopting NPT statistical ensemble. 2 fs time step was used in the complete dynamics. The simulations were performed using NAMD2.13 software whereas; statistical analyses and visualizations were performed using VMD software.[74-75]

Free energy calculations: MM-PBSA method was used to calculate the free energy of association ($\Delta G_{association}$) between the *trans*-**1** and corresponding α-CD/β-CD from different faces.[76-78] $\Delta G_{association}$ was calculated from the difference of the free energies of the complex ($\Delta G_{complex}$) and the free *trans*-**1** ($\Delta G_{trans-\mathbf{1}}$) and the free α-CD/β-CD (ΔG_{CD}) using the following equation:

$$\Delta G_{association} = \Delta G_{Complex} - \Delta G_{trans-\mathbf{1}} - \Delta G_{CD} \qquad \text{... (1)}$$

The distance between the centre of mass (COM) of azobenzene moiety in *trans*-1 with cyclodextrin: From the fluctuation of the COM, the stability of the inclusion complex could be evaluated. Thus, we observed that COM distance highly fluctuates to render a broader distribution in the β-CD system from both the faces, while for α-CD a narrow distribution, implying a more stable complexation. From our analyses of the trajectory mentioned in above sections, it is clear that the *trans*-**1** exhibited loose binding with β-CD and a tighter binding with α-CD.

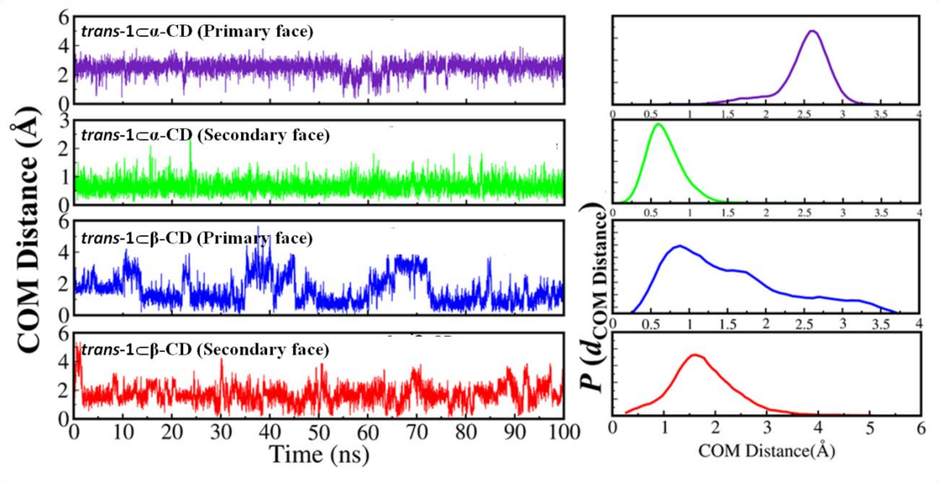

Figure 2.20: Variation of distance between COMs of the azobenzene moiety of *trans*-**1** and glycosidic oxygen atoms of cyclodextrin along the MD trajectory and corresponding probability distribution functions of the COM distances.

MD simulations for α-CD along with adamantyl amine (Ada) Ada with the α-CD showed drastic RMSD changes (Figure 2.21). Initially, the inclusion complex formation between Ada and α-CD was initiated. After ~56 ns (in the dynamics), the Ada started leaving that site resulting in dissociation of the inclusion complex as reflected from the drastic RMSD change. The α-CD formed a closed basket-like structure due to the arrangement of the primary face hydroxyl groups to result minimal interaction of Ada with the α-CD moiety. However, for β-CD owing to the formation of a stable inclusion complex with Ada, very less structural fluctuation was recorded in RMSD plots.

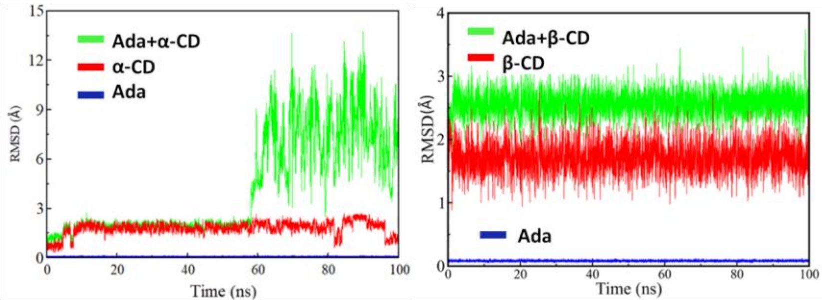

Figure 2.21: RMSD plot showing structural fluctuation of the inclusion complexes involving α-CD or β-CD molecules upon adding competitive guest Ada.

2.4.8. Calculation of the thermodynamic parameters

Arrhenius equaiton:

$$\boldsymbol{ln(k) = lnA - \frac{E_a}{RT}}$$

Where, k is the reaction rate constant. T is the absolute temperature, R is the universal gas constant, A is pre-exponential factor, E_a is activation energy. By plotting $ln(\boldsymbol{k})$ *vs.* $1/T$, value of E_a was determined.

Eyring equation:

$$\boldsymbol{ln\left(\frac{k}{T}\right) = ln\left(\frac{k_b}{h}\right) - \frac{\Delta G^{\ddagger}}{RT}}$$

Where, k_b is Boltzmann constant, h is Planck's constant and $\Delta G^{\ddagger}$ is the Gibbs energy of activation. By plotting, $\boldsymbol{ln\left(\frac{k}{T}\right)}$ *vs.* $1/T$, Gibbs energy of activation was determined. $\Delta H^{\ddagger}$ (enthalpy of activation) and $\Delta S^{\ddagger}$ (entropy of activation) were calculated using the following equation,

$$\boldsymbol{\Delta G^{\ddagger} = \Delta H^{\ddagger} - \mathrm{T}\Delta S^{\ddagger}}$$

2.4.9. Seeded supramolecular polymerization

For the generation of the nanofiber seeds, 1 mL of pre-assembled nanofibrous solution of *trans*-**1** (2 mM) in water was probe-sonicated using a *QSonica* (model number Q700; power 700 watts and frequency 20 kHz) probe sonicator using a 4417 number microtip at an amplitude of 15% for 5 min. Using *Image-J* software 100 nanofibers across different areas were randomly picked and frequency statistics over the nanofiber length was performed to calculate the number average (L_n) and weight average (L_w) lengths, along with the corresponding PDI, as L_w/L_n.

$$L_w = \frac{\sum_{i=1}^{n} N_i L_i^2}{\sum_{i=1}^{n} N_i L_i}$$

$$L_n = \frac{\sum_{i=1}^{n} N_i L_i}{\sum_{i=1}^{n} N_i}$$

$$PDI = \frac{L_w}{L_n}$$

For chemical seeding experiments, the *trans*-**1** (1 mM) fiber seeds and off-pathway chemodormant state (*trans*-**1** ⊂ β-CD) (4 mM) were incubated in water at 25 °C. Upon introduction of 1-adamantyl amine (4 mM), a competitive host-guest inclusion complex of ada ⊂ β-CD rendered free *trans*-**1** with subsequent elongation of seeds as monitored through CD spectroscopy and AFM images. A saturation plateau indicated completion of the cycle 1. Half of the solution was taken, and a sequential addition of the chemodormant state, followed by activation with chemical cue and fiber elongation was performed in cycle 2. A control seeding experiment with *trans*-**1** seeds incubated in an off-pathway trapped state, *trans*-**1** ⊂ α-CD and competitive guest, did not exhibit any elongation of the seeds.

For photoseeding experiments, the *trans*-**1** (1 mM) fiber seeds were incubated un-agitated with the off-pathway photodormant metastable states of *cis*-**1** (4 mM) in water at 25 °C. Upon irradiating with visible light, the photodormant states were activated to *trans*-**1** to render the elongation of the seeds which was monitored through CD spectroscopy till a saturation plateau for the process was obtained. The length of the fibers was ascertained from AFM image analysis marking the end of cycle. Half of the solution was taken, and a sequential addition of photodormant states to the above solution followed by activation with visible irradiation leads to further fiber elongation and saturation in the CD signal with time marked the end of cycle 2.

2.4.10. Piezoelectric measurements

The piezoelectric response of the peptide nanofibers was measured using piezoresponse force microscopy (PFM) with a *Bruker multimode-8* scanning probe microscope in contact mode. The data were acquired using a conductive Pt-Ir coated probe with a spring constant ~ 3 N/m. An external bias of 20 V was applied between the probe and the sample with a lock-in drive frequency of 12 kHz and drive amplitude of 4 V to measure the butterfly loop (amplitude response). The 20 μL solution of self-assembled fibers and the twisted bundles of *trans*-**1**, chemo- and photodormant samples (2 mM) were drop casted on a conducting ITO-coated glass substrate and dried overnight.

For a piezoelectric nanogenerator, the 200 μL sample was drop-casted on two ITO-coated flexible conducting sheets (2 cm × 1.5 cm) followed by overnight drying. The sheets were kept together *albeit* with a non woven acrylic coated adhesive paper spacer of thickness 0.5 mM to construct the electrode terminals, connected using copper wires. The voltage and current data was recorded using a Keysight DSO X1102G and a Keithley electrometer 6514, respectively.

2.5. References

1. T. F. A. D. Greef, M. M. J. Smulders, M. Wolffs, A. P. H. J. Schenning, R. P. Sijbesma and E. W. Meijer, *Chem. Rev*, 2009, **109**, 5687.
2. T. Aida, E. W. Meijer and S. I. Stupp, *Science*, 2012, **325**, 813.
3. D. B. Amabilino, D. K. Smith and J. W. Steed, *Chem. Soc. Rev.*, 2017, **46**, 2404.
4. S. I. Stupp and L. C. Palmer, *Chem. Mater.*, 2014, **26**, 507.
5. P. Korevaar, C. Schaefer, T. F. A. D. Greef and E. W. Meijer, *J. Am. Chem. Soc.* 2012, **134**, 13842.
6. N. Ponnuswamy, G. D. Pantos, M. M. J. Smulders and J. K. M. Sanders, *J. Am. Chem. Soc.* 2012, **134**, 566.
7. S. Debanath, S. Roy, Y. M. Abul-Haija, P. W. J. M. Frederix, R. M. Ramalhete, A. R. Hirst, N. Javid, N. T. Hunt, S. M. Kelly, J. Angulo, Y. Z. Khimyak and R.V. Ulijin, *Chem. Eur. J.*, 2019, **25**, 7881.
8. H. Kar, D. W. Gehrig, F. Laquai and S. Ghosh, *Nanoscale,* 2015, **7**, 6729.
9. C. Kulkarni, S. Balasubramanian, S. J. George, *Chem. Phys. Chem.*, 2013, **14**, 661.
10. C. Kulkarni, K. K. Bejagam, S. P. Senanayak, K. S. Narayan, S. Balasubramanian, S. J. George, *J. Am. Chem. Soc.* 2015, **137**, 3924.
11. E. Mattia and S. Otto, *Nat. Nanotechnol.*, 2015, **10**, 111.
12. P. A. Korevaar, C. J. Newcomb, E. W. Meijer and S. I. Stupp, *J. Am. Chem. Soc.* 2014, **136**, 8540
13. P. A. Korevaar, S. J. George, A. J. Markvoort, M. M. J. Smulders, P. A. J. Hilvers, A. P. H. J. Schenning, T. F. A. D. Greef and E. W. Meijer, *Nature*, 2012, **481**, 492.
14. S. Ogi, K. Sugiyasu, S. Manna, S. Samitsu and M. Takeuchi, *Nat. Chem.*, 2014, **6**, 188.
15. R. D. Mukhopadhyay and A. Ajayaghosh, *Science*, 2015, **349**, 241.
16. M. Wehner and F. Wurthner, *Nat. Rev. Chem.*, 2020, **4**, 38.
17. S. Ogi, V. Stepanenko, J. Thein and F. Würthner, *J. Am. Chem. Soc.*, 2016, **138**, 670.
18. A. Sorrenti, J. L. Iglesias, A. J. Markvoort, T. F. A. D. Greef and T. M. Hermans, *Chem. Soc. Rev.*, 2017, **46**, 5476.
19. S. A. P. V. Rossum, M. T. Solsona, J. H. van Esch, R. Eelkema and J. Boekhoven, *J. Chem. Soc. Rev.*, 2017, **46**, 5519.
20. R. merindol and A. Walther, *Chem. Soc. Rev.*, 2017, **46**, 5588.
21. E. A. J. Post and S. P. Fletcher, *Chem. Sci.*, 2020, **11**, 9434.
22. S. N. Living, J. S. Valera, R. Gómez and L. Sánchez, *Small*, 2018, **14**, 1702437.
23. S. Maity, J. Ottele, G. M. Santiago, P. W. J. M. frederix, P. Kroon, O. Markovitch, M. C. A. Stuart, S. J. Marrink, S. Otto and W. H. Roos, *J. Am. Chem. Soc.*, 2020, **142**, 13709.
24. T. Fukui, J. D. Garcia-hernandez, R. Liam, S. Lei, G. R. Whittell and I. Manners, *J. Am. Chem. Soc.*, 2020, **142**, 15038.
25. K. Dai, J. R. Fores, C. Wanzke, B. Winkeljaan, A. M. Bergmann, O. Leileg and J. Boekhoven, *J. Am. Chem. Soc.*, 2020, **142**, 14142.
26. A. Pal, M. Malakoutikhah, G. Leonetti, M. Tezcan, M. Colomb-delsuc, V. D. Nguyen, J. van der Guchet and S. Otto, *Angew. Chem. Int. Ed.*, 2015, **54**, 7852.
27. S. Ogi, V. Stepanenko, K. Sugiyasu, M. Takeuchi and F. Wurthner, *Angew., Chem. Int. Ed.*, 2015, **54**, 7852.
28. T. Sakurai, S. Teki, M. Takeuchi and K. Sugiyasu, *Nat. Chem.*, 2017, **9**, 493.
29. E. E. Greciano, B. Matarranz and L. Sanchez, *Angew. Chem., Int. Ed.*, 2018, **57**, 4697.
30. T. Fukui, N. Sasaki, M. Takeuchi and K. Sugiyasu, *Chem. Sci.*, 2019, **10**, 6770.
31. G. Ghosh, P. Dey and S. Ghosh, *Chem. Commun.*, 2020, **56**, 6757.

32. M. Endo, T. Fukui, S. H. Jung, S. Yagai, M. Takeuchi, K. Sugiyasu, *J. Am. Chem. Soc.*, 2016, **138**, 14347.
33. S. Dhiman and S. J. George, *RSC Adv.*, 2018, **8**, 18913.
34. G. Ghosh and S. Ghosh, *Chem. Commun.*, 2018, **54**, 5720.
35. J. Kang, D. Miyajima, T. Mori, Y. Inoue, Y. Itoh and T. Aida, *Science*, 2015, **347**, 646.
36. K. Jalani, A. D. Das, R. Sasmal, S. S. Agasti and S. J. George, *Nat. Commun*, 2020, **11**, 3967.
37. P. A. Korevaar, T. F. A. de Greef, E. W. Meijer, *Chem. Mater.* 2014, **26**, 576.
38. A. Mishra, D. B. Korlepara, S. Balasubramanian, S. J. George, *Chem. Commun.* 2020, **56**, 1505.
39. A. Sarkar, R. Sasmal, C. Empereur-mot,; D. Bochicchio, S. V. K. Kompella, K. Sharma, S. Dhiman, B. Sundaram, S. S. Agasti, G. M. Pavan, S. J. George, *J. Am. Chem. Soc.* 2020, **142**, 7606.
40. M. Wehner, M. I. S. Rohr, M. Buhler, V. Stepanenko, W. Wagner, F. Wurthner, *J. Am. Chem. Soc.* 2019, **141**, 6092.
41. E. Krieg, M. M. C. Bastings, P. Besenius and B. Rybtchinski, *Chem. Rev.* 2016, **116**, 2414.
42. A. Brito, Y. M. Abul-haija, R. Novoa-carballal, R. L. Reis, R. L. R. V. Uljin, R. A. Pires and I. Pashkuleva, *Chem. Sci.*, 2019, **10**, 2385.
43. M. P. Hendricks, K. Sato, L. C. Palmer and S. I. Stupp, *Acc. Chem. Res.*, 2017, **50**, 2440.
44. S. Bera, S. Guerin, H. Yuan, J. O'Donnell, N. P. Reynolds, O. Maraba, W. Ji, L. J. W. Shimon, P. A. Cazade, S. A. M. Tofail, D. Thompson, R. Yang and E. Gazit, *Nat. Commun.* 2021, **12**, 2634.
45. D. Gupta, R. Sasmal, J. P. Joseph, C. Miglani, S. S. Agasti and A. Pal, *Nanoscale*, 2020, **12**, 18692
46. A. Singh, J. P. Jospeh, D. Gupta, I. Sarkar, A. Pal, *Chem. Commun.*, 2018, **54**, 10730
47. J. P. Joseph, A. Singh, D. Dupta, C. Miglani and A. Pal, *ACS Appl. Mater. Interfaces*, 2019, **11**, 28213.
48. N. Gupta, A. Singh, N. Dey, S. Chattopadhyay, J. P. Joseph, D. Gupta, M. Ganguli and A. Pal, *Chem. Mater.*, 2021, **33**, 589.
49. S. Guerin, A. Stapleton, D. Chovan, R. Mouras, M. Gleeson, C. Mckeown, Md. Noor, C. Silien, F. M. F. Rhen, A. L. Kholkin, N. Liu, T. Soulimane, S. A. M. Tofail and D. Thompson, *Nat. Mater.*, 2018, **17**, 180.
50. A. Kholkin, N. Amdursky, I. Bdikin, E. Gazit and G. Rosenman, *ACS Nano.*, 2010, **4**, 610.
51. M. M. Lerch, M. J. Hansen, W. A. Velema, W. Szymanski and B. L. Feringa, *Nat. Commun.*, 2016, **7**, 12054.
52. A. Harada, Y. Takashima and M. Nakahata, *Acc. Chem. Res.*, 2014, **47**, 2128.
53. A. A. Beharry and G. A. Woolley, *Chem. Soc. Rev.*, 2011, **40**, 4422.
54. M. Kathan and S. Hecht, *Chem. Soc. Rev.*, 2017, **46**, 5536.
55. E. Fuentes, M. Gerth, J. A. Berrocal, C. Matera, P. Gorostiza, I. K. Voets, S. Pujals and L. Albertazzi, *J. Am. Chem. Soc.*, 2020, **142**, 10069.
56. S. Chen and R. Wetzel, *Protein Sci.* 2001, **10**, 887.
57. S. M. M.Reddy, G.Shanmugam and A. B. Mandal, *Org. Biomol. Chem.* 2014, **12**, 6181.
58. J. M. Kuiper and J. B. F. N. Engberts, *Langmuir*, 2004, **20**, 1152.
59. J.-H. Lee, K. Heo, K. Schulz-Schönhagen, J. H. Lee, M. S. Desai, H. Jin and S.-W. Lee, *ACS Nano* 2018, **12**, 8138－8144.
60. K. Ryan, J.Beirne, G. Redmond, J. I. Kilpatrick, J. Guyonnet, N.-V. Buchete, A. L. Kholkin and B. J. Rodriguez, *ACS Appl. Mater. Interfaces* 2015, **7**, 12702－12707.
61. A. Gruverman, M. Alese and D. Meier, *Nat. Commun.* 2019, **10**, 1661.
62. V. Gupta, A. Babu, S. K. Ghosh, Z. Mallick, H. K. Mishra, D.Saini and D. Mandal, *Appl. Phys. Lett.* 2021, **119**, 252902.
63. D. Mandal, S. Yoon and K. J. Kim, *Macromol. Rapid Commun.* 2011, **32**, 831.
64. M. J. Frisch, G. W. Trucks, H. B. Schlegel, G. E. Scuseria, M. A. Robb, J. R. Cheeseman, G. Scalmani, V. Barone, B. Mennucci, G. A. Peterson, *et al*., Gaussian 09 Program, Gaussian Inc., *Wallingford*, 2009.
65. U. C. Singh and P. A. Kollman, *J. Comput Chem*., 1984, **5**, 129

66. D. A. Case, T. E. Cheatham, T. Darden, H. Gohlke, R. Luo, K. M. Merz, A. Onufriey, C. Simmerling, B. Wang and R. J. Woods, *J. Computat. Chem.*, 2005, **26**, 1668.

67. S. J. Weiner, P. A. Kollman, D. A. Case, U. C. Singh, C. Ghio, G. Alagona, S. Profeta and P. Weiner. *J. Am. Chem. Soc.*, 1984, **106**, 765.

68. J. Wang, R. M. Wolf, J. W. Caldwell, P. A. Kollman and D. A. Case, *J. Comput. Chem.*, 2004, **25**, 1157.

69. M. Böckmann, C. Peter, L. D. Site, N. L. Doltsinis, K. Kremer and D. Marx, *J. Chem. Theory Comput*., 2007, **3**(5),1789.

70. K. N. Kirschner, A. B. Yongye, S. M. Tschampel, J. González-Outeiriño, C. R. Daniels, B. L. Foley and R. J. Woods, *J. Comput. Chem.*, 2008, **29**, 622.

71. J. A. Maier, C. Martinez, K. Kasavajhala, L. Wickstorm, K. E. Hauser and C. Simmerling, *J. Chem. Theory. Comput*., 2015, **11**, 3696.

72. L. L. C. Schrödinger, The PyMOL Molecular Graphics System, Version 1.8, 2015.

73. D. A. Case, I. Y. Ben-Shalom, S. Brozell, D. S. Cerutti, T. E. Cheatham, V. W. D. Cruzeiro, T. A. Darden, R. E. Duke, D. Ghoreishi, M. K. Gilson, H. Gohlke, *et al*., AMBER **2018**, University of California, San Francisco.

74. P. Mark and L. Nilsson, *J. Phys. Chem.*, 2001, **105**, 9954.

75. T. Darden, D. York and L. Peterson, *J. Chem. Phys.* 1993, **98**, 10089.

76. J. C. Phillips, D. J. Hardy, J. D. C. Maia, J. E. Stone, J. V. Ribeiro, R. C. Bernardi, R. Buch, G. Fiorin, J. Hénin, W. Jiang, R. McGreevy, M. C. R. Melo, *et al*., *J. Chem. Phys.*, 2020, **153**, 044130.

77. W. Humphrey, A. Dalke and K. Schulten, *J. Molec. Graphics*, 1996, **14**, 33.

78. B. R. Miller, Jr. T.D. McGee, J. M. Swails, N. Homeyer, H. Gohlke. A. E. Roitberg, *J. Chem. Theory. Comput.* 2012**, 8**, 3314.

3

Stimuli-responsive Self-assembly-disassembly in Peptide Amphiphiles to endow Block-co-fibers and Tunable Piezoelectric Response

Supramolecular assemblies with well-defined structural attenuation toward varied functional implications are an emerging area in mimicking natural biomaterials. In that regard, redox stimuli-responsive ferrocene moiety can reversibly change between non-polar ferrocenyl and polar ferrocenium cation which endows interesting modular features to the building block toward self-assembly/disassembly. We designed a series of ferrocene anchored peptide fragment ^{N}*VFFAKK*^{C} *using hydrophobic alkyl spacers of different chain lengths. Increasing spacer length between the redox-responsive and self-assembling motifs increases the propensity to form robust nanofibers, that can be physically crosslinked to form hydrogels. Controlled redox response of the ferrocene moiety in tandem with pH control provided access to structural control over the peptide nanostructures and tunable mechanical strengths. Further, such redox-sequestered dormant states hinders the spontaneous nucleation process that we exploit toward seeded supramolecular polymerization to form block co-fibers comprised of redox-responsive periphery and non-responsive cores. Finally, such redox sequestration of peptide self-assembly renders an on-off piezoelectric response for potential utilization in peptide bioelectronics.*

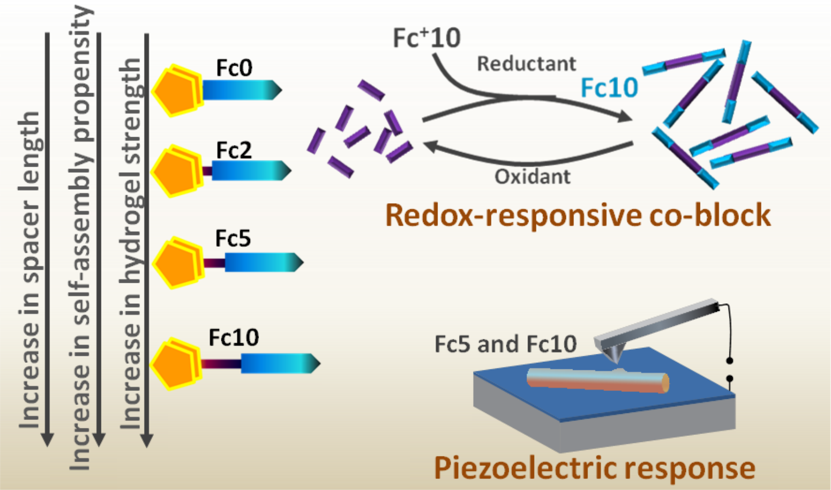

3.1. Introduction

Mimicking and creating life-like features mediated by synthetic non-equilibrium systems have attracted a great interest in the recent past, but it still remains a challenging task to achieve in the lab. The field of supramolecular polymerization has witnessed a remarkable upsurge with respect to the design of functional soft adaptive materials with more intricate physical, chemical and mechanical properties.[1-5] Thus, it is very crucial to precisely tune, control and optimize the dynamic non-covalent interactions among the molecules to regulate the morphology, length and polydispersity of the self-assembled nanostructures. Further, the inception of pathway complexity - a strategy to dictate the fate of self-assembly towards multiple pathways upon tweaking the conditions, provided a paradigm shift in self-assembly to generate materials with several nanostructures.[6-9] A detailed understanding of the complex energy landscape of supramolecular polymerization to achieve spatiotemporal control provides us with mechanistic knowledge to induce adaptive artificial materials with intelligently coded structural and functional information. In this context, living supramolecular polymerization attracted great attention as an excellent methodology to achieve precise self-assembled nanostructures through seed-mediated growth of monomers.[10-19] However, the spontaneous nucleation of monomers posed a potent drawback with regard to controlling the self-assembling process; nevertheless, it can be retarded by trapping the monomers in metastable dormant states. Recently, a few strategies have been demonstrated to retard spontaneous self-assembly by rationally designing the monomer or altering the environmental conditions.[20-24] Moreover, such a strategy necessitates reversible control over self-assembly/disassembly for stimuli-responsive pathway sequestration.

Model systems based on the minimalistic peptides have therefore attracted great interest owing to the compatibility with biological systems and facile synthetic protocol for desired functionality.[25-29] Most interestingly, the peptides undergo association and dissociation by various non-covalent interactions to self-organize and endow dynamic nature to the self-assembled system. Furthermore, to accomplish more controlled and tunable properties in the functional materials, rational incorporation of the stimuli-responsive motifs in the peptide amphiphiles is an interesting strategy.[30-32] Thus, external triggers such as pH,[33-36] light,[37-39] temperature,[40-41] redox,[42-45] enzyme activation,[46-48] ionic strength,[49] induce a high degree of chemical and biophysical versatility in peptide self-assembly toward specific and smart applications.[50] Among them, redox-responsive motifs tethered self-assembled structures draw their relevance in many biochemical redox-responsive processes to induce morphological transformations toward constructing dynamic and adaptive systems.[51- 52] In this context, ferrocene is a promising non-polar moiety that has reversible oxidative and reductive properties with iron acting as a redox center. Typically, ferrocene moiety shows a reversible electrochemical characteristic versus saturated calomel electrode (SCE) at a redox potential of +0.403 V.[53] Thus, a reversible oxidation of nonpolar ferrocene motif to a polar ferrocenium cation might render a remarkable structural manipulation for the self-assembly pathway. Recently, a number of ferrocene–peptide conjugates have been developed to probe the self-assembling behaviors in both organic and aqueous media.[54-58] However, merely controlling the self-assembly process is not sufficient to design intelligent biomimetic materials; rather it demands elegant rational strategies employing the concepts of pathway complexity to achieve structural control that can be translated into functional materials like energy harvesters. In this regard, ferrocene conjugated peptides that can be regulated with external stimuli are suitable molecule for developing predictive, precise and on-demand programmable nanostructures. Our group recently reported pathway-driven self-assembly of peptide amphiphile inspired from on Aβ(1-42) amyloid to precisely control the size and shape of one-dimensional nanofibers and two-dimensional nanosheets that further dictated the mechanical stiffness and molecular recognition of the resulting hydrogel.[59-61]

Herein, we designed a number of ferrocene anchored peptide amphiphiles that differ only in the length of the spacer linking the ferrocenyl moiety with the self-assembly promoting peptide fragment. The spacer chain length dictated the overall self-assembly behavior involving the transition from nanoparticles to nanofibers and redox properties of the peptide amphiphiles (Scheme 31). Controlled redox response of the ferrocene moiety in tandem with pH control provided access to structural control over the peptide nanostructures and tunable mechanical strengths. Such redox controlled self-assembly/disassembly rendered the formation of off-pathway dormant metastable nanoparticles, that were efficiently exploited toward retarding the spontaneous self-assembly process. Moreover, such redox-mediated strategy with judicious on-demand activation was exploited towards seeded supramolecular polymerization to develop mixed co-block nanofibers with redox-sensitive peripheral blocks to non-responsive core with precision. Finally, exploiting the multiple directional amide hydrogen bonding mediated polarization in self-assembled peptide nanofibers, we demonstrated an elegant redox-sequestration of self-assembly pathways to result in on-off piezoresponsive peptide nanostructures. Taken together, this work unravels a new strategy to access complex and functional supramolecular peptide nanostructures in a rational manner toward peptide bioelectronics.

3.2. Results and discussion

3.2.1. Self-assembly of the functional peptides

We designed a series of peptide amphiphiles based on amyloid Aβ(1-42) inspired peptide sequence ^{N}VFFA^{C} with pendant redox-responsive ferrocene (Fc) moiety at the *N*-terminal of the peptide and polar lysine moieties at the *C*-terminal. For a thorough understanding of the strength of self-assembly, β-sheet forming ^{N}VFFA^{C} peptide fragment were connected with a rather bulky Fc moiety using spacers of variable hydrophobic carbon chains (Scheme 3.1). Thus, Fc-VFFAKK **(Fc0**) involves direct tethering of Fc with the peptide fragment while the other ferrocene anchored peptide amphiphiles: Fc-C$_2$-VFFAKK (**Fc2**), Fc-C$_5$-VFFAKK (**Fc5**), Fc-C$_{10}$-VFFAKK (**Fc10**) differ by the length of the hydrophobic spacers (*n*) from two, five and ten methylenic carbons respectively. By virtue of the non-covalent interactions such as directional hydrogen bonding among the amide moieties and strong π−π interactions among the phenylalanine side chains, the fragment, VFFAKK drives the self-aggregation of peptide building blocks.

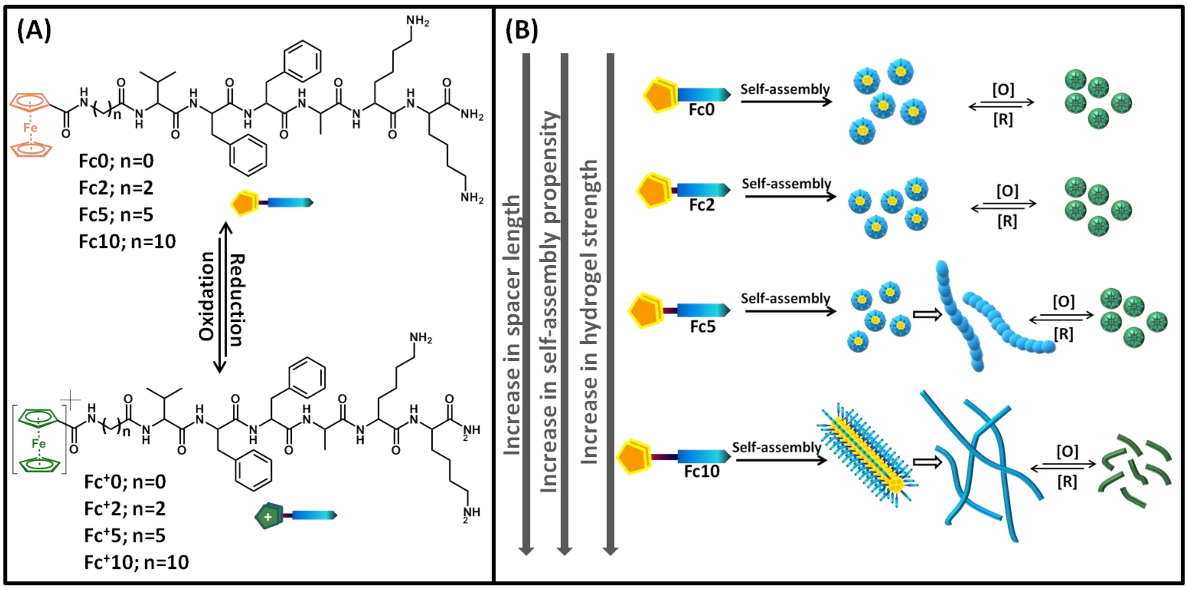

Scheme 3.1: (A) Molecular structure of peptide amphiphiles with varying spacer lengths and reversible oxidation-reduction. (B) Schematic diagram of redox-responsive assembly-disassembly of the ferrocene tethered peptides to furnish tunable nanostructures *e.g.* nanofibers and nanoparticles.

However, we were curious to investigate the role of a rather bulky ferrocene moiety at a gradually altered distance from the self-assembly promoting peptide fragment. Thus, the self-assembly propensity of the peptide amphiphiles was investigated using UV-vis and circular dichroism (CD) spectra. Firstly, we studied the self-assembly of ferrocene anchored peptides with varied spacer lengths in water. The UV-vis spectra for all peptide amphiphiles amphiphiles (**Fc0, Fc2, FC5 and Fc10**) in water showed absorption maxima at 445 nm at room temperature which is characteristic of the ferrocene moiety (Figure 3.1A). CD spectroscopy was employed to understand the aggregation behaviour of all the peptides. **Fc0** without any spacer, **Fc2** and **Fc5** with short spacers exhibited random coil secondary structures that remained unchanged even after ageing for four days (Figure 3.1B-C). On the contrary, freshly dissolved **Fc10** in water showed β-sheet structure with a negative Cotton band centred at 217 nm and a positive Cotton band centred at 200 nm that was further enhanced with aging owing to the formation of robust self-assembled structures. We observed that no spacer or a shorter spacer in **Fc0**, **Fc2** and **Fc5** did not lead to any defined self-assembled secondary structure formation in water presumably due to the proximity of the bulky Fc group to the peptide sequence, thereby hindering the efficient β-sheet formation. Also hydrophobic contribution is absent or little. Moreover, CD studies depicted the critical aggregation concentration for **Fc10** to exhibit formation of β-sheet at 1 mM whereas peptides with short spacer length did not exhibit any transition to β-sheet structures even at higher concentrations (Figure 3.1D). Furthermore, atomic force microscopy (AFM) images showed the morphology of aggregates for the ferrocene anchored peptides. While **Fc0** and **Fc2** furnish nanoparticles of diameter 50-100 nm in water (Figure 3.1E-F), **Fc5** showed the presence of nanoparticles (40-50 nm) along with nanofiber morphology (Figure 3.1G). On closer observation, it was noted that nanoparticles were fused to form nanofiber (height ~5 nm) (Figure 3.1G inset). However, **Fc10** formed stable robust nanofibers with a diameter of ~10 nm and height of ~ 4-5 nm (Figure 3.1H). This clearly suggested a role of rigid and bulky ferrocene moiety to provide steric hindrance and thereby inhibiting the formation of highly stacked β-sheet secondary structures. In **Fc0** and **Fc2** peptide amphiphiles, it rather hindered the potential self-assembly process and remained in nanoparticle morphologies. Interestingly, the role of ferrocene got negated upon distancing it from the peptide fragment with a long hydrophobic spacer in **Fc10**. Thus, the introduction of the linker between ferrocene and peptide ensures flexibility and better packing of β-sheet secondary structures in **Fc10** that further improved its self-assembly propensity toward nanofibrous morphology.

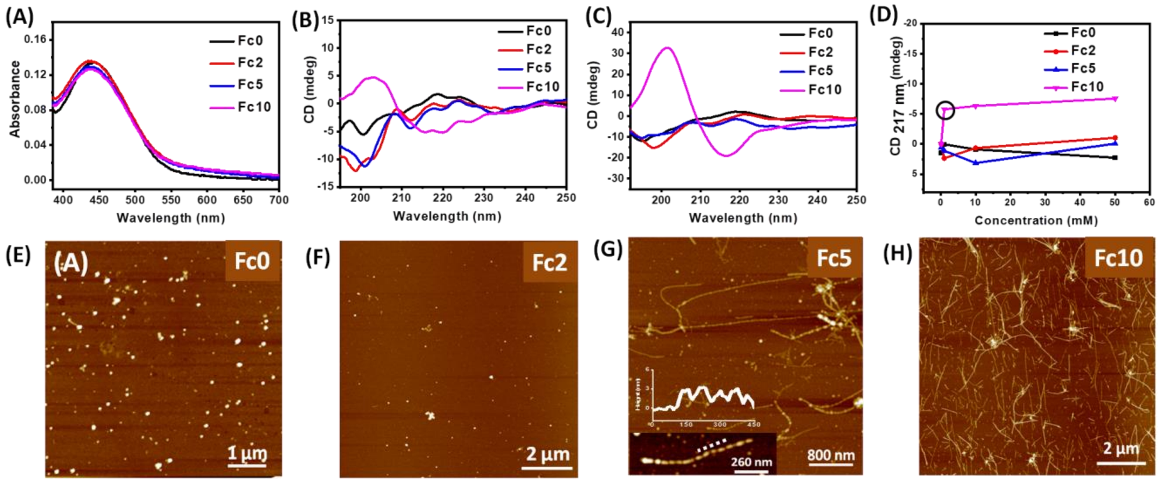

Figure 3.1: (A) UV-vis spectra of ferrocene anchored peptide sequences in water (concentration = 0.5 mM). CD spectra of the peptides (B) in monomeric state immediately after dissolving and (C) in self-assembled state after one day incubation in water (concentration = 0.1 mM) (D) CD signal at 217 nm was monitored with increasing concentration of the Fc-peptides. Concentration marked with circle represents the critical concentration in **Fc10** to induce self-assembly. All CD spectra were recorded after three days of incubation and concentration for recording spectra was maintained at 0.1 mM. AFM images of self-assembled peptides in water at room temperature. (E) **Fc0** and (F) **Fc2** exhibit nanoparticles (G) **Fc5** showed the nanoparticles fused to form nanofibrous morphology, (H) **Fc10** showed long nanofibers (concentration = 1 mM).

Next, we investigated the influence of pH on the self-assembling behavior of ferrocene anchored peptides. At a moderate pH range of 6.5 to 7, the amine side chains of lysine were protonated having a net positive charge that endowed electrostatic repulsions to inhibit the self-assembly. These repulsions are not significant if the other non-covalent interactions such as hydrogen bonding and π-π dominate over the distant and antagonist Fc moieties in **Fc10** to furnish robust assemblies. However, for peptides assembly with short spacer length, minimizing these electrostatic repulsions are extremely crucial. Thus, upon increasing pH to 9-11, the amine side chains of lysine became deprotonated and resulted in minimal repulsive interactions. CD spectra depicted a convincing transition from random coil structure to β-sheet secondary structure for **Fc5** upon increasing pH of the solution (Figure 3.2C). AFM image of **Fc5** in basic pH also depicted the formation of robust nanofibers with height 4-5 nm (Figure 3.2F). However, **Fc0** and **Fc2** furnished random coil structures even in basic conditions that indicated the dominance of the antagonistic effect of bulky Fc motifs over the self-assembling peptide (Figure 3.2A-B,E). Notably, **Fc10** remained unaffected and exhibited β-sheet structure in both acidic and basic pH (Figure 3.2D). Thus, **Fc10** with stronger non-covalent interactions among the amide bonds and hydrophobic collapse among long methylene spacers renders the β-sheet structure intact to negate the effect of pH.

However, **Fc5** having an optimum balance of spacer length and side chain repulsive interactions furnished pH mediated self-assembly. Further, we studied the effect of increasing ionic strength over the **Fc5** peptide self-assembly. For this, we employed phosphate and sulphate anions using sodium sulphate (SS) and sodium phosphate buffer (SPB) (2 mM) to peptide (10 mM) solution in water. CD spectra depict no structural transformation of **Fc5** peptide solution as upon adding anions to the self-assembled nanostructures of **Fc5** (Figure 3.2G-H). However, in higher salt concentration the peptide amphiphiles start to exhibit gelation behavior.

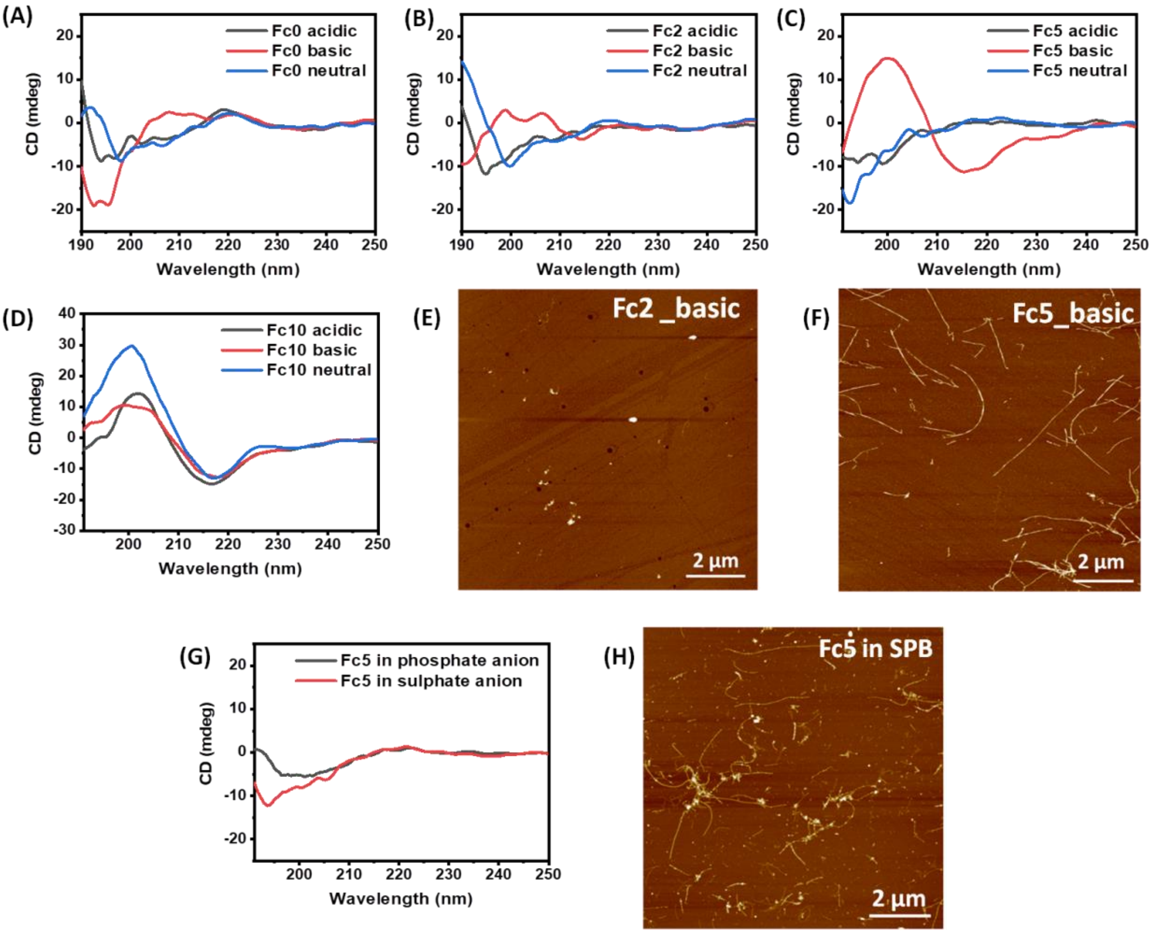

Figure 3.2: CD Spectra of (A) **Fc0,** (B) **Fc2,** (C) **Fc5 and** (D) **Fc10** in acidic (pH = 4-6), neutral (pH = 6.5-7.5) and basic (pH = 9-11) conditions. CD spectra of **Fc5** depict transition of the random coil structure to β-sheet secondary structure on increasing pH. (E) AFM image showed no change in morphology of **Fc2** in basic conditions; however, (F) **Fc5** depicts nanofibrous morphology in basic conditions. (G) CD spectra of **Fc5** in the presence of sulphate and phosphate salt (concentration of salt = 2 mM) depict no assemblies at increased ionic strength. (Concentration of peptides for recording CD spectra = 0.1 mM) (H) AFM image of **Fc5** in SPB depict no effect of ionic strength on self-assemblies (concentration = 1 mM).

3.2.2. Redox-responsive self-assembly and disassembly

Next, we exploited the redox-responsive behavior of ferrocene having a redox potential of +0.4 V. The chemical oxidation propensity of ferrocene was exploited by adding the oxidizing agent to investigate the assembly-disassembly transition of the peptide amphiphiles. The addition of 1 molar equivalent of $Fe(ClO_4)_3$ as an oxidizing agent to the peptide solution resulted in the appearance of dark green colour indicating the conversion of ferrocenyl residue to ferrocenium cation. UV-vis spectra clearly indicated the oxidation of the ferrocene group to the ferrocenium cation (Figure 3.3A). The iIntroduction of $Fe(ClO_4)_3$ shifted the absorption peak at 636 nm which was characteristic of the oxidized ferrocenium ion. Further addition of 1 molar equivalent of reducing agent (ascorbic acid) to the above solution reconverted the ferrocenium ion into ferrocene with obvious colour change from dark green to yellow. The absorption band at 636 nm disappeared indicating reconversion to ferrocene species on the addition of ascorbic acid. In the control experiments, the same amount of oxidizing agent, $Fe(ClO_4)_3$ and the reducing agent were added in sequence to water showing no peaks at 445 or 635 nm. Therefore, the redox-stimuli can switch between the ferrocenyl and ferrocenium cation states, which in turn played a critical role in the assembly and disassembly of the peptide assemblies. Interestingly, oxidation efficacy was observed to decrease after the self-assembly of peptide amphiphiles (Figure 3.3B). The self-assembled nanostructures furnished a decrease in absorption intensity compared to monomeric peptides even at high concentrations of $Fe(ClO_4)_3$ (Figure 3.3C). Next, we studied the effect of the consecutive oxidation-reduction on **Fc5** and **Fc10** peptides and they were found to be robust and did not degrade even after multiple redox cycles (Figure 3.3D). CD spectra indicated that even after the oxidation of **Fc10**, the β-sheet secondary structure was still present but with a decrease in signal intensity (Figure 3.3E). Further, CV data revealed reversible oxidation processes in the ferrocene conjugated peptides (**Fc5** and **Fc10**) at approximately ~0.4–0.5 V. This electrochemical behaviour showed that the peptide conjugation did not exhibit a significant effect on the oxidation potentials. Moreover, CV of **Fc5** and **Fc10** depicted a decline in oxidation and reduction propensity upon self-assembly from the freshly dissolved monomers. More so, pH-mediated self-assembly for **Fc5** reduced the redox sensitivity to minimal and could be attributed to the unavailability of non-polar ferrocene moiety for oxidation as they are buried inside the self-assembled nanostructures (Figure 3.3F-G). Interestingly, AFM images of **Fc⁺5** depicted the morphology transition to nanoparticles on oxidation of the ferrocene moiety (Figure 3.3H). Ferrocenium ion being polar would disturb the hydrophobic-hydrophilic balance of the peptide amphiphiles that is necessary for self-assembly in water. In the case of **Fc10**, long self-assembled nanofibers transformed into short nanofibers of **Fc⁺10** (Figure 3.3I). The redox-responsive Fc motif stays far apart from the self-assembling peptide fragment of **Fc10** and hence redox stimulus was unable to completely diminish the strong β-sheet stacked nanofibrous morphology. For **Fc0** and **Fc2**, the presence of an oxidant did not lead to any structural transformation and continued to exhibit nanoparticle morphologies.

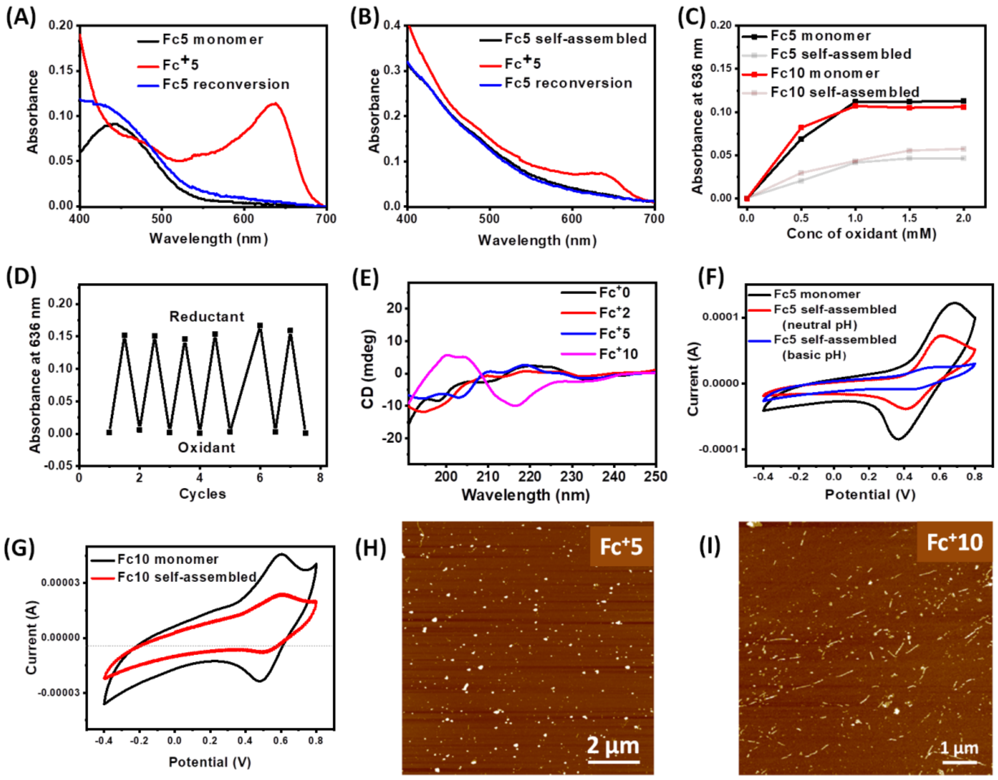

Figure 3.3: Redox-responsiveness of the ferrocene anchored peptides. UV-vis spectra of the (A) freshly dissolved **Fc5** (B) self-assembled peptide solution with absorption maxima at 445 nm; on the addition of oxidant ($Fe(ClO_4)_3$), peak at 636 nm appears and further addition of the reducing agent (ascorbic acid) exhibited disappearance of the peak at 636 nm. (c) The absorption maxima monitored at 636 nm depict a decrease in oxidation efficiency in self-assembled nanofibers compared to the monomeric form of both **Fc5** and **Fc10**. (D) Oxidation and reduction of **Fc5** for multiple cycles depicting stability and reversibility towards the redox response. (E) CD spectra after oxidation of ferrocene conjugated peptides depicted that the β-sheet secondary signature of **Fc10** was still present with decreased intensity. CV data depicted a decrease in oxidation efficacy after self-assembly for (F) **Fc5** and (G) **Fc10**. Morphology change upon addition of oxidizing agent $Fe(ClO_4)_3$ (H) nanofibrous morphology of **Fc5** was completely converted to the nanoparticles of **Fc⁺5**, (I) long nanofibers of **Fc10** converted to short fibers of **Fc⁺10**.

3.2.3. Physical crosslinking to hierarchical hydrogel network formation

At physiological pH, these ferrocene conjugated peptides are positively charged due to the protonation of the amines of the lysine side chain. The addition of anionic species to these positively charged peptides can form a network structure due to the ionic cross-linking that can further improve the properties of aggregates. We envisaged various negatively charged ions from the Hofmeister series (Cl^-, OAc^-, SO_4^{2-}, PO_4^{3-}) towards the cross-linking ability which led to the hydrogel formation. The peptide amphiphiles were aged overnight and then an aqueous solution of anions was added into a vial and the resulting solution vortexed for 30 s. After that, the solutions were incubated at room temperature overnight without disturbance. The gelation at 10 mM concentration was verified by using the "stable to the inversion of a vial" method. The vial was subsequently inverted to check the gel formation. Singly charged anions such as chloride and acetate ions were incapable of inducing any hierarchical network formation. Moreover, the peptide solution where nanofibers were not present (**Fc0** and **Fc2**) for entanglement remained in the free-flowing sol state even after incubation with the double/triple negatively charged counter ions *e.g.* sulphate and phosphate (10 mM) for a longer time. Interestingly, sulphate and phosphate anions formed physical cross-linking with **Fc5** and **Fc10** nanofibers and transformed the peptide solution into hydrogel (Figure 3.4A). It is noteworthy that the sulphate anion furnished a relatively weaker hydrogel as compared to the phosphate ion presumably due to a relatively lower negative charge for ionic cross-linking. This was confirmed by the frequency-independent behaviour in oscillatory rheological studies (Figure 3.4B-C). Moreover, the storage moduli (G') values for the **Fc5** and **Fc10** hydrogels in phosphate buffer were found to be higher than that in sulphate. Also, the hydrogels of **Fc10** exhibited much higher G' values as compared to that of **Fc5** hydrogel. Further, we also investigated the self-healing ability of these hydrogels using thixotropy studies (Figure 3.4D). The peptide amphiphile **Fc10** showed remarkably improved gelation ability and thixotropic behavior with the highly cross-linked network (Figure 3.4E). Furthermore, we envisaged the gel-sol (assembly-disassembly) phase transition of the peptides hierarchical network induced by oxidizing agent and sol-gel transition on subsequent addition of reducing agent. **Fc5** hydrogel network with fragile fibers was destroyed in the presence of an oxidant that further decreased the mechanical strength of the formed hydrogel by an order of magnitude. We observed from the vial inversion test that **Fc10** remained in a hydrogel state even after oxidation, *albeit* with the decrease in mechanical strength by one order of magnitude

(Figure 3.4F-G). Moreover, upon the addition of the reducing agent, **Fc$^+$5** and **Fc$^+$10** were reconverted into **Fc5** and **Fc10** to regain the mechanical strength (Figure 3.4H). This clearly illustrated the reversible tuning of the mechanical properties of the hydrogels with redox-responsive stimuli.

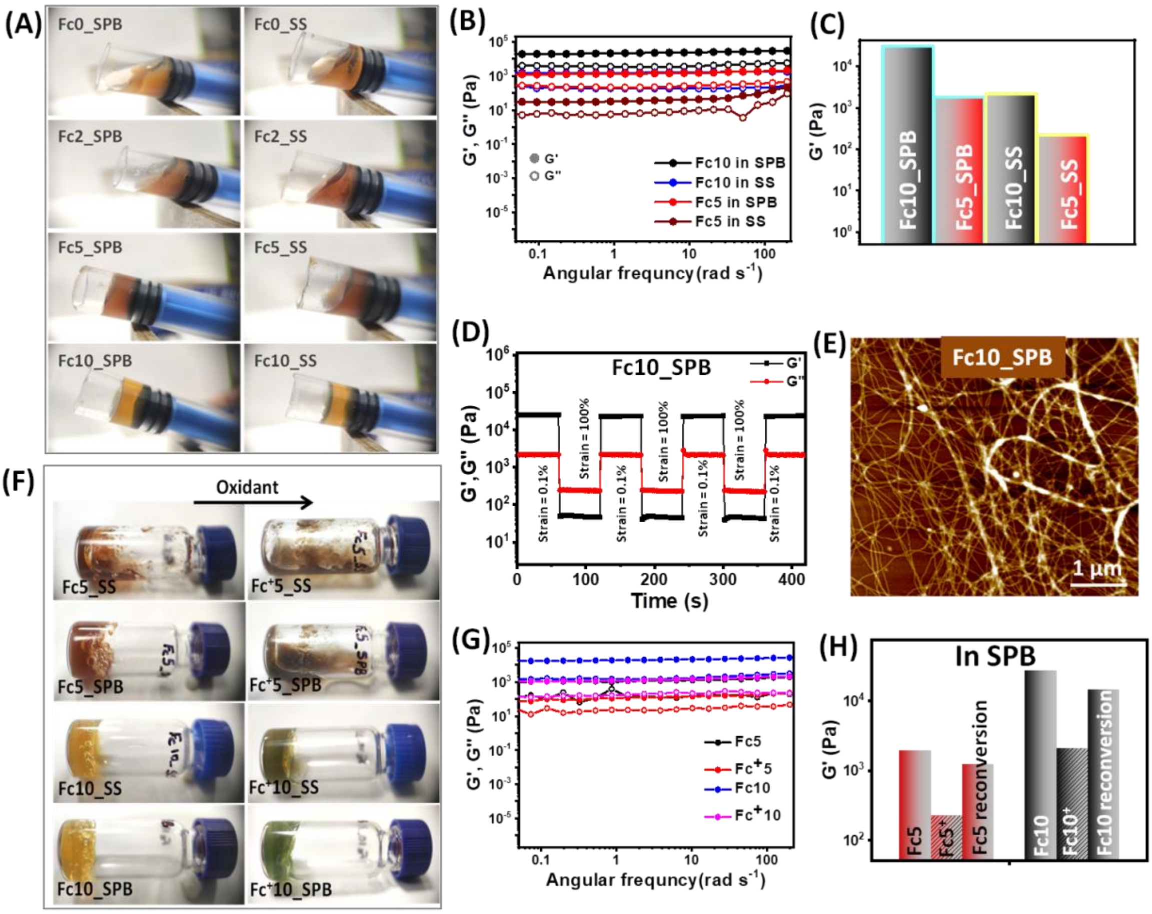

Figure 3.4: (A) Ionic strength mediated sol–gel phase transition experiment for ferrocene tethered peptides in sodium phosphate buffer (SPB) and sodium sulphate (SS) (10 mM, pH = 7.4). (B) Oscillatory frequency sweep of **Fc5** and **Fc10** in SPB and sodium sulphate. (C) Bar diagram showing comparison of storage moduli (G', Pa) for the hydrogel networks of **Fc5** and **Fc10** in SS and SPB. (D) Thixotropic studies for the **Fc10** hydrogel in SPB upon applying 0.1% and 100% strain for 3 cycles. Black and red colour indicate storage modulus (G', Pa) and loss modulus (G", Pa) respectively. (E) AFM image of cross-linked hydrogel network of **Fc10**. (F) Effect of the oxidation on hydrogel; **Fc5** hydrogels got disrupted and converted to sol in the presence of the oxidant, $Fe(ClO_4)_3$. On the contrary, **Fc10** hydrogel still remains in a weak gel state. (G) Oscillatory frequency sweep of **Fc5, Fc$^+$5, Fc10** and **Fc$^+$10** in SPB. (H) Bar diagram of rheological studies of the hydrogels before (**Fc5** and **Fc10)**, after (**Fc$^+$5** and **Fc$^+$10)** the oxidation and with subsequent reduction with ascorbic acid (**Fc5** and **Fc10** reconversion) to indicate a weakening of hydrogel network on oxidation and regaining of strength after reduction.

3.2.4. Seeded supramolecular polymerization to block-co-fiber

Furthermore, such redox-responsive self-assembly/disassembly of the peptide amphiphiles was envisaged as an excellent approach to retard and activate the supramolecular polymerization. Thus, we utilized the concepts of seeded supramolecular polymerization in a two-component system comprised of redox-sensitive and redox-insensitive molecules toward controllable peptide nanostructures (Figure 3.5A). In this strategy, a preformed peptide fiber renders a seed-mediated elongation upon adding an active monomer, but the reactivity of the monomer might promote spontaneous secondary nucleation to render final supramolecular polymers with uncontrolled morphology and dimension. Interestingly, by the intervention of redox sequestered disassembly of active monomer we circumvented the high local concentration of the active monomer for secondary nucleation thereby resulting a seamless nucleation driven elongation. Thus, we prepared seeds from the peptide whose self-assembly remains unaffected by any external stimuli. We used the C_{10}-VFFAKK peptide as a non-redox-responsive peptide composed of the hydrophobic alkyl chain that self-assembled in water to form long robust nanofibers of micrometer length scale (Figure 3.5B).[61] These fibers were probe-sonicated to achieve seeds with uniform size (L_n = 252 nm) and narrow dispersity (PDI = 1.11) (Figure 3.5C, F). Further, in a separate eppendorf, we employed redox-responsive **Fc10** that exhibited morphological changes on rationally tweaking the solvent and redox environment. **Fc10** self-assembled to form nanofibers in 10% HFIP-water composition that on oxidation with $Fe(ClO_4)_3$ transformed into metastable nanoparticles of **Fc^+10**. Upon incubating these nanoparticles with the seed solution of C_{10}-VFFAKK (seed**:**nanoparticles = 1**:**3), no significant changes were observed. However, reduction of **Fc^+10** to **Fc10** with ascorbic acid followed by incubation for one day at room temperature rendered us with the seed-mediated growth of the fibers. We noticed an increase in the length of fibers to L_n ~ 1082 nm indicating the growth of **Fc10** at both ends of the seeds to form co-block nanofibers (Figure 3.5D, G). Further, the addition of oxidizing agent rendered disassembly of the redox-responsive peripheral blocks composed of **Fc10** to furnish the original fiber seeds, as the non-responsive core of **C_{10}-VFFAKK** fiber remained intact (L_n = 282 nm) (Figure 3.5E, H). In the control experiment, **C_{10}-VFFAKK** seeds were incubated with the nanoparticles of **C_{10}-VFFAKK** in 10% HFIP-water composition, which resulted in the elongation of nanofibers due to active ends of seeds. However, these grown fibers remain unaffected in the presence of redox stimuli (Figure 3.6B-C).

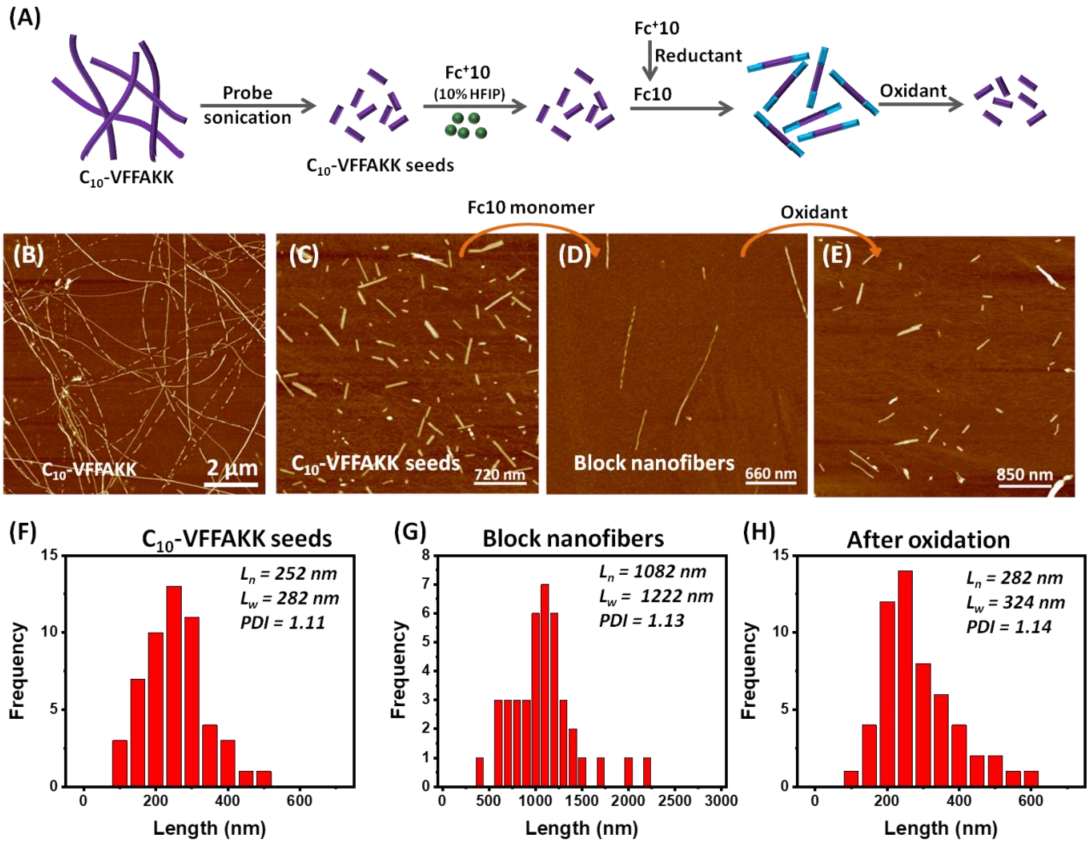

Figure 3.5: (A) Schematic diagram of redox-responsive seeded supramolecular polymerization demonstrating seed formation, addition of metastable nanoparticles and reduction mediated activation to furnish supramolecular mixed block, that can be reversibly shorten with oxidation. AFM images of (B) peptide nanofibers of **C$_{10}$-VFFAKK** with uncontrolled length and (C) probe sonicated seeds of **C$_{10}$-VFFAKK**. (D) The seeds incubated with **Fc$^+$10** and subsequently reduced to **Fc10** to undergo seeded growth to form supramolecular co-block nanofibers. (E) The elongated fiber got chewed up at the ends upon addition of oxidizing agent Fe(ClO$_4$)$_3$ due to the disassembly of peripheral redox-responsive blocks.

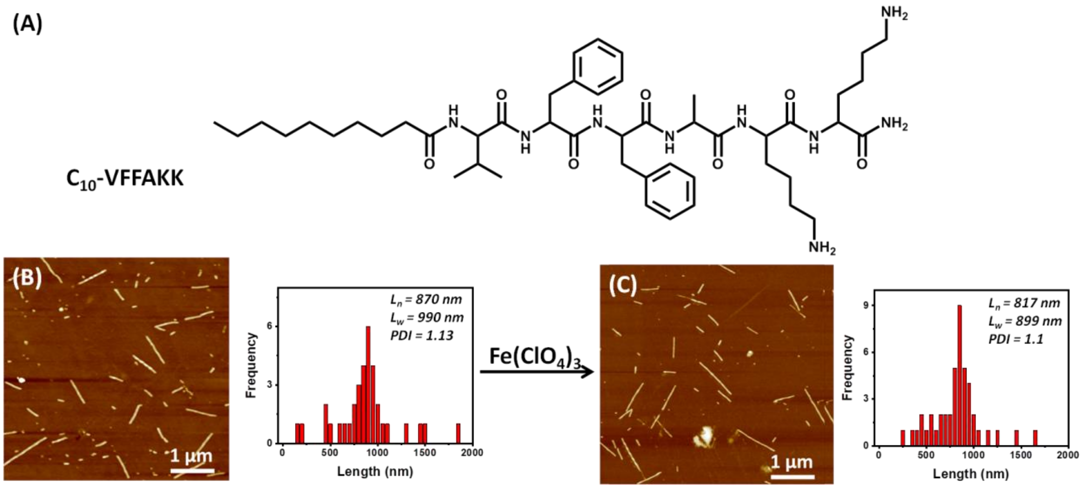

Figure 3.6: (A) Molecular structure of **C$_{10}$-VFFAKK.** (B) AFM image of **C$_{10}$-VFFAKK** seeds incubated with **C$_{10}$-VFFAKK** metastable nanoparticles showed elongated fibers with length of 870 nm. (D) This nanofiber remains unaffected on incubation with oxidising agent.

This established an interesting approach by cross-seeding of redox-responsive and non-responsive units to access supramolecular mixed co-block by the intervention of redox stimuli. This established an interesting approach to access supramolecular mixed block by the intervention redox-mediated self-assembly/disassembly.

3.2.5. Redox-responsive tunable piezoelectric response

Further, we were interested to correlate such redox-responsive structural transformation of the **Fc10** and **Fc5** peptides for tunable piezoelectric behavior through piezoresponse force microscopy (PFM). A typical piezoelectric material generates electric charges in response to applied mechanical stress (direct piezoelectricity) or generates mechanical deformation upon application of the electric field (converse piezoelectricity). Of late, there has been growing interest in the soft bioelectronics area with dipeptides exhibiting piezoelectricity owing to the non-centrosymmetric nature of the β-sheet.[62-65] However, the tunable functional piezoelectric response of self-assembled peptides is scarce in the literature which prompted us to investigate our redox-controlled peptide nanostructures. In nanofibers, the individual dipole moments of the amide bonds added up to a large resulting dipole, while nanoparticles did not generate any resultant dipole moment owing to lack of directionality (Figure 3.7A). Such specific alignment of the dipoles could produce spontaneous resultant polarization along the non-centrosymmetric β-sheet fibers. However, oxidative transformation to the metastable nanoparticles turns off the piezoresponse. The samples were prepared on conducting indium tin oxide (ITO) coated glass substrate and subsequent converse PFM measurements were acquired by monitoring the amplitude or phase response of the samples to an applied external bias.[66-67] For the peptide nanostructures lying flat on ITO substrate we measured vertical piezoelectric co-efficient (**d_{33}**). The self-assembled **Fc10** nanofibers exhibited enhanced piezoresponse with a characteristic amplitude loop (**d_{33}** ~ 8.4 pm/V) that clearly showed the expansion/compression inside piezoelectric nanofibers to attain the maximum deformation (change in amplitude) at max applied bias voltage under positive and negative polarity (Figure 3.7B). The corresponding phase response revealed the characteristics of switchable dipoles depending on the type of applied bias polarity. However, **Fc^+10** nanoparticles in 10% HFIP-water did not exhibit such amplitude change response upon applying the external bias (Figure 3.7C). Interestingly, the nanostructures of **Fc5** exhibited a rather suppressed piezoresponse (**d_{33}** ~ 5.2 pm/V) owing to the presence of nanoparticles and nanofibers contributing to a lower component of polarization in the vertical **d_{33}** direction (Figure 3.7D). However, upon oxidation, the **Fc^+5** nanoparticles did not exhibit any such piezoresponses (Figure 3.7E). This clearly indicated a structural deformation owing to the oxidation of the ferrocene moiety to render the diminishing piezoelectric response in the peptide nanofibers.

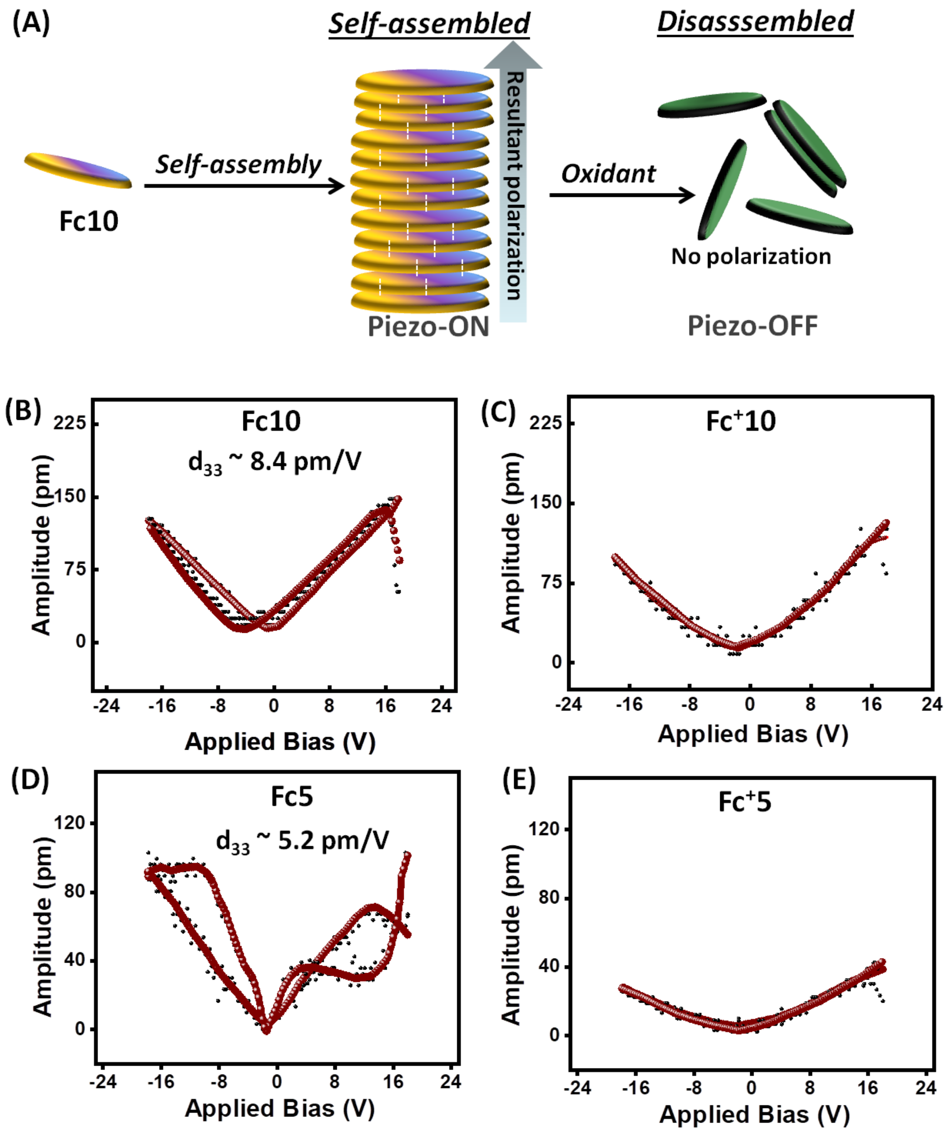

Figure 3.7: (A) Schematic representation of self-assembly in **Fc10** to generate resultant polarizations to endow piezoelectric response that can be switched off upon oxidative disassembly. PFM amplitude loops acquired for (B) self-assembled **Fc10** and (C) **Fc$^+$10** metastable nanoparticles (D) self-assembled **Fc5** and (E) nanoparticles of **Fc$^+$5**.

3.3. Conclusions

In summary, we demonstrated for the first time an elegant pathway driven supramolecular polymerization in amyloid inspired peptide amphiphile tethered with redox-responsive ferrocene moiety toward designing precise peptide nanostructures with predictive piezoresponse. We designed ferrocene tethered peptide amphiphiles with varied spacer lengths linking redox-responsive ferrocene moiety with peptide fragment. Tweaking of peptide spacer length dictated the propensity of self-assembly and redox properties that further regulated the mechanical strength of the physically cross-linked hydrogel networks. Such redox-responsive materials with precise control over nanostructures were studied extensively with UV-vis, CD spectra, CV, rheology and microscopy. Moreover, this work establishes a new strategy where the self-assembly/disassembly precision can be achieved within the nanofibers by employing stimuli-responsive blocks. We developed redox-responsive supramolecular co-block nanofibers for **Fc10** peptide through two-component seeded supramolecular polymerization. Interestingly, here only peripheral blocks are sensitive to redox agent and show self-assembly/disassembly behaviour while the central core remains intact with external chemical stimuli. Finally, we demonstrated ferrocene conjugated peptide for the tunable piezoelectric response as mediated by redox controlled structural manipulations. It opens a new strategy to design and develop smart functional soft materials by using peptide engineering and bioelectronics.

3.4. Experimental section

3.4.1. Materials and methods

All the Fmoc protected amino acids, β-alanine, 6-aminohexanoic acid, 11-aminoundecanoic acid, ferrocene, 9-fluorenylmethoxycarbonyl chloride, ascorbic acid and iron (III) perchlorate were purchased from Sigma. Fmoc-Rink Amide MBHA resin (0.56 mmol/g loading) from NovaBiochem (EMD Millipore) was used as a solid support to synthesize *C*-terminal amide peptides on 0.1 mmol scale. Analytical grade solvents and Milli-Q water was used for studies.

Reverse phase HPLC was performed with *Waters* Alliance HPLC system, using *Nucleodur* analytical column (C_{18} stationary phase, 5 μm, 4.6 × 250 mm). Samples were injected with auto sampler and detected by photodiode array (PDA) detector. Electrospray Ionization Mass Spectrometry (ESI/MS) was performed with *Waters Aquire QDa* detector.

UV-vis measurements were recorded in *Shimadzu UV-2600* spectrophotometer with wavelength range of 800 to 200 nm.

Circular Dichroism spectra were recorded using *JASCO J-1500* Spectrometer, Easton, MD, USA. Samples were scanned for wavelength range from 190 nm to 450 nm with scan speed of 200 nm min^{-1} at 25 ºC. Typically, CD spectra were recorded at concentration of 10 mM. AFM images were recorded on a *Bruker multimode 8* scanning probe microscope. Aqueous sample was deposited on the silicon wafer and after 5-7 min sample was dried under nitrogen. Images were recorded in tapping mode with scan rate of 0.5 to 0.9 Hz with silicon cantilever (*Bruker*).

3.4.2. Synthetic and characterization of peptide amphiphiles

Fmoc protection of amine group of 6-Aminohexanoic acid, β-alanine and 11-Aminoundecanoic acid: 6-amino hexanoic acid (4.6 mmol, 600 mg) was dissolved in 9 mL of dioxane-water (2**:**1) solution. The mixture was cooled to 0 ºC and 1 M aqueous NaOH (4.6 mL) was added followed by addition of Fmoc chloride (5.06 mmol, 1.3 g) as solid powder. The reaction mixture was stirred at room temperature for 5 h and after that solution was concentrated. The aqueous layer was washed once with ethyl acetate (20 mL). Then, the aqueous layer was acidified with 1 M HCl (pH = 1) and extracted with ethyl acetate (15 mL) three times. All the organic layers were dried over anhydrous $MgSO_4$, filtered and concentrated. The obtained compound was dissolved in dichloromethane. Addition of hexane renders white precipitates as product.

Same procedure was followed for Fmoc- protection of amine group of β-alanine and 11-Aminoundecanoic acid.

Fmoc-β-alanine (Fmoc-C_2-COOH):

Percentage yield = 65%

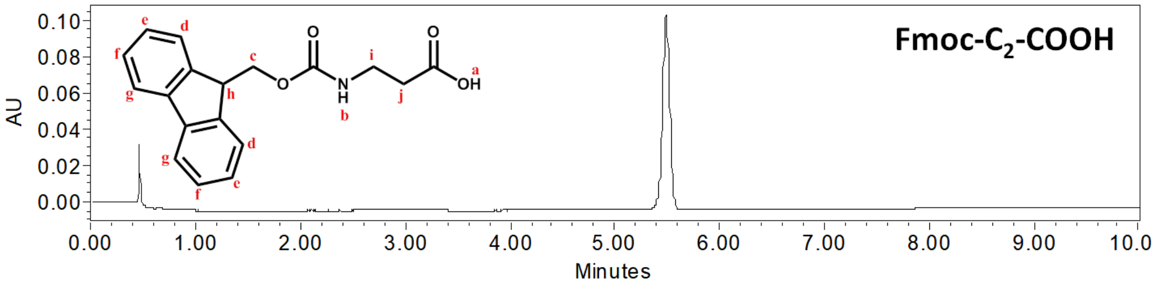

^{1}H NMR ([d_6]-DMSO): δ =12.08 (s, 1 H, a-H), 7.95-7.74 (m, 4 H, e-H ,f-H), 7.50-7.42 (m, 4 H, g-H, d-H), 7.25 (t, *J* = 8 Hz, 1 H, b-H), 4.44 (d, *J* = 8 Hz, 2 H, c-H), 4.34 (t, *J* = 8 Hz, 1 H, h-H), 3.11 (m, 2 H, i-H), 2.5 (t, J = 9.2 Hz, 2 H, j-H) ppm.

Fmoc-aminohexanoic acid (Fmoc-C$_5$-COOH):

Percentage yield = 68%

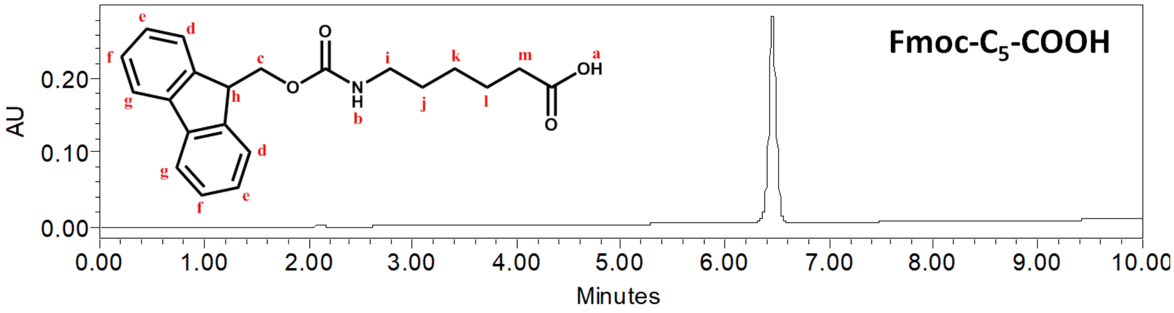

^{1}H NMR ([d_6]-DMSO): δ = 12.04 (s, 1 H, a-H), 7.95-7.74 (m, 4 H, e-H, f-H), 7.47-7.39 (m, 4 H, g-H, d-H), 7.33 (t, J = 9.2 Hz, 1 H, b-H), 4.35 (d, J = 8 Hz, 2 H, c-H), 4.26 (t, J = 8 Hz,1 H, h-H), 3.01 (m, 2 H, i-H), 2.25 (t, J = 9.2 Hz, 2 H, m-H), 1.55 (m, 2 H, l-H), 1.47 (m, 2 H, j-H), 1.30 (m, 2 H, k-H) ppm.

Fmoc-aminoundecanoic acid (Fmoc-C$_{10}$-COOH):

Percentage yield = 62%

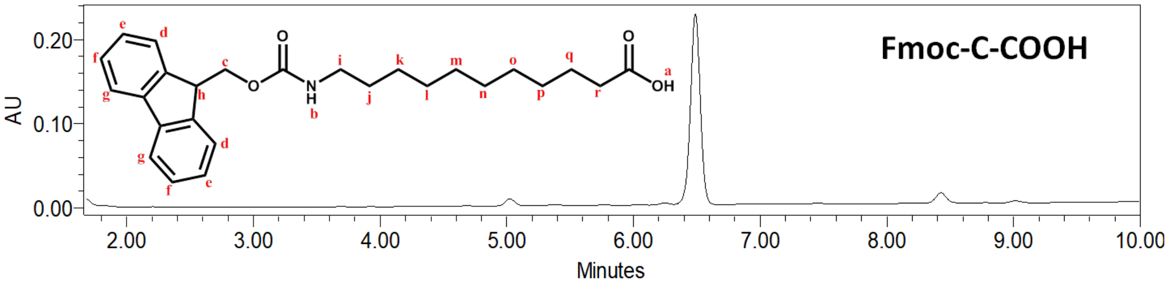

^{1}H NMR ([d_6]-DMSO): δ = 11.8 (s, 1 H, a-H), 7.70-7.53 (m, 4 H, e-H, f-H), 7.33-7.24 (m, 4 H, g-H, d-H), 7.2 (t, J = 9.2 Hz, 1 H, b-H), 4.34 (d, J = 8 Hz, 2 H, c-H), 4.15 (t, J = 8 Hz, 1 H, h-H), 3.11 (t, J = 8 Hz, 2 H, i-H), 2.28 (t, J = 9.2 Hz, 2 H, r-H), 1.57 (m, 2 H, j-H), 1.43 (m, 2 H, q-H), 1.21 (s, 12 H, k-H, l-H, m-H, n-H, o-H, p-H) ppm.

Figure 3.8: HPLC traces and ^{1}H NMR values of Fmoc- protected β-alanine, 6-amino hexanoic acid and 11-Aminoundecanoic acid. For recording HPLC traces, analytical HPLC was used with solvent gradient of 50 → 95% CH$_3$CN in H$_2$O (0.1% HCOOH additive) with flow rate of 1 mL/min over 10 min.

Synthesis of ferrocene carboxylic acid: Ferrocene-monocarboxylic acid was synthesized according to modified literature.[68]

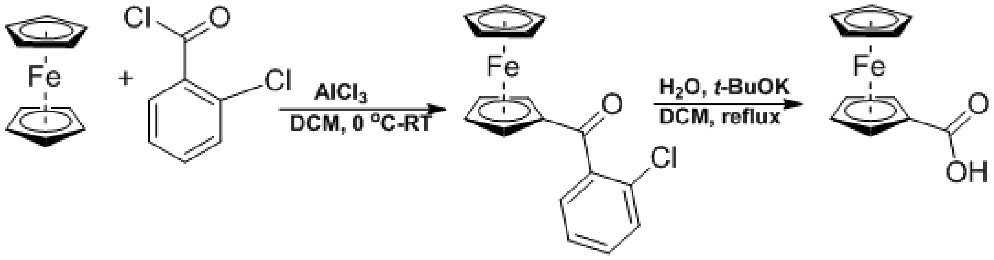

Synthesis of 2-chlorobenzoyl ferrocene: The three-necked round bottomed flask was maintained at an inert atmosphere and ferrocene (16.1 mmol), 2-chlorobenzoyl chloride (16.1 mmol) and dichloromethane (DCM) (35 mL), was added. The flask was kept in an ice bath. When the solution has been chilled thoroughly, anhydrous aluminum chloride (16.8 mmol) was added slowly over 20 min maintaining temperature of reaction mixture remains below 5° C. Deep blue color appears and reaction mixture was stirred for 30 min in ice conditions and subsequently stirring at room temperature for 2 hours.

The reaction mixture is cooled again in ice and added 50 mL of water to it followed by vigorous stirring for 30 min. This aqueous layer was extracted with DCM (10 mL x 2). The combined DCM layers were washed with water (10 mL), 10% NaOH (10 mL). The DCM layer dried over $MgSO_4$, filtered and concentrated in rotary evaporator resulting in red viscous product.

Percentage yield = 94%

^{1}H NMR ($CDCl_3$): δ = 7.50 (dd, 1 H, phenyl), 7.44 (dd, 1 H, phenyl), 7.40 (dt, 1 H, phenyl), 7.34 (dt, 1 H, phenyl), 4.74 (t, 2 H, Cp), 4.59 (t, 2 H Cp), 4.27 (s, 5 H, Cp) ppm.

Synthesis of Ferrocenecarboxylic acid: In a round-bottomed flask, take 25 mL of dry 1,2-dimethoxyethane, potassium tert-butoxide (30.8 mmol), water (9.2 mmol) which form a slurry. Add crude (2-chlorobenzoyl)ferrocene (7.7 mmole) to it and reflux the red reaction mixture under nitrogen for 2 h. The reaction mixture was cooled and poured into 100 mL of water. The solution was washed with diethyl ether (15 mL x 3) which are combined and back-extracted with 10% NaOH (10 mL x 2). The aqueous phases were then combined and acidified with concentrated HCl. The yellow precipitate was filtered and air-dried.

Percentage yield = 80%

^{1}H NMR ([d_6]-DMSO): δ = 7.97 (s, 1 H, COOH), 4.72 (t, 2 H , Cp), 4.38 (t, 2 H, Cp), 4.19 (s, 5 H, Cp) ppm.

<u>Synthesis of peptides</u>: Microwave-assisted peptide synthesizer of *Liberty Blue CEM*, Matthews, NC, USA was used to synthesize peptide sequences following standard microwave Fmoc-solid phase peptide protocols.

Peptides were synthesized on rink amide MBHA resin at 0.1 mmol scale following standard microwave Fmoc-solid phase peptide Synthesis (SPPS) protocols. Fmoc protected amino acids (0.2 M) was coupled with ferrocene carboxylic acid (0.2 M) using diisopropyl carbodiimide (DIC) and oxyma pure in *N, N*'dimethylformamide (DMF). Fmoc deprotection was carried out with 20% piperazine in DMF (containing 10% ethanol) in microwave at 75 °C. Resin bound peptide was filtered, washed with DMF and dichloromethane and allowed to dry. The peptide was cleaved from the resin using 10 mL of cleavage cocktail mixture (trifluoroacetic acid (TFA)/water (95**:**5, v/v)). The mixture was shaken for 3 h at the room temperature followed by removal of the resin through filtration and the filtrate was concentrated to volume of approximately 1 mL. The resultant residue was precipitated by drop wise addition to ice cold diethyl ether. The precipitated product was centrifuged for 15 min at 7000 rpm at 4 °C. The precipitates were washed 3 times with cold diethyl ether and air dried.

3.4.3. Characterization of peptides

The synthesized peptide was re-dissolved in CH_3CN/H_2O (1:9) to analyze the purity of the peptides by reverse phase HPLC with mobile phase acetonitrile and water containing 0.1% formic acid, confirmed by positive ion electronspray mass spectrometry and stored at -20°C. The standard gradient used for analytical HPLC was 5 → 95% CH_3CN in H_2O (0.1% HCOOH additive) with flow rate of 1 mL/min over 30 min.

Fc0: ^1H NMR (D_2O, 500 MHz): δ = 7.25-7.07 (10 H, f-H), 4.49 (4 H, a-H, b-H), 4.17-3.8 (9 H, c-H, i-H, j-H), 2.90 (5 H, g-H, o-H), 1.70 (8 H, l-H, n-H), 1.37 (7 H, m-H, k-H), 0.75 (6 H, h-H) ppm.

Calculated exact mass for $C_{49}H_{67}FeN_9O_7$ = 949.45. In positive mode: found $[MH^+]$ = 950.66, $[MH_2]^{2+}$ = 476.10.

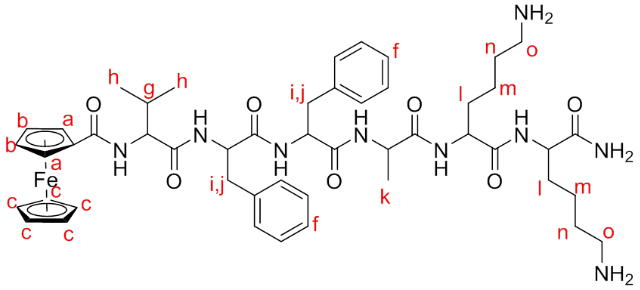

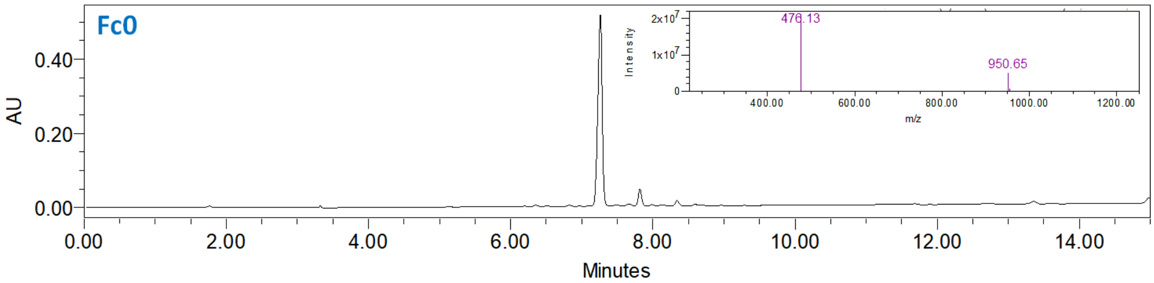

Fc2: ^{1}H NMR (D_2O, 500 MHz): δ = 7.23-7.04 (10 H, f-H), 4.45 (4 H, a-H, b), 4.14 (9 H, c-H, i-H, j-H), 3.21 (2 H, d-H), 2.82 (5 H, g-H, o-H), 2.01 (2 H, r-H), 1.60 (11 H, l-H, n-H, k-H), 1.31 (4 H, m-H), 0.75(6 H, h-H) ppm.

Calculated exact mass for $C_{52}H_{72}FeN_9O_7$ = 1020.49. In positive mode: found [MH^+] = 1021.73, [MH_2]$^{2+}$ = 511.61.

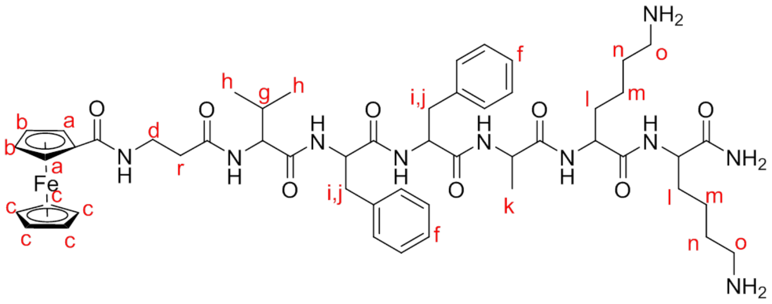

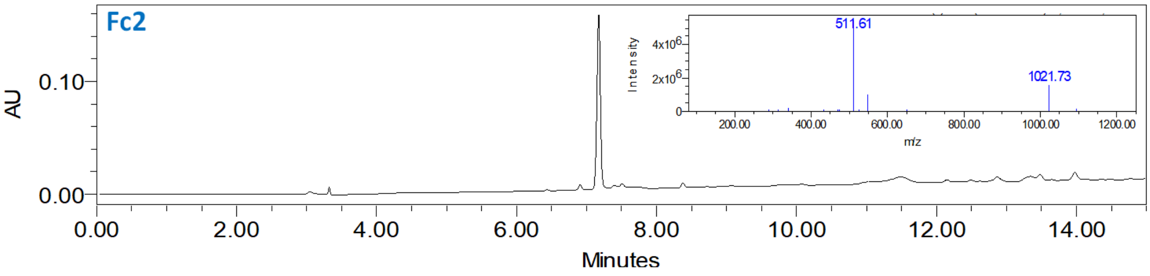

Fc5: ^{1}H NMR (D_2O, 500 MHz): δ = 7.33-7.04 (10 H, f-H), 4.45 (4 H, a-H, b-H), 4.19-3.8 (9 H, c-H, i-H, j-H), 3.21 (2 H, d-H), 2.91 (5 H, g-H, o-H), 2.14 (2 H, r-H), 1.60 (11 H, l-H, n-H, k-H), 1.37 (6 H, p-H, q-H, e-H), 1.27 (4 H, m-H), 0.75-0.69 (6 H, h-H).

Calculated exact mass for $C_{55}H_{78}FeN_9O_7$ = 1062.54. In positive mode: found $[MH^+]$ = 1063.80, $[MH_2]^{2+}$ = 532.61.

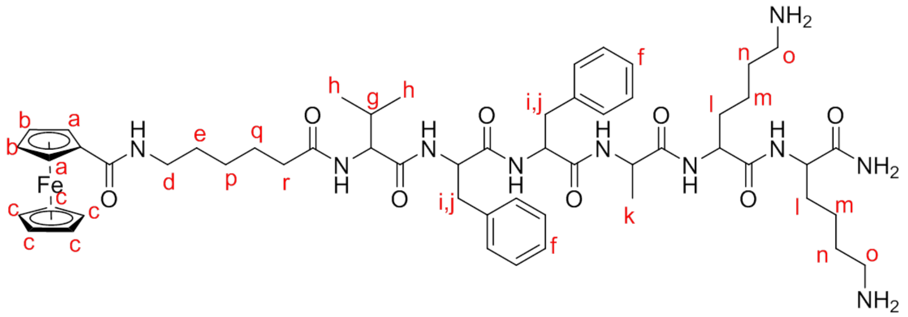

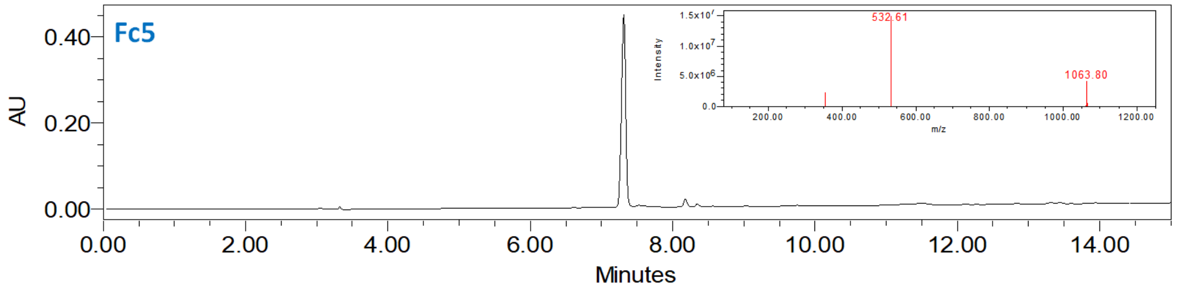

Fc10: ^{1}H NMR (D_2O, 500 MHz): δ = 7.25-7.07 (10 H, f-H), 4.45 (4 H, a-H, b-H), 4.19-3.8 (9 H, c-H, i-H, j-H), 3.21 (2 H, d-H), 2.91 (5 H, g-H, o-H), 2.14 (2 H, r-H), 1.60 (11 H, l-H, n-H, k-H), 1.37 (6 H, p-H, q-H, e-H), 1.27 (4 H, m-H), 1.19 (10 H, s-H, t-H, u-H, v-H, w-H), 0.72(6 H, h-H) ppm.

Calculated exact mass for $C_{60}H_{88}FeN_9O_7$ = 1132.61. In positive mode: found $[MH^+]$ = 1133.86, $[MH_2]^{2+}$ = 567.64.

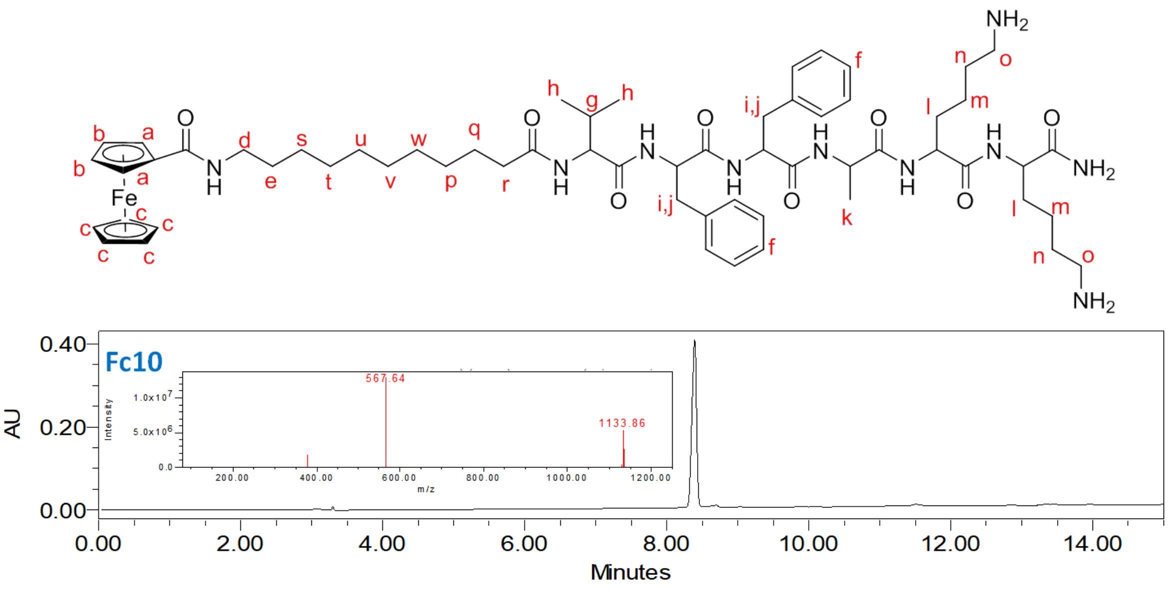

3.4.4. Self-assembly of peptides

Ferrocene anchored peptides (**Fc0**, **Fc2**, **Fc5** and **Fc10**) were taken in water and mechanically agitated for 1-2 min to dissolve at room temperature. The stock solution of peptides was prepared at 10 mM concentration. After incubation for a day, the formation of the self-aggregated nanoparticles and nanofibers mediated by hydrogen bonding and π-π interactions were confirmed by the AFM images. For oxidation of the Fc moieties, the stock solution of $Fe(ClO_4)_3$ (concentration = 1 M) was prepared and a required aliquot was added to the peptide solution (1 eq).

For investigating pH-mediated self-assembly, the peptides were taken in water and agitated. Further, the pH of 10 mM peptide solution was adjusted using sodium hydroxide for basic pH > 8 and hydrochloric acid for acidic pH < 6. The solutions were incubated at room temperature for one day for self-assembly. For investigating the effect of ionic strength on the self-assembly, the 10 mM peptide solutions were incubated with sodium sulphate or sodium phosphate buffer (2 mM).

For hydrogel formation, 4 μL of 1 M sodium phosphate buffer (pH = 7.4) or sodium sulphate (10 mM, pH = 7.4) was added to 400 μL of self-assembled peptide solution (concentration = 10 mM), incubated for one day and the resulting solution was mechanically agitated. Upon incubating at room temperature for 1 day, the negatively charged phosphates electrostatically interact with the positively charged lysine side chain of peptide nanofibers to render a physically cross-linked network structure to eventually result in hydrogel. For complete oxidation of Fc-peptide nanofibers in hydrogel state, two equivalents of oxidizing agent $Fe(ClO_4)_3$ were added.

3.4.5. Rheological studies

Rheological measurements were carried out on Anton Parr Physica MCR 302 rheometer using parallel plate of diameter 25 mm (PP-25). Rheological investigations were performed on the peptide hydrogels using parallel plate geometry of diameter 25 mm (PP-25). The hydrogel was placed in the centre of the rheometer plate. The temperature was maintained at 25 ºC using a peltier temperature controller attached to a Julabo chiller. The frequency sweep experiments were performed using a constant strain of 0.1% in the linear viscoelastic region of frequency range from 0.01-200 rad/s to demonstrate the stability of the hydrogels. Thixotropic studies were carried out with the gel network being completely broken at 100% strain, however, it recovers its gelation ability when the strain value was switched back to 0.1%. Three consecutive cycles of high (100%) and low strain (0.1%) were applied at a constant angular frequency of 10 rad/s.

3.4.6. Electrochemical analysis

The Fc-conjugated peptide was immobilized on the surface of the pencil graphite electrode **(**PGE), used EDC-NHS coupling at the surface of the activated pencil graphite electrode and the Fc conjugated peptide. First, pencil graphite was activated by 25 cycles of CV at a scan rate of 0.1 V/S with the potential range of -0.5 V to +2 V using H_3PO_4 as the supporting electrolyte. Typically for sample preparation, 20 µL of 0.2 M EDC-NHS was dropcasted on the surface of the activated pencile graphite electrode and air dried. For recording CV of monomeric solution of **Fc5** and **Fc10**, 30 µL of peptide in HFIP solution was dropcasted and air dried. Similarly for self-assembled **Fc5** and **Fc10**, 30 µL solution of one day aged self-assembled peptide in water was dropcasted on the activated graphite electrode and dried in desiccator.

Cyclic voltammetry (CV) studies were performed on Metrohm MULTI AUTOLAB M204 potentiostat/galvanostat using standard three electrode system. Cyclic voltammograms were obtained at room temperature using the three-electrode system comprised of peptide samples on pencil graphite electrode as a working electrode, platinum electrode as an auxiliary electrode and Ag/AgCl as the reference electrode. Analysis of CV data was done on Nova 1.11 software. CV studies were done with 10 mM phosphate buffer as a primary analyte solution and scanned over a potential range of -0.4V to +0.8V. For monomeric peptide amphiphile, the sample was prepared in HFIP while, the self-assembled peptides were prepared in water.

3.4.7. Seeded supramolecular polymerization

For generation of seeds, 500 μL of pre-assembled nanofibrous solution of **C_{10}-VFFAKK** (concentration = 2 mM) was probe sonicated using QSonica (model number Q700, power 700 watts and frequency 20 kHz) probe Sonicator at an amplitude of 15% for ~2 minutes. AFM image was recorded for analysis using *Image-J* software with the random selection of seeds. A frequency statistics over the nanofiber length was performed to calculate the number average (L_n) and weight average (L_w) lengths along with the corresponding PDI as L_w/L_n.

Further, redox-sensitive peptide **Fc^+10** was taken in hexafluoroisopropanol (HFIP) and an aliquot from the HFIP stock solution of the peptide was then injected in seed solution into water to render a final peptide concentration of 2 mM in 10 v/v% HFIP-water (ratio of seed and nanoparticles = 1**:**3). To induce seeded growth in the above solution, metastable nanoparticles of **Fc^+10** peptide were reduced to **Fc10** in the presence of ascorbic acid and incubated for one day at room temperature to enable self-assembly. At this stage, the AFM image depicted the increased length of the nanofibers. However, the addition of one equivalent of $Fe(ClO_4)_3$ rendered immediate disassembly of redox-responsive peripheral blocks to shorten the nanofiber's length.

3.4.8. Piezoelectric measurements

The self-assembled fibers of **Fc10** and metastable nanoparticles of **Fc^+10** (10 mM) were drop-casted on conducting ITO-coated glass substrate and dried overnight. The piezoelectric response of the peptide nanofibers was measured using piezoresponse force microscopy (PFM) with a *Bruker multimode-8* scanning probe microscope in contact mode. The data were acquired using a conductive Pt-Ir coated probe with a spring constant of ~ 3 N/m. An external bias of 20 V was applied between the probe and sample with a lock-in drive frequency of 12 kHz and drive amplitude of 4 V to measure the butterfly loop (amplitude response) and hysteresis loop (phase response).

3.5. References

1. T. F. A. De Greef, M. M. J. Smulders, M. Wolffs, A. P. H. J. Schenning, R. P. Sijbesma and E. W. Meijer, *Chem. Rev.*, 2009, **109**, 5687-5754.
2 T. Aida, E. W. Meijer and S. I. Stupp, *Science*, 2012, **335**, 813-817.
3. L. Yang, X. Tan, Z. Wang and X. Zhang, *Chem. Rev.*, 2015, **115**, 7196-7239.
4. D. B. Amabilino, D. K. Smith and J. W. Steed, *Chem. Soc. Rev.*, 2017, **46**, 2404-2420.
5. S. I. Stupp and L. C. Palmer, *Chem. Mater.*, 2014, **26**, 507.
6. E. Mattia and S. Otto, *Nat. Nanotechnol.*, 2015, **10**, 111.
7. P. A. Korevaar, C. J. Newcomb, E. W. Meijer and S. I. Stupp, *J. Am. Chem. Soc.* 2014, **136**, 8540.
8. P. A. Korevaar, S. J. George, A. J. Markvoort, M. M. J. Smulders, P. A. J. Hilvers, A. P. H. J. Schenning, T. F. A. D. Greef and E. W. Meijer, *Nature*, 2012, **481**, 492.
9. P. Korevaar, C. Schaefer, C.; T. F. A. D. Greef, E.W. Meijer, *J. Am. Chem. Soc.* 2012, **134,** 13482.
10. S. Ogi, K. Sugiyasu, S. Manna, S. Samitsu and M. Takeuchi, *Nat. Chem.*, 2014, **6**, 188-195.
11. J. Kang, D. Miyajima, T. Mori, Y. Inoue, Y. Itoh and T. Aida, *Science*, 2015, **347**, 646-651.
12. S. Ogi, V. Stepanenko, K. Sugiyasu, M. Takeuchi and F. Würthner, *J. Am. Chem. Soc.*, 2015, **137**, 3300-3307.
13. S. H. Jung, D. Bochicchio, G. M. Pavan, M. Takeuchi and K. Sugiyasu, *J. Am. Chem. Soc.*, 2018, **140**, 10570-10577.
14. A. Pal, M. Malakoutikhah, G. Leonetti, M. Tezcan, M. Colomb-Delsuc, V. D. Nguyen, J. van der Gucht and S. Otto, *Angew. Chem. Int. Ed.*, 2015, **54**, 7852-7856.
15. M. Wehner and F. Würthner, *Nat. Rev. Chem.*, 2020, **4**, 38-53.
16. G. Ghosh, P. Dey and S. Ghosh, *Chem. Commun.*, 2020, **56**, 6757-6769.
17. J. S. Valera, R. Gómez and L. Sánchez, *Small*, 2018, **14**, 1702437.
18. D. Mukhopadhyay Rahul and A. Ajayaghosh, *Science*, 2015, **349**, 241-242.
19. J. B. Gilroy, T. Gädt, G. R. Whittell, L. Chabanne, J. M. Mitchels, R. M. Richardson, M. A. Winnik and I. Manners, *Nat. Chem.*, 2010, **2**, 566-570.
20. M. Endo, T. Fukui, S. H. Jung, S. Yagai, M. Takeuchi and K. Sugiyasu, *J. Am. Chem. Soc.*, 2016, **138**, 14347-14353.
21. K. Jalani, A. D. Das, R. Sasmal, S. S. Agasti and S. J. George, *Nat. Commun.*, 2020, **11**, 3967.
22. A. Aliprandi, M. Mauro and L. De Cola, *Nat. Chem.*, 2016, **8**, 10-15.
23. S. Ogi, N. Fukaya, Arifin, B. B. Skjelstad, Y. Hijikata and S. Yamaguchi, *Chem. Eur. J*, 2019, **25**, 7303-7307.
24. D. S. Pal, H. Kar and S. Ghosh, *Chem. Eur. J*, 2016, **22**, 16872-16877.
25. A. Levin, T. A. Hakala, L. Schnaider, G. J. L. Bernardes, E. Gazit and T. P. J. Knowles, *Nat. Rev. Chem.*, 2020, **4**, 615-634.
26. B. O. Okesola and A. Mata, *Chem. Soc. Rev.*, 2018, **47**, 3721-3736.
27. X. Hu, M. Liao, H. Gong, L. Zhang, H. Cox, T. A. Waigh and J. R. Lu, *Curr. Opin. Colloid Interface Sci.*, 2020, **45**, 1-13.
28. A. Brito, Y. M. Abul-Haija, D. S. da Costa, R. Novoa-Carballal, R. L. Reis, R. V. Ulijn, R. A. Pires and I. Pashkuleva, *Chem. Sci.*, 2019, **10**, 2385-2390.
29. M. P. Hendricks, K. Sato, L. C. Palmer and S. I. Stupp, *Acc. Chem. Res.*, 2017, **50**, 2440.
30. S. Wong, M. S. Shim and Y. J. Kwon, *J. Mater. Chem. B*, 2014, **2**, 595-615.
31. M. Ikeda, T. Tanida, T. Yoshii and I. Hamachi, *Adv. Mater.*, 2011, **23**, 2819-2822.
32. J. Huang and A. Heise, *Chem. Soc. Rev.*, 2013, **42**, 7373-7390.
33. B. F. Lin, K. A. Megley, N. Viswanathan, D. V. Krogstad, L. B. Drews, M. J. Kade, Y. Qian and M. V. Tirrell, *J. Mater. Chem.*, 2012, **22**, 19447-19454.
34. J. Rodríguez-Hernández and S. Lecommandoux, *J. Am. Chem. Soc.*, 2005, **127**, 2026-2027.
35. J. P. Schneider, D. J. Pochan, B. Ozbas, K. Rajagopal, L. Pakstis and J. Kretsinger, *J. Am. Chem. Soc.*, 2002, **124**, 15030-15037.

36. S.-Y. Qin, S.-S. Xu, R.-X. Zhuo and X.-Z. Zhang, *Langmuir*, 2012, **28**, 2083-2090.
37. X. Zhang, C. Dong, W. Huang, H. Wang, L. Wang, D. Ding, H. Zhou, J. Long, T. Wang and Z. Yang, *Nanoscale*, 2015, **7**, 16666-16670.
38. Y. Zhao, B. Lei, M. Wang, S. Wu, W. Qi, R. Su and Z. He, *J. Mater. Chem. B*, 2018, **6**, 2444-2449.
39. P. Fatás, J. Bachl, S. Oehm, A. I. Jiménez, C. Cativiela and D. Díaz Díaz, *Chem. Eur. J*, 2013, **19**, 8861-8874.
40. C. Chen, Z. Wang and Z. Li, *Biomacromolecules,* 2011, **12**, 2859-2863.
41. L. Klouda and A. G. Mikos, *Eur. J. Pharm. Biopharm.*, 2008, **68**, 34-45.
42. Z.-Y. Li, J.-J. Hu, Q. Xu, S. Chen, H.-Z. Jia, Y.-X. Sun, R.-X. Zhuo and X.-Z. Zhang, *J. Mater. Chem. B*, 2015, **3**, 39-44.
43. Z. Guo, S. Li, Z. Liu and W. Xue, *ACS Biomater. Sci. Eng.*, 2018, **4**, 988-996.
44. C. J. Bowerman and B. L. Nilsson, *J. Am. Chem. Soc.*, 2010, **132**, 9526-9527.
45. D. B. Rasale, I. Maity and A. K. Das, *Chem. Commun.*, 2014, **50**, 11397-11400.
46. S. Toledano, R. J. Williams, V. Jayawarna and R. V. Ulijn, *J. Am. Chem. Soc.*, 2006, **128**, 1070-1071.
47. A. R. Hirst, S. Roy, M. Arora, A. K. Das, N. Hodson, P. Murray, S. Marshall, N. Javid, J. Sefcik, J. Boekhoven, J. H. van Esch, S. Santabarbara, N. T. Hunt and R. V. Ulijn, *Nat. Chem.*, 2010, **2**, 1089-1094.
48. M. Hughes, S. Debnath, C. W. Knapp and R. V. Ulijn, *Biomater. Sci.*, 2013, **1**, 1138-1142.
49. R. Zou, Q. Wang, J. Wu, J. Wu, C. Schmuck and H. Tian, *Chem. Soc. Rev.*, 2015, **44**, 5200-5219.
50. Y. Shen, X. Fu, W. Fu and Z. Li, *Chem. Soc. Rev.*, 2015, **44**, 612-622.
51. J. P. Wojciechowski, A. D. Martin and P. Thordarson, *J. Am. Chem. Soc.*, 2018, **140**, 2869-2874.
52. D. Spitzer, L. L. Rodrigues, D. Straßburger, M. Mezger and P. Besenius, *Angew. Chem. Int. Ed.*, 2017, **56**, 15461-15465.
53. A. Paul, R. Borrelli, H. Bouyanfif, S. Gottis and F. Sauvage, *ACS Omega*, 2019, **4**, 14780-14789.
54. B. Adhikari and H.-B. Kraatz, *Chem. Commun.*, 2014, **50**, 5551-5553.
55. R. Afrasiabi, and H.-B. Kraatz, *Chem. Eur. J.* 2013**, 19,** 17296.
56. S. Martić, M. Labib,; P. O. Shipman, H.-B. Kraatz, *Dalton Trans.* 2011**, 40,** 7264.
57. B. Adhikari, C. Singh, A. Shah, A. J. Lough and H.-B. Kraatz, *Chem. Eur. J.*, 2015, **21**, 11560-11572.
58. S. Beheshti, A. Lataifeh, H.-B. Kraatz, *J. Organomet. Chem.* 2011, **696,** 1117.
59. J. P. Joseph, A. Singh, D. Gupta, C. Miglani and A. Pal, *ACS Appl. Mater. Interfaces*, 2019, **11**, 28213-28220.
60. A. Singh, J. P. Joseph, D. Gupta, I. Sarkar and A. Pal, *Chem. Commun.*, 2018, **54**, 10730-10733.
61. D. Gupta, R. Sasmal, J. P. Joseph, C. Miglani, S. S. Agasti and A. Pal, *Nanoscale*, 2020, **12**, 18692.
62. J.-H. Lee, K. Heo, K. Schulz-Schönhagen, J. H. Lee, M. S. Desai, H.-E. Jin and S.-W. Lee, *ACS Nano*, 2018, **12**, 8138-8144.
63. K. Ryan, J. Beirne, G. Redmond, J. I. Kilpatrick, J. Guyonnet, N.-V. Buchete, A. L. Kholkin and B. J. Rodriguez, *ACS Appl. Mater. Interfaces*, 2015, **7**, 12702-12707.
64. S. Bera, S. Guerin, H. Yuan, J. O’Donnell, N. P. Reynolds, O. Maraba, W. Ji, L. J. W. Shimon, P. A. Cazade, S. A. M. Tofail, D. Thompson, R. Yang and E. Gazit, *Nat. Commun.* 2021, **12**, 2634.
65. A. Gruverman, M. Alese and D. Meier, *Nat. Commun.* 2019, **10**, 1661.
66. V. Gupta, A. Babu, S. K. Ghosh, Z. Mallick, H. K. Mishra, D.Saini and D. Mandal, *Appl. Phys. Lett.* 2021, **119**, 252902.
67. D. Mandal, S. Yoon and K. J. Kim, *Macromol. Rapid Commun.* 2011, **32**, 831.
68. P. C. Reeves, *Org Synth.*, 1977, 56, 28.

4

Enzyme Responsive Chiral Self-sorting in Amyloid-inspired Minimalistic Peptide Amphiphiles

Self-sorting is a spontaneous phenomenon that ensures the formation of complex yet ordered multicomponent systems and conceptualizes the design of artificial and orthogonally functional compartments. In the present study, we envisage chirality-mediated self-sorting in β-amyloid-inspired minimalistic peptide amphiphile (C_{10}*-L/D-VFFAKK)-based nanofibers. The fidelity and stereoselectivity of chiral self-sorting was ascertained by Förster resonance energy transfer (FRET) by the judicious choice of a pyrene (Py)-hydroxy coumarin (HOCou) donor–acceptor pair tethered to the peptide sequences. Seed-promoted elongation of the homochiral peptide amphiphiles investigated by AFM image analyses and Thioflavin-T (ThT) binding study further validated the chiral recognition of the L/D peptide nanofibers. Moreover, direct visualization of the chirality-driven self-sorted nanofibers is reported using super-resolution microscopy that exhibits enantioselective enzymatic degradation for L-peptide fibers. Such enantioselective weakening of the hydrogels may be used for designing stimuli-responsive orthogonal compartments for delivery applications.*

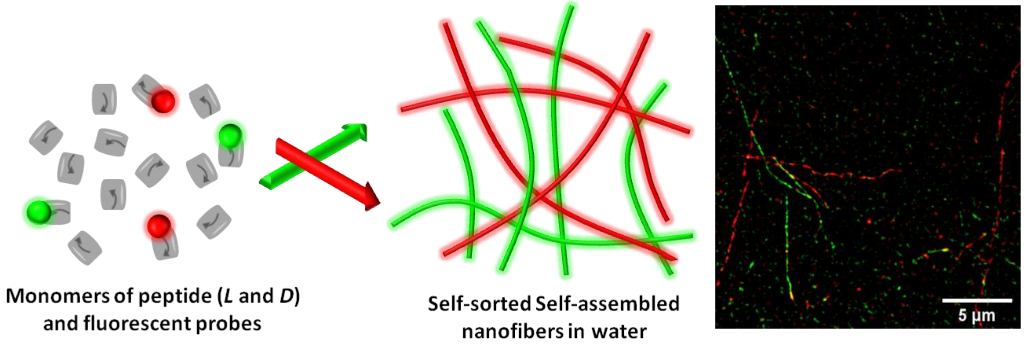

4.1. Introduction

Nature has an excellent ability to design multifunctional materials that require organization of complex multicomponent systems in a set of subsystems mediated by the orthogonal relationships among the structural components.[1-2] Such compartmentalization underlines the significance of orthogonal recognitions that manifest in a number of interesting natural biological processes *e.g.* enzyme recognizing the isomerization or structural mutation of the substrate, dynamic self-assembly/disassembly of microtubules and filaments, that retains the integrity of the extracellular matrices.[3-5] In this regard, self-sorting- the ability to distinguish between the self and non-self, plays an important role to the formation of specific self-assembled structures rather than all possible ensembles of unspecific architectures.[6-7] The orthogonal nature of the components, ranging from molecular level to micrometer level stems from the interaction sites, which may be based on structural mismatch, dynamic covalent bond, stoichiometry, pH variation, thermodynamic *vs* kinetic control in tandem with other external conditions *e.g.* temperature, solvent, and concentration.[8-13] In a bid to mimic the natural self-sorting process, a number of systems with good fidelity of the self-sorting ability have been explored over recent times.[14-16] Tweaking of the structural motifs *e.g.* spacer size and shape, or spacer–spacer interactions, plays pivotal roles in designing interesting self-sorted fibers, cages and hydrogels.[17-27] Of late, super-resolution microscopy has been employed to investigate supramolecular polymerization, especially to probe dynamics and self-sorting behaviors.[28-30] Recently, George *et al.* exploited the technique to probe self-sorted, random, and block supramolecular copolymers during the multicomponent supramolecular polymerization process.[31]

The Self-sorting process driven by chiral recognition addresses the evolution of homochirality in prebiotic earth with the preference for one enantiomer in natural molecules by employing autocatalytic self-replication process. However, controlling the self-assembly with stereo-specificity in a multicomponent system involving an enantiomeric pair in one pot is rather daunting task for chemists owing to the labile conformation and adaptability towards similar recognition sites of the enantiomers.[32] Sijbesma *et al.* and George *et al.* exploited the chiral motif of *trans*-1,2-bis(amido)cyclohexane to develop self-sorted systems, which could be ascertained from differential FRET investigations.[33-34] Such chirality-driven self-sorting was exploited by Aida *et al.* to achieve enantioselective supramolecular polymerization.[35] In this regard, peptides having multiple chiral amino acid motifs are ideal as tweaking of the chirality may provide vital cues to the self-assembly pathway. Fuhrhop and Dzwolak *et al.* demonstrated the formation of a heterochiral β-sheets precipitation from a homochiral mixture of poly(*D*-lysine) and poly(*L*-lysine) α-helices.[36-37] Similarly, the heterochiral helix was preferred over the homochiral ones in triple helix of collagen mimetic peptides as shown by Nanda *et al.*[38] Moreover, stereospecific peptide assemblies are of substantial interest for preventing amyloidogenesis using *D* peptides as an inhibitor for fibril growth.[39-44] However, the preference of homo *vs.* heterochiral stacks was found to be system dependent; Maggio *et al.* Nowick *et al.* and Hilvert *et al.* reported Aβ(1-40) peptides opting for homochiral aggregation,[39-42] while Nilsson *et al.* showed heterochiral selectivity in peptide aggregation inspired from β-hairpin or β-amyloid.[43] Interestingly, Schneider *et al.* demonstrated a peptide sequence that undergoes β-hairpin folding and self-assembly to form hydrogel network with a four-fold enhancement in mechanical properties upon co-assembly of enantiomers.[44] Thus, the fidelity of the chiral differentiation leading to either co-assembly or self-sorting and lack of convenient analytical techniques to quantify the process are challenges when investigating the chirality-driven self-sorting process. In that regard, it is interesting to design suitable enantiomeric model host peptides and corresponding fluorophores with the stereochemistry mismatch to understand the implications of the chiral recognition. Moreover, visualization of the orthogonal nature of the self-assembly is exciting and pave a way to design complex systems with stereoselective disassembly response upon external cues *e.g.* proteolase. Peptides by virtue of a range of non-covalent interactions *e.g.* side chain interactions and hydrogen bonding have the ability to recognize their own monomer and thereby propagate *via* supramolecular polymerization.[45] Such growth in one or two dimensions for peptide nanostructures has been elegantly controlled by living supramolecular polymerization *via* seeding and cross-seeding-mediated elongation.[46-48] Herein, we demonstrate a rational design of the enantiomeric peptide amphiphiles with the sequence, ${}^{N}\mathrm{VFFA}^{C}$ as inspired by the Aβ42 amyloid nucleating core. The competitive formation of self-sorted fibers over the co-assembled fibers is investigated in details using peptide fluorophores having donor and acceptor FRET pairs. We postulate chiral-recognition-driven efficient fluorescence energy transfer in the homochiral peptide co-assembly and quantify the chiral self-sorting in the self-assembled nanofibers. The nucleation-mediated growth for the peptide amphiphiles is evident from the seeding and cross-seeding experiments, as observed from the AFM image analyses and time-dependent Thioflavin-T (ThT) binding assays indicating the chirality-driven orthogonal growth of nanofibers. Chirality-driven self-sorted peptide fibers were directly visualized by super-resolution structured illumination microscopy (SR-SIM) for the first time. Lastly, the orthogonal nature of the assembly was established with the enantioselective enzymatic degradation of the *L*-peptide fibers and consequential weakening of the mechanical strength of hydrogels.

4.2. Results and discussion

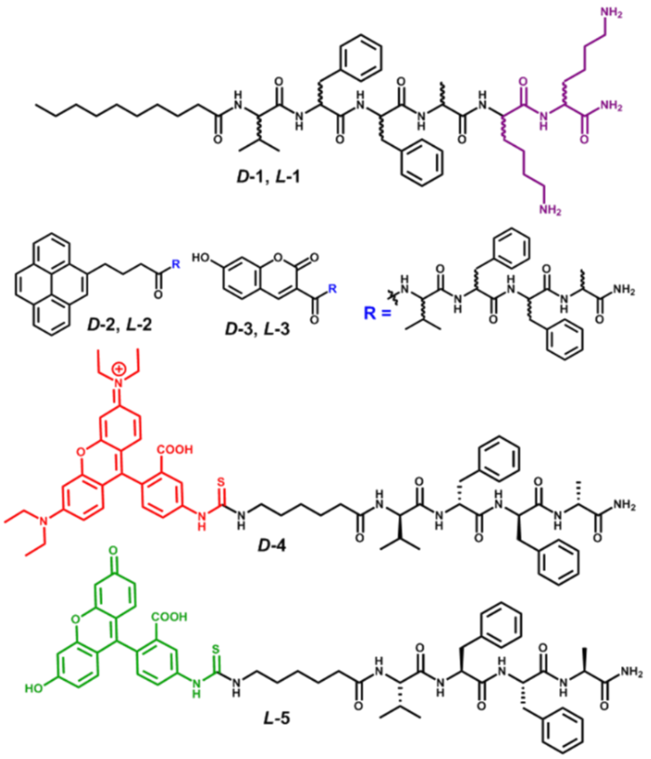

Scheme 4.1: Molecular structures of the peptide amphiphiles (***L*-1** and ***D*-1**), fluorescent probes, ***L*-2** and ***D*-2** anchored with pyrene, ***L*-3** and ***D*-3** anchored with hydroxycoumarin, ***D*-4** and ***L*-5** with RBITC and FITC moieties attached to ^{N}VFFA^{C} peptide segment respectively.

We designed the peptide amphiphiles ***L*-1** and ***D*-1** by tethering a hydrophobic C_{10} alkyl chain to the *N* terminal of the peptide sequence, ^{N}VFFAKK^{C} with either *L* or *D* enantiomers of the amino acids (Scheme 4.1). The hydrophobic-hydrophilic balance in the peptide amphiphiles and the interplay of attractive hydrogen bonding among amide functionalities, π-π stacking interactions among the side chains and van der Waal's forces among the alkyl chains render the self-assembly in water or Tris-HCl buffer (pH = 7.4). Morphological investigations of the peptide assembly as visualized by TEM and AFM revealed the presence of self-assembled micrometer long fibers with diameters ~ 7.5 ± 1 nm and long radii of curvatures (Figure 4.1A-H). Interestingly, the mixture of peptide amphiphiles ***L*-1** and ***D*-1** also formed a stable and clear solution, unlike the previous reports showing unstable assembly leading to eventual precipitation upon mixing enantiomeric peptide amphiphiles.[49] The mixture of ***L*-1** and ***D*-1** peptides showed similar fibers, which hardly differed from the enantiomeric nanofibers (Figure 4.1C,G).

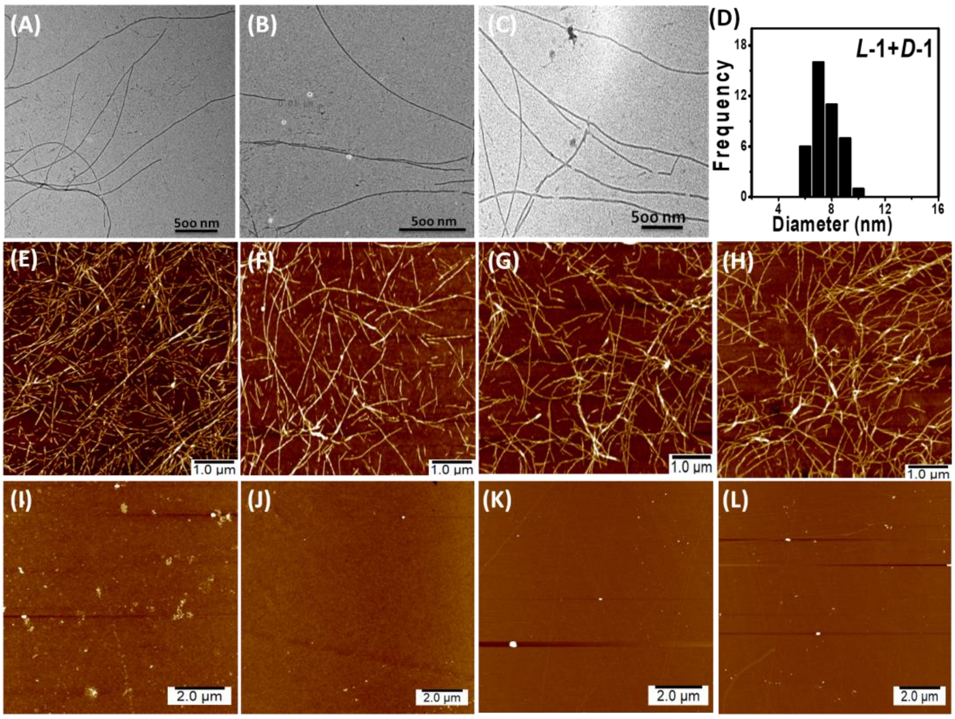

Figure 4.1: TEM images and AFM height images of the peptide ***L*-1** (A, E), ***D*-1** (B, F) and mixture of ***L*-1** and ***D*-1** **(C,G)** in water at room temperature (concentration = 1 µM for TEM and 100 µM for AFM). (D) Histogram analyses for diameter distribution of the peptide amphiphiles. (H) AFM image of ***L*-1** and ***D*-1** peptide mixed in powder form followed by addition of water (solid phase mixing). AFM images of fluorescent probes (1 mM) in water upon dilution from DMSO stock solution. (I) ***L*-2** (J) ***D*-2** (K) ***L*-3** and (L) ***D*-3** showed absence of supramolecular peptide nanofibers.

The small-angle X-ray (SAXS) profile of the fibers were fitted with a model for non-interacting cylinders with a monodisperse cylindrical form factor, which resulted micellar rods of diameter ~ 6.8 ± 0.3 nm (Figure 4.2A), in corroboration with the microscopic data. The scattering profiles for the 1**:**1 solution mixture of the pre-assembled ***L*-1** and ***D*-1** peptide fibers resembled that from dissolution of 1**:**1 solid mixture of the same peptide amphiphiles. Circular Dichroism (CD) spectroscopy of self-assembled peptide nanofiber of ***L*-1** exhibited characteristic negative Cotton band at 216 nm with a concomitant positive band at 197 nm, while that of ***D*-1** showed mirror image bisignated CD signals at 216 and 199 nm, characteristics of peptide β-sheet structure (Figure 4.2B). However, 1**:**1 equimolar mixture of nanofiber solutions and dissolution of 1**:**1 solid mixture of both amphiphiles showed no signature of the overall chirality, which is identical to a simple theoretical sum of the enantiomeric peptide amphiphiles. CD gives the resultant spectra and does not distinguish between the self-sorted or co-assembled fibers. For the nanofiber solutions of ***D*-1** and ***L*-1** pair, we varied the mixing ratio from 1:0 to 0:1 and studied the change in CD spectra (Figure 4.2C-D). On increasing the proportion of ***D*-1**, the CD signal at 216 nm increases and the positive cotton band at 199 nm decreases. Such linear change in the CD signal corroborated the theoretical lines calculated from CD spectra of each enantiomers and indicated minimal or no interaction among the peptide components. Also, this indicated the presence of self-sorted fibers that do not follow majortity rule principle as observed in chiral co-assembly owing to mismatch penalty of the opposite enantiomers in the robust hydrophobic peptide segment *VFFA* (Figure 4.2E). These peptide nanofibers could be lyophilized and kept in the powdered form for a long period of time; however, upon re-dispersing in water, an almost immediate formation of the peptide nanofibers without any loss in their chiral signature was observed (Figure 4.2F).

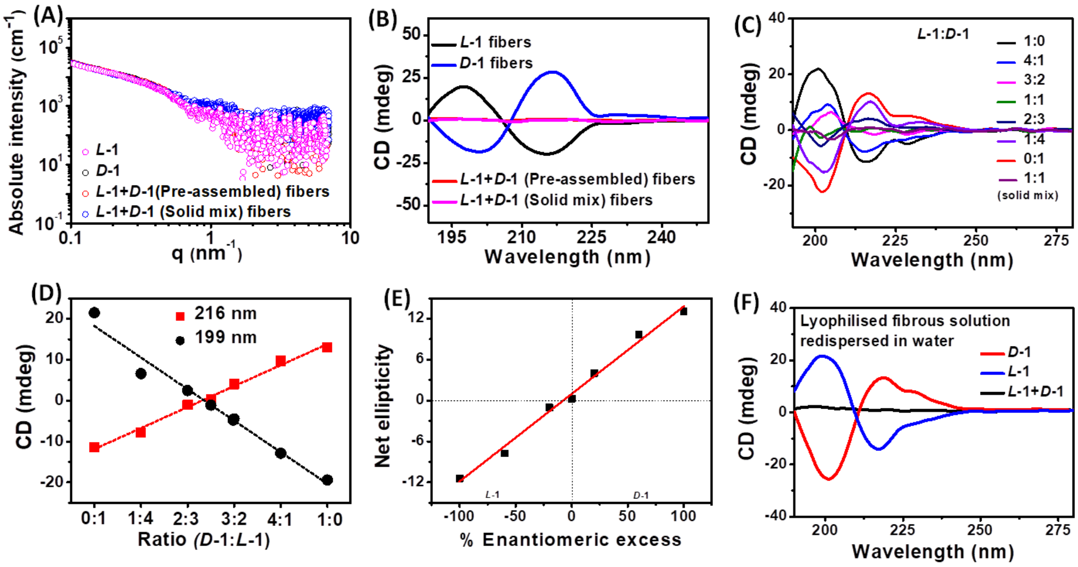

Figure 4.2: (A) SAXS profiles recorded at 25 ºC in water for the individual ***D*-1**, ***L*-1,** for the mixture of peptide amphilphiles in 1:1 ratio (total concentration 10 mM). Solution mixture of ***D*-1** and ***L*-1** fibers and solid mixture ***D*-1** and ***L*-1** peptide followed by dissolution in water for self-assembly. Data fitted with non-interacting porod cylinder model shows diameter ~ 6.8 ± 0.3 nm for all peptide fibers (10 mM). (B) CD spectra of ***L*-1**, ***D*-1** and equimolar mixture of ***L*-1** and ***D*-1** (120 µM). (C) CD spectra recorded for the mixture of peptides nanofiber solutions with different ratios of ***L*-1** and ***D*-1** (100 µM) and equimolar solid phase mixing of ***L*-1** and ***D*-1** followed by dissolution in water. (D) Change in ellipticity at 216 nm and 199 nm with different ratio of ***L*-1** and ***D*-1** fibers. (E) Corresponding plot of net ellipticity at 216 nm with enantiomeric excess. (F) The peptide solutions in water were lyophilized to solid powder and CD spectra were recorded upon redispersing them in water. The redissolved peptide retains its chirality akin to the original peptide fibers.

ThT binding to the nanofibers exhibiting an increase in the fluorescence intensity and FT-IR peaks at 1625 cm^{-1} (amide I) and 1548 cm^{-1} (amide II) indicated the existence of parallel β-sheet for 1D nanofibers (Figure 4.3).

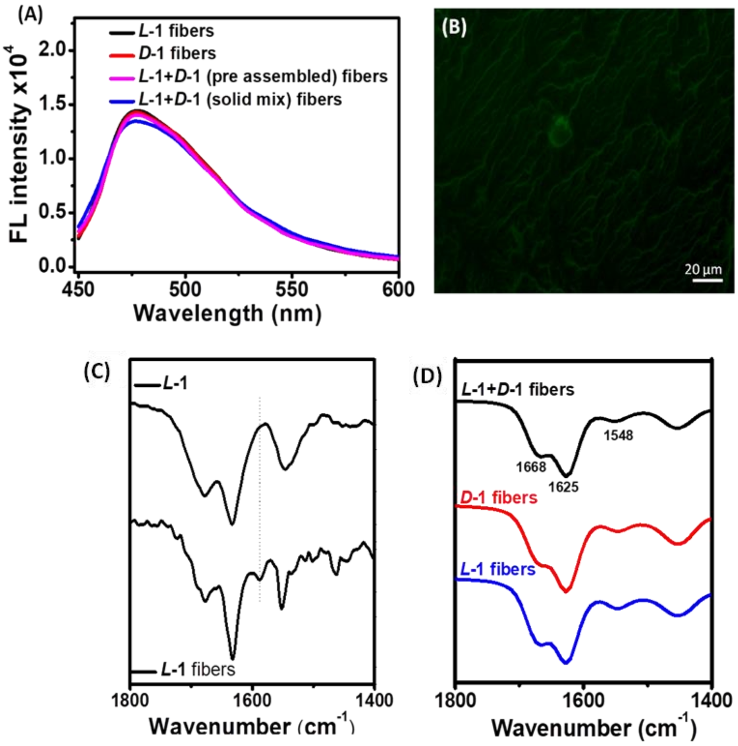

Figure 4.3: Fluorescence emission spectra as a consequence of ThT binding to ***L*-1** and ***D*-1** peptides and their mixture (1**:**1), both pre-assembled fibers mixture and solid phase mixing followed by assembly. (B) Fluorescent imaging of ThT binding to mixture of ***L*-1** and ***D*-1** peptide fibers. (C) FT-IR spectra for ***L*-1** peptide and ***L*-1** peptide nanofibers (after lyophilisation) with KBr pellet. (D) Parallel β-sheet in peptide solution ***L*-1, *D*-1** peptide nanofibers and their mixture in D_2O (5 mM).

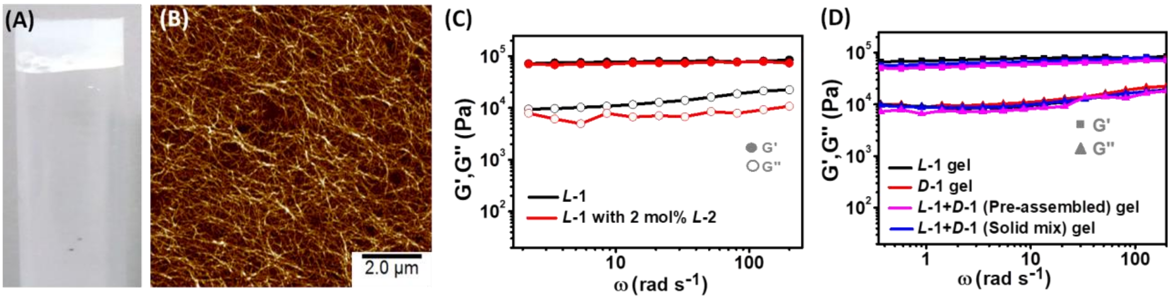

Figure 4.4: (A) digital picture of the hydrogel and (B) AFM imaging shows networked mesh of nanofibers in ***L*-1** + ***D*-1** gel (1 wt%). (C) Frequency sweep oscillatory rheology measurments for the hydrogels from ***L*-1** and ***L*-1** with 2 mol% ***L*-2** containing 2 v/v% DMSO. (D) Rheology for the hydrogels made from ***L*-1**, ***D*-1** and equimolar mixture of ***L*-1** and ***D*-1** (10 mM in sodium phosphate buffer, pH = 7) showing similar mechanical strength.

In sodium phosphate buffer (10 mM) at pH 7, the peptide amphiphiles with positively charged lysine at the surface formed network structures as mediated by the ion-bridge interaction with doubly charged phosphate anion to eventually form hydrogel (Figure 4.4A-B).[47-48] Rheological investigation of the hydrogels produced from the enantiomeric nanofibers and equimolar mixture of *L* and *D* peptide showed similar mechanical properties indicating no interference of one enantiomer with the properties of other self-assembled enantiomer in the nanofibrous mixture (Figure 4.4C-D).

To investigate the chiral recognition in the supramolecular peptide nanofibers, we designed the fluorescent probes, ***L*-2** and ***D*-2** containing pyrene (Py), ***L*-3** and ***D*-3** containing hydroxy coumarin (HOCou) moieties tethered to the peptide sequence, $^{N}VFFA^{C}$ respectively (Scheme 4.1). These fluorescent probes were insoluble in water; hence the stock solution were prepared in DMSO and added to Tris-HCl buffer while performing experiments. The absence of polar lysine amino acids in the fluorescence probes led to alteration in the hydrophobic-hydrophilic balance resulting in non-specific aggregation in 2% DMSO-Tris HCl buffer (Figure 4.1I-L). Hence, we investigated their co-assembly with the host peptide amphiphiles ***L*-1** and ***D*-1**.

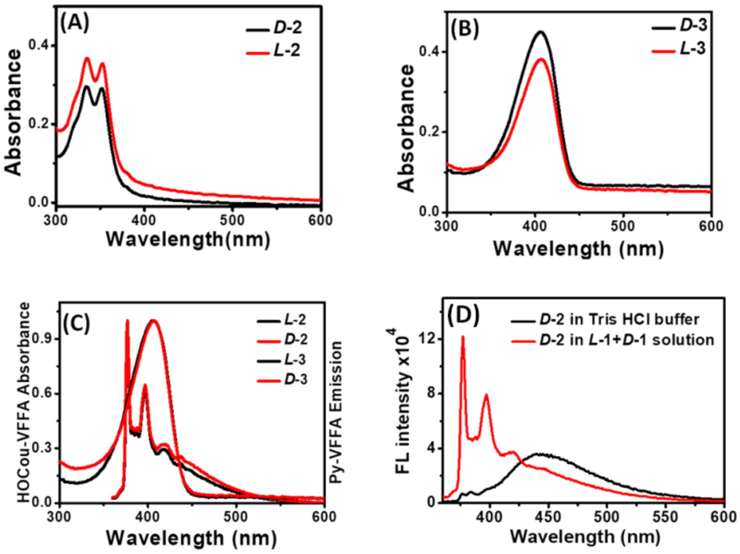

Figure 4.5: UV spectra of fluorescent peptides in Tris-HCl buffer (pH = 7.4) (A) Pyrene based donor probe (***L*-2** and ***D*-2**), (B) hydroxycoumarin based acceptor probe (***L*-3** and ***D*-3**) (10 μM) (stock was prepared in DMSO). (C) Overlap between the emission spectra of pyrene donor probe (***L*-2** and ***D*-2** in ***L*-1** and ***D*-1** peptide solution respectively) and absorbance spectra of the hydroxycoumarin accepter probe *(**L*-3** and ***D*-3** in ***L*-1** and ***D*-1** peptide solution respectively). This demostrates the probes to be perfect FRET pair with a forster radius of 3.9 nm.[59] Pyrene excimer peak for ***D*-2** in Tris-HCl buffer at 430-480 nm in the absence of host peptide and characteristic monomeric pyrene peak for ***D*-2** in the range of 375-410 nm in the presence of host peptide solution of ***L*-1** and ***D*-1**.

The emission spectrum of Py-VFFA (as in ***L*-2** and ***D*-2**) and the excitation spectrum of HCou-VFFA (as in ***L*-3** and ***D*-3**) showed a substantial spectral overlap, necessary for the FRET process with pyrene as donor and hydroxycoumarin as acceptor (Figure 4.5).[50] It also confirmed that the introduction of the fluorescent probes into the *VFFA* moiety did not result in any change in the optical properties of the fluorophores. We envisaged the investigation of the chirality-driven self-sorting or co-assembly of the peptides using FRET as an efficient tool to understand and quantify the phenomena. The pyrene probe molecules (***L*-2** and ***D*-2**) were found to be more or less randomly dispersed in the micelles of the corresponding amphiphiles (***L*-1** and ***D*-1**), since a band due to the excited-state pyrene dimers (typical $\lambda_{max} \approx 480$ nm) was absent when less than 2 mol% (relative to ***L*-1** or ***D*-1**) of ***L*-2** or ***D*-2** was added (Figure 4.5D). In a binary solution mixture of ***L*-1** and ***D*-1** nanofibers in Tris-HCl buffer (pH = 7.4), when donor and acceptor probes with *D* chirality were introduced, both these probes would confine into the homochiral assembly of host ***D*-1** peptide, leading to an increase in the FRET intensity (Figure 4.6A-B). The increased energy transfer is attributed to the increased fraction of HCou (acceptor) that is within a few nanometers of Py. Upon excitation of the Py donor at 347 nm in binary solution mixture of ***L*-1** and ***D*-1** containing ***D*-2** and ***D*-3**, an increase in wavelength at 450 nm with a concomitant decrease at 375-420 nm was observed. The corresponding excitation spectra ($\lambda_{em} = 450$ nm) accounts for an efficient FRET process arising from pyrene and HOCou moieties (Figure 4.7). Upon increasing the percentage of the acceptor, ***D*-3** the FRET intensity gradually increased and indicated an efficient homochiral co-assembly of ***D*-1, *D*-2** and ***D*-3** in a binary mixture of ***L*-1** and ***D*-1** host nanofibers. However, for the donor and acceptor probes having opposite chirality in the binary mixture, they would rather confine into their respective host peptides to provide two self-sorted homochiral assemblies. Thus, a mixture of ***L*-1** and ***D*-1** host nanofibers containing ***D*-2** and ***L*-3** fluorophores, upon excitation at $\lambda_{ex} = 347$ nm, did not result in a significant increase in the FRET intensity monitored at the wavelength of 450 nm. This indicated a chirality driven self-sorting to result different homochiral yet self-sorted assemblies of ***D*-1**/***D*-2** and ***L*-1**/***L*-3**, thereby, rendering the donor-acceptor probes to be distant enough for successful energy transfer. The extent of self-sorting efficiency was calculated to be 84%. However, interestingly on heating and vortexing the solution, the self-sorting efficiency was found to decrease, indicating the kinetic nature of the self-sorting process. Such behavior is similar to the reports showing the transition of pleated sheet to rippled β-sheet formation.[40-41]

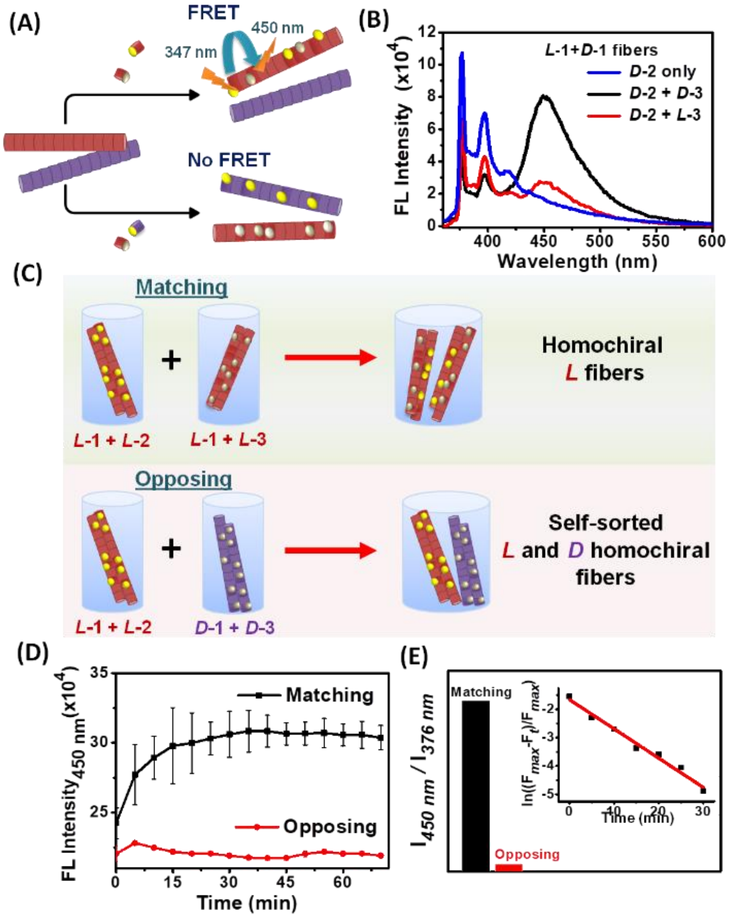

Figure 4.6: (A) Schematic representation of FRET studies involving mixture of peptide nanofibers containing fluorescence probes. Red and purple colors represent ***L*-1** and ***D*-1** enantiomeric peptide nanofibers respectively. The arrows show introduction of matching chirality (***L*-2** and ***L*-3**, above) and opposing chirality (***D*-2** and ***L*-3**, below) donor-acceptor probes. (B) Changes in the emission spectra of the mixture of ***D*-1** and ***L*-1** peptides (50 µM each) in Tris-HCl buffer (pH = 7.4) containing 0.25 µM ***D*-2** (Blue trace); FRET intensity increases upon adding matching probe ***D*-3** (Black trace) and marginal increase in intensity upon adding opposing ***L*-3** (Red trace) (Note: direct emission of acceptor probe was subtracted from each graph). (C) Schematic representation of mixing experiment for homochiral *L* peptides (***L*-2** in ***L*-1** and ***L*-3** and ***L*-1**) denoted as matching and segregated *L* & *D* homochiral fibers (***L*-2** in ***L*-1** and ***D*-3** in ***D*-1**) as opposing (peptide: probe = 200:1). (D) Time dependent change in the fluorescence intensity at 450 nm; probes of matching chirality (black trace), probes of opposing chirality (red trace). (E) Bar diagram showing difference in FRET ratio for matching and opposing mixing. Inset shows first order kinetics of mixing for matching case (R^{2} = 0.98).

Furthermore, the difference in the self-sorted and co-assembled supramolecular polymerization processes was investigated using time-dependent fluorescence spectroscopy. Fluorescent probe ***L*-2** (0.25 µM) was taken in ***L*-1** host peptide (100 µM) and mechanically agitated to form homochiral donor probes-peptide nanofibers. Similarly, ***L*-3** (0.25 µM) was taken in ***L*-1** (100 µM) to form homochiral acceptor probes-peptide nanofibers (Figure 4.6C). After incubating both the homochiral nanofibers for 2 days at room temperature, equal volumes of these two solutions were mixed without agitation and emission spectra were monitored over time. The peak intensity at 450 nm was found to increase with time followed by reaching saturation within 30 min (Figure 4.6D). The rate constant ($k = 1.73 \times 10^{-3}\ s^{-1}$) with reasonably fast timescale indicates a diffusion controlled process for probe doped nanofibrils across the homochiral peptide nanofibers to bring the pyrene-hydroxycoumarin probes in close proximity.[51] However, for the mixing of ***D*-3** (0.25 μM) in ***D*-1** host peptide (100 μM) and ***L*-2** (0.25 μM) in ***L*-1** host peptide (100 μM), the fluorescence emission intensity at 450 nm did not show any change with time. This suggests that the probes remain inside their respective homochiral peptide nanofibers to form self-sorted peptide nanofibers, until they were mechanically agitated.

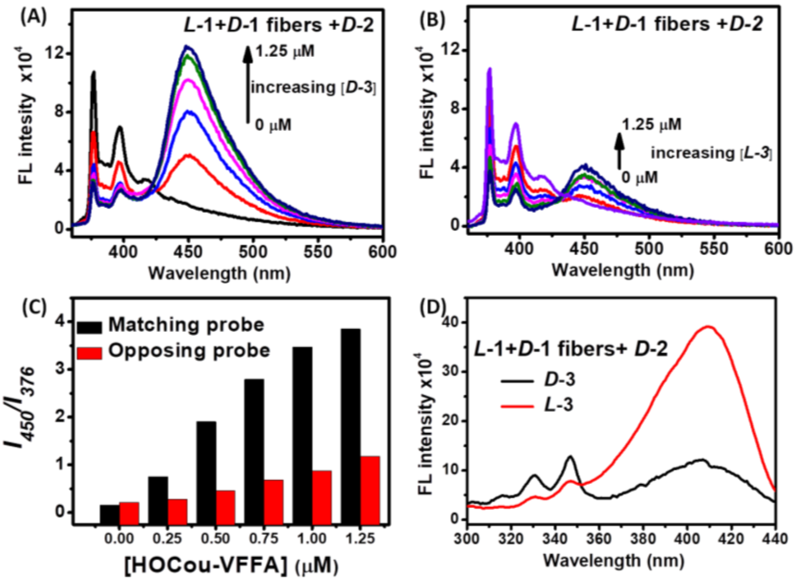

Figure 4.7: Changes in the emission spectra of of ***L*-1** and ***D*-1** peptide nanofibers solution (50 μM each) in Tris-HCl buffer (pH = 7.4); adding 2 μL ***D*-2** (50 μM). (A) Homochiral case; increasing amount of ***D*-3**. (B) Heterochiral case; increasing amount of ***L*-3**. (Note: direct emission of hydroxycoumarin probe was subtracted from each graph) (C) FRET ratio (I_{450}/I_{376}) is increasing with acceptor concentration with significant difference in homochiral and heterochiral cases with matching and opposing chiral probes respectively. (D) The corresponding excitation scan with emission wavelength of 450 nm.

The peptides with an amyloid nucleating sequence can undergo nucleation-elongation process to form nanofibers.[47] The polydispersed fibers from ***L*-1** were probe-sonicated for 5 min to obtain short uniform nanofibers (seeds) (L_n = 135 nm) with a reasonably narrow polydispersity index (PDI) (Figure 4.8C). The peptide amphiphiles taken in 10 v/v% HFIP-water exhibited formation of metastable nanoparticles as a result of solvent mediated trapping of the spontaneous self-assembly process.[47] For a typical homochiral seeding experiment, ***L*-1** seeds and the nanoparticles of ***L*-1** at a ratio of 1:1 were incubated to grow unagitated for 24 h (Figure 4.8A). The AFM images analyses showed that the growth of the ***L*-1** seeds to resulted in an almost doubling of the length of the fiber length (L_n = 269 nm) (Figure 4.8B). The cross-seeding experiment involving the incubation of the ***L*-1** fiber seeds with the ***D*-1** nanoparticle showed a bimodal distributions of fiber lengths with one length regime matching with the dimension of ***L*-1** fiber seeds suggesting ineffective cross-seeding. However, the presence of the long fibers indicated eventual inherent growth of ***D*-1** fibers after 1 day (Figure 4.8D).These experiments were performed upto two cycles with grown fibers from first cycle becomes seeds and incubated with fresh ***L*-1** or ***D*-1** nanoparticle exhibiting growth of seeds with matching chirality but not in non-matching case (Figure 4.9).

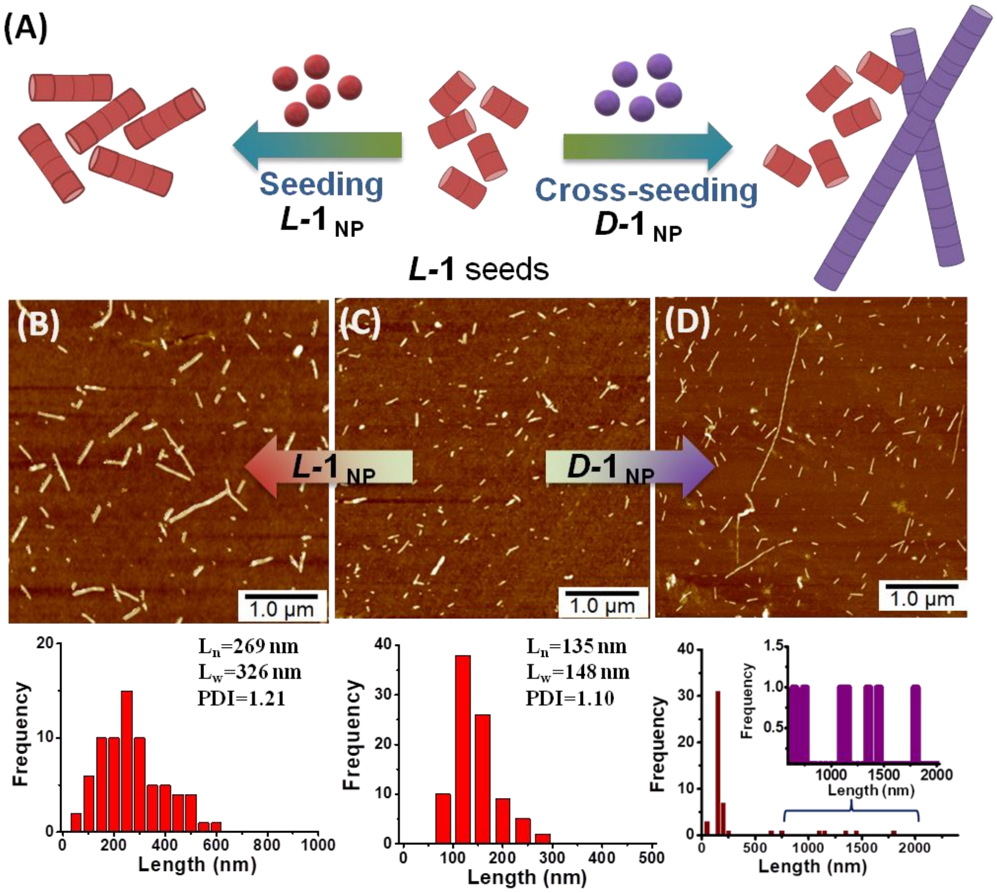

Figure 4.8: (A) Color coded schematic diagram of seeding and cross-seeding experiments involving the seeds and metastable nanoparticles (NPs). (B) AFM images recorded after 24 h of incubating the ***L*-1**$_{\text{NP}}$ to ***L*-1** seeds; (C) seeds of ***L*-1** and (D) seeds of ***L*-*1*** with ***D*-1**$_{\text{NP}}$. AFM images were recorded after 24 h at RT (10 µM). (E) Bimodal length distribution of the cross-seeded system ***L*-1** seeds/***D*-1**$_{\text{NP}}$.

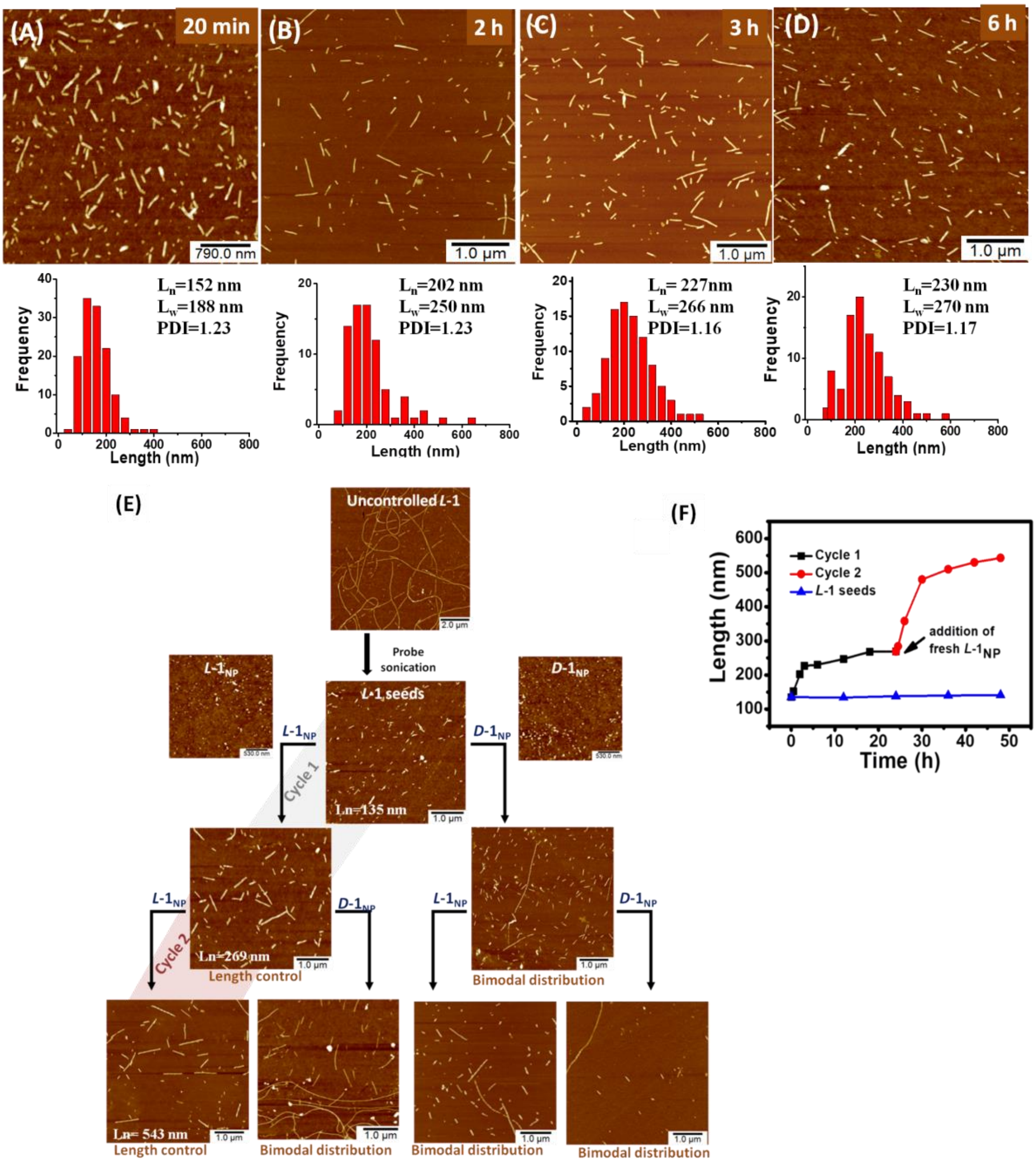

Figure 4.9: AFM height images and histogram length analyses for (A) ***L*-1** seeds and incubated ***L*-1** seeds with metastable nanoparticles of ***L*-1** and monitored after (A) 20 min, (B) 2 h, (C) 3h and (D) 6 h. (E) Seeding (***L*-1** seeds/***L*-1** monomer) and cross-seeding (***L*-1** seeds/***D*-1** monomer) experiment monitored through AFM images show orthogonal assembly in heterochiral system and living nature of seeds for homochiral case. (F) Growth of ***L*-1** fiber seeds upon sequencial addition of ***L*-1** monomer.

Next, nucleation-elongation kinetics of the peptide fibers was monitored by ThT fluorescence in a continuous assay. The ***L*-1** or ***D*-1** seeds were added to a freshly prepared solution of the corresponding enantiomers in 10 v/v% HFIP-water. The growth of the fibers as observed by monitoring change in intensity of ThT fluorescence at 480 nm ($\lambda_{ex} = 440$ nm) with time. Addition of fresh peptide solution of the same chirality as of seeds did not display any lag phase, thereby confirming a homochiral seed-mediated growth (Figure 4.10). However, a significant lag phase was observed in the case of seeds with reciprocal chirality similar to unseeded growth (Figure 4.10), thereby confirming the enantioselectivity of the seed-mediated growth. However, probe sonicated seeds of ***L*-1** and ***D*-1** did not show change in fluorescence intensity with time, suggesting the inability of seeds to grow on their own with time and absence of secondary nucleation process.

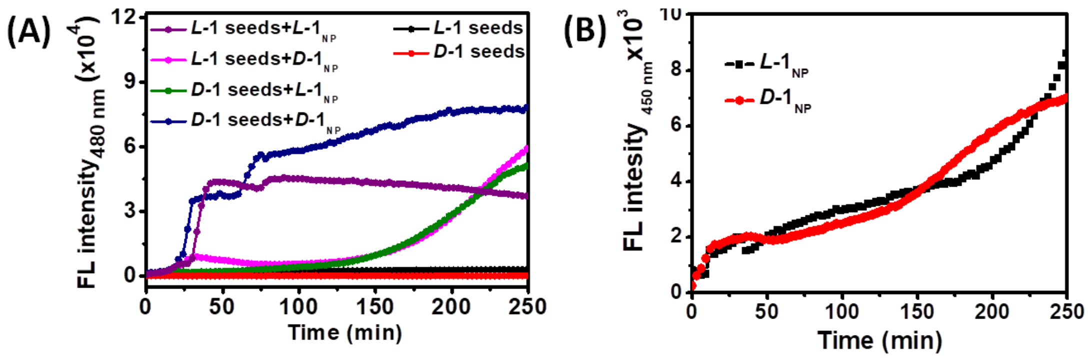

Figure 4.10: (A) Seeded growth with enantioselective seeds and freshly dissolved ***L*-1**$_{\mathbf{NP}}$ for ***L*-1** seeds/***L*-1**$_{\mathbf{NP}}$ and ***D*-1** seeds/***D*-1**$_{\mathbf{NP}}$ shows no ‘lag’ time (100 µM). Cross seeded Solutions of ***L*-1** seeds/***D*-1**$_{\mathbf{NP}}$ or ***D*-1** seeds/***L*-1**$_{\mathbf{NP}}$ shows ‘lag’ period. Kinetics was monitored by binding of fluorescent ThT dye (0.4 µM) (B) Growth of freshly dissolved solution of peptide amphiphiles (metastable nanoparticles) in 10 v/v% of HFIP-water (concentration = 100 µM).

With the self-sorted chiral supramolecular nanofibers (***L*-1/*D*-1**) in hand, we next sought to directly visualize these orthogonal fibres by confocal laser scanning microscopy (CLSM) and super-resolution structured illumination microscopy (SR-SIM). For this purpose, two distinct fluorescent labels that could selectively stain the individual fibers for visualization were employed. Thus, rhodamine-B isothiocyanate (RBITC) tethered *D* peptide (***D*-4**) and fluorescein isothiocyanate (FITC) tethered *L* peptide (***L*-5**), having ^{N}VFFA^{C} sequence were designed (Scheme 4.1). The host peptide solutions containing the fluorophores were drop casted on a glass slide to record CLSM and SR-SIM images in green channel I (Ex-488 nm) and red channel II (Ex-561 nm) respectively. Thus, ***L*-5** stained nanofibers of ***L*-1** appeared as green, but these structurally defined nanofibers were not observed at all when ***L*-5** was incubated with ***D*-1** peptides (Figure 4.11). In contrast, ***D*-4** probe stained the ***D*-1** fibers as red, but not ***L*-1** fibers. As expected, SIM images demonstrated the enantioselective staining of the fibers with greater clarity and could clearly be visualized down to a structural feature of ~123 nm (Figure 4.12). Moreover, Figure 4.13 show the SIM images of the four-component (***L*-1, *L*-5, *D*-1** and ***D*-4**) mixture that indicate the presence of orthogonal green and red fibers as visualized using channel I and channel II. The merged images show that the homochiral green fiber (**_L_-1/_L_-5**) and red fibers (**_D_-1/_D_-4**) do not overlap throughout the area. The cross-section intensity profile plot of the fluorescence signatures establishes the presence of completely self-sorted nanofibers with a Pearson correlation coefficient value of 0.31 indicated almost no correlation between the red and green fibers (Fig. 4F).[53-56] This is the first example of direct visualization of chirality-driven self-sorted peptide fibers.

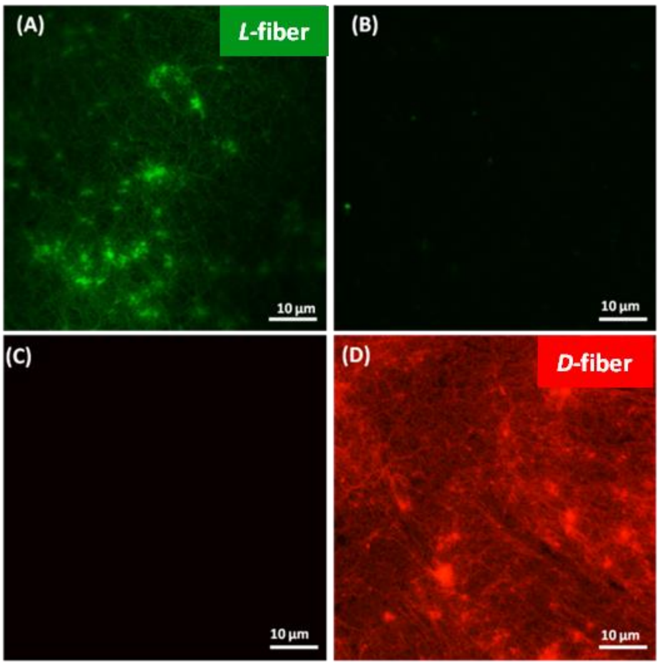

Figure 4.11: Confocal images of single-component fibres **_L_-1** (A) stained with **_L_-5** (B) **_D_-4**, (C) **_D_-1** stained with **_L_-5** and (D) **_D_-4** [peptide] = 1mM, [probe] = 1.5 µM. The green and red images were acquired in 488 and 561 channels, respectively. The selective staining indicated on homochiral peptide probe stacks.

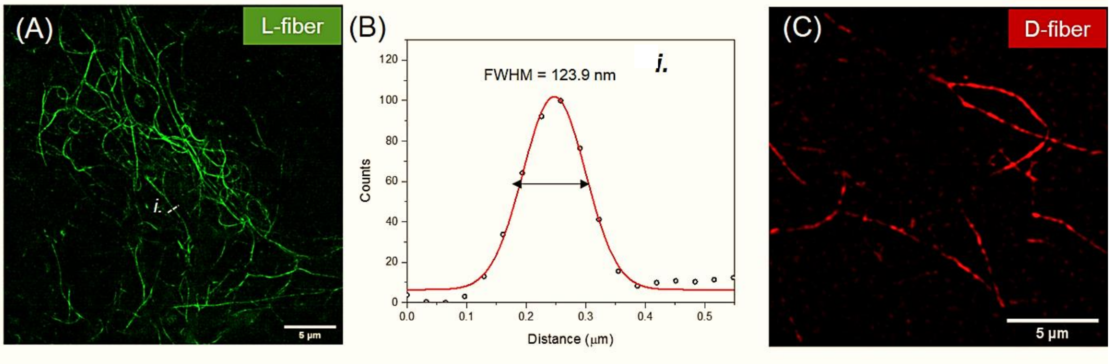

Figure 4.12: Super-resolution structured illumination microscopic images of self-assembled fibers stained with fluorescent probe (A) **_L_-1** stained with **_L_-5** (C) **_D_-1** stained with **_D_-4** [peptide] = 40 µM, [probe] = 0.4 µM. (B) The diameter of the selected single green fiber (*i*) has been shown to be ~ 123 nm by SIM method. The green and red images were acquired in 488 and 561 channels, respectively.

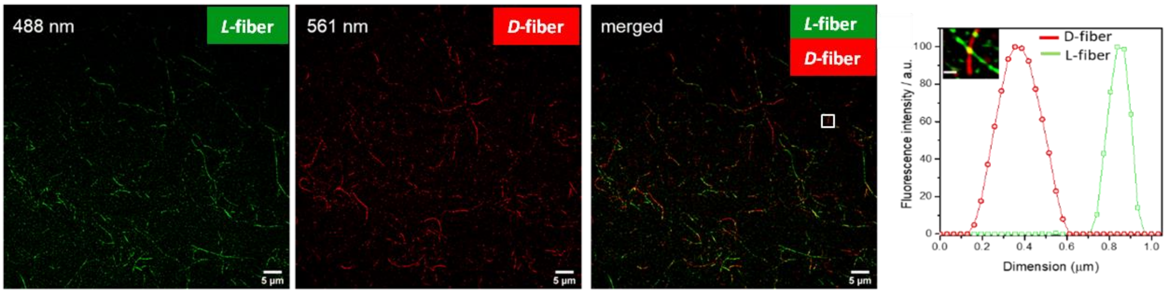

Figure 4.13: Visualization of self-sorted fibers of ***L*-1** and ***D*-1** in four-component system (***L*-1**, ***L*-5**, ***D*-1** and ***D*-4**) with images collected from channel I (488 nm), channel II (561 nm) and the merged channels I and II. Plot of fluorescent intensity along the white lines drawn in the merged images (inset). [Peptide] = 40 µM, [probe] = 0.4 µM. Scale bar 10 µm 500 nm (inset).

Furthermore, the proteolytic enzyme responsiveness of the self-sorted fibers was investigated upon incubating the fibers with chymotrypsin in phosphate buffer saline (pH = 7.4) at 45 ºC for 5 h (peptide**:**enzyme = 100**:**1). The detailed HPLC-MS study confirmed the selective degradation of the *L*-peptides at the C-termini of phenylalanines to result new peaks at 24 & 26 min accounting for fragmented peptides, while the *D*-peptides were stable under the same condition (Figure 4.14), in corroboration with literature report.[57-58] SIM images for the green fiber (***L*-1**/***L*-5**) showed the disappearance of fiber morphologies after 5 h of incubation with chymotrypsin, while the red fibers (***D*-1**/***D*-4**) showed proteolytic stability (Figure 4.15 and 4.16).

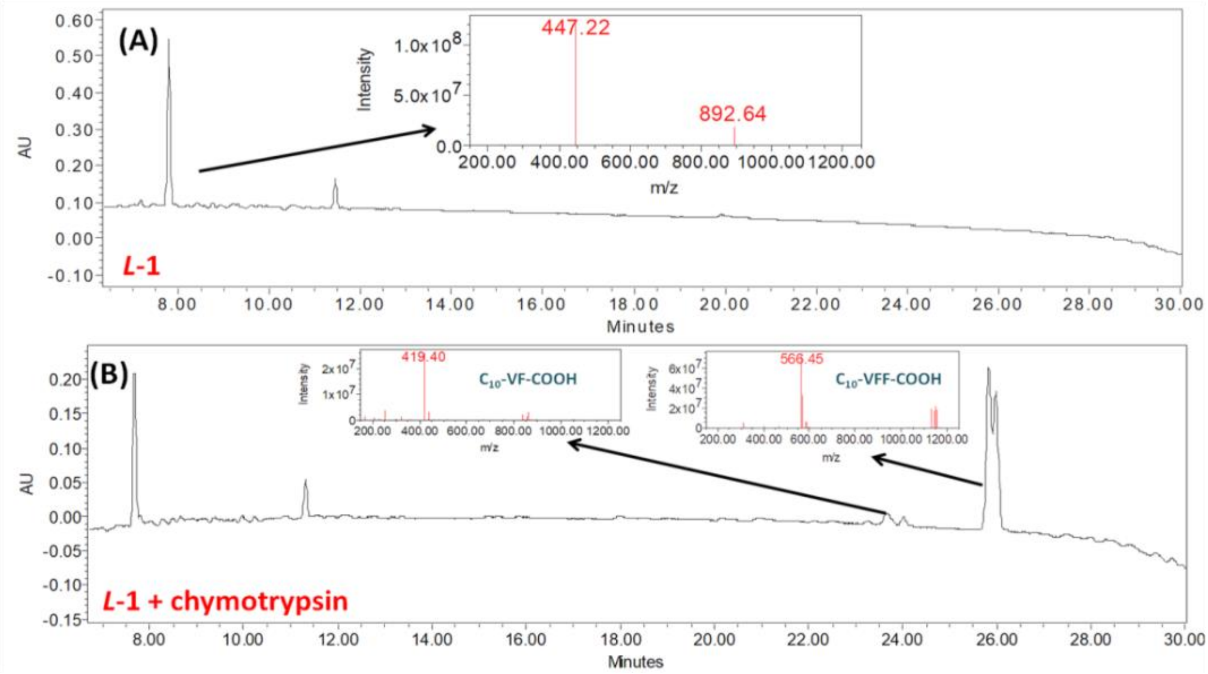

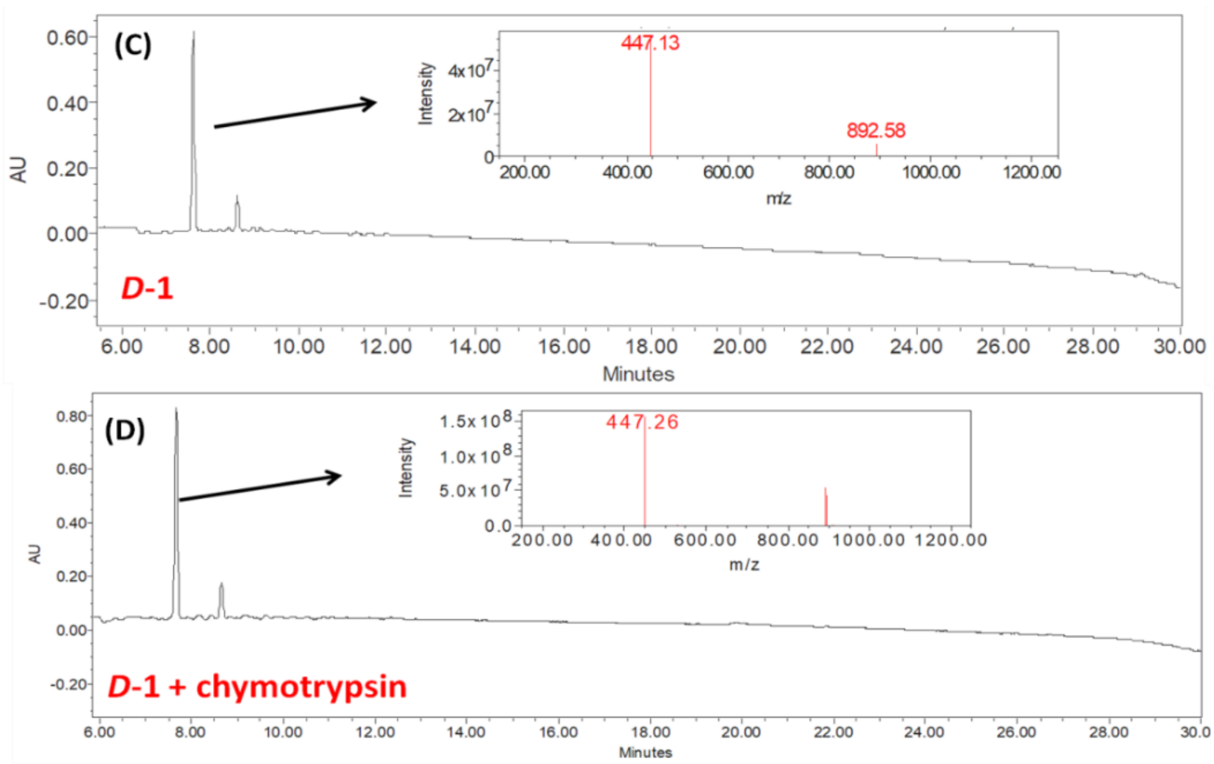

Figure 4.14: HPLC traces of ***L*-1** peptide (A) before and (B) 5 h after adding chymotrypsin showing peptide degradation. Mass traces of the peak at 26 min and 24 min shows presence of fragent accounting for amide bond breakage at the C-termini of phenylalanines (inset). HPLC traces of ***D*-1** peptide (A) before and (B) 5 h after adding chymotrypsin showing proteolytic stability for the ***D*-1** peptide. Peptide**:**enzyme = 50**:**1 incubated in PBS (pH = 7.4) at 37 ºC for 5 h.

Next, the addition of the enzyme onto the four component mixture, led to a gradual disappearance of green *L*-peptide fibers with the red fiber remaining unchanged. Noticeably, the otherwise self-sorted (with weak correlation value) fibers started showing good correlation in the merged channel (Figure 4.15C & 4.17). This suggested the enzyme mediated proteolysis for ***L*-5** fluorophores, resulting in negatively charged fragments (Figure 4.18), which in turn interact with the positively charged red *D*-fibers (***D*-1**/***D*-4**) electrostatically, resulting a high correlation coefficient (0.57). The hydrogels from ***L*-1** and ***D*-1** (10 mM) were incubated with chymotrysin at 37 ºC for variable time periods and the mechanical strength was ascessed using frequency sweep oscillatory rheology measurements (Figure 4.19). The elastic moduli of the ***L*-1** hydrogel was found to gradually decrease over time, while those of ***D*-1** hydrogel did not exhibit any significant changes, confirming the enantioselective enzymatic degradation in corroboration with the HPLC-MS data.

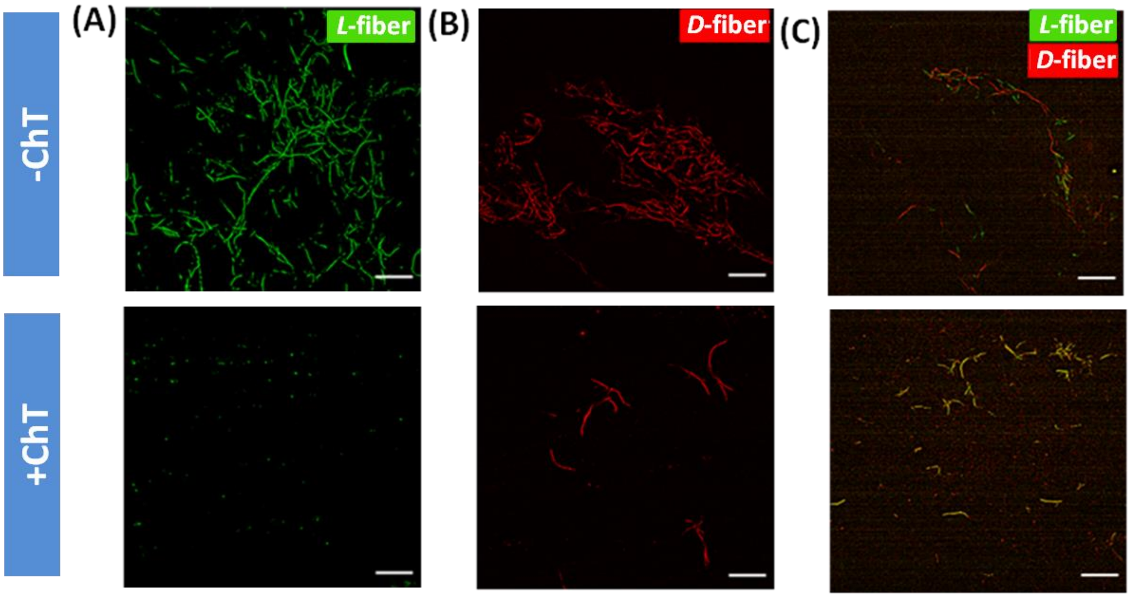

Figure 4.15: Enantioselective response upon proteolytic disassembly of peptide fibers. Left and right panels are peptide fibers without and with chymotrypsin. (A-B) SIM images for single component ***L*-1** fibers with ***L*-5** probe and ***D*-1** fibers red ***D*-4** probes without and with chymotrypsin in phosphate buffer saline (pH = 7.4) at 45 °C for 5 h (Peptide: Enzyme = 100:1). (C) SIM images for the self-sorted fibers of four-component system (***L*-1, *L*-5, *D*-1** and ***D*-4**) without and with chymotrypsin collected from the merged channels I and II. It exhibit good correlation of the green and red fibers post enzyme treatment. Scale bar 10 µm (A-C).

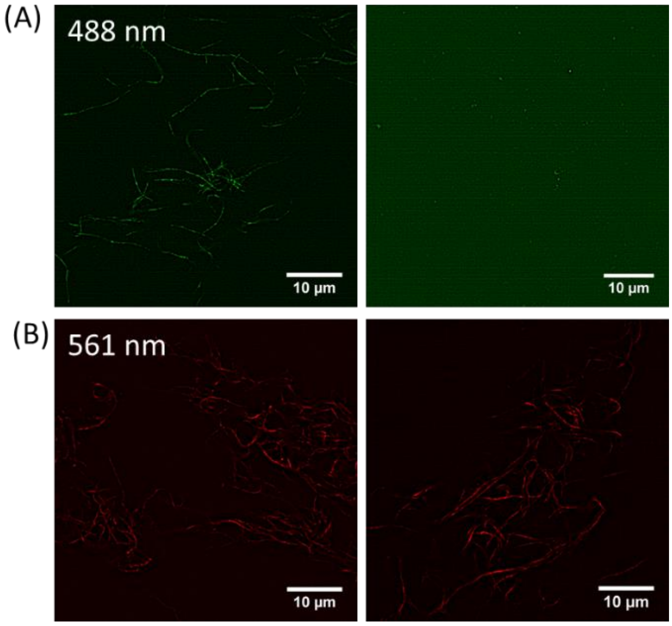

Figure 4.16: (A) SIM images of self-assembled ***L*-1** fibers stained with green fluorescent probe ***L*-5** incubated without (left) and with (right) chymotrypsin for 5 h in PBS (pH = 7.4) at 37 °C (Upper panel show images acquired in green channel, 488 nm). Upper right images does not show any nanofibers in green channel, suggesting complete degradation of the *L*-peptides. (B) SIM images of self-assembled ***D*-1** fibers stained with red fluorescent probe ***D*-4** incubated without (left) and with (right) chymotrypsin for 5 h in PBS (pH = 7.4) at 37 °C. Lower right image shows presence of red fibers indicating proteolytic stability *D*-peptides. Peptide**:**enzyme = 100**:**1.

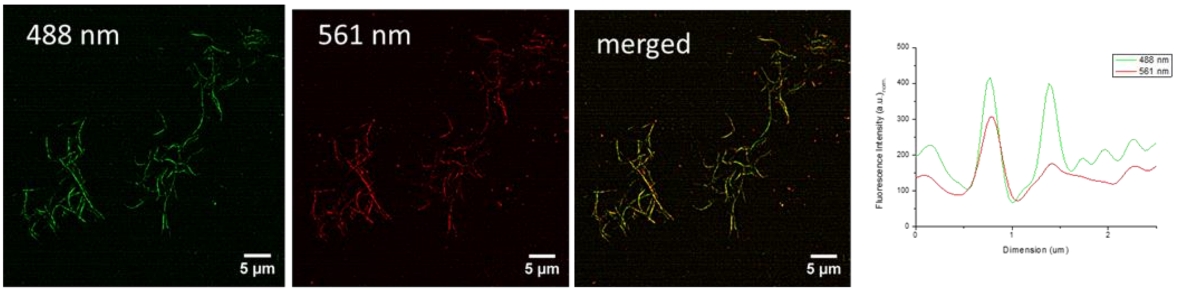

Figure 4.17: SIM images of four component system containing self-sorted ***D*-1** fibers stained with red fluorescent probe ***D*-4** and ***L*-1** fibers stained with green fluorescent probe ***L*-4** after incubating with chymotrypsin for 5 h in PBS (pH = 7.4) at 37 °C. Peptide: enzyme = 100**:**1. (A-D) show images acquired in green, red, merged channel and fluorescent intensity for the ***D*-1** fibers with green ***D*-4** in absence and in presence of chymotrypsin.

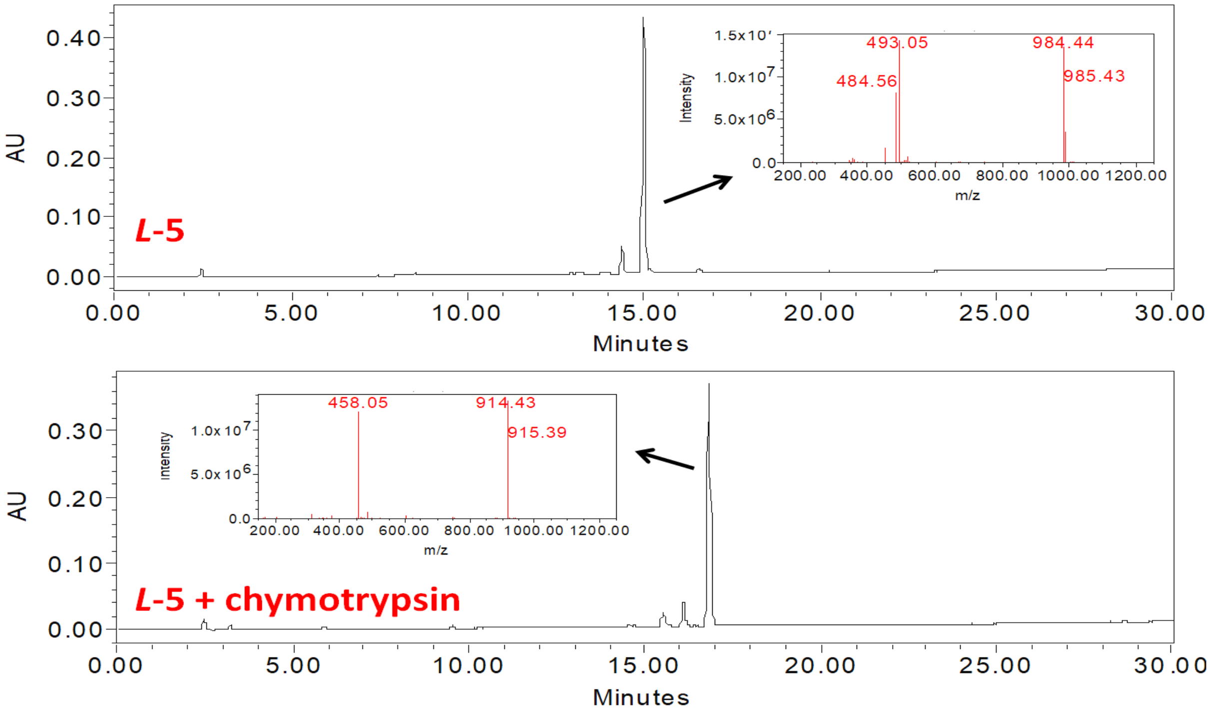

Figure 4.18: HPLC traces of ***L*-5** peptide (A) before and (B) 5 h after adding chymotrypsin showing peptide degradation. Inset of A shows mass trace for the peak at 15 min for ***L*-5** peptide. Inset of (B) shows mass traces of the peak at 17 min shows presence of fragent accounting for amide bond breakage at the C-terminus of phenylalanine (deleting one alanine amino acid).

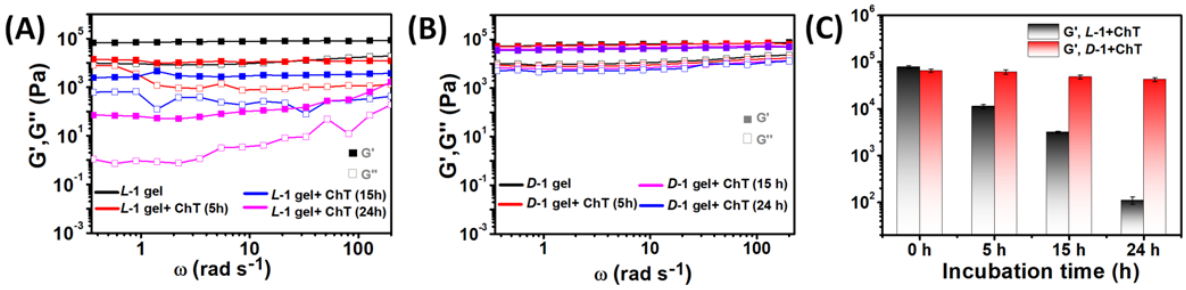

Figure 4.19: Oscillatory frequency sweep measurements for the hydrogels from (A) ***L*-1** and (B) ***D*-1** amphiphiles upon incubation with chymotrypsin for 0, 5, 15 and 24 h at 37 ºC in phosphate buffer of pH 7.4. (C) Bar diagram demonstrates the gradual decrease in G' values for ***L*-1** hydrogels while G' values for ***D*-1** hydrogels stayed almost unchanged upon chymotrypsin mediated enantioselective hydrogel degradation. [Peptide]: [Enzyme] = 100:1 peptide concentration = 10 mM.

4.3. Conclusions

In summary, we have reported a minimalistic peptide amphiphile pair that demonstrates chirality-driven self-sorting to render segregated enantiomeric nanofibers in water. We have demonstrated the fidelity of the self-sorted system by utilizing structurally similar chiral FRET pairs, which was further validated with the seeding and cross-seeding methodologies. Moreover, for the first time, we have directly visualized the chirality-driven self-sorted peptide nanofibers utilizing a super-resolution SIM technique which exhibited orthogonal self-assembly with respect to structure and function. Finally, we have shown enantioselective hydrolysis of the *L*-fibers over *D*-fibers for the first time by super-resolution microscopy. This results in enantioselective weakening of the hydrogel strength and may potentially be used for stimuli-responsive hydrogel mediated drug delivery applications in future. We postulate that the present study provides a deeper understanding of self-sorting events and may have implications in the design of mutually orthogonal functional biomimetic supramolecular systems. It is noteworthy to mention that our minimalistic peptide is an interesting system to understand the self-assembly of β-sheet forming enantiomeric peptides. The peptide consists of nonpolar (VFFA) and polar (KK) domains. For homochiral self-sorting events, the side chains of adjacent peptides in β-sheet arrangement will be pointing in the same direction. The nonpolar domain favours this arrangement owing to the hydrophobic and aromatic interactions among side chains. On the other hand, for heterochiral coassembled nanofibers, the side chains of adjacent peptides fall in opposite directions. The charged lysine side chain would prefer to experience minimum electrostatic repulsion as possible in heterochiral assemblies. However, amyloid inspired nonpolar domain is mainly responsible for β-sheet secondary structure resulting in homochiral self-sorted nanofibers. Such enantioselective nanofiber formation in our model peptide is similar to enantioselective fiber growth reported in β2-microglobulin and β-amyloid proteins.

4.4. Experimental section

4.4.1. Materials

All the reagents and amino acids were purchased from Sigma or TCI; standard amino acids with *L* and *D* configuration were either purchased directly or synthesized as protected Fmoc amino acids with the standard side chain protection with >99% chiral purity.[60] Hexafluoro isopropanol (HFIP), Pyrene butyric acid, Fluorescein isothiocyanate (FITC) and Rhodamine B isothiocyanate (RBITC) were also purchased from Sigma and 7-hydroxy carboxylic acid was synthesized with already reported procedure.[61] Chymotrypsin of bovine pancreatic origin (type II, protein composition ≥ 85%) was purchased from Sigma-Aldrich. C-terminal amide peptides and fluorescent probes were synthesized on a 0.1 mmol scale using Fmoc-Rink Amide MBHA resin (0.52 mmol/g loading) from NovaBiochem (EMD Millipore). All solvents were either synthesis or analytical grade and Milli-Q water was used throughout the studies.

4.4.2. Synthesis and characterization of peptides

Peptides and fluorescent probes were synthesized on rink amide MBHA resin at 0.1 mmol scale following standard microwave Fmoc-solid phase peptide synthesis (SPPS) protocols. Amino acids were coupled using diisopropyl carbodiimide (DIC) and oxyma in dimethylformamide (DMF). Fmoc deprotection was performed with 20% piperazine in DMF (containing 10% ethanol) in the microwave at 75 °C. Resin bound peptide was filtered, washed with DMF and dichloromethane and allowed to dry. The peptides were cleaved from the resin using 10 mL of cleavage cocktail mixture (trifluoroacetic acid (TFA)/triisopropylsilane (TIPS) / Water (95: 2.5: 2.5, v/v/v)). The mixture was shaken for 3 h at room temperature followed by removal of the resin through filtration and the filtrate was concentrated to a volume of approximately 1 mL. The resultant residue was precipitated by dropwise addition of ice cold diethyl ether. The precipitated product was centrifuged for 15 min at 7000 rpm at 4 °C. The precipitates were washed 3 times with cold diethyl ether and air dried. For the synthesis of ***D*-4** and ***L*-5** probes, VFFA peptidyl-resins were coupled with Fmoc- amino hexanoic acid and were reacted with Rhodamine B isothiocyanate (RBITC) and Fluorescein isothiocyanate (FITC) respectively in excess of DIPEA.[62] The peptides (***L*-1** and ***D*-1**) were re-dissolved in CH_3CN/H_2O (1:9) to analyse the purity of peptides by reverse phase HPLC with mobile phase acetonitrile and water containing 0.1% formic acid. To alleviate the chances for self-assembly during HPLC purification, the peptides in powder form were dissolved in HFIP and dried once again. The solid residue of fluorescent probes (***L*-2**, ***D*-2**, ***L*-3**, ***D*-3**, ***D*-4** and ***L*-5**) were re-dissolved in DMSO and confirmed by ESI-MS and stored at -20°C. The standard gradient used for analytical HPLC for both peptides (***L*-1** and ***D*-1**) was 5 → 95%CH_3CN in H_2O (0.1% HCOOH additive) with a flow rate of 1 mL/min over 30 min. Injection volume for ***L*-2**, ***D*-2**, ***L*-3** and ***L*-3** is 5 μL (1 mM) with gradient method 70 → 95%CH_3CN in H_2O (Additive 0.1% HCOOH) over 15 min.

***D*-1:** Calculated exact mass for $C_{48}H_{77}N_9O_7$ = 891.59, In positive mode: found $[MH^+]$ = 892.78, $[MH_2]^{2+}$ =447.08. Purity: 98 %

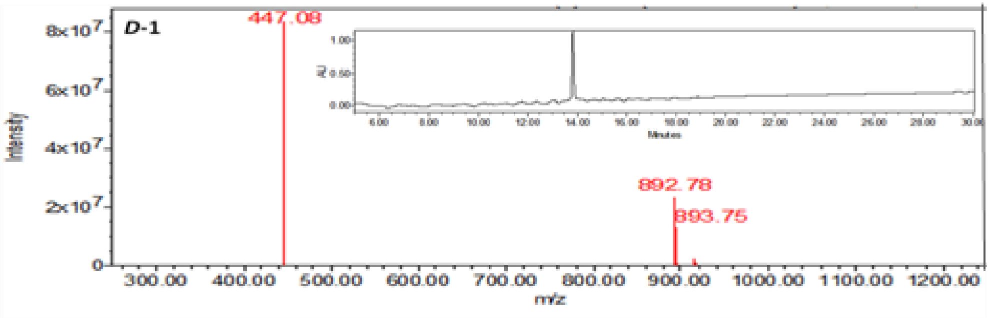

***L*-1:** Calculated exact mass for $C_{48}H_{77}N_9O_7$ = 891.59, In positive mode: found $[MH^+]$ = 892.74, $[MH_2]^{2+}$ =447.05. Purity: 98 %

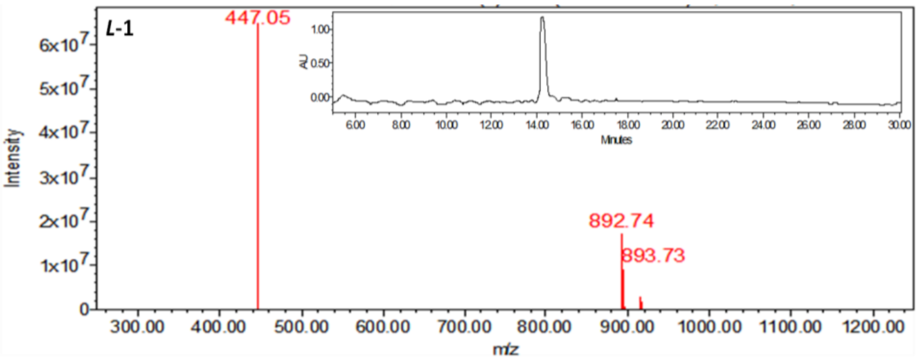

***D*-2:** Calculated exact mass for $C_{46}H_{49}N_5O_5$ = 751.37, In positive mode: found $[M+Na]^+$ = 774.69. Purity: 92 %

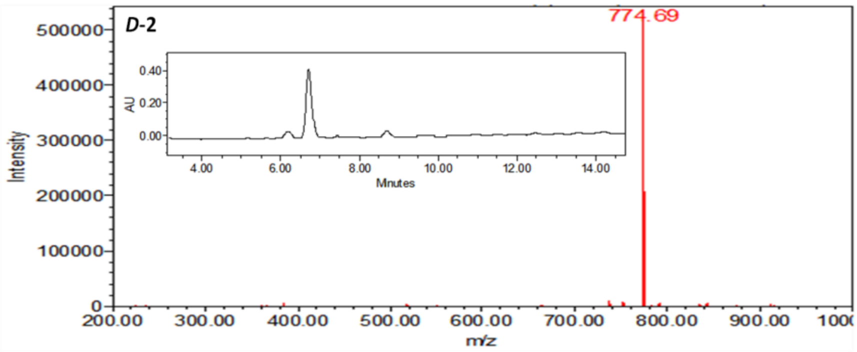

***L*-2:** Calculated exact mass for $C_{46}H_{49}N_5O_5$ = 751.37, In positive mode: found $[M+Na]^+$ = 774.72. Purity: 93 %

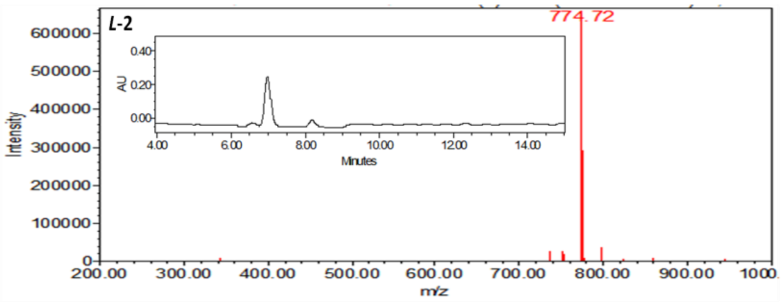

D-3: Calculated exact mass for $C_{36}H_{39}N_5O_8$ = 669.28, In negative mode found: $[M]^-$ = 668.56. Purity: 95 %

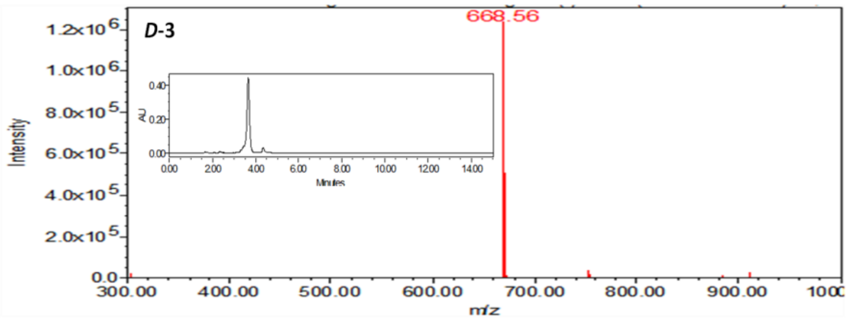

***L*-3:** Calculated exact mass for $C_{36}H_{39}N_5O_8$ = 669.28, In negative mode found: $[M]^{-=}$ 668.62. Purity: 96 %

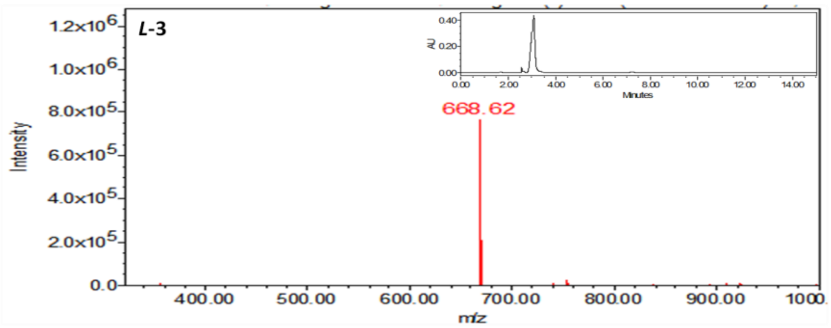

***D*-4:** Calculated exact mass for $C_{61}H_{76}N_9O_8S$ = 1095.56, In negative mode found: $[M]^{-}$ = 1094.81. Purity: 93%

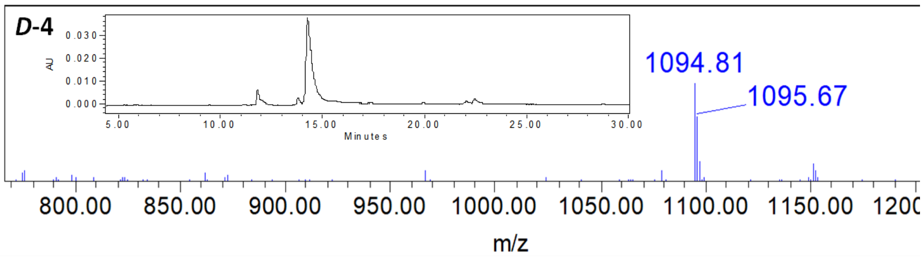

***L*-5:** Calculated exact mass for $C_{53}H_{57}N_7O_{10}S$ = 983.39, In negative mode found: $[M]^{+}$ = 982.74. Purity: 98 %

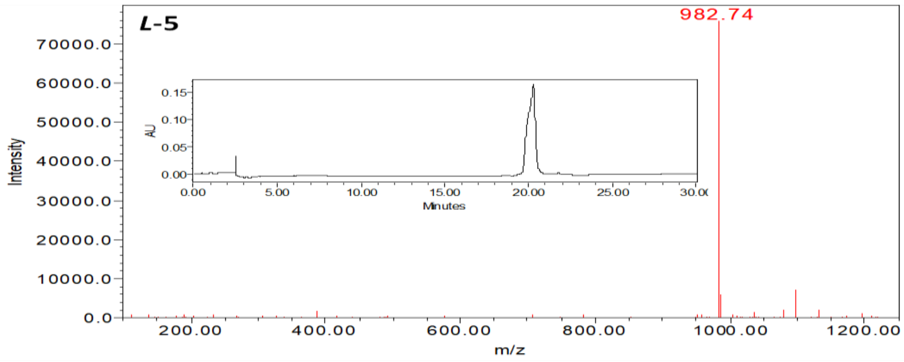

4.4.3. Self-assembly of peptides and hydrogel formation

Peptides (***L*-1** and ***D*-1**, concentration = 2 mM) were taken in water or Tris-HCl buffer (pH = 7.4) and dissolved by mechanically agitated for 1-2 min at room temperature. After incubation for a day, the formation of self-assembled peptide nanofibers mediated by hydrogen bonding and π-π interactions were confirmed by AFM and TEM images.

For hydrogel formation, peptide amphiphiles with a higher concentration (10 mM) were dissolved in sodium phosphate buffer (10 mM, pH = 7.4) by mechanical agitation. Upon incubating at room temperature for one day, the negatively charged phosphates electrostatically interact with the positively charged peptide nanofibers to render network structure to eventually form hydrogel.

Fluorescent probes were soluble in DMSO and did not form self-assembled nanostructures upon injecting DMSO stocks of the probes into Tris-HCl buffer (pH = 7.4) or water.

4.4.4. Microscopic investigation

Negative stained TEM was performed using *JEOL JEM 2100* with a Tungsten filament at an accelerating voltage of 120 kV. The sample (6 μL) was deposited on carbon coated copper grid and stained with the aqueous solution of uranyl acetate (1%; w/v) for 2 min and the excess solution was wicked off with a filter paper. The TEM grid was dried overnight under reduced pressure.

AFM imaging was performed on a *Bruker multimode 8* scanning probe microscope. 10 µL of 0.15 mM of the peptide solution was drop-casted on a silicon wafer. After 5 minutes, the silicon wafer was washed with 500 μL water using micropipette to remove excess peptide. Then the sample was dried under nitrogen. AFM height images were recorded in tapping mode with a silicon cantilever (*Bruker*) and analysed using the software NanoScope Analysis 1.5. Typical scan rates were between 0.6 - 1.0 Hz.

4.4.5. Spectroscopic Investigation

4.4.5.1. Circular dichroism spectra: CD spectra were recorded using *JASCO J-1500* Circular Dichroism Spectrometer, Easton, MD, USA. The peptide solution was added to demountable cells (0.1 mm path length, Hellma) and scanned for the wavelength range from 190 nm to 400 nm with a scan speed of 50 nm min^{-1} at 20 ºC. The reported spectra are the average of 3 scans.

4.4.5.2. Thioflavin-T binding study: Thioflavin-T (ThT) exhibits emission band at 480-500 nm upon binding to the ordered secondary structures of peptides (λ_{ex} = 440 nm). For performing experiments, 2 μL of ThT solution (50 μM DMF stock) was added to 200 μL of 0.4 mM aqueous peptide solution.

4.4.5.3. Fluorescence spectroscopy: Fluorescence emission spectra were recorded using FS5 spectrofluorometer from Edinburgh instruments. Spectrums were recorded with a scan slit and offset slit of 2 nm each with dwell time of 0.1 s at 25 °C. 100 μL solution of ***L*-1** (100 μM) and ***D*-1** (100 μM) peptide nanofibers in Tris-HCl buffer (pH = 7.4) were mixed together to render each of their final concentration of 50 μM and total peptide concentration to be 100 μM. Then 2 μL of 50 μM stock of ***D*-2** solution in DMSO was added (final concentration of fluorescent probe is 0.5 μM; ratio of peptide to probe is 200:1) and the mixture was vortexed and sonicated for 2 min in order to ensure the absence of excimer of pyrene molecule (~480 nm). The solution was excited at 347 nm and emission spectra were recorded for the range of 360-600 nm. ***D*-3** (homochiral probe) or ***L*-3** (heterochiral probe) was added to the mixture (with increasing proportions of HOCou probe) followed by vortexing and sonication for 1 min to ensure the uptake of fluorescent peptides into the host peptide nanofibers.

Förster energy-transfer efficiency (Φ_{ET}) was calculated by the following equation:

$$FRET\ Efficiency = \left(1 - \frac{F_{DA}}{F_D}\right).100\%$$

F_D is the fluorescence intensity of the donor in the absence of the acceptor; F_{DA} is the fluorescence intensity of the donor in the presence of the acceptor.

The degree of self-sorting was estimated from:

$$Self - sorting = \left(1 - \frac{Em_{Hetero} - Em_{Blank}}{Em_{Homo} - Em_{Blank}}\right).100\%$$

4.4.6. SAXS study

Small-angle X-ray scattering (SAXS) profiles obtained from kinetically controlled nanofibers of peptides were fitted with a model for non-interacting long cylinders with a cylindrical form factor with a gaussian distribution of core radius. The fitting was carried out using SASfit software. Good fits were obtained for SAXS data with the cylindrical model fit having core and shell radii of 1.5 (± 0.2) nm and 1.9 (± 0.2) nm, respectively.

The intensity formula used to describe the fit for the SAXS data was

$$I= \int K_{Cyl}\ (Q,\eta_{core} - \eta_{shell},R,L,x) + K_{Cyl}\ (Q,\eta_{shell} - \eta_{solv},R + \Delta R,L,x)^2 dx$$

Where, $_{\text{Cyl}}(Q, \Delta\eta, R, L, x) = 2\pi R^2 L \Delta\eta \left(\frac{J_1(QR\sqrt{1-x^2})\sin(QLx/2)}{(QR\sqrt{1-x^2})\, QLx/2}\right)$

Input Parameters for model core-shell long cylinder:

R: core radius of cylinder, ΔR: shell thickness, L: length of cylinder, $\Delta\boldsymbol{\eta}$: scattering contrast.

4.4.7. Measurement of kinetics of mixing for probe doped homochiral *L* nanofibers

The rate constant, *k*, for the kinetic of mixing was determined by fitting the data to the first-order equation:

$$Ln\left(\frac{F_{max} - F_t}{F_{max}}\right) = -kt$$

Where F_t and F_{max} are the fluorescence intensities at 450 nm at times *t* and the maximum value obtained after the system has reached equilibrium. The negative slope of the line provides the apparent rate constant *k*.

4.4.8. Rheological studies

Rheological investigations were performed on the peptide hydrogels using parallel plate geometry of diameter 25 mm (PP-25). The hydrogel was placed in the centre of the rheometer plate. The temperature was maintained at 25 ºC using a peltier temperature controller attached to a Julabo chiller. The frequency sweep experiments were performed using a constant strain of 0.1% in the linear viscoelastic region of frequency range from 0.01-200 rad/s to demonstrate the stability of the hydrogels. An oscillatory stress amplitude sweep experiment was performed at a constant angular frequency of 10 rad/s for the strain range 0.01 - 100 at 25 ºC to calculate the linear viscoelastic region.

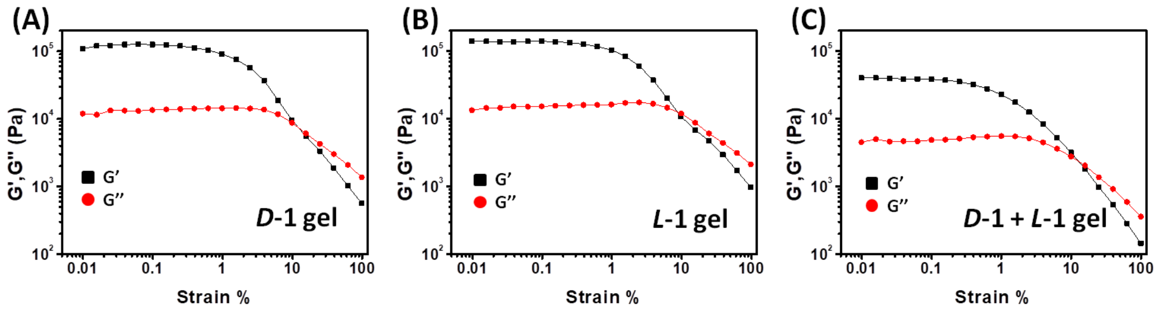

Figure 4.20: Amplitude sweep measurements for the hydrogels (A) ***D*-1** (B) ***L*-1** and (C) ***D*-1** + ***L*-1.**

4.4.9. Seeded supramolecular polymerization

4.4.9.1. Generation of Seed: 500 μL of pre-assembled nanofibrous solution of ***L*-1** (1 mM) was probe sonicated using QSonica (model number Q700, power 700 watts and frequency 20 kHz) probe Sonicator using 4417 number microtip at an amplitude of 15% for ~5 minutes. The length of peptide nanofibers was determined using Image-J Software. 100 random fibers were selected from different areas of the images and a histogram was generated by choosing bin and frequency in Microsoft Excel. The average fiber lengths and polydispersity indices (PDI) were estimated by calculating number average length (L_n) and weight average length (L_w) by the following equations:

$$L_w = \frac{\sum_{i=1}^{n} N_i L_i^2}{\sum_{i=1}^{n} N_i\, L_i}$$

$$L_n = \frac{\sum_{i=1}^{n} N_i\, L_i}{\sum_{i=1}^{n} N_i}$$

$$PDI = \frac{L_w}{L_n}$$

Where, N_i is the number of fibers and of length L_i, and n is the number of fibers examined in each sample.

4.4.9.2. Seeded growth of fibers: The peptide amphiphiles were taken in 10 v/v% HFIP-water to result in metastable nanoparticles that remain stable for 3 h. For the seeding and cross-seeding experiment, the ***L*-1** seed was incubated un-agitated with freshly dissolved peptide nanoparticles of ***L*-1** or ***D*-1** in 1:1 ratio. The growth of the fibers was ascertained from AFM image analysis and time-dependent ThT binding assay.

4.4.9.3. Seed-mediated growth studies with ThT binding: Kinetics of seed-mediated growth of β-sheet forming nanofibers was monitored by ThT fluorescence in a continuous assay. Fluorescence readings (ex. 440 nm, em. 480 nm) were performed every 3 min with shaking for 1 s between readings for experiments; FL intensity at 480 nm was monitored for up to 250 min at 25 °C. For seeding and cross-seeding experiments, each well had 50 μL of 100 μM peptide seeds, 50 μL of nanoparticle solution in 10% HFIP (100 μM) and 0.4 μM of ThT dye.

4.4.10. Fluorescence microscopy

4.4.10.1. Confocal laser scanning microscopy:

The nanofibrous solution stained with respective dye (30 μL) was drop-casted on a glass slide and covered with coverslip. The slides were kept at room temperature for overnight drying before imaging. The images were recorded with 488 nm and 561 nm laser excitation at 100X.

4.4.10.2. Super-resolution microscopy:

Structured illumination microscopy (SIM) was carried out using an inverted Zeiss ELYRA PS1 microscope. Two lasers have been used for excitation: 488 nm (200 mW) and 561 nm (200 mW) for respective excitation of fluorophores. Imaging was performed using a Zeiss oil–immersion objective (alpha Plan–apochromat DIC 63x/1.40 Oil DIC M27, numerical aperture (NA) 1.40 oil) using 100 ms exposure time and 5% of the laser power from both the lasers: 488 nm (26 w.cm^{-2}) and 561 nm (22 w.cm^{-2}).

The appropriate concentration of self–assembled fibers (1: 100 (v/v) dilution from 0.4 mM stock) were taken in an eppendorf tube (PBS, pH 7.4). 10 µL of above solution were drop-casted onto a glass slide. A clean coverslip was placed on top of it and proceed for fluorescence microscopy using structured illumination method. The self–sorted fibers of *D* and *L*, (0.4 mM) were diluted in 100 µL PBS, pH 7.4 (1**:**100 (v/v)) and kept in an eppendorf tube. 10 µL of the solution were drop-casted onto a glass slide. A clean coverslip was placed on top of it and proceed for fluorescence microscopy using structured illumination method.

4.4.11. Enzymatic responsiveness of the fibers

The self–assembled fibers of ***L*-1** or ***D*-1** (0.5 mM) were incubated with chymotrypsin (10 µM) in phosphate buffer saline of pH = 7.4 at 37 ºC for 5 h in sample vial and HPLC was recorded to explore the emergence of new peak owing to proteolysis. The peak was characterized for the fragment peptides for the cleavage site by using HPLC-MS spectrometry. The HPLC chromatogram was recorded with acetonitrile and water (0.1% formic acid as additive) as mobile phase (gradient flow of 20 to 100 v/v% acetonitrile over 30 min, flow rate = 1 mLmin^{-1}). While ***L*-1** showed the emergence of a new peak indicating fragment species, ***D*-1** exhibited proteolytic stability under similar conditions.

4.5. References

1. T. Aida, E. W. Meijer and S. I. Stupp, *Science*, 2012, **325**, 813.
2. Z. He, W. Jiang and C. Schalley, *Chem. Soc. Rev.*, 2015, **44**, 779.
3. L. P. Garcia and D. B. Amabilino, *Chem. Soc. Rev.*, 2007, **36**, 941.
4. M. B. Omary, P. A. Coulombe and W. H. I. Mclean, *N. Engl. J. Med.*, 2004, **351**, 2087.
5. E. Fuchs and D. W. Cleveland, *Science*, 1998, **279**, 514.
6. M. M. Safont-Sempere, G. Fernández and F. Würthner, *Chem. Rev.*, 2011, **111**, 5784.
7. C. R. South, C. Burd and M. Weck, *Acc. Chem. Res.*, 2007, **40**, 63.
8. P. Mukhopadhyay, A. Wu and L. Isaacs, *J. Org. Chem.*, 2004, **69**, 6157.
9. O. Ikkala and G. T. Brinke, *Science*, 2002, **295**, 2407.
10. J. M. Pollino and M. Weck, *Chem. Soc. Rev.*, 2005, **34**, 193.
11. H. Frisch, J. P. Unsleber, D. Lüdeker, M. Peterlechner, G. Brunklaus, M. Waller and P. Besenius, *Chem. Int. Ed.*, 2013, **52**, 10097.
12. Y. M. Abul-haija, S. Roy, P. W. J. M. Frederix, N. Javid and R.V. Ulijn, *Small*, 2014, **10**, 973.
13. K. Osowska and S. Miljani, *J. Am. Chem. Soc.*, 2011, **133**, 724.
14. S. Ghosh, X. Li, V. Stepanenko and F. Würthner., *Chem. Eur. J.*, 2008, **14**, 11343.
15. M. R. Molla, A. Das and S. Ghosh, *Chem. Eur. J.*, 2010, **16**, 10084.
16. A. Kaeser, I. Fischer, R. Abbel, P. Besenius, D. Dasgupta, M. A. J. Gillisen, A. Kaeser, G. Portale, A. L. Stevens, L. M. Herz and A. P. H. J. Schenning, *ACS Nano*, 2013, **7**, 408.
17. A. Pal, S. Karthikeyan and R. P. Sijbesma, *J. Am. Chem. Soc.*, 2010, **132**, 7842.
18. D. Schultz and J. R. Nitschke, *Proc. Natl. Acad. Sci.* USA, 2005, **102**, 11191.
19. M. Hutin, C. J. Cramer, L. Gagliardi, A. Rehaman, M. Shahi, R. Cerny and J. R. Nitschke, *J. Am. Chem. Soc.*, 2007, **129**, 8774.
20. K. Mahata, M. L. Saha, and M. Schmittel, *J. Am. Chem. Soc.*, 2010, **132**, 15933.
21. Y. Kimura, M. Takenaka, M. Ouchi, T. Terashima, *Macromolecules,* 2020, **ASAP**.
22. E. R. Draper, E. G. B. Eden, T. O. Mcdonald and D. J. Adams, *Nature Chem.*, 2015, **7**, 848.
23. K. L. Morris, L. Chen, J. Raeburn, O. R. Sellick, P. Cotanda, A. Paul, P. C. Griffiths, S. M. King, R. K. O. Reilly, L. C. Serpell and D. J. Adams, *Nature Commun.*, 2013, **4,** 1480.
24. M. Koenigs, A. Pal, H. Mortazavi, G. Pawar, K. Storm and R. P. Sijbesma, *Macromolecules*, 2014, **47**, 2712.
25. M. M. Smith and D. K. Smith, *Soft Matter*, 2011, **7**, 4856.
26. C. Colquhoun, E. R. Draper, E. G. B. Eden, B. N. Cattoz, K. L. Morris, L. Chen, T. O. Mcdonald, A. E. Terry, C. Gri, L. C. Serpell and D. J. Adams, *Nanoscale*, 2014, **6**, 13719-13725.
27. K. Sugiyasu, S. ichiro. Kawano, N. Fujita and S. Shinkai, *Chem. Mater.*, 2008, **20**, 2863.
28. S. Onogi, H. Shigemitsu, T. Yoshii, T. Tanida, M. Ikeda, R. Kubota and I. Hamachi, *Nature Chem.*, 2016, **8**, 743.
29. L. Albertazzi, D. van der Zwaag, C. M. Leenders, R. Fitzner, R. W. van der Hofstad and E. W. Meijer, *Science*, 2014, **344**, 491.
30. R. M. P. da Silva, D. van der Zwaag, L. Albertazzi, S S. Lee and E.W. Meijer, *Nat. Commun*, 2016, **7,** 11561.
31. A. Sarkar, R Sasmal, C. Empereur-mot, D. Bochichio, S. V. K. Kompella, K. Sharma, S. Dhiman, B. Sundaram, S. S. Agasti G. M. Pavan, S. J. George, *J. Am. Chem. Soc.* 2020, **142**, 7606.
32. H. Jędrzejewska and A. Szumna, *Chem. Rev*, 2017, **117**, 4863.
33. A. Pal, P. Besenius and R. P. Sijbesma, *J. Am. Chem. Soc.* 2011, **133,** 12987.
34. A. Sarkar, S. Dhiman, A. Chalishazar and S. J. George, *Angew. Chem. Int. Ed.*, 2017, **56**, 13767.
35. J. Kang, D. Miyajima, T. Mori, Y. Inoue, Y. Itoh and T. Aida, *Science*, 2015, **347**, 646.
36. J. H. Fuhrhop, M. Krull and G. Biildt, *Angew. Chem., Int. Ed. Engl.* 1987, **26**, 699.
37. W. Dzwolak, R. Ravindra, C. Nicolini, R. Jansen and R. Winter, *J. Am. Chem. Soc.* 2004, **126**, 3762.
38. F. Xu, I. J. Khan, K. Mcguinness, A. S. Parmar, T. Silva, N. S. Murthy and V. Nanda, *J. Am. Chem. Soc.*, 2013, **135**, 18762.

39. W. P. Esler, E. R. Stimson, J. B. Fishman, J. R. Ghilardi, H. V Vinters, P. W. Mantyh and J. E. Maggio, *Biopolymers,* 1999, **49**, 505.
40. D. M. Chung and J. S. Nowick, *J. Am. Chem. Soc*., 2004, **126**, 3062.
41. V. Torbeev, M. Grogg, J. Ruiz, R. Boehringer, A. Schirer, P. Hellwig and D. Hilvert, *J. Pept. Sci.* 2016, **22**, 290.
42. H. Wadai, K. Yamaguchi, S. Takahashi, T. Kanno, T. Kawai, H. Naiki and Y. Goto, *Biochemistry*, 2005, **44**, 157.
43. R. J. Swanekamp, J. T. M. DiMaio, C. J. Bowerman and B. L. Nilsson, *J. Am. Chem. Soc*., 2012, **134**, 5556.
44. K. J. Nagy, M. C. Giano, A. Jin, D. J. Pochan and J. P. Schneider, *J. Am. Chem. Soc*., 2011, **133**, 14975.
45. J. Wang, K. Liu, R. Xinga and X. Yan, *Chem. Soc. Rev.*, 2016, **45**, 5589.
46. A. Pal, M. Malakoutikhah, G. Leonetti, M. Tezcan, M. Colomb-delsuc, V. D. Nguyen, J. Van Der Gucht and S. Otto, *Angew. Chem. Int. Ed.*, 2015, **54**, 7852.
47. A. Singh, J. P. Joseph, D. Gupta, I. Sarkar and A. Pal, *Chem. Commun*., 2018, **54**, 10730.
48. J. P. Joseph, A. Singh, D. Gupta, C. Miglani and A. Pal, *ACS Appl. Mater. Interfaces* 2019, **11**, 28213.
49. T. Koga, M. Matsuoka and N. Higashi, *J. Am. Chem. Soc.*, 2005, **127**, 17596.
50. M. A. Hossain, H. Mihara and A. Ueno, *J. Am. Chem. Soc.*, 2003, **125**, 11178.
51. N. E. botterhuis, S. Karthikeyan, A. J. H. Spiering and R. P. Sijbesma, *Macromolecules* 2010, **43**, 745.
52. E. Mattia, A. Pal, G. Leonetti and S. Otto, *Synlett* 2017, **28**, 103.
53. J. W. D. Comeau, S. Costantino and P. W. Wiseman, *Biophys. J.* 2006, **91**, 4611.
54. J. Adler and I. Parmryd, *Cytom. Part A*. 2010, **77A**, 733.
55. S. Dilipkumar, R. Manjithaya, P. P. Mondal, *RSc. Adv.*, 2015, **5**, 13175.
56. R. Arppe, M. R. C. Temboury, C. Hempel, and T. J. Sorensen, *PLoS. One,* 2017, **12**, e0188359.
57. S. M. Miller, R. J. Simon, S. Ng, R. N. Zuckermann, J. M. Kerr and W. H. Moos, *Drug. Develop. Res*. 1995, **35**, 20.
58. R. J. Swanekamp, J. J. Welch and B. L. Nilsson, *Chem. Commun*., 2014, **50**, 10133.
59. P. Wu and L. Brand. *Anal. Biochem*. 1994, **218**, 1.
60. D. R. Bolin, I. I. Sytwu, F. Humic and J. Meienhofer *Int. J. Peptide Protein Res.*, 1989, **33**, 353.
61. K. F. Chilvers, J. D. Perry, A. L. James and R. H. Reed, *J. Appl. Microbiol.* 2001, **91,** 1118.
62. M. Jullian, A. Hernandez, A. Maurras, K. Puget, M. Amblard, J. Martinez and G. Subra, *Tetrahedron Lett*, 2009, **50**, 260.

5

Fidelity of Self-sorting and Mixed Co-block Supramolecular Polymerization in Peptides Dictated by Methylene Spacer Between Bis-urea Motifs

Despite the recent advances in supramolecular polymerization, controlling the spatial distribution and order in self-assembled systems is still challenging. In this regard, multicomponent systems with minimum structural variation are of great importance to design highly complex materials with orthogonal functions. Thus, it is interesting to investigate the structural fidelity of multiple peptide amphiphiles to furnish possible self-assembled scenarios such as randomly co-assembled, self-sorted or mixed co-block nanofibers. In this chapter, we have designed two peptide amphiphiles that differ in the methylene spacer length between the bis-urea motifs. β-sheet forming amyloid-inspired peptide sequence VFFAK is anchored onto the bis-urea motifs flanking the methylene spacers. Here, methylene spacer length i.e. four and six carbon between bis-urea motifs is the driving parameter for the fidelity towards self-sorting or co-assembly, which was elegantly studied by anchoring Cy3 or Cy5 fluorophores through FRET and super-resolution microscopy. The two-component peptide system differing in spacer size is realized to create randomly co-assembled and orthogonal networks. Co-assembly of monomers results in the random sequence of monomers in a fiber, owing to the efficient intermolecular H bonding between the urea units with the same methylene spacer. On the contrary, self-sorted homomeric nanofibers are achieved with non-matching methylene spacer. Finally, supramolecular block co-polymers is obtained with seed-mediated supramolecular polymerization employing fiber seeds and monomer of matching methylene spacer length.

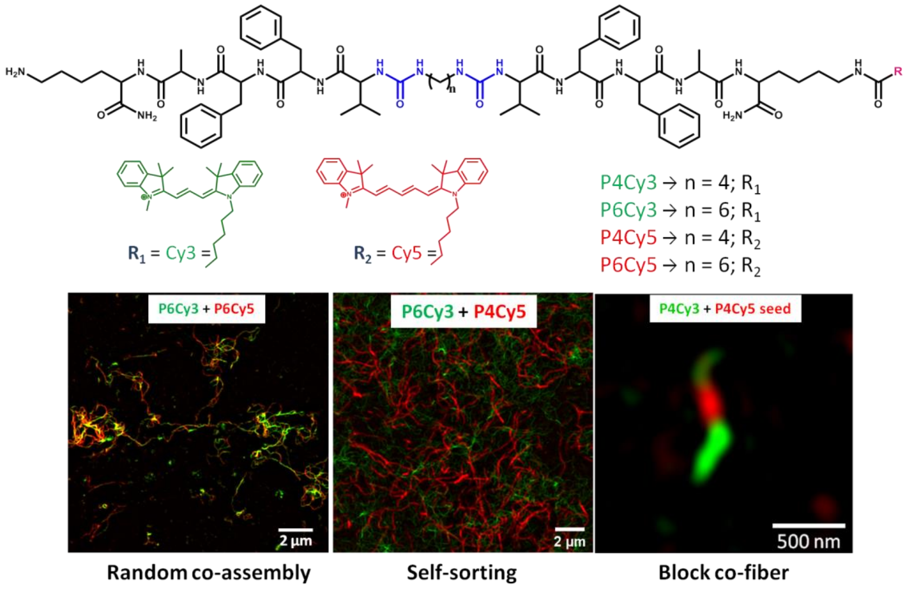

5.1. Introduction

The field of supramolecular polymerization has emerged as a powerful strategy to achieve well-defined, precise and controlled nanostructures starting from simple synthetic molecules.[1-2] Over the recent few years, chemists have exploited a wide range of strategies and techniques under non-equilibrium conditions to obtain perfect spatiotemporal control over the supramolecular architectures. Such control is achieved by supramolecular analogue of living radical polymerization, living supramolecular polymerization. In order to mimic such highly ordered structural and functional complexity of biological systems in artificial materials, multiple self-assembling components need to be employed. Such multicomponent self-assembly to fabricate sophisticated nanoarchitectures demands harnessing of judicious synergistic properties from its components[3-5], however, the protocols to design them with coexisting molecules towards compartmentalization are rather challenging and still in infancy. Thus, multiple building blocks that are mixed in a solution may result in the emergence of several possible outcomes. The molecules can either randomly, specifically or alternatively co-assemble or they can segregate between their own-self and non-self. Such orthogonal self-assembly with the individual assemblies coexists to develop a self-sorted system.[6-17] Mostly, in these systems the basis of defined self-sorted or co-assembled nanostructure originates from the environmental conditions and nature of individual building blocks specifically through non-covalent interaction sites. In the early examples of supramolecular self-sorting, Adams *et al.* reported an elegant self-sorting driven by the different pK_a of monomers.[12-13] Later, Würthner and co-workers described a dynamic self-sorting phenomenon with two perylene-bisimide amphiphiles.[18] Similarly, Sijbesma *et al.* demonstrated the self-sorting in rod-like micelles of bis-urea bolaamphiphiles through exciplex formation and FRET.[6,19] Recently, our group and Subi George's group[17,20] reported chirality-driven self-sorting with minimum structural variation in peptide and organic molecules respectively. The events of self-assembly occur at the molecular level, making them difficult to be studied by the convenient microscopy and spectroscopy techniques as these tools do not underpin what is happening at nanostructures level.[21] In this regard, Meijer *et al.* investigated the structure and molecular exchange pathways in supramolecular aggregates utilizing stochastic optical reconstruction microscopy (STORM) – a super-resolution technique.[22] Later, along with the group of Samuel Stupp, they examined the dynamic behavior of peptide amphiphiles in one-dimensional nanofibers.[23] For multicomponent systems, Hamachi *et al.* reported the first example of in-situ real-time imaging of the self-sorted nanostructures composed of two distinct building blocks, short peptide and amphiphilic phosphate.[10] since these molecules are structurally quite different, they are prone to undergo orthogonal self-assembly. They used confocal laser scanning microscopy (CLSM) and super-resolution imaging technique (stimulated emission depletion (STED) microscopy) to image the self-assembled nanofibers. However, molecular recognition mediated self-sorting in multicomponent systems with minimum structural variation is a rather interesting and challenging task. In this context, super-resolution microscopy serves as a powerful tool for gaining insight into the mechanism of co-assembly, self-sorting and most interestingly mixed block co-fiber formation.

Supramolecular co-block nanostructures are analogous to the covalent co-polymer and have not been explored much in detail. This definitely promises to provide emergent properties which can be derived and modulated with different blocks.[24-25] Supramolecular co-blocks with rationally designed ordered segments hold promise to construct nanostructures for applications like p-n heterojunctions.[24] In this context, seeded supramolecular polymerization plays a vital role to incorporate a range of functionalities through predictive pre-programmed supramolecular co-block. In the pioneering work by Winnnik and Manners[26-28] and recently by Sugiyasu and Takeuchi,[29] crystallization-driven self-assembly approach was elegantly realized to prepare supramolecular block co-polymeric nanostructures. Würthner *et al.* reported for the first time the formation of A-B-A and B-A-B supramolecular block copolymers via seeded supramolecular polymerization in two-component perylene bisimides (PBIs) under precise kinetic control.[30] Recently, George *et al.* manipulated the thermodynamic and kinetic pathways of small monomers in two component system to accomplish sequence controlled supramolecular co-polymerization.[31-32] Later, they have delineated the formation of multiple blocks in tri-component supramolecular system. Undoubtedly, these limited reports nourished the field of supramolecular block copolymerization but still, well-defined structures are rather elusive that require a rational yet elegant system design.

In this chapter, we investigated the structural fidelity of multiple peptide amphiphiles to furnish conceivable self-assembled outcomes such as randomly co-assembled, self-sorted or co-block nanofibers. We designed the peptide bolaamphiphiles that differ minimally in the methylene spacer length between bis-urea motifs with tethering VFFAK on the periphery of bis-urea (Scheme 5.1A). The methylene spacer (*i.e.* four and six carbon) between bis-urea motifs is the driving parameter for the fidelity towards self-sorting or co-assembly. Further, green colored Cy3 and red colored Cy5 fluorophore were anchored on the peptide bolaamphiphiles to gain more insight of self-assembled outcomes using super-resolution microscopy. The two-component peptide system differing in spacer size was realized to create randomly co-assembled and orthogonal networks (Scheme 5.1B-C). Further, supramolecular block co-polymers were achieved with seeded supramolecular polymerization by employing fiber seeds with monomer of matching spacer length (Scheme 5.1D).

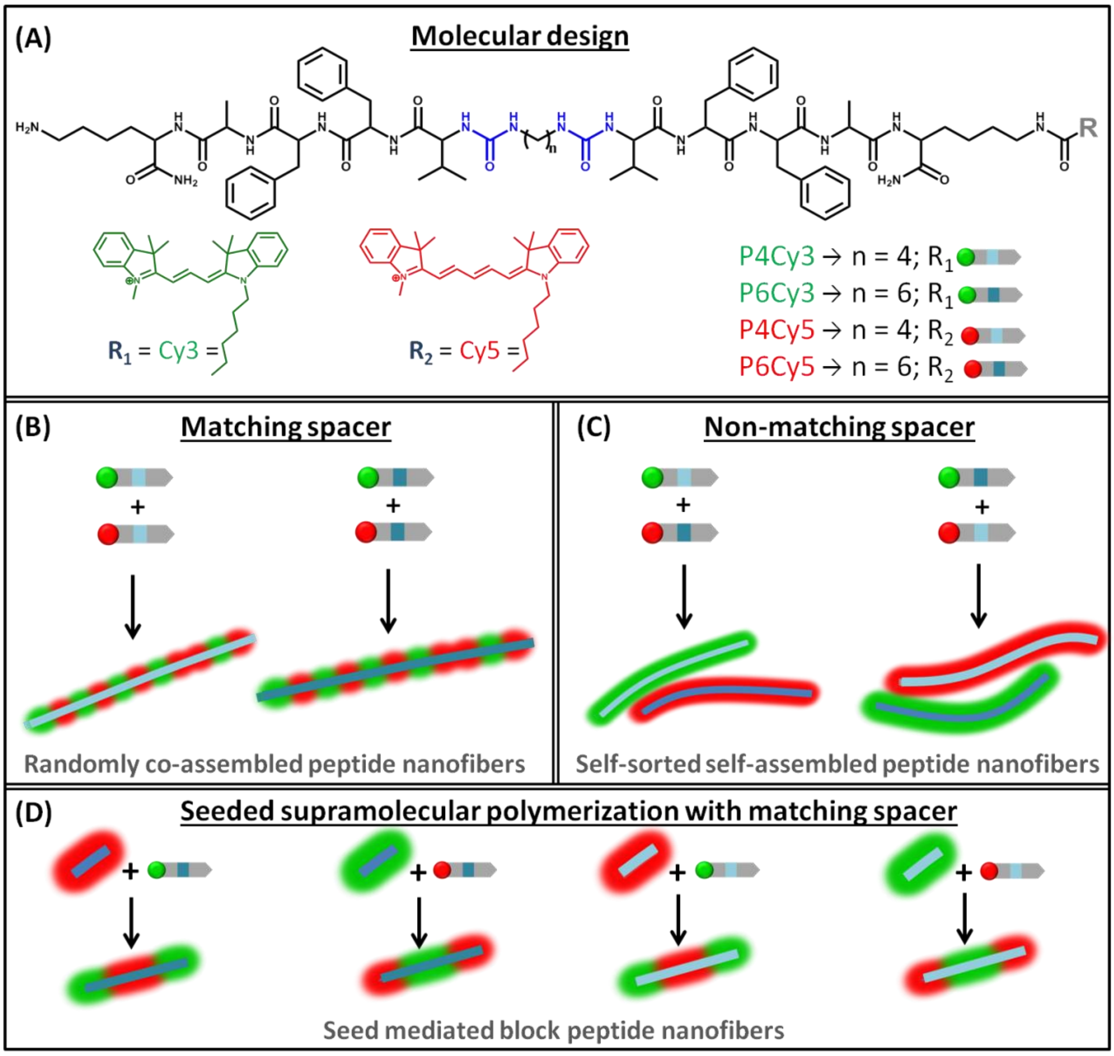

Scheme 5.1: (A) Molecular structures of the monomers **P4Cy3**, **P6Cy3**, **P4Cy5** and **P6Cy5** used for co-assembled, self-sorted and co-block peptide nanofibers. Schematic representation of two-component peptide self-assembly into (B) randomly co-assembled fibers, (C) self-sorted fibers and (D) seed-mediated mixed co-block nanofibers.

5.2. Results and discussion

We designed and synthesized bis-urea peptide bolaamphiphiles differing in hydrophobic methylene spacer of chain lengths four and six carbons between two urea motifs. The amyloid inspired peptide sequence VFFAK that flanked the bis-urea motifs encourages self-assembly by virtue of various non-covalent interactions like H bonding operating among urea and amide functionalities and π-π interactions among side chain and hydrophobic spacer provides van der Waal's interactions. These peptides (**P4** and **P6**) with perfect hydrophobic-hydrophilic balance were taken in water for self-assembly. After incubation for 1 day, the micrometer long self-assembled nanofibers with height ~ 3 nm were observed through AFM imaging (Figure 5.1).

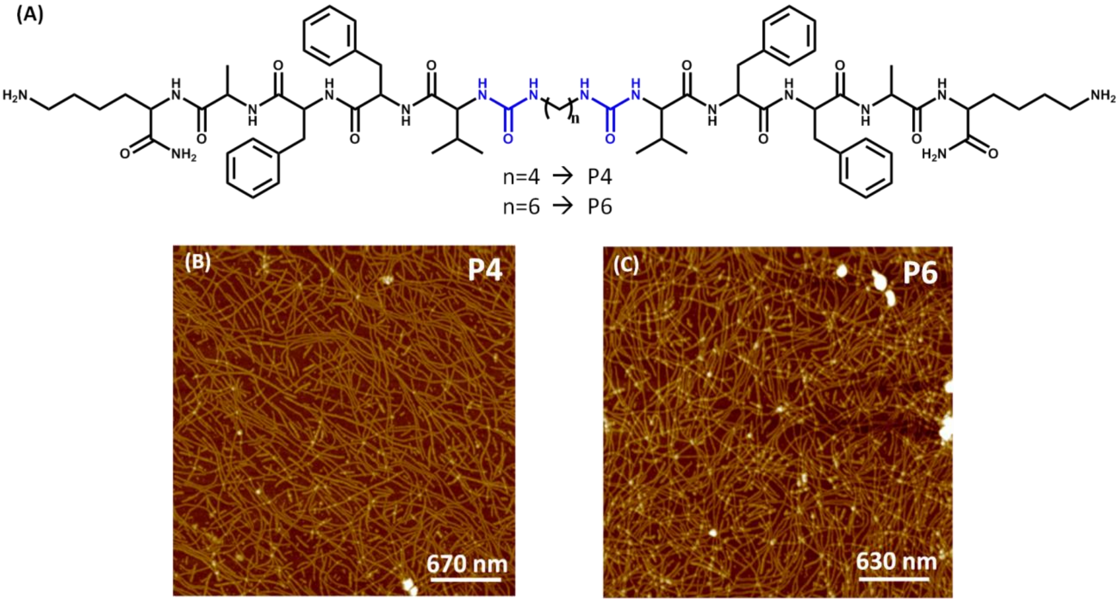

Figure 5.1: (A) Chemical structure of symmetric peptide bola-amphiphiles (**P4**, **P6**) with different spacer lengths between bis-urea motifs. AFM images of (B) **P4** and (C) **P6** peptides show self-assembled nanofibrous morphology in water.

Next, in order to facilitate direct visualization of peptide nanostructures, bis-urea peptides were selectively stained with two distinct fluorescent dyes which enable them to be monitored under CLSM and super-resolution structured illumination microscopy (SR-SIM) (Scheme 5.1). Cy3 and Cy5 were chosen as fluorophores due to their excellent photo-physical properties and were considered good FRET pair. Peptide **P4** was coupled with two distinct fluorescent molecules (Cy3 and Cy5) resulting into two sets of fluorescent peptides **P4Cy3** and **P4Cy5**. Similarly, peptide **P6** was also tethered with fluorophores resulting in two distinct fluorescent peptides **P6Cy3** and **P6Cy5**. It is noteworthy that peptides have only single fluorophore molecule attached while the bi-functional fluorescent peptides were found to have solubility issues. UV-vis spectra showed that anchoring of the dyes with peptides did not influence their optical properties. Thus, upon dissolving in water Cy3 coupled peptides (**P4Cy3** and **P6Cy3**) exhibited absorption maxima at 550 nm, while for **P4Cy5** and **P6Cy5** the absorption maxima were observed at 643 nm, that were similar to Cy3 and Cy5 respectively (Figure 5.2A).

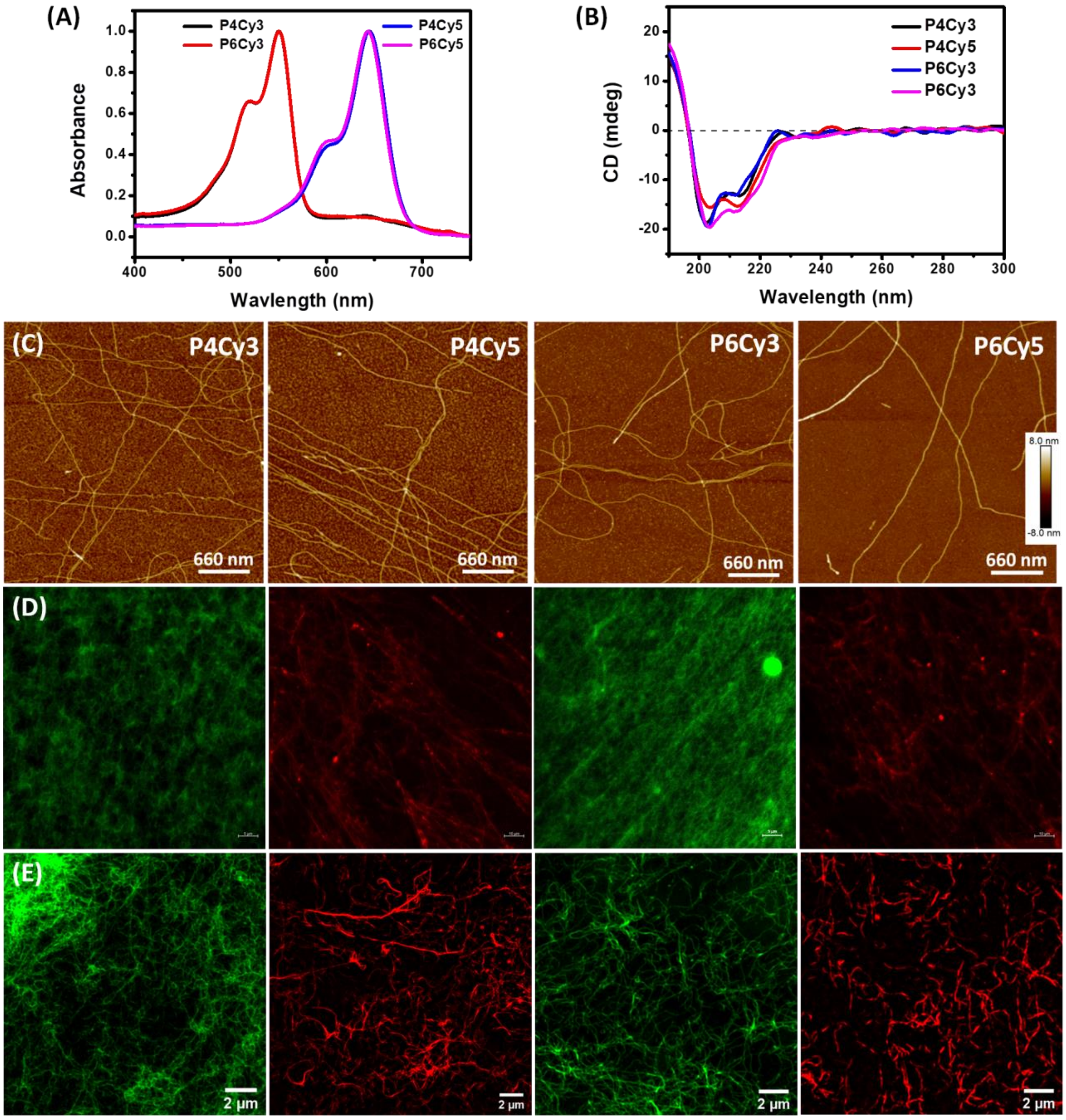

Figure 5.2: Self-assembly of fluorescent peptides (A) UV-vis spectra shows the absorption maxima for **P4Cy3**, **P4Cy5** at 550 nm and **P6Cy3**, **P6Cy3** at 643 nm (B) CD spectra of self-assembled peptides in water depicting β-sheet secondary structure. (C) AFM height images showed nanofibers of self-assembled peptides. (D) CLSM images of self-assembled fluorescent nanofibers; green fibers for **P4Cy3** and **P6Cy3** (viewed in channel 1, 561 nm) and red fibers for **P4Cy5** and **P6Cy5** (viewed in channel 2, 642 nm) (E) SIM-super-resolution images of self-assembled fluorescent nanofibers. (Concentration = 0.5 mM)

Next, the peptides were incubated in water for one day to form supramolecular assemblies at room temperature. The circular dichroism (CD) spectra of self-assembled peptides exhibited a negative Cotton peak at 205 nm and a positive Cotton peak at 191 nm depicting the presence of a shifted β-sheet secondary structure in the solution (Figure 5.2B). Further, AFM images of the peptides depict the presence of very long nanofibers with a high aspect ratio (Figure 5.2C). These fibers exhibited indistinguishable morphology from each other and therefore it was difficult to recognize the origin of individual building blocks upon mixing. However, due to the emissive nature of fluorophores Cy3 and Cy5, the supramolecular assemblies could be visualized using CLSM (Figure 5.2D). While we could observe green and red fluorescent nanoassemblies owing to the presence of Cy3 and Cy5 fluorophores tethered to the peptides, the resolution was rather poor to clearly observe the nanostructures. Therefore we resorted to utilize SR-SIM that improved the visualization of nanofibers with better resolution. The self-assembled peptide solutions were drop-casted on a glass slide and SR-SIM images were recorded in green channel with laser of $\lambda = 561$ nm (for **P4Cy3** and **P6Cy3**) and red channel with the laser of $\lambda = 642$ nm (for **P4Cy5** and **P6Cy5**). We observed long one-dimensional homomeric fluorescent nanofibers with green and red emission labelled with the respective dyes (Figure 5.2E). These fluorescent labelled peptide assemblies are similar to their unlabelled counterparts (**P4** and **P6**) but directly seeing them under microscope provides us with a powerful handle for further tuning the nanostructural assemblies *e.g.* co-assembly or self-sorting.

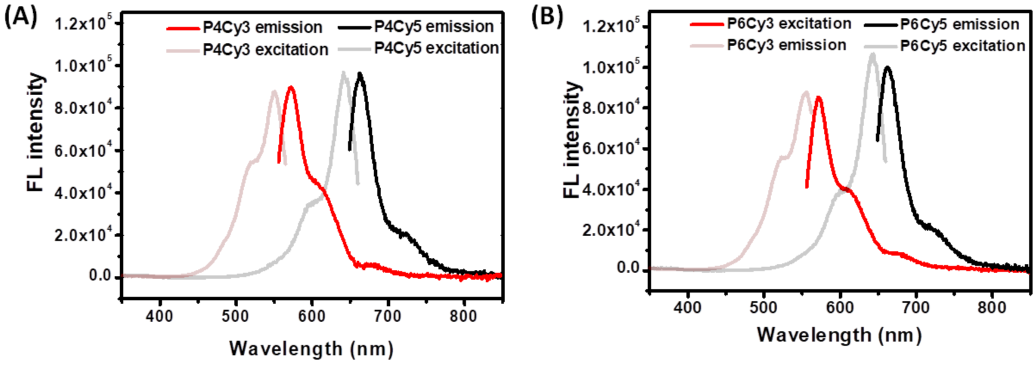

Figure 5.3: (A) Overlap between the emission spectra of **P4Cy3** donor probe and excitation spectra of the **P4Cy5** accepter probe demonstrates the probes to be perfect FRET pair. (B) Similar overlap was observed in peptide with six methylene spacer.

To investigate the fidelity of the molecular recognition driven by the minute structural variation (here, changing two methylene spacer units) in resulting self-assembled peptide nanofibers, we employed FRET experiments. These bis-urea peptides coupled with Cy3 and Cy5 show a region of overlap between emission spectra of the donor (Cy3 coupled peptides) and absorbance spectra of the acceptor (Cy5 coupled peptides) making them excellent FRET pair with Förster radius of 50 Å (Figure 5.3).[23] Thus in Cy3, Cy5 pendent peptide amphiphile as FRET pair, **P4Cy3** or **P6Cy3** act as a FRET donor while Cy5 coupled peptides **P4Cy5** or **P6Cy5** act as FRET acceptor. Moreover, irradiating the sample with the wavelength of 550 nm will directly excite Cy3 (excitation maximum: 550 nm, emission maximum: 570 nm) but not Cy5 (excitation maximum: 643 nm, emission maximum: 670 nm). FRET acceptor peptides **P4Cy5** and **P6Cy5**, will emit only if it receives energy from Cy3 tethered peptide amphiphiles, which can only occur if the two fluorophores exhibit spatial proximity. If this transfer of energy arises, donor (**P4Cy3** or **P6Cy3**) emission is suppressed while acceptor (**P4Cy5** or **P6Cy5**) emission increases. For performing the FRET studies, the monomeric solution of donor peptide (for instance, **P4Cy3**) in acetonitrile-water (1**:**1) was taken and injected into water having the final solvent composition of 2% acetonitrile in water (Figure 5.4A). Then, the monomeric solution of acceptor peptide with matching spacer (**P4Cy5**) was added and subsequently incubated for one day for self-assembly. The presence of matching spacer chain length renders the system co-assembled with high fidelity owing to the efficient H bonding interactions among urea and amide bonds. In this case, the FRET signal with enhanced acceptor emission at λ = 670 nm and reduced donor emission with λ = 570 nm was observed (Figure 5.4B) due to energy transfer between FRET pair (Cy3 and Cy5 moieties) as both peptides have no selectivity and stacked in the same fiber. Energy transfer suggests the spatial proximity and hence co-assembly of two different fluorescent peptides. However, on incubating monomeric solution having different spacer (**P6Cy5**) with **P4Cy3**, the FRET signal was found to be weak indicating negligible energy transfer between fluorescent probes. Thus, FRET studies suggested that in the matching spacer case, the peptides were randomly co-assembled, whereas for the non-matching spacer length, due to ineffective interactions with structural dissimilarity does not let the peptides to pack efficiently and therefore they prefer to aggregate with their like ones and self-segregated forming pure assemblies in water. Moreover, the percentage of self-sorting was calculated according to equation 5.1 (details in section 5.4.5) using emission fluorescene intensity at 673 nm for matching (Em_{matching}) and non-matching ($Em_{\text{non-matching}}$) spacer (Figure 5.4B). Hence, we can conclude that peptide amphiphiles with non-matching spacer length have high fidelity towards self-sorting ~ 90%.

$$Self - sorting = \left(1 - \frac{Em_{non-matching} - Em_{Blank}}{Em_{matching} - Em_{Blank}}\right).100\% \qquad \text{...... equation (5.1)}$$

In another set of experiment, all fluorescent peptides were allowed to self-assemble as illustrated in Figure 5.4C. The self-assembled solutions were then mixed and fluorescence spectra were recorded to investigate the FRET. For the binary fiber mixture of non-matching spacer case (**P4Cy3** fiber & **P6Cy5** fiber pair or **P6Cy3** fiber & **P4Cy5** fiber pair) no FRET was observed. Interestingly, for two-component fiber mixing even with matching spacer case (**P4Cy3** fiber & **P4Cy5** fiber pair or **P6Cy3** fiber & **P6Cy5** fiber pair) did not show any FRET signal. (Figure 5.4D). Moreover, monitoring fluorescence intensity at acceptor emission (670 nm) with time suggests no monomer exchange once the peptides self-assemble (Figure 5.4D, inset).

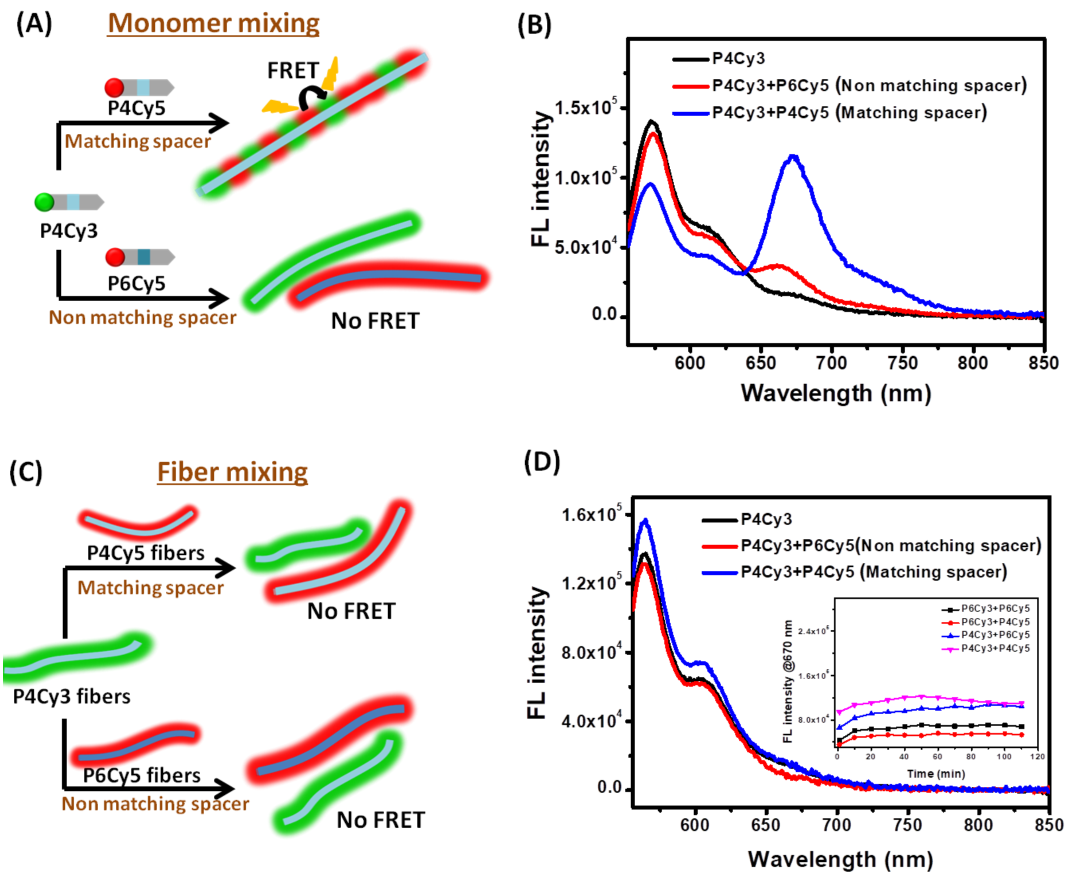

Figure 5.4: (A) Schematic representation of co-assembly and self-sorting when peptides were mixed in monomeric form, for example for **P4Cy3** peptide mixed with **P4Cy5** and **P6Cy5**. (B) FRET studies for monomer mixing experiments indicate enhanced FRET signal for matching spacer case (**P4Cy3** and **P4Cy5**) compared to non-matching spacer case (**P4Cy3** and **P6Cy5**). (C) Schematic representation for mixing of the peptides in self-assembled state. This scenario resulted in self-sorted fibers even with the same spacer (**P4Cy3** fiber and **P4Cy5** fiber) indicating low monomer exchange in self-assembled nanofibers. (D) No FRET response was observed for matching as well as non-matching spacer case.

While FRET experiments provided useful information in terms of energy transfer, but it did not furnish any spatially resolved information regarding the peptide self-assembly. Next, we employed SIM-super-resolution microscopy to gain more insights about the self-sorted versus the co-assembled assemblies due to its high resolution and colour-coded imaging ability.

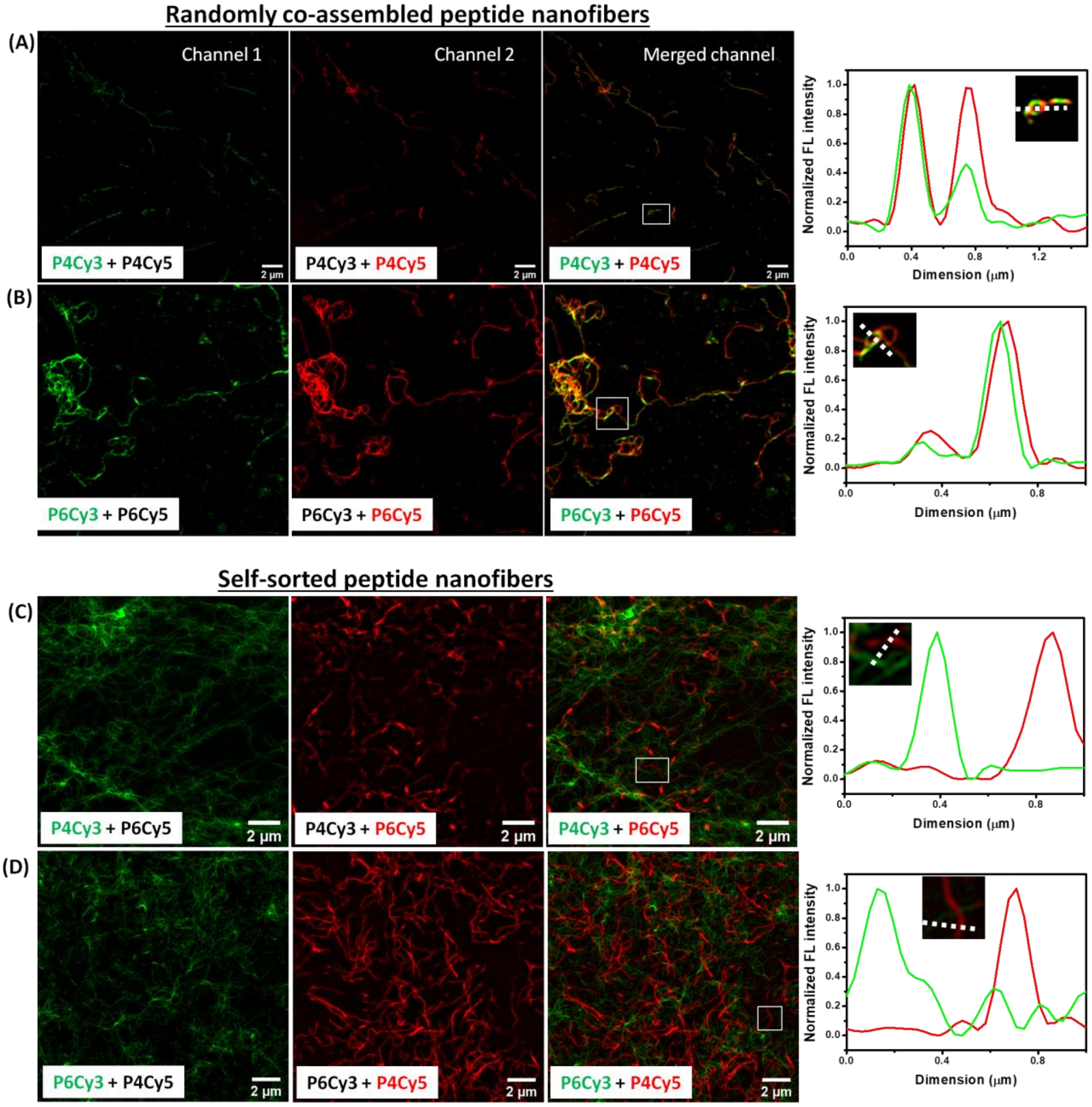

Figure 5.5: Direct visualization of co-assembled and self-sorted nanofibers. SIM images and fluorescence intensity profile showed complete overlapping of green and red fluorescent fibers furnishing the randomly co-assembled fibers from the peptides with the same spacer length (A) **P4Cy3** and **P4Cy5** (B) **P6Cy3** and **P6Cy5**. SIM images showed orthogonal green and red fibers depicting self-sorted nanofibers on mixing two components with non-matching spacer- (C) **P4Cy3** and **P6Cy5** (D) **P6Cy3** and **P4Cy5**.

These fluorophore-conjugated peptides are the perfect model to carry out SR-SIM imaging in green channel (λ_{ex} = 561 nm) and red channel 2 (λ_{ex} = 642 nm). The pair of peptide amphiphiles with matching methylene spacer, *e.g.* monomeric form of **P4Cy3** & **P4Cy5** pair or **P6Cy3** & **P6Cy5** pair was incubated to self-assemble for one day and then the images were recorded in individual and merged channels. These images unambiguously showed that green or red fibers were virtually indistinguishable as they co-assembled on the same nanofiber. The fluorescence intensity profile depicts the information regarding the spatial distribution of the dye-labelled peptide in a nanofiber. The plots have complete overlapping in green and red regions attributing to the co-assembly among nanofibers of matching spacer size peptide amphiphile (Figure 5.5A-B). Interestingly, upon mixing the peptide with non-matching spacer (**P4Cy3** & **P6Cy5** pair or **P6Cy3** & **P4Cy5** pair) in monomeric form and they were visualized in green and red and merged emission channels. The SIM images clearly showed no spatial correlation between green-emitting fibers and red-emitting fiber (Figure 5.5C-D). Moreover, plot of cross section fluorescent intensity profile showed no overlapping in red and green areas suggesting formation of self-sorted nanofibers with homomeric assemblies.

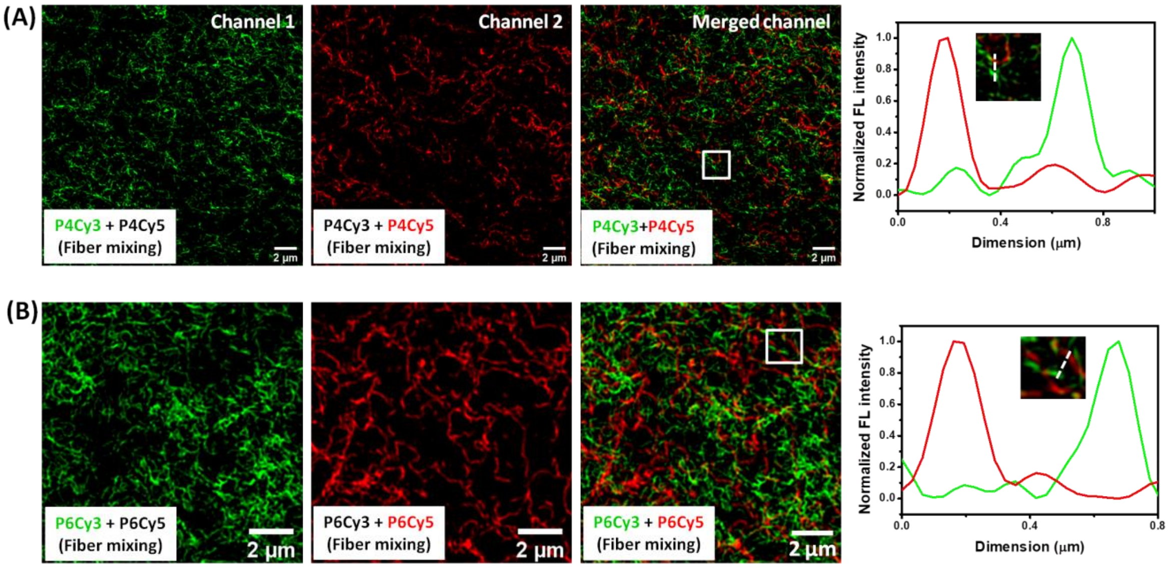

Figure 5.6: Super-resolution images along with fluorescence intensity profile of pre-assembled fiber mixing depicting low monomer exchange after self-assembly for matching spacer (A) **P4Cy3** and **P4Cy5** and (B) **P6Cy3** and **P6Cy5**.

We also perceived that once self-assembled fibers are formed, they have low monomer exchange on mixing peptide amphiphiles with matching as well as non-matching spacer. The self-assembled peptides bearing different fluorophores with either matching (**P4Cy3** fiber & **P4Cy5** fiber or **P6Cy3** fiber & **P4Cy5** fiber) or non-matching (**P4Cy3** fiber & **P6Cy5** fiber or **P6Cy3** fiber & **P4Cy5** fiber) spacer were mixed and observed under super-resolution microscope with corresponding fluorescent intensity plots (Figure 5.6). In correlation with the FRET measurements, these observations suggest that these peptides do not exhibit a dynamic nature in solution.

After a thorough investigation of randomly co-assembled and self-sorted nanofibers, next, we were interested in co-block nanofibers. Random co-assembly of the fluorescent peptide amphiphiles suggested that the construction of two-component supramolecular block copolymers required a low structural mismatch. Therefore, the peptide amphiphiles of matching spacer length were attempted for examining the formation of precisely controlled supramolecular block co-polymers. Firstly, the polydisperse fibers were probe sonicated for two minutes to obtain short uniform nanofibers (seeds) with the approximate length of 300 nm (Figure 5.8). The stock solution of non-aggregated peptide amphiphile was taken in DMSO. To carry out typical seeding experiment, seeds with either fluorophore; for instance, **P4Cy5** seeds were incubated with non-aggregated peptide amphiphile tethered with alternate dye *i.e.* **P4Cy3**. The seeds and monomer were mixed in 1:1 ratio and incubated for one day at room temperature. The supramolecular mixed co-block nanofibers of peptide amphiphiles were visualized by SIM images where Cy5 labelled seeds (Here, **P4Cy5**) show up red emission channels and the green coloured supramolecular blocks were constructed at the periphery of the fibers.

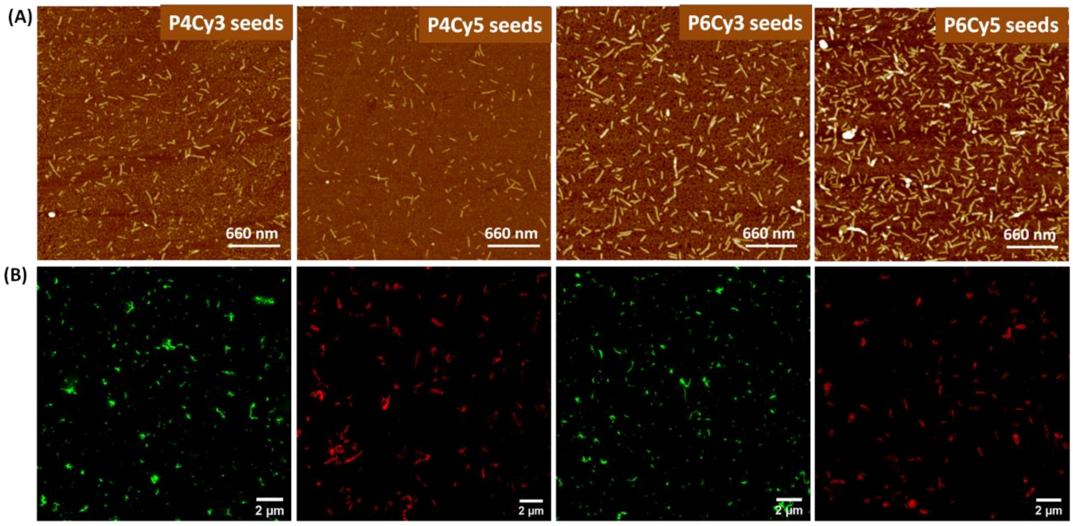

Figure 5.7: Seeds prepared by probe sonication of uncontrolled grown long peptide nanofibers were observed from (A) AFM images and (B) super-resolution microscopy.

On closer observation, we found out the average length of the inner block which was composed of **P4Cy5** seeds to be ~ 300 nm, whereas periphery blocks have length of ~200 nm. In all the cases, with alternate seeds and monomer we had achieved such precise control over the size of blocks that can be very elegantly visualized through super-resolution microscopy. These mixed co-blocks have high potential to be tuned with different functionalities for orthogonal applications.

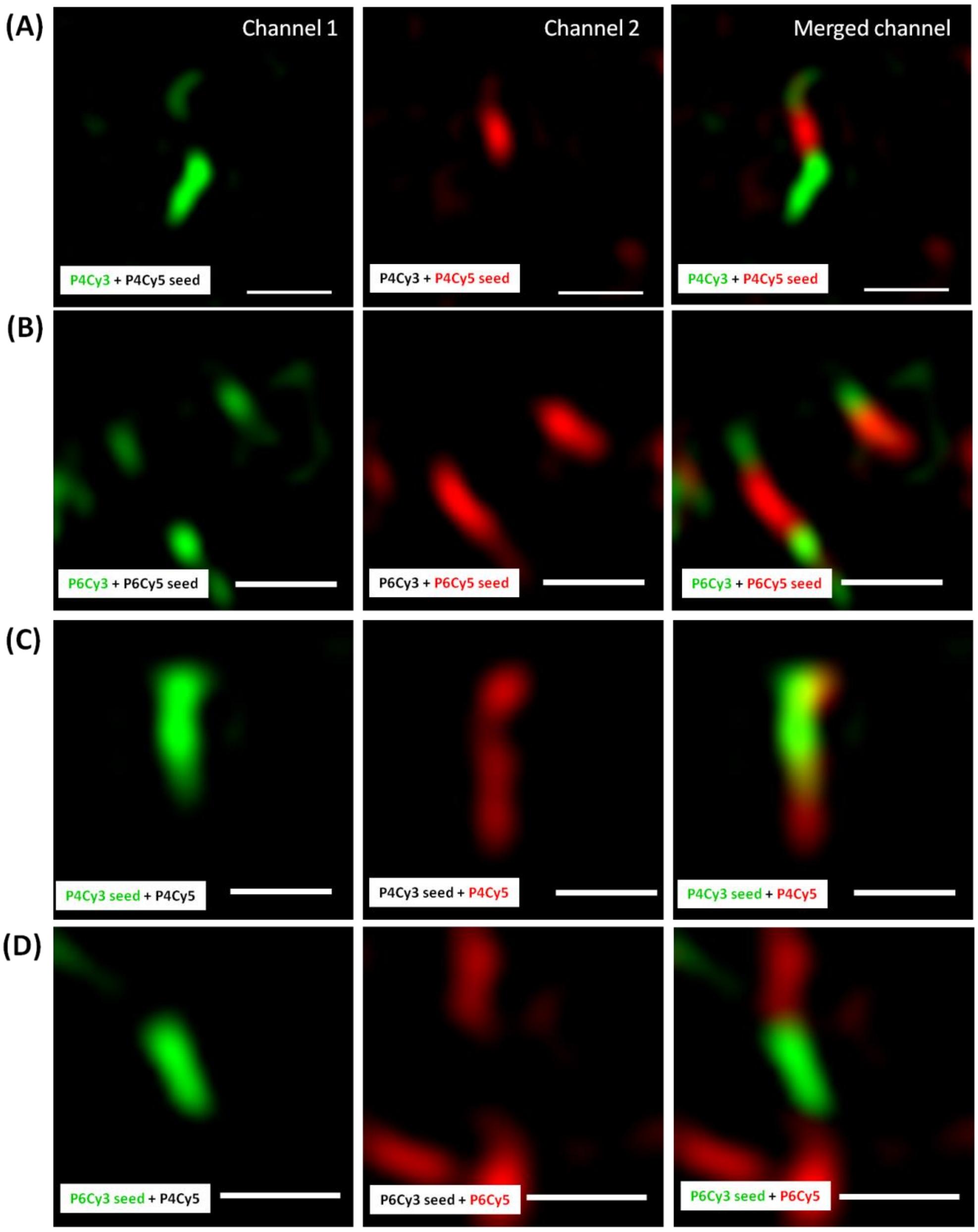

Figure 5.8: SIM images depicting supramolecular block copolymers with matching spacer length of peptide amphiphile (Scale bar = 500 nm).

5.3. Conclusions

In summary, we demonstrated the self-assembled long nanofibrous morphology of the amyloid inspired peptide bolaamphiphiles that can be elegantly visualized through super-resolution microscopy. In two-component system, self-assembly of peptides manifests into co-assembled or self-sorting nanofibers with matching or non-matching hydrophobic spacer length respectively. Interestingly, we have observed that on mixing already self-assembled nanofibers, there is low monomer exchange leading to self-sorting fibers even for peptides with matching spacer. Detailed analyses by FRET experiments and super-resolution microscopy suggested that fidelity towards self-sorting was dictated by spacer length flanked by H bonding urea motifs to show the ability towards compartmentalization. Additionally, taking the advantage of suitable non-covalent interactions in peptides with matching spacer, the formation of supramolecular mixed block co-polymers were achieved through seeded supramolecular polymerization. Moreover, the super-resolution microscopy was efficiently employed to visualize the formation of such supramolecular mixed blocks. We envision that such kind of multicomponent non-covalently linked stable block co-polymers may access novel properties that can find future applications in the diverse field of supramolecular electronics.

5.4. Experimental section

5.4.1. Materials and methods

Fmoc-Lys(Alloc)-OH, triethylamine, *N*,*N*-diispropylethylamine (DIPEA), HBTU, 1,4-diisocyanatobutane and hexamethylene diisocyanate were purchased from Sigma Aldrich. Cy3 and Cy5 dyes were synthesized following the reported procedure described in the next section. HPLC grade acetonitrile, HPLC water, ethanol and dimethylformamide (DMF) were ordered from Merck.

Peptide ^{N}VFFAK^{C} was synthesized using a *Liberty Blue CEM,* Matthews, NC, USA microwave-assisted peptide synthesizer following standard microwave Fmoc-solid phase peptide protocols. Reverse phase HPLC was performed with *Waters* Alliance HPLC system, using *Waters Reliant* analytical column (C_{18} stationary phase, 5 µm, 4.6 × 250 mm). The samples were injected through auto-sampler and detected by photodiode array (PDA) detector at λ = 550 nm and 643 nm for Cy3 and Cy5 coupled peptides. Peptides were separated using *Nucleodur* C18 semi-preperative column. Electronspray Ionization Mass Spectrometry (ESI/MS) was performed with *Waters Aquire QDa* detector in suitable scan mode. Typical cone voltage is 15V and capillary voltage is 0.8V.

5.4.2. Synthesis of cyanine dyes

Cy3 and Cy5 fluorescent dyes were synthesized according to reported procedures. [33-35]

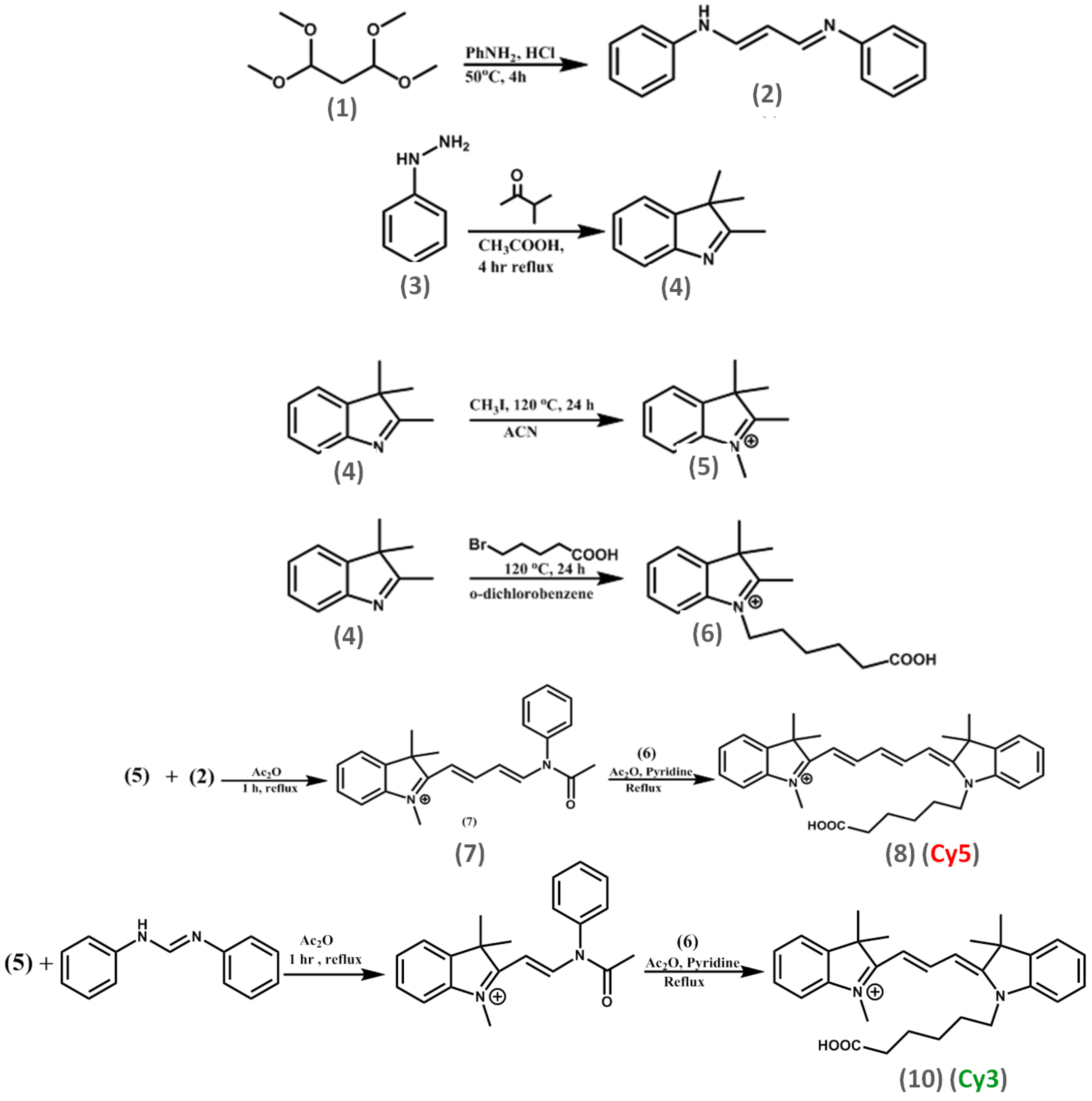

Synthesis of 2: An aqueous solution of concentrated HCl (0.6 M, 15 mL) and 1,1,3,3 tetramethoxy propane (**1**) (1 mL) was heated to 50 ºC, then a solution of water (21 mL), HCl (1.5 mL) and aniline (1.09 mL) was added drop-wise. During the addition of aniline solution, the colourless reaction mixture gradually changes to orange. The reaction reached completion after 4 hr and the precipitates were isolated by filtration to result in the desired product **2**.

Percentage yield = 75%

^{1}H NMR ($CDCl_3$, 400 MHz): δ = 8.89 (t, 2 H, *J* = 12 Hz, h-H), 8.22 (s, 1 H, j-H) 7.45 - 7.41 (m, 8 H, a-H, b-H, e-H, g-H), 7.25 (d, 2 H, d-H) 6.48 (m, 2 H, c-H, f-H) ppm

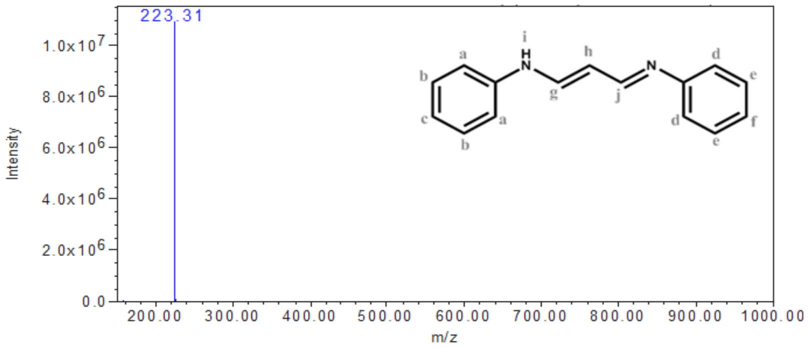

Figure 5.9: Mass spectra of **2** (malonaldehyde dialinine).

Synthesis of 4: Phenylhydrazine (**3**) (9.24 mmol, 0.9 mL) was suspended in acetic acid (30 mL) to which 3-methyl-2-butanone (10.16 mmol, 1.08 mL) was added and the reaction was refluxed for 4 hr. Upon cooling to room temperature the solvent was removed under reduced pressure. The residue was diluted with 1 M NaOH, extracted with DCM and washed with saturated sodium carbonate to render the red coloured product **4**.

Percentage yield = 72%

^{1}H NMR ($CDCl_3$, 400 MHz): δ = 7.34 (m, 1H, f-H), 7.28 (m, 2 H, d-H, e-H), 7.18 (m, 1 H, c-H), 2.28 (s, 3 H, b-H), 1.30 (s, 6 H, a-H) ppm.

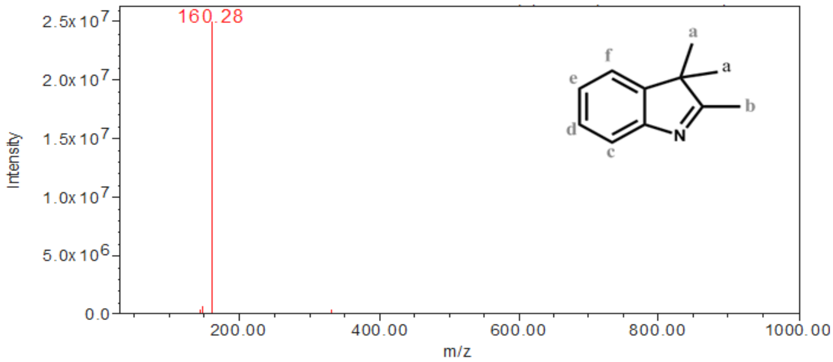

Figure 5.10: Mass spectra of **4** (2,3,3-trimethylindolenine).

Synthesis of 5: 2,3,3-trimethylindolenine **(4)** (6.28 mmol, 1.01mL) was dissolved in acetonitrile (5 mL) and then methyl iodide (6.91 mmol, 0.43 mL) was added. The reaction mixture was heated at reflux for 7 h and cooled to room temperature. The precipitates were collected by filtration and washed with diethyl ether followed by drying in vacuo over KOH pellets to result in **5**.

Percentage yield = 95%

^{1}H NMR ([d6]-DMSO, 400 MHz): δ = 7.91 (m, 1 H, f-H), 7.83 (m, 1 H, d-H), 7.64 (m, 2 H, e-H, c-H), 3.97 (s, 3 H, g-H), 2.77 (s, 3 H, b-H), 1.53 (s, 6 H, a-H) ppm.

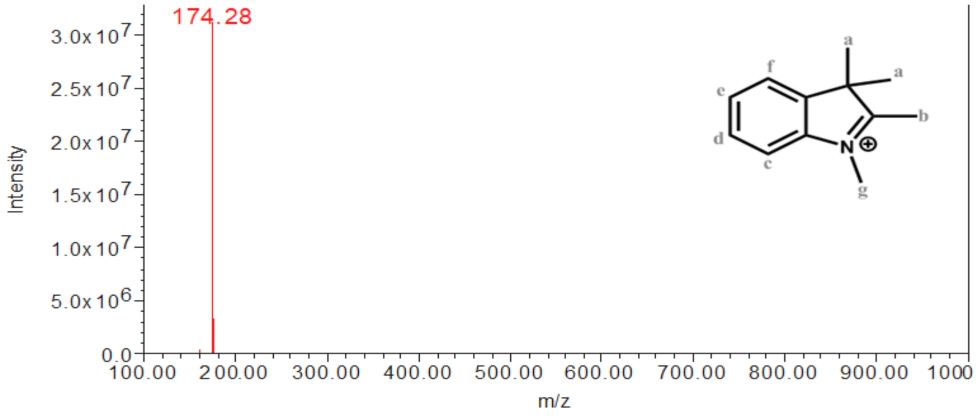

Figure 5.11: NMR and Mass spectra of **5** (1,2,3,3-tetramethylindolium).

Synthesis of 6: A mixture of 6-bromohexanoic acid (6.28 mmol, 1.2 g) and 2,3,3-trimethylindolenine (**4**) (5.58 mmol, 500 mg) in o-dichlorobenzene (7 mL) was heated to 120 ºC for 24 h. After this, the reaction mixture was cooled to room temperature, filtered and the precipitates were washed successively with hexane and diethyl ether to render **6**.

Percentage yield = 85%

^{1}H NMR ([d$_6$]-DMSO): δ = 7.97 (m, 1 H, f-H), 7.85 (m, 1 H, d-H), 7.62 (m, 2 H, e-H, c-H), 4.46 (t, *J* = 8Hz, 2 H, g-H), 2.86 (s, 3 H, b-H), 2.25 (t, *J* = 7.2 Hz, 2 H, k-H), 1.85 (m, 2 H, h-H), 1.58 (m, 2 H, j-H), 1.54 (s, 6 H, a-H), 1.43 (m, 2 H, i-H) ppm.

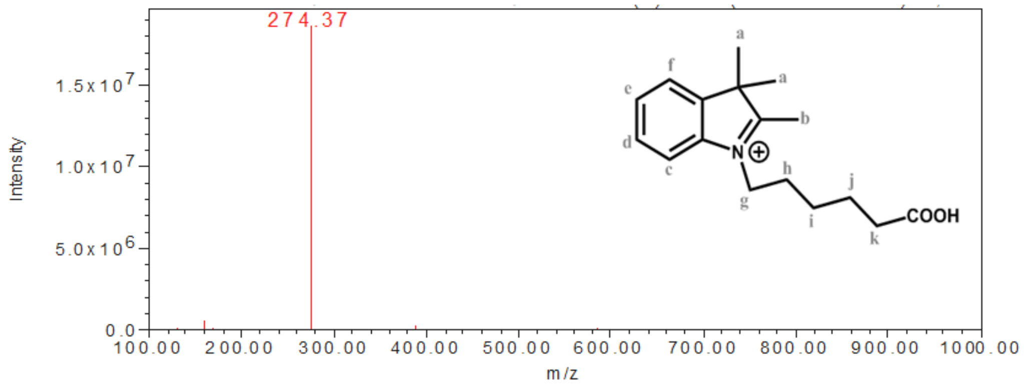

Figure 5.12: NMR and Mass spectra of **6** (1-(5-Carboxypentyl)-2,3,3-trimethyl-indolium).

Synthesis of 8 (Cy5): 1,2,3,3- Tetramethylindolium **(5)** (0.574 mmol, 100 mg) and malonaldehyde dialinine **(2)** (0.861 mmol, 223 mg) in acetic anhydride (1.1 mL) were heated at reflux under nitrogen. After 30 minutes, the reaction mixture was cooled to room temperature. The solution of 1-(5-Carboxypentyl)-2,3,3-trimethyl-indolium (**6**) (0.975 mmol, 267 mg) in anhydrous pyridine (2.1 mL) was then added to the reaction mixture and stirred under inter atmosphere at ambient temperature for 2 h. The solvent was removed in vacuo and the residue was dissolved in chloroform and precipitated with hexane. The supernatant was decanted off and the residual oil was dissolved in chloroform, washed with water and 0.1 M HCl. The organic layer was separated, dried over sodium sulphate. The HPLC peak with retention time of 16.5 min corresponds to product **8** which was further confirmed with NMR and mass spectra.

Percentage yield = 45%

^{1}H NMR ([d_6]-DMSO, 500 MHz): δ = 8.32 (t, J = 16 Hz, 2 H, s-H, u-H), 7.60 (m, 2 H, c-H, g-H), 7.39 (m, 4 H, e-H, f-H, j-H, i-H), 7.25 (m, 2 H, d-H, h-H), 6.65 (t, J = 15.5 Hz, t-H), 6.30 (d, J = 17 Hz, 1H, r-H), 6.27 (d, J = 17 Hz, v-H), 4.09 (t, J = 8.7 Hz, 2 H, k-H), 3.60 (s, 3 H, q-H), 2.13 (t, J = 9 Hz, 2 H, o-H), 2.01 (m, 2 H, l-H), 1.68 (s, 12 H, a-H, b-H), 1.55 (m, 2 H, n-H), 1.39 (m, 2 H, m-H) ppm.

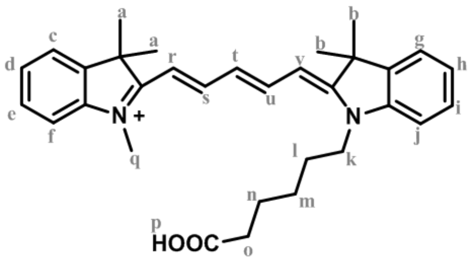

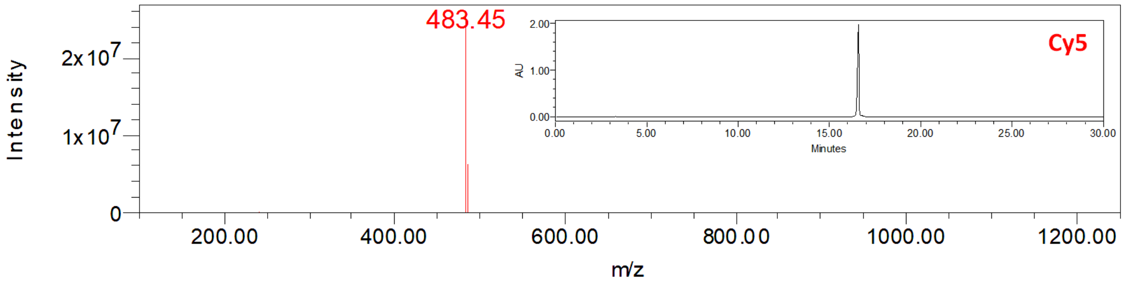

Figure 5.13: Mass spectra and HPLC chromatogram (inset) for **8** (Cy5).

Synthesis of 10 (Cy3): 1,2,3,3- tetramethylindolium **(5)** (0.574 mmol, 100 mg) and N,N'-diphenylformamidine (**9**) (0.861 mmol, 223 mg) in acetic anhydride (1.1 mL) was heated at reflux under nitrogen. After 30 minutes, the reaction mixture was cooled to room temperature. The solution of 1-(5-Carboxypentyl)-2,3,3-trimethyl-indolium (**6**) (0.975 mmol, 267 mg) in anhydrous pyridine (2.1 mL) was then added to the reaction mixture and stirred under inter atmosphere at ambient temperature for 2 h. The solvent was removed in vacuum. The residue was dissolved in chloroform and precipitated with hexane. The supernatant was decanted off and the residual oil was dissolved in chloroform, washed with water and 0.1 M HCl. The organic layer was separated, dried over sodium sulphate. The HPLC peak with retention time 15 min corresponds to product **10** that was further confirmed with NMR and mass spectra.

Percentage yield = 42%

^{1}H NMR ([d$_6$]-DMSO, 500 MHz): δ = 7.64 (m, 2 H, c-H, g-H), 7.45 (m, 4 H, e-H, f-H, j-H, i-H), 7.29 (m, 2 H, d-H, h-H), 6.53 (d, J = 17 Hz, 1H, r-H), 6.50 (d, J =17 Hz, t-H), 4.09 (t, J = 8.7 Hz, 2 H, k-H), 3.66 (s, 3 H, q-H), 2.22 (t, J = 9 Hz, 2 H, o-H), 1.8 (m, 2 H, l-H), 1.68 (s, 12 H, a-H, b-H), 1.55 (m, 2 H, n-H), 1.43 (m, 2 H, m-H) ppm.

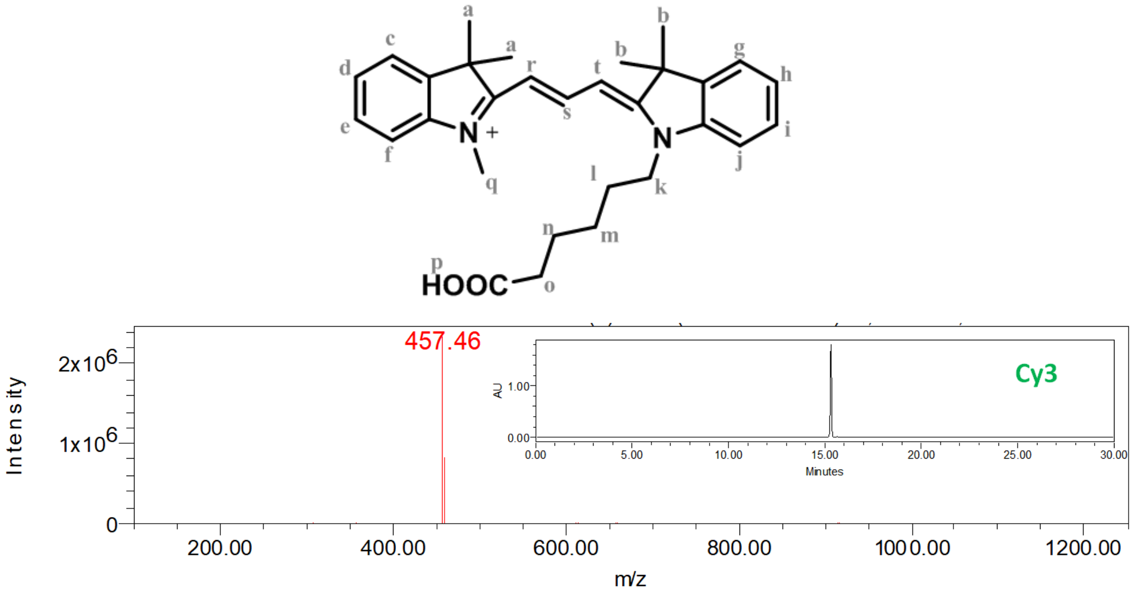

Figure 5.14: Mass spectra and HPLC chromatogram (inset) for **9** (Cy3).

5.4.3. Synthesis and characterization of peptides

Fluorescent dyes labelled and unlabelled peptides were synthesized on rink amide MBHA resin at 0.1 mmol scale following the standard microwave Fmoc-solid phase peptide synthesis (SPPS) protocols. For the synthesis of desired peptides first, peptide sequence VFFAK attached to the resin at *C*-terminal and free amine at *N*-terminal was synthesized. All the amino acids were coupled using DIC and oxyma in DMF. Fmoc deprotection was performed with 20% piperazine in DMF (containing 10% ethanol) in the microwave at 75

°C. Resin bound peptide was filtered, washed with DMF followed by dichloromethane and allowed to dry. Next, the spacer with C4 or C6 diisocyanate was coupled with peptide on both sides to furnish peptide-urea conjugate. The procedure for the synthesis of **P4** involve peptide (0.1 mmol) having free amine at the *N*-terminal and attached to resin at *C*-terminal suspended in dry DMF and triethylamine (0.125 mmol) and 1,4-diisocyanatobutane (0.05 mmol) was added. Similarly, for the synthesis of **P6**, triethylamine (0.125 mmol) and hexamethylene diisocyanate (0.05 mmol) was added to the peptidyl resin in DMF. The resin solution was kept for stirring at room temperature for 8 h.

For obtaining unlabelled peptides, after coupling the obtained peptide was cleaved from resin using 10 mL cleaving solution: (TFA)/TIPS/Water (95: 2.5: 2.5, v/v/v)). The mixture was shaken for 3 h at room temperature followed by removal of the resin through filtration. The filtrate was concentrated to a volume of approximately 1 mL and the resultant residue was precipitated by drop-wise addition of chilled diethyl ether. The precipitated product was centrifuged for 15 min at 7000 rpm at 4 °C. The precipitates were washed 3 times with cold diethyl ether and air dried.

However, for further coupling of the fluorescent dye molecules to the peptide, the following procedure was followed. The side chain deprotection of Lys(Alloc) residue was selectively deprotected. The resin coupled peptide (0.1 mmol) was taken and a mixture of $Pd(OAc)_2$ (0.3 equiv), PPh_3 (1.5 equiv), *N*-methylmorpholine (NMM) (10 equiv), and $PhSiH_3$ (10 equiv) in dry DCM (10 mL) was added to the peptidyl resin and stirred at room temperature for 12 h. After that, resin was filtered and washed thoroughly with THF, DMF, diethyldithiocarbamate (DEDTC), DMF and DCM. Now, the obtained peptidyl-resins (0.1 mmol) with free amine group (of lysine side chain) was swollen in dry DMF (10 mL) followed by the addition of HBTU (1 equiv) and DIPEA (1.5 equiv) and fluorescent dye (Cy3 or Cy5) (1 equiv). In total four fluorescent peptides were synthesized with distinct spacer and fluorophore: **P4Cy3**, **P6Cy3**, **P4Cy5** and **P6Cy5**. The resin suspension was shaken for 5 h and filtered. After filtration, the resin was washed with DMF and DCM, and air dried. Finally, the peptides were cleaved from the resin using 10 mL of cleavage cocktail solution (TFA/TIPS/Water (95: 2.5: 2.5, v/v/v)) and precipitated in cold diethyl ether.

According to the above synthesis procedure, the probability of achieving peptides with dye coupled on both ends is very high. However, through analytical HPLC_MS, we observed that single dye coupled peptides were major product, therefore we isolated the peak corresponding to single dye couple peptides. For recording HPLC, all peptides were re-dissolved in CH_3CN/H_2O (1:1) and purified by semi-preparative reverse phase HPLC with mobile phase acetonitrile and water containing 0.1% formic acid and lyophilized. The mass of these peptides was confirmed by ESI-MS. The standard gradient used for analytical HPLC for all peptides was 5 → 95% CH_3CN in H_2O (0.1% HCOOH additive) with a flow rate of 1 mL/min over 15 min. Further, the peptides were re-dissolved in DMF to erase the self-assembling history created while performing HPLC purification. The peptides were stored at -20 °C.

P4: Calculated exact mass for $C_{70}H_{102}N_{16}O_{12}$ = 1358.79, In positive mode: found $[MH]^{2+}$ = 680.43

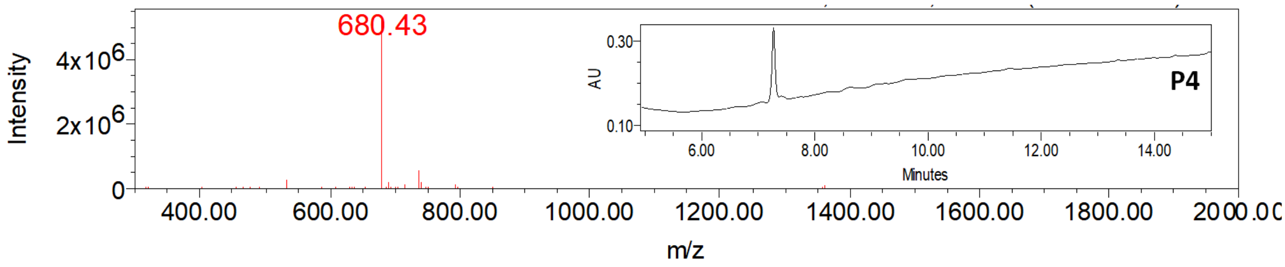

P6: Calculated exact mass for $C_{72}H_{106}N_{16}O_{12}$ = 1386.82, In positive mode: found $[MH]^{2+}$ = 694.45

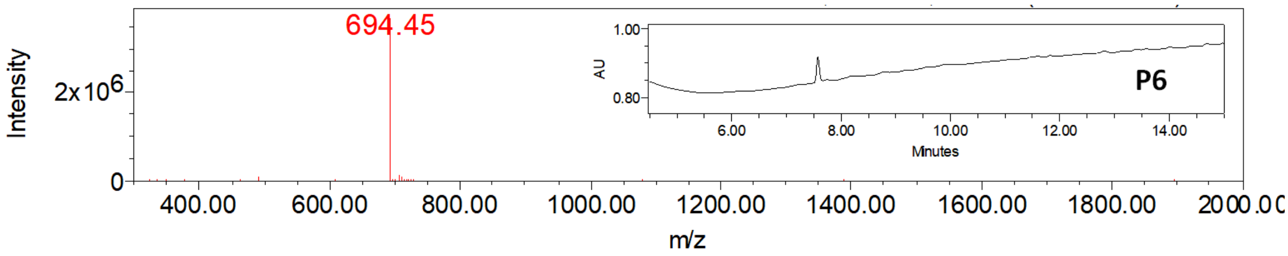

P4Cy3: Calculated exact mass for $C_{100}H_{139}N_{18}O_{13}^{+}$ = 1800.08, In positive mode: found $[MH]^{2+}$ = 900.15

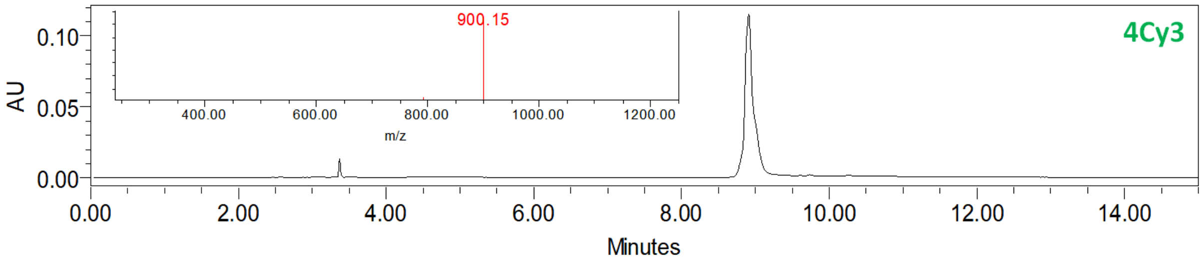

P6Cy3: Calculated exact mass for $C_{102}H_{143}N_{18}O_{13}^+$ = 1828.11, In positive mode: found $[MH]^{2+}$ = 914.22

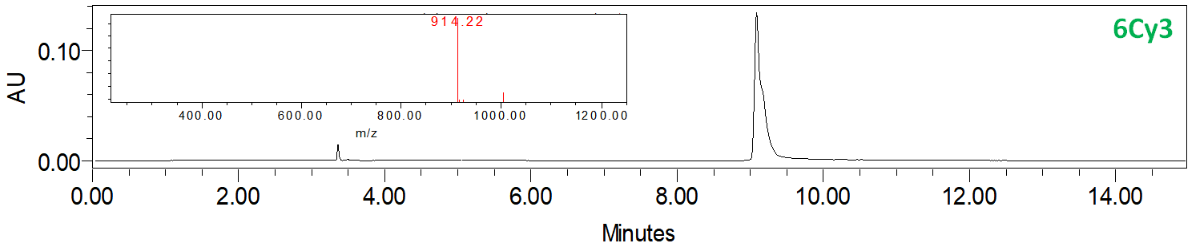

P4Cy5: Calculated exact mass for $C_{102}H_{141}N_{18}O_{13}^+$ = 1826.09, In positive mode: found $[MH]^{2+}$ = 913.17

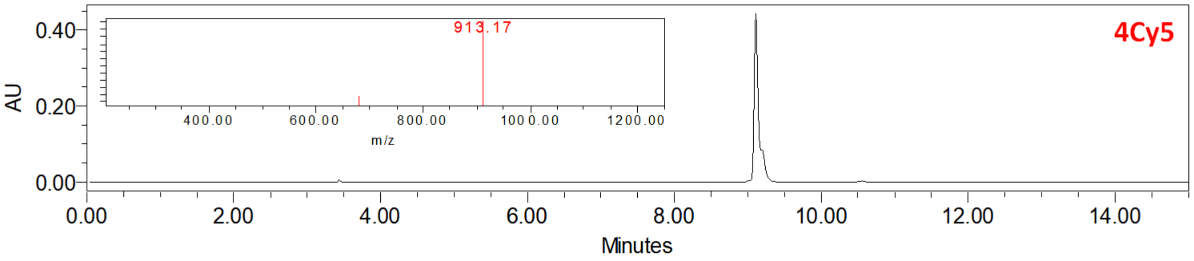

P6Cy5: Calculated exact mass for $C_{104}H_{145}N_{18}O_{13}^+$ = 1854.12, In positive mode: found $[MH]^{2+}$ = 927.21

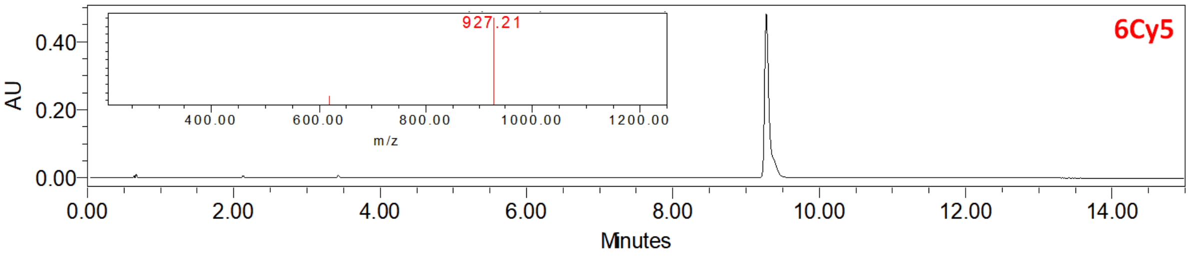

5.4.4. Self-assembly of peptides

Purified unlabelled peptides (**P4** and **P6**) and the fluorescent dye labelled peptides (**P4Cy3**, **P4Cy5**, **P6Cy3** and **P6Cy5** in concentration = 2 mM were taken in 5% ACN-water and mechanically agitated for 1-2 min to dissolve at room temperature. After incubation for a day, AFM and SIM-super-resolution images were recorded to observe the formation of self-assembled peptide nanofibers mediated by strong hydrogen bonding among urea and amides and π-π interactions among phenylalanine side chain.

In solvent composition of 50% acetonitrile (ACN) in water, the peptides were present in monomeric form. For further self-assembly, the above solution was injected into water to render solvent composition of 5% acetonitrile in water. Typically, 10 µL of 20 mM peptide solution in ACN-water (1:1) was injected to 90 μL of water to obtain concentration of peptide to be 2 mM in 5% ACN-water.

Peptides are completely soluble in DMSO and do not form self-assembled nanostructures.

5.4.5. Fluorescence spectroscopy

Fluorescence emission spectra were recorded using FS5 spectrofluorometer from Edinburgh instruments. Spectra were recorded with scan slit and offset slit of 2 nm each with a dwell time of 0.1 s at 25 °C. 100 μL solution of donor peptide (**P4Cy3** or **P6Cy3**, concentration = 200 μM) and acceptor peptide (**P4Cy5** or **P6Cy5**, concentration = 200 μM) were mixed together to render each of their final concentration of 50 μM and total peptide concentration of 100 μM. 2 μL of 2 mM stock of donor peptide (**P4Cy3** or **P6Cy3**, concentration = 200 μM) and acceptor peptide (**P4Cy5** or **P6Cy5**, concentration = 200 μM) solution in DMSO was added to 200 μL water to render final concentration of fluorescent probe 50 μM. The mixture was vortexed for 2 min and incubated for one day. The solution was excited at 550 nm and emission spectra were recorded for the range of 556-800 nm.

The degree of self-sorting was estimated as:

$$Self - sorting = \left(1 - \frac{Em_{Matching} - Em_{Blank}}{Em_{Non-matching} - Em_{Blank}}\right).100\%$$

Where, $Em_{Matching}$ is the emission intensity at 673 nm for matching spacer (**P4Cy3** and **P4Cy5**), $Em_{Non\text{-}matching}$ is the emission intensity in case of non-matching spacer (**P4Cy3** and **P6Cy5**) and Em_{Blank} is the intensity at 653 nm without the addition of acceptor (**P4Cy3**).

5.4.6. Fluorescence microscopy (CLSM and SIM)

Confocal laser scanning microscopy images were taken with LSM 880 (Carl Zeiss) equipped with an confocal detector. The samples were excited with 561 and 642 lasers, respectively. The fluorescence images of the fibres were acquired using an inverted Zeiss ELYRA PS1 microscope in Structured Illumination mode. Two lasers were used for the experiments: 561 nm (source: 200 mW) and 642 nm (source: 150 mW) for excitation of the respective fluorophores. Imaging experiments were performed using a Zeiss oil–immersion objective (Plan–apochromat DIC 63×/1.40 Oil DIC M27, numerical aperture (NA) 1.40 oil) with 100 ms exposure time and 5% of the LASER power for both the channels. Fluorescence light was spectrally filtered with emission filters (MBS– 561+EF BP 570–

650/LP 750 for laser line 561 and MBS–642+EF LP 655 for laser line 642) and imaged using a PCO edge sCMOS camera. Structured illumination images were processed using structured illumination analysis package of Zen2.0 software (from Zeiss). Additional image analysis and colour adjustments were performed using *ImageJ* and *Origin 8.5* softwares.

10 µL of 0.5 mM fluorescent peptide amphiphiles in water were drop-casted onto a glass slide. A clean coverslip was placed on top of it and proceed for CLSM or super-resolution microscopy using structured illumination method. For co-assembled fibers, the two-component peptide **P4Cy3** & **P6Cy5** or **P4Cy3** & **P6Cy5** were incubated at room temperature to form supramolecular nanofibers in 5% ACN-water. For self–sorted fiber, the peptide pair of **P4Cy3** & **P6Cy5** or **P4Cy3** & **P6Cy5** in 5% ACN-water was kept un-agitated at room temperature. The fluorescent nanofibrous solution (10 µL) was drop-casted on a glass slide and covered with coverslip. The slides were kept at room temperature for overnight drying before imaging. All these samples are further proceed for fluorescence microscopy and the images were recorded with 561 nm and 642 nm laser excitation at 630X.

5.4.7. Seeded supramolecular polymerization

Generation of Seed: Pre-assembled nanofibrous solution (400 µL) of dye coupled peptides (2 mM) were probe sonicated using QSonica (model number Q700, power 700 watts and frequency 20 kHz) probe Sonicator using 4417 number microtip at an amplitude of 15% for ~2 minutes.

Seeded growth of fibers: The peptide amphiphiles were taken in DMSO with no self-assembled nanostructures. For seeding experiments, peptide conjugated to one coloured dye in DMSO was injected into the aqueous solution of the seeds labelled with alternate coloured dye rendering the final solvent composition of 2% DMSO in water. This solution was incubated un-agitated for one day at room temperature. The growth of the fibers was ascertained from SIM images.

5.5. References

1. G. Vantomme and E. W. Meijer, *Science*, 2019, **363**, 1396-1397.
2. T. F. A. de Greef and E. W. Meijer, *Nature*, 2008, **453**, 171-173.
3. E. R. Draper and D. J. Adams, *Chem. Soc. Rev.*, 2018, **47**, 3395-3405.
4. P. Besenius, *J. Polym. Sci. A: Polym. Chem.*, 2017, **55**, 34-78.

5. J. Boekhoven, M. Koot, T. A. Wezendonk, R. Eelkema and J. H. van Esch, *J. Am. Chem. Soc.*, 2012, **134**, 12908-12911.
6. A. Pal, P. Besenius and R. P. Sijbesma, *J. Am. Chem. Soc.*, 2011, **133**, 12987-12989.
7. A. Heeres, C. van der Pol, M. Stuart, A. Friggeri, B. L. Feringa and J. van Esch, *J. Am. Chem. Soc.*, 2003, **125**, 14252-14253.
8. Z. He, W. Jiang and C. A. Schalley, *Chem. Soc. Rev.*, 2015, **44**, 779-789.
9. M. M. Safont-Sempere, G. Fernández and F. Würthner, *Chem. Rev.*, 2011, **111**, 5784-5814.
10. S. Onogi, H. Shigemitsu, T. Yoshii, T. Tanida, M. Ikeda, R. Kubota and I. Hamachi, *Nat. Chem.*, 2016, **8**, 743-752.
11. H. Shigemitsu, T. Fujisaku, W. Tanaka, R. Kubota, S. Minami, K. Urayama and I. Hamachi, *Nat. Nanotechnol.*, 2018, **13**, 165-172.
12. K. L. Morris, L. Chen, J. Raeburn, O. R. Sellick, P. Cotanda, A. Paul, P. C. Griffiths, S. M. King, R. K. O'Reilly, L. C. Serpell and D. J. Adams, *Nat. Commun.*, 2013, **4**, 1480.
13. E. R. Draper, E. G. B. Eden, T. O. McDonald and D. J. Adams, *Nat. Chem.*, 2015, **7**, 848-852.
14. D. J. Cornwell, O. J. Daubney and D. K. Smith, *J. Am. Chem. Soc.*, 2015, **137**, 15486-15492.
15. A. Sandeep, V. K. Praveen, K. K. Kartha, V. Karunakaran and A. Ajayaghosh, *Chem. Sci.*, 2016, **7**, 4460-4467.
16. J. van Herrikhuyzen, A. Syamakumari, A. P. H. J. Schenning and E. W. Meijer, *J. Am. Chem. Soc.*, 2004, **126**, 10021-10027.
17. B. Narayan, K. K. Bejagam, S. Balasubramanian and S. J. George, *Angew. Chem. Int. Ed.*, 2015, **54**, 13053-13057.
18. D. Görl, X. Zhang, V. Stepanenko and F. Würthner, *Nat. Commun.*, 2015, **6**, 7009.
19. A. Pal, S. Karthikeyan and R. P. Sijbesma, *J. Am. Chem. Soc.*, 2010, **132**, 7842-7843.
20. A. Sarkar, S. Dhiman, A. Chalishazar and S. J. George, *Angew. Chem. Int. Ed.*, 2017, **56**, 13767-13771.
21. G. Yu, X. Yan, C. Han and F. Huang, *Chem. Soc. Rev.*, 2013, **42**, 6697-6722.
22. L. Albertazzi, D. van der Zwaag, M. A. Leenders Christianus, R. Fitzner, W. van der Hofstad Remco and E. W. Meijer, *Science*, 2014, **344**, 491-495.
23. R. M. P. da Silva, D. van der Zwaag, L. Albertazzi, S. S. Lee, E. W. Meijer and S. I. Stupp, *Nat. Commun.*, 2016, **7**, 11561.
24. W. Zhang, W. Jin, T. Fukushima, A. Saeki, S. Seki and T. Aida, *Science*, 2011, **334**, 340-343.
25. B. Adelizzi, A. Aloi, A. J. Markvoort, H. M. M. Ten Eikelder, I. K. Voets, A. R. A. Palmans and E. W. Meijer, *J. Am. Chem. Soc.*, 2018, **140**, 7168-7175.
26. X. Wang, G. Guerin, H. Wang, Y. Wang, I. Manners and A. Winnik Mitchell, *Science*, 2007, **317**, 644-647.
27. F. H. Schacher, P. A. Rupar and I. Manners, *Angew. Chem. Int. Ed.*, 2012, **51**, 7898-7921.
28. H. Qiu, Y. Gao, V. A. Du, R. Harniman, M. A. Winnik and I. Manners, *J. Am. Chem. Soc.*, 2015, **137**, 2375-2385.
29. S. H. Jung, D. Bochicchio, G. M. Pavan, M. Takeuchi and K. Sugiyasu, *J. Am. Chem. Soc.*, 2018, **140**, 10570-10577.
30. W. Wagner, M. Wehner, V. Stepanenko and F. Würthner, *J. Am. Chem. Soc.*, 2019, **141**, 12044-12054.
31. A. Sarkar, R. Sasmal, C. Empereur-mot, D. Bochicchio, S. V. K. Kompella, K. Sharma, S. Dhiman, B. Sundaram, S. S. Agasti, G. M. Pavan and S. J. George, *J. Am. Chem. Soc.*, 2020, **142**, 7606-7617.
32. A. Sarkar, T. Behera, R. Sasmal, R. Capelli, C. Empereur-mot, J. Mahato, S. S. Agasti, G. M. Pavan, A. Chowdhury and S. J. George, *J. Am. Chem. Soc.*, 2020, **142**, 11528-11539.
33. M. Gerowska, L. Hall, J. Richardson, M. Shelbourne and T. Brown, *Tetrahedron*, 2012, **68**, 857-864.
34. X. Jia, Q. Chen, Y. Yang, Y. Tang, R. Wang, Y. Xu, W. Zhu and X. Qian, *J. Am. Chem. Soc.*, 2016, **138**, 10778-10781.
35. M. V. Kvach, A. V. Ustinov, I. A. Stepanova, A. D. Malakhov, M. V. Skorobogatyi, V. V. Shmanai and V. A. Korshun, *Eur. J. Org. Chem.*, 2008, **2008**, 2107-2117.

Publications

1. *Enzyme responsive chiral self-sorting in amyloid-inspired minimalistic peptide amphiphiles. **Gupta, D.;** Sasmal, R.; Singh, A.; Joseph, J. P.; Miglani, C.; Agasti, S. S.; Pal, A. *Nanoscale*, 2020, **12**, 18692-18700.

2. *Photochemically sequestered off-pathway dormant states of peptide amphiphiles for predictive on-demand piezoresponsive nanostructures. **Gupta, D.**; Bhatt. A.; Gupta, V.; Miglani, C.; Joseph, J. P.; Ralhan, J.; Mandal, D.; Ali, M. E.; Pal, A. *Chem. Mater.*, 2022, 34, 10, 4456-4470.

3. *Stimuli-responsive self-assembly-disassembly in peptide amphiphiles to endow block-co-fibers and tunable piezoelectric response. **Gupta, D.**; Gupta, V.; Nath, D.; Miglani, C.; Ali, M. E.; Pal, A. *ACS Appl. Mater. Interfaces*, 2022, Accepted.

4. *Fidelity of urea spacer towards self-sorting and co-block formation in peptide amphiphiles. **Gupta, D.**; Kalita, S.; Agasti, S.S.; Pal, A. (under preparation).

5. Pathway driven self-assembly and living supramolecular polymerization in amyloid inspired peptide amphiphile. Singh, A.; Joseph J. P.; **Gupta, D.;** Sarkar, I.; Pal, A. *Chem. Commun.*, 2018, **54**, 10730-10733.

6. Tandem interplay of the host-guest interaction and photoresponsive supramolecular polymerization to 1D and 2D functional peptide materials. Joseph J. P.; Singh, A.; **Gupta, D**.; Miglani, C.; Pal, A. *ACS Appl. Mater. Interfaces*, 2019, **11**, 28213−28220.

7. Photoresponsive chain collapse in flexo-rigid functional copolymer to modulate self-healing behavior. Joseph, J. P.; Miglani, C.; Singh, A.; **Gupta, D.;** Pal, A. *Soft Matter*, 2020, **16**, 2506-2515.

8. Delineating synchronized control of dynamic covalent and non-covalent interactions for polymer chain collapse towards cargo localization and delivery. Joseph J. P.; Miglani, C.; Bhatt A.; Ray D.; Singh, A.; **Gupta, D**.; Aswal V. K.; Ali, M. E.; Pal, A. *Polym. Chem.*, 2021, **12**, 1002-1013.

9. Pathway-driven peptide-bioglass nanocomposites as dynamic and self-healable matrix. Gupta, N.; Singh, A.; Dey, N.; Chattopadhyay, S.; Joseph, J. P.; **Gupta, D.;** Ganguli, M.; Pal A. *Chem. Mater.* 2021, **33**, 2, 589–599.

10. Photo-thermally Switchable Peptide Nanostructures towards Modulating Catalytic Hydrolase Activity. Singh, A., Joseph, J. P., **Gupta, D.;** Miglani, C.; Mavlankar, N.; Pal, A. *Nanoscale*, 2021, **13**, 13401-13409.

11. Modulation of flexo-rigid balance in photoresponsive thymine grafted copolymers towards designing smart healable coating. Miglani, C.; Joseph, J. P.; Singh, A.; **Gupta, D.**; Pal, A. *RSC Adv*., 2021, **11**, 39376-39386.

12. Unraveling on-demand strain-stiffening in nanofibrous peptide−polymer conjugates to mimic contractility in actinomyosin networks. Joseph, J. P.; Gupta, N.; Miglani, C.; Nath, D.; Singh, A.; **Gupta, D.;** Pal, A. *Chem. Mater.*, 2022, 34, 10, 4364-4374.

13. Anion responsive transient self-assembly. Pradhan, M. K.; **Gupta, D.**; Miglani, C.; Pal, A; Shrivastava, A. (under review)

(N.B. * Articles included in this thesis)

Awards

1. ***Best Poster Presentation*** Award in 8th Indian Peptide Symposium (2021) at Indian Institute of Science, Bengaluru.

2. ***Best Oral Presentation*** award in Nanotechnology for better living-2021 at National Institute of Technology, Srinagar.

3. ***Best Poster Presentation*** Award in 1st Annual Meeting of Chemical Biology Unit organized by Institute of Nano Science and Technology, Mohali.

4. ***Best Poster Presentation*** Award in 26th CRSI-National symposium in chemistry 2020 held at VIT, Vellore.

5. ***Best Poster Presentation*** Award in 10th Bengaluru INDIA NANO 2018 held at The Lalit Ashok, Bengaluru.

About the Author

Deepika Gupta
Ph.D. Research Scholar
Institute of Nano Science and Technology (INST) &
Indian Institute of Science Education and Research (IISER)
Mohali, Punjab, India

Deepika Gupta was born on 9th January, 1993 in Kapurthala, Punjab (India). She obtained her B.Sc. degree (2013) from DAV College, Jalandhar and M.Sc. degree in Chemistry (2015) at Dr. B. R. Ambedkar NIT Jalandhar under the supervision of Dr. Rajeev Jindal. During her M.Sc., she pursued a research internship at IIT Kanpur in lab of Dr. SP Rath with summer fellowship from Indian Academy of Sciences. She started her Ph.D. on July 2016 with Dr. Asish Pal at INST Mohali. Her research interests include minimalistic peptide amphiphiles to impart precise structural control and compartmentalization via supramolecular polymerization. During her Ph.D. she authored various research articles in reputed international journals. She had also presented her research work through poster and oral lectures in a number of prestigious national and international conferences.